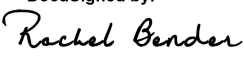


## Distribution Agreement

In presenting this thesis or dissertation as a partial fulfillment of the requirements for an advanced degree from Emory University, I hereby grant to Emory University and its agents the non-exclusive license to archive, make accessible, and display my thesis or dissertation in whole or in part in all forms of media, now or hereafter known, including display on the world wide web. I understand that I may select some access restrictions as part of the online submission of this thesis or dissertation. I retain all ownership rights to the copyright of the thesis or dissertation. I also retain the right to use in future works (such as articles or books) all or part of this thesis or dissertation.

DocuSigned by:  
Signature:   
D0F5937E1797493...

Rachel Bender  
Name

3/15/2023 | 10:38 AM EDT  
Date

**Title**            Expanding the molecular toolkit: From scaffold synthesis to measuring mechanotransduction

**Author**           Rachel Bender

**Degree**           Doctor of Philosophy

**Program**        Chemistry

**Approved by the Committee**

Khalid Salaita

*Advisor*

Brian Dyer

*Committee Member*

Adam Marcus

*Committee Member*

**Accepted by the Laney Graduate School**

Kimberly Jacob Arriola, PhD, MPH

*Dean, James T. Laney School of Graduate Studies*

**EXPANDING THE MOLECULAR TOOLKIT TO MEASURE CELL FORCE: FROM  
SCAFFOLD SYNTHESIS TO MEASURING MECHANOTRANSDUCTION**

By

Rachel Lynn Bender  
B.A., Capital University, 2017

Advisor: Khalid Salaita, Ph.D.

An abstract of a  
dissertation submitted to the Faculty of the  
James T. Laney School of Graduate Studies of Emory University  
in partial fulfillment of the requirements for the degree of  
Doctor of Philosophy in Chemistry  
2023

## ABSTRACT

### EXPANDING THE MOLECULAR TOOLKIT TO MEASURE CELL FORCE: FROM SCAFFOLD SYNTHESIS TO MEASURING MECHANOTRANSDUCTION

By

Rachel Lynn Bender

Mechanical communication is a concept central to all life. Cells transmit and transduce piconewton level forces with the extracellular matrix and it is these forces that guide cell function. Through a process known as mechanotransduction, cells use the receptors that coat their cell membrane to convert mechanical cues from their surroundings into biochemical responses that control the force generating machinery inside the cell. Foundational work focused on studying the forces generated by entire cells by measuring the amount of deformation they caused on different substrates. Indeed, the techniques used in these studies are still widely used today; however, the focus of this dissertation is on another, more refined, class of techniques known as molecular force sensors which provide information on the forces mediated through discrete interactions. One class of these sensors are those that are immobilized onto a scaffold and measure the forces generated by external cell receptors. In Chapter 2, we describe the characterization of the trans-cyclooctene/tetrazine reaction for producing scaffolds to immobilize biomolecules such as molecular force sensor. We demonstrate that these scaffolds are degradation resistant and can be homogeneously functionalized with molecular sensors for measuring the integrin generated forces of fibroblasts. In Chapter 3, we use these scaffolds to immobilize a new class of force probes constructed of peptide nucleic acids (PNA), a synthetic nucleic acid that is resistant to enzyme degradation and binds with a high affinity to other oligonucleotides. We demonstrate that PNA-based force sensors improve the resolution of tension imaging in aggressive cancer cell lines, and likely report on the upper levels of integrin mediated cell force. Finally, in Chapter 4, we describe the synthesis of a new reversible shearing DNA probe to study the effect that molecular force extension curves have on mechanotransduction. We demonstrate that integrins are sensitive to the geometries of their ligands and are capable of detecting abrupt changes in resistive force that occur throughout the extracellular matrix. In summary, this work contributes new tools for studying cell mechanical forces over extended time and force ranges and expands our understanding of the role ligand geometry plays in receptor mediated mechanotransduction.

**EXPANDING THE MOLECULAR TOOLKIT TO MEASURE CELL FORCE: FROM  
SCAFFOLD SYNTHESIS TO MEASURING MECHANOTRANSDUCTION**

By

Rachel Lynn Bender  
B.A., Capital University, 2017

Advisor: Khalid Salaita, Ph.D.

A dissertation submitted to the Faculty of the  
James T. Laney School of Graduate Studies of Emory University  
in partial fulfillment of the requirements for the degree of  
Doctor of Philosophy in Chemistry  
2023

## ACKNOWLEDGEMENTS

I would like to thank my advisor, Dr. Khalid Salaita, for his mentorship and support throughout my Ph.D. Khalid's scientific creativity is inspiring and I'm grateful to have had the opportunity to train with him. I have also appreciated the support of my committee members, Dr. Brian Dyer and Dr. Adam Marcus and their valuable insight into my projects and graduate career. I would also like to thank Ms. Joan Lewis, my high school chemistry teacher, and Dr. Tracey Murray, my undergraduate biochemistry professor for inspiring me to pursue chemistry and ultimately my Ph.D. I'm grateful to know these incredible women in science.

My graduate experience would not have been the same without my lab-mates in the Salaita Lab. I was fortunate to have Dr. Josh Brockman and Dr. Anna Kellner as mentors throughout my graduate experience, and will always be thankful for their scientific input, friendships, and allowing me to illegally sub-let their bench space when I first began. I am also grateful for my time working with Dr. Hiroaki Ogasawara who became a great mentor and friend in the lab, and whom I was fortunate to work closely with for several years of my graduate career. Graduate school would not have been the same without the "Atlanta family" that I've made outside of graduate school. I have been fortunate to find local families at both at my church and in several orchestras and appreciate the support of everyone who has been part of this journey.

Lastly, I would like to thank my parents for their love and support. From a young age they encouraged my questions and curiosities, allowing me to incessantly share "fun facts" that I had learned. I don't know that they envisioned that behavior leading to me becoming a student for 23 years, but I will always be thankful to have them as my cheerleaders.

## TABLE OF CONTENTS

<b>DISTRIBUTION AGREEMENT</b>	<b>i.</b>
<b>APPROVAL SHEET</b>	<b>ii.</b>
<b>ABSTRACT COVER PAGE</b>	<b>iii.</b>
<b>ABSTRACT</b>	<b>iv.</b>
<b>COVER PAGE</b>	<b>v</b>
<b>ACKNOWLEDGEMENTS</b>	<b>vi.</b>
<b>TABLE OF CONTENTS</b>	<b>vii.</b>
<b>LIST OF TABLES</b>	<b>xi.</b>
<b>LIST OF FIGURES</b>	<b>xii.</b>
<b>LIST OF SCHEMES</b>	<b>xiii.</b>
<b>CHAPTER 1: Introduction</b>	<b>1</b>
<b>1.1. Cell structure and mechanotransduction</b>	<b>2</b>
<b>1.2. Measuring cell forces using synthetic tension sensors</b>	<b>6</b>
1.2.1 Fluorescence in synthetic tension sensors	7
1.2.2 Force response behavior of synthetic tension sensors	10
1.2.3 Analog surface immobilized tension sensors	11
1.2.4 Digital surface immobilized tension sensors	13
1.2.4.1 DNA hairpin sensors	14
1.2.4.2 DNA rupture sensors	18
<b>1.3 Limitations of existing nucleic acid force sensors</b>	<b>22</b>
1.3.1 Biostability	23
1.3.2 Measuring “real-time” cell integrin forces > 19 pN	23
<b>1.4 Dissertation scope and outline</b>	<b>25</b>
<b>CHAPTER 2: Surface tethering of biomolecules using the reaction between trans-cyclooctene and tetrazine</b>	<b>27</b>
<b>2.1. Abstract</b>	<b>27</b>
<b>2.2. Introduction</b>	<b>28</b>
<b>2.3. Results</b>	<b>32</b>
2.3.1 TCO/Tz iEDDA surfaces are more homogenous than Biotin/STVD surfaces	32
2.3.2 TCO/Tz iEDDA surfaces are more resistant to degradation than Biotin/STVD surfaces	37
2.3.3 TCO/Tz iEDDA surfaces are superior scaffolds for studying mechanotransduction	39
	<b>41</b>

## 2.4. Discussion

<b>CHAPTER 3 PNA tension probes expand the measurable force range of nucleic acid integrin force sensing technology</b>	<b>44</b>
<b>3.1 Abstract</b>	<b>44</b>
<b>3.2 Introduction</b>	<b>45</b>
3.2.1 Protein-based force sensors	46
3.2.2 Peptide nucleic acids (PNA)	49
3.2.3 Characterization of PNA	50
<b>3.3 Results</b>	<b>53</b>
3.3.1 Synthesis and design of PNA force sensors	53
3.3.2 Characterization of PNA force sensors	54
3.3.3 PNA sensors report on the forces generated by fibroblasts	58
3.3.4 PNA sensors report on the upper levels of integrin force generated by muscle cells	61
3.3.5 PNA force sensors report on cancer cell mechanics with improved resolution over DNA sensors	63
<b>3.4 Discussion</b>	<b>65</b>
<b>CHAPTER 4: Cell adhesion receptors detect the force-extension curve of their ligands</b>	<b>68</b>
<b>4.1 Abstract</b>	<b>68</b>
<b>4.2 Introduction</b>	<b>69</b>
4.2.1 Design of molecular force sensors	69
4.2.2 Modeling polymer behavior: force extension graphs	71
4.2.3 Polymer force-extension behaviors	73
4.2.4 Worm-like chain model	74
4.2.5 Molecular springs with secondary structure	76
4.2.6 How force influence the kinetics and thermodynamics of unfolding	77
4.2.7 Mechanotransduction depends on outside-in and inside-out signaling	80
4.2.8 Integrins detect the force-extension curve of their ligands	81
<b>4.3 Results</b>	<b>84</b>
4.3.1 Synthesis and design of reversible probes	84
4.3.2 RU and RS probes have identical $\Delta G$ 's of unfolding but differ in their molecular extension curves	86
4.3.3 Platelet integrin forces unfold RU but not RS probes	88
4.3.4 Fibroblast integrins unfold RS and RU probes in a time-dependent	89

fashion	
4.3.5 Fibroblasts show enhanced mechanical signal when cultured on RU <sub>cRGD</sub> probes compared to RS <sub>cRGD</sub> probes	91
4.3.6 Focal adhesions have lower turnover rates in fibroblasts cultured on RU <sub>cRGD</sub> probes compared to RS <sub>cRGD</sub> probes	94
<b>4.4 Discussion</b>	<b>97</b>
<b>CHAPTER 5: Conclusions and future outlook</b>	<b>105</b>
<b>5.1 Summary of Advances</b>	<b>105</b>
5.1.1 Discussion of biological limitations	107
<b>5.2 Outstanding questions and directions in developing nucleic acid nanotechnology for mechanobiology applications</b>	<b>108</b>
<b>5.3 Areas of exploration in mechanobiology</b>	<b>109</b>
<b>APPENDIX A SUPPORTING INFORMATION</b>	<b>112</b>
<b>A.1 Characterizing the trans-cyclooctene and tetrazine iEDDA reaction for use in surface modifications for mechanobiology applications</b>	<b>112</b>
<b>A.1.1 Materials</b>	<b>112</b>
<b>A.1.2 Equipment</b>	<b>113</b>
<b>A.1.3 Methods</b>	<b>113</b>
A.1.3.1 Synthesis of tension probes	113
A.1.3.2 Surface preparation	115
A.1.3.3 DNA hybridization	115
A.1.3.4 Imaging chamber assembly	116
A.1.3.5 Cell culture	116
A.1.3.6 Image acquisition and analysis	116
<b>A.1.4 Figures, tables, and schemes</b>	<b>119</b>
<b>A.2 PNA tension probes expand the measurable force range of nucleic acid force sensing technology</b>	<b>122</b>
<b>A.2.1 Materials</b>	<b>122</b>
<b>A.2.2 Equipment</b>	<b>123</b>
<b>A.2.3 Methods</b>	<b>123</b>
A.2.3.1 PNA oligomer synthesis	123
A.2.3.2 Tension probe synthesis	124
A.2.3.3 Surface preparation	126
A.2.3.4 DNA hybridization	127

A.2.3.5	Imaging chamber assembly	127
A.2.3.6	Cell culture	127
A.2.3.7	Image acquisition and analysis	127
<b>A.2.4</b>	<b>Note 1 – van't Hoff analysis of PNA duplexes</b>	<b>128</b>
<b>A.2.5</b>	<b>Figures, table, and schemes</b>	<b>129</b>
<b>A.3</b>	<b>Cell adhesion receptors detect the force-extension curve of their ligands</b>	<b>135</b>
<b>A.3.1</b>	<b>Materials</b>	<b>135</b>
<b>A.3.2</b>	<b>Equipment</b>	<b>136</b>
<b>A.3.3</b>	<b>Methods</b>	<b>137</b>
A.3.3.1	Synthesis of substructures for tension probes	137
A.3.3.2	Synthesis of DNA tension probes	142
A.3.3.3	Synthesis of fluorescently labeled human fibronectin	147
A.3.3.4	Electron Spray Ionization (ESI) mass spectroscopy	147
A.3.3.5	Characterization of reversible probes	148
A.3.3.6	Surface preparation	148
A.3.3.7	DNA hybridization	148
A.3.3.8	Imaging chamber assembly	149
A.3.3.9	Fibroblast staining	149
A.3.3.10	Platelet handling	151
A.3.3.11	Cell culture	151
A.3.3.12	Cell transfection	151
A.3.3.13	Image acquisition and analysis	152
<b>A.3.4</b>	<b>Note 2 – van't Hoff analysis of RS and RU probes</b>	<b>154</b>
<b>A.3.5</b>	<b>Note 3 – oxDNA simulation</b>	<b>157</b>
<b>A.3.6</b>	<b>Figures, tables, and schemes</b>	<b>160</b>
		<b>178</b>
	<b>APPENDIX B: GLOSSARY AND COMMON ABBREVIATIONS</b>	
	<b>APPENDIX C: PERMISSIONS</b>	<b>184</b>
	<b>REFERENCES</b>	<b>196</b>

## LIST OF TABLES

Table A1	Oligonucleotide sequences and chemical structures of modifications used in Chapter 2	119
Table A2	Oligonucleotides used in Chapter 3	129
Table A3	Oligonucleotides used in Chapter 4	160
Table A4	Thermodynamic parameters of RS probes at indicated concentrations in 1X PBS	164
Table A5	Thermodynamic parameters of RU probes at indicated concentrations in 1X PBS	165

## LIST OF FIGURES

Figure 1	Cells physically deform their substrates	2
Figure 2	Structure of a cell membrane	3
Figure 3	Overview of the mechanotransduction mechanism	4
Figure 4	Mechanism of integrin activation	4
Figure 5	Timeline of tension sensor development	7
Figure 6	Jablonski diagram of fluorescence	8
Figure 7	Molecular sensor classifications	10
Figure 8	Schemes of analog MTFM PEG sensors	12
Figure 9	Structure of DNA hairpin tension sensor	14
Figure 10	Effects of G/C nucleobase content and loop size on the predicted F1/2 of hairpin tension sensors.	15
Figure 11	Initial DNA hairpin design and use	17
Figure 12	Schematic of a single oligonucleotide hairpin	18
Figure 13	Conformations of DNA rupture	18
Figure 14	Schematic of Tension Gauge Tether (TGT)	21
Figure 15	Schematic of reversible shearing probe	24
Figure 16	Common techniques for surface immobilization of biomolecules	30
Figure 17	Characterization of biotin and TCO coated glass surfaces	32
Figure 18	TCO/Tz iEDDA surfaces are more densely functionalized and more homogenous than Biotin/STVD surfaces	33
Figure 19	TCO/Tz iEDDA surfaces have reduced levels of non-specific binding of biomolecules than Biotin/STVD surfaces	34
Figure 20	Kinetics of DNA binding to Biotin/STVD and TCO/Tz iEDDA surfaces	36
Figure 21	TCO/Tz iEDDA surfaces are resistant to thermal degradation	38
Figure 22	TCO/Tz iEDDA surfaces are resistant to protease degradation	39
Figure 23	Biotin/STVD and TCO/Tz iEDDA surfaces as scaffolds for measuring cell force	40
Figure 24	Probe-based methods to measure cellular mechanotransduction events	46
Figure 25	Basic design of protein-based Genetically Encoded Tension Sensors (GETS)	47

Figure 26	Structure of the titin protein tension sensor	48
Figure 27	Structures of synthetic nucleic acids	49
Figure 28	Structural properties of peptide nucleic acids (PNA)	50
Figure 29	Chemical structure of PNA and scheme of PNA force sensors	54
Figure 30	Thermodynamic characterization of PNA- and DNA-based force sensors	55
Figure 31	PNA force sensors are resistant to nuclease and protease degradation	57
Figure 32	PNA force sensors report on the forces generated by fibroblasts	59
Figure 33	Fibroblasts do not exert a $T_{Tol}$ large enough to rupture sPNA:PNA force sensors	60
Figure 34	PNA force sensors report on the upper levels of cell integrin force in muscle cells	62
Figure 35	PNA force sensors improve signal resolution of forces generated by cancer cells	64
Figure 36	Converting between force and energy	71
Figure 37	Model of a force extension curve	72
Figure 38	Extension behavior of protein and DNA	75
Figure 39	Models of ideal chains and worm-like chains	76
Figure 40	Reaction coordinate diagram of two-state model of polymer unfolding	78
Figure 41	Design and characterization of RS and RU probes	83
Figure 42	Synthesis of RS and RU probes	86
Figure 43	Thermodynamic parameters of RS and RU probes	88
Figure 44	Mouse platelets exert sufficient force to open $RU_{cRGD}$ probes	89
Figure 45	Mouse embryonic fibroblasts respond to $RS_{cRGD}$ and $RU_{cRGD}$ probes differently	90
Figure 46	Nuclear:cytoplasmic YAP is greater in MEFs cultured on $RU_{cRGD}$ probes	92
Figure 47	Fibronectin is greater in MEFs cultured on $RU_{cRGD}$ probes	93
Figure 48	Integrin activation is greater in MEFs cultured on $RU_{cRGD}$ probes	94
Figure 49	Tension turnover is higher in MEFs cultured on $RS_{cRGD}$ probes	95
Figure 50	Focal adhesion turnover is higher in MEFs cultured on $RS_{cRGD}$ probes	96
Figure 51	The force extension trajectory of RS probes perturbs mechanotransduction	100
Figure 52	Integrin activation is greatest in MEFs cultured on $T9_{cRGD}$ probes	101

Figure 53	Molecular clutch modeling reveals that cells form more active clutches on RU <sub>cRGD</sub> probes than RS <sub>cRGD</sub> probes	102
Figure 54	Changes in mechanotransduction are not due to a difference in force ramp rate on RS and RU probes	103
Figure A1	Chemical structures of modifications used in Chapter 2	119
Figure A2	HPLC characterization of DNA used in Chapter 2	120
Figure A3	Calibration curve used for determining molecular density of probes	121
Figure A4	Chemical structures of oligo modifications used in Chapter 3	129
Figure A5	General synthetic scheme for PNA oligomers	129
Figure A6	Synthesis of PNA and DNA force sensors	130
Figure A7	cRGD azide characterization	132
Figure A8	Tetrazine cRGD azide characterization	132
Figure A9	Chapter 3 DNA characterization	133
Figure A10	sPNA top characterization	133
Figure A11	HPLC trace of sPNA top C terminal TCO	133
Figure A12	sPNA top C terminal cRGD characterization	134
Figure A13	sPNA bottom N terminal Cy3B, N terminal methyltetrazine characterization	134
Figure A14	HPLC trace of uPNA bottom N terminal Cy3B, C terminal methyltetrazine	134
Figure A15	Chemical structures of oligo modifications used in Chapter 4	160
Figure A16	Characterization of Chapter 4 product 15	163
Figure A17	Characterization of Chapter 4 product 17	163
Figure A18	DNA thermal melting analysis reveals that RS and RU probes have identical $\Delta G$ at 37 °C	164
Figure A19	Force extension curves simulated by oxDNA software	165
Figure A20	Procedure for vinculin analysis using ImageJ	166
Figure A21	Reversible probes report on real-time tension signal	166
Figure A22	Culturing cells on tension probes does not alter cell biology	167
Figure A23	Stress fiber formation is higher in MEFs plated on RU <sub>cRGD</sub> probes	167
Figure A24	MEFs plated on irreversible shearing cRGD (IS <sub>cRGD</sub> ) probes have lower	168

	markers of mechanotransduction than MEFs plated on RS and RU probes.	
Figure A25	Total integrin $\beta 1$ levels are the same in cells plated on RS <sub>CRGD</sub> and RU <sub>CRGD</sub> probes	169
Figure A26	RS <sub>CRGD</sub> and RU <sub>CRGD</sub> probe density on glass surface.	169
Figure A27	Force extension curves of previously published work simulated by oxDNA software	170
Figure A28	Total integrin $\beta 1$ levels are the same in cells plated on RS <sub>GRGDS</sub> and RU <sub>GRGDS</sub> probes.	170
Figure A29	MEFs plated on RS <sub>GRGDS</sub> probes have higher nuclear:cytoplasmic YAP translocation than MEFs plated on RU <sub>GRGDS</sub> probes.	171
Figure A30	MEFs plated on T9 <sub>CRGD</sub> probes have higher nuclear:cytoplasmic YAP translocation than MEFs plated on RS <sub>CRGD</sub> probes.	171
Figure A31	Characterization of Chapter 4 product 1	172
Figure A32	Characterization of Chapter 4 product 2	172
Figure A33	Characterization of Chapter 4 product 3	172
Figure A34	Characterization of Chapter 4 product 4	173
Figure A35	Characterization of Chapter 4 product 5	173
Figure A36	Characterization of Chapter 4 product 6	173
Figure A37	Characterization of Chapter 4 product 7	174
Figure A38	Characterization of Chapter 4 product 8	174
Figure A39	Characterization of Chapter 4 product 9	174
Figure A40	Characterization of Chapter 4 product 10	175
Figure A41	Characterization of Chapter 4 product 11	175
Figure A42	Characterization of Chapter 4 product 12	175
Figure A43	HPLC trace of Chapter 4 product 13	176
Figure A44	Characterization of Chapter 4 product 14	176
Figure A45	Characterization of Chapter 4 product 16	176
Figure A46	Characterization of irreversible shearing probes used in Chapter 4	177

## LIST OF SCHEMES

Scheme A1	Synthetic scheme to generate reversible shearing and unzipping probes	161
Scheme A2	Synthesis of irreversible DNA probes	162

## CHAPTER 1 INTRODUCTION

*Adapted from Bender, R. L., Salaita, K. "Molecular Force Sensors", 2022, ACS In Focus*

It is well known that cells possess a "sense of taste." A cell's "sense of taste" can be used to sense changes in analyte concentration or pH and modulate a biochemical response to receptor binding. However, cells also possess a "sense of touch" that allows them to detect and respond to their physical environment. Right now, every cell in your body is pushing and pulling as part of its normal function. When you breathe, cells in your airway generate the forces required for lung expansion and fluid clearance. Every heartbeat causes expansion and contraction of blood vessels and associated cells and tissues. T cells generate mechanical forces as they move around to identify and kill invasive cells, cancer cells generate forces to migrate and metastasize to other areas of the body, and stem cells rely on mechanical cues to differentiate during development.

The idea that cells generate force and that these forces can regulate cell behavior was first noted in the 1800's.(2) However, nearly 100 years passed before the scientific community began developing the tools necessary to study such phenomena. Early studies demonstrated simply that individual cells could generate forces at measurable magnitudes. The first report of such a finding occurred in 1980 when the Harris lab measured mechanical forces generated by locomoting fibroblasts cultured on a layer of silicon that wrinkled when a cell generated force (Fig. 1).(3)

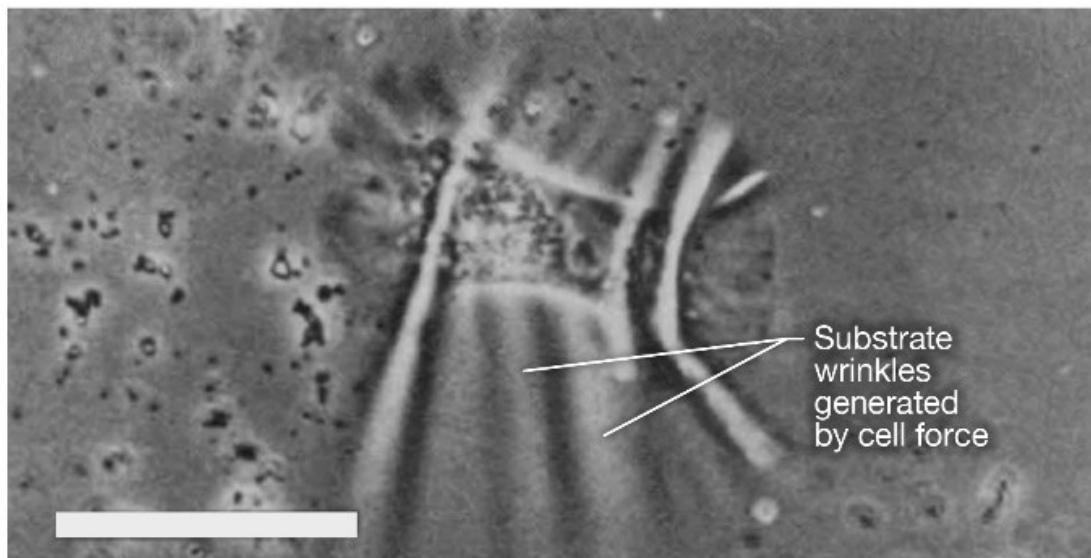


**Figure 1. Cells physically deform their substrates.** Fibroblasts cultured on a layer of silicon physically deformed the substrate as they were migrating. The wrinkles observed on the substrate demonstrated that cells are capable of mechanically altering their environment and served as a foundation for the field of molecular tension sensor development. Reprinted with permission from *Molecular Force Sensors*; Copyright 2022 American Chemical Society

This revolutionary finding catalyzed the field of mechanobiology and the desire to measure mechanical forces in cells led to the development of techniques such as traction force microscopy (TFM) and micropillar functionalized substrates, which rely on measuring the displacement of the substrate to determine the amount of stress exerted by cells.(4-6) These techniques are valuable tools for measuring the overall force generated by a population of cells, along with the force produced when cells migrate or divide. However, a cell's mechanical behavior is dynamic and involves a number of biochemical processes mediated by receptor-ligand interactions that cannot be captured using such bulk force measurements.

### 1.1 Cell structure and mechanotransduction

Receptor-ligand interactions that mediate the translation of mechanical information into biochemical information occur across the phospholipid membrane. In eukaryotic cells, the

phospholipid membrane is embedded with receptor molecules, ion channels, cholesterol, and an assortment of proteins and surrounds the cytoplasm containing proteins, nucleic acids, and organelles (**Fig. 2**).

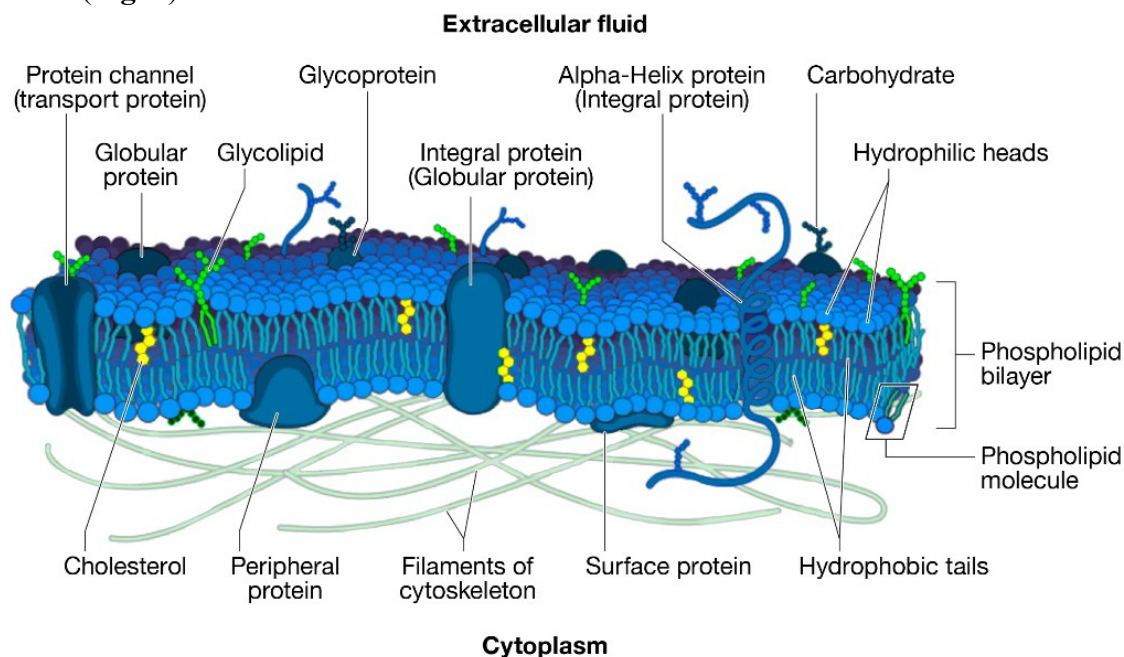


**Figure 2. Structure of a cell membrane.** The cell membrane serves as a barrier through which communication between the cytoplasmic components of a cell and the environment surrounding the cell occurs. The membrane is a complex arrangement of phospholipids, cholesterol, proteins, ion channels, and receptor molecules. Receptor molecules, such as integrins, sense mechanical input from the cell's surrounding environment, and transduce the mechanical signal into biochemical signals that guide cell fate. Reprinted with permission from *Molecular Force Sensors*; Copyright 2022 American Chemical Society

The cell is surrounded by the extracellular matrix (ECM), a collection of proteins, proteoglycans, and adhesive glycoproteins. Receptors, such as integrins, on the surfaces of the phospholipid membrane recognize these proteins and convert the mechanical signal into biochemical pathways that guide cell function and control focal adhesion formation, actin distribution, nuclear pore opening, gene expression, and protein production through a process known as mechanotransduction (**Fig. 3**). (7-9)

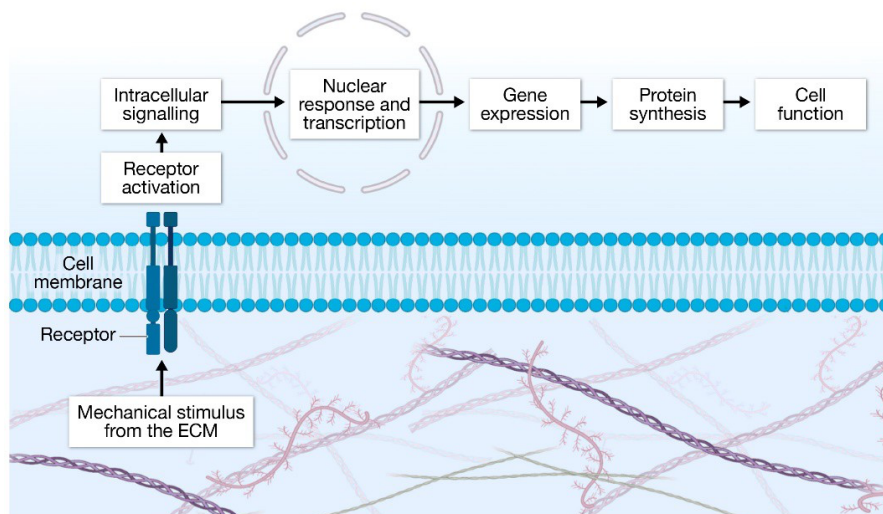


**Figure 3. Overview of the mechanotransduction mechanism.** Reprinted with permission from *Molecular Force Sensors*; Copyright 2022 American Chemical Society

During cell adhesion to the ECM, integrins undergo a conformational change that shifts the integrin from a low- affinity to high-affinity state for ligand binding (10, 11). When the integrin binds a ligand in the ECM, it activates a signaling cascade that results in the formation of focal adhesions and cell-surface attachment (**Fig. 4**).

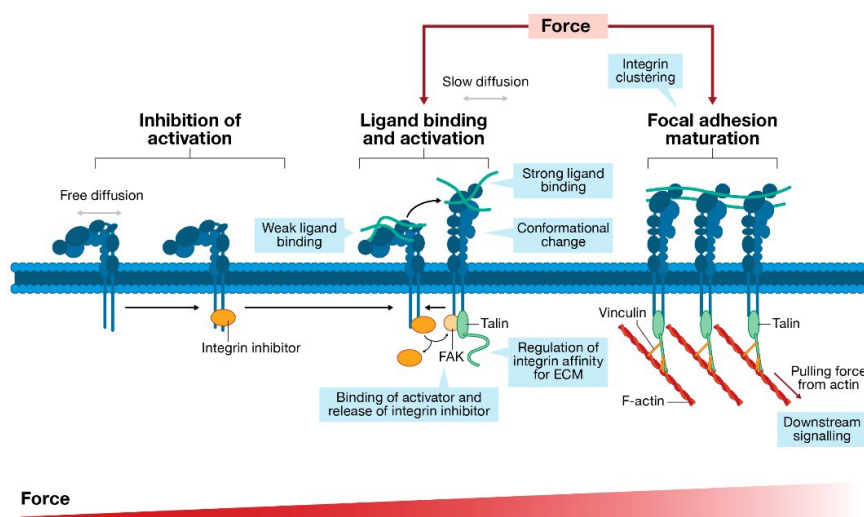


**Figure 4. Mechanism of integrin activation.** Reprinted with permission from *Molecular Force Sensors*; Copyright 2022 American Chemical Society

Based on structural data, integrins have been observed to occupy three main conformations – bent closed, extended closed, and extended open.(10, 11) When integrins are in the bent-closed state, they show greater mobility in the membrane. The activation of integrins and their switching from the bent closed state to the extended open state can be triggered through inside-out signaling such as talin binding to the cytoplasmic tail of the receptor, or outside-in signaling by receptors binding clustered and mechanically active ECM ligands. In the case of mechanotransduction, upon binding of a ligand, the integrin undergoes a conformational change and FAK and talin are recruited. As the cell exerts force through the ligand-bound integrin, multiple integrins begin to cluster and cytoskeletal components such as vinculin and actin are recruited, leading to formation of mature focal adhesions. Clustering of integrins along with the recruitment of vinculin and actin allow the cell to generate the forces needed to spread, migrate, and divide, and cause a biochemical response in the form of a downstream signaling cascade.

This signaling cascade begins with the recruitment of nascent adhesion markers such as FAK, talin, and paxillin. In addition to upregulating cell adhesion proteins such as N-cadherin and desmoplakin, FAK binds talin, a protein that links integrins with the actin cytoskeleton and promotes integrin activation.(12, 13) When talin binds it undergoes a conformational change, exposing a site for vinculin binding.(14) Vinculin then binds to actin filaments, which make up the cell's cytoskeleton and generate the forces needed for cell adhesion, spreading, and migration. Therefore, the simultaneous binding of vinculin to talin and actin effectively links the cell's internal actin cytoskeleton with the external surface receptors. Hence, the cell's actin-mediated physical response is controlled by the forces associated with receptor-ligand interactions on the cell surface.

It is important to note that these forces typically occur on the piconewton (pN) scale – a scale one billion times smaller than the force you feel when holding a paper clip in your hand. For additional context, the motor protein kinesin applies a force of approximately 6 pN when carrying a vesicle.(15, 16) Studying the role of mechanotransduction in cell function is critical to gaining a full understanding of cell biology, as well as understanding processes such as stem cell differentiation, cancer progression, and immune cell function.

## **1.2 Measuring cell forces using synthetic tension sensors**

The development of synthetic tension sensors created a new pathway of discovery for measuring cellular forces (**Fig. 5**). As previously mentioned, techniques such as TFM and micropillar arrays give insight into total force that a cell is exerting. However, more refined tension sensors were needed to elucidate the roles of individual membrane receptors such as integrins. To address this need, the Salaita group developed surface-anchored tension sensors almost one decade ago.(17, 18) Tension sensors are modular and can be engineered using different molecular springs including peptides, polymers, and nucleic acids, and typically rely on fluorescence readout as an indicator of cell force.

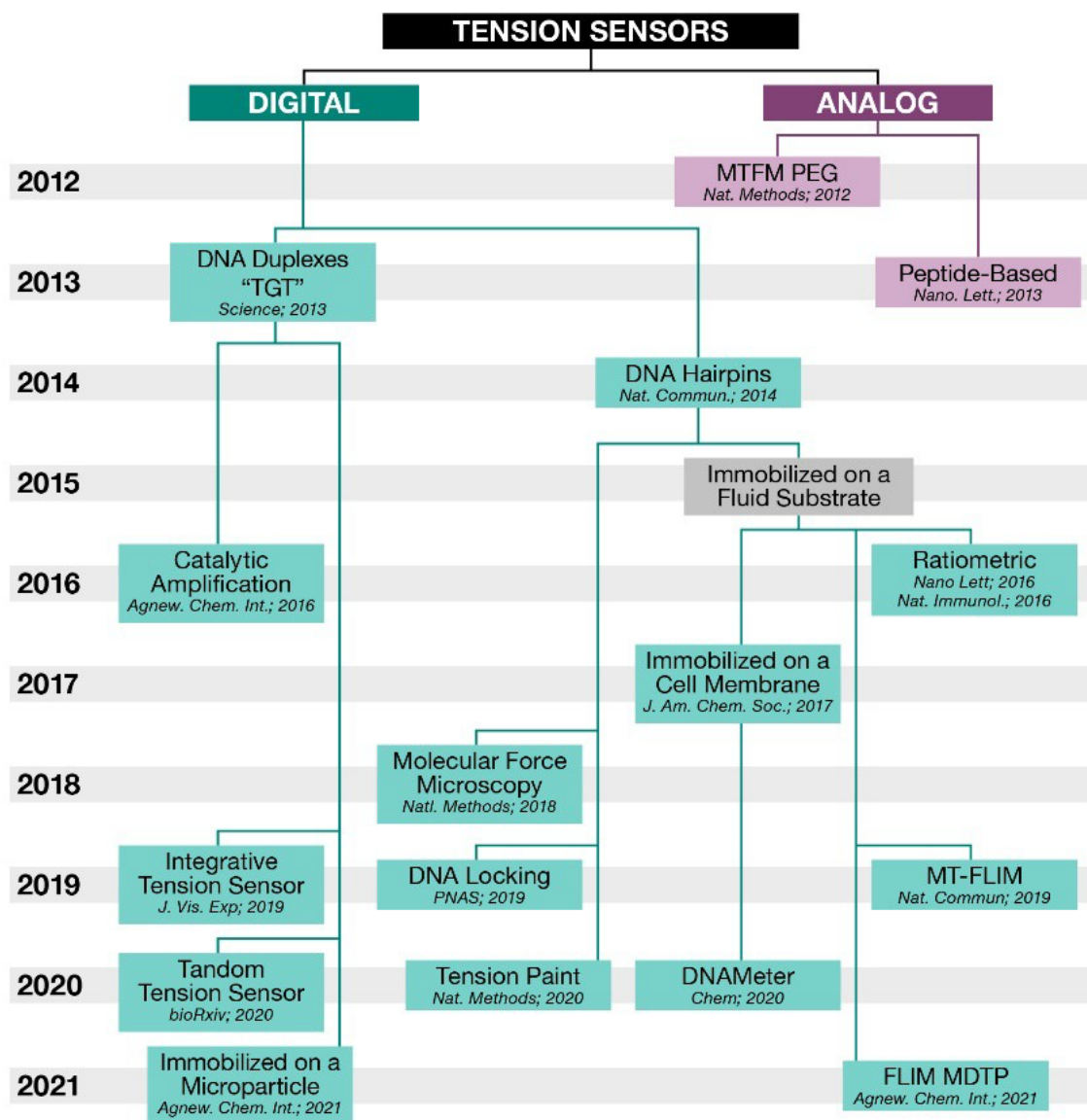


**Figure 5. Timeline of tension sensor development.** Note that this list is not comprehensive, but that each example is the first report of each sensor in a peer-reviewed publication. Reprinted with permission from *Molecular Force Sensors*; Copyright 2022 American

### 1.2.1 Fluorescence in synthetic tension sensors

Very generally, fluorescence is the process by which a substance absorbs light, and then re-emits this energy as a photon, typically at a longer wavelength (lower energy). A donor absorbs light and transitions to a higher energy state (excited electronic state). From there, it donates its energy

to an acceptor that either fluoresces or phosphoresces as it decays back to its ground state energy conformation. In contrast to fluorescence, in which the chromophore relaxes down to the ground state from its excited singlet state, phosphorescence occurs when the chromophore undergoes intersystem crossing into a triplet state before decaying down to its ground state. It is important to note that only the excited state of a donor can undergo FRET.

Fluorescence requires the excitation of a chromophore from a ground electronic state to an excited singlet electronic state. This excitation is driven when the chromophore absorbs a photon that is matched in energy with the energy needed for the transition. The nature of the transition from the excited state to the ground state is dependent on the molecular structure of the fluorophore. In certain molecules that tend to be highly conjugated and rigid, the excited state ( $S_1$ ) relaxes back down to the ground electronic state ( $S_0$ ) and emits the excess energy in the form a photon, which is fluorescence (**Fig. 6**).

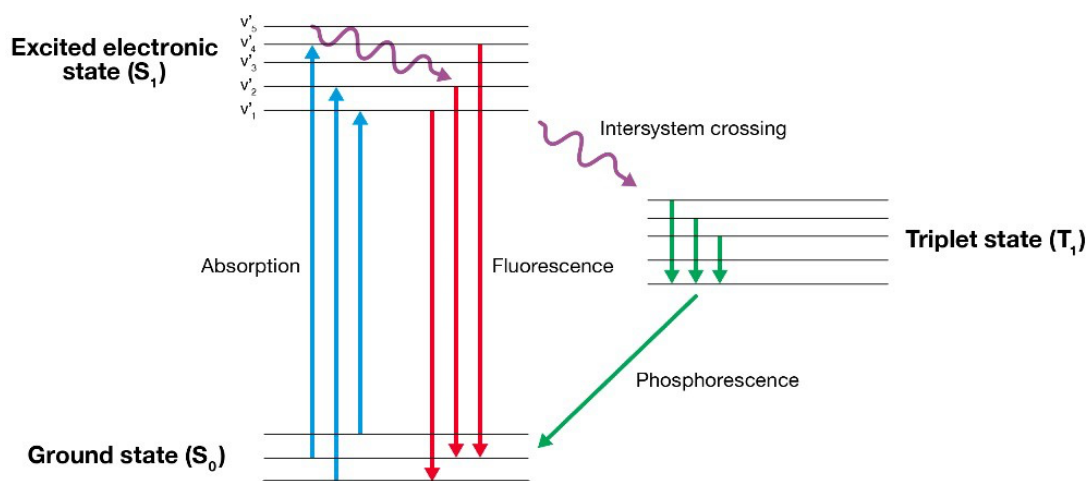


**Figure 6. Jablonski diagram of fluorescence.** Reprinted with permission from *Molecular Force Sensors*; Copyright 2022 American Chemical Society

The timescale for fluorescence is typically ~nanoseconds, meaning that the molecules will spend several nanoseconds in the excited electronic state prior to generating fluorescence. Because vibrational relaxations are rapid (~picosecond time scale), the molecule will typically relax down to the ground vibrational level ( $v'=0$ ) of the excited electronic state ( $S_1$ ) and then fluorescence from this state to any one of the vibrational levels of the ground electronic state ( $S_0$ ). As a result of this relaxation, fluorescence is typically Stokes shifted (shifted to longer wavelengths) compared to the absorbance wavelength.

Because fluorescence is sensitive to environmental conditions such as temperature, buffer, metal ions, and small molecules, it is often used as a sensor, but requires care when using fluorescence for chemical analysis (61, 62). Fluorescence as a readout requires careful analysis but is a valuable tool in molecular sensor research. Because of this rapid response, fluorescence can be used to detect conformational changes that occur at the nanometer length scale. Additionally, since the technique is performed optically, researchers can study systems in relatively non-invasive ways, which is a valuable feature for live-cell studies (63).

Molecular force sensors rely on fluorescence as a readout method. Consequently, microscopy forms the basis for the majority of readout methods. One of the simplest microscopy-based readout methods is intensity-based. This method involves measuring the fluorescent signal generated as a cell exerts force on the tension sensors. This method requires minimal equipment and measurements can be made using a standard fluorescence microscope. As a result, intensity-based measurements have been widely used in molecular tension sensor studies and will be the readout method used for the majority of this work.

### 1.2.2 Force response behavior of synthetic tension sensors

Tension sensors have two general force response functions: analog or digital (**Fig. 7**). Analog sensors respond to external forces by gradually extending and hence the applied force is inferred based on the average extension of sensors, which can be imaged as ensembles of molecules or as single molecules. These analog sensors behave more like a macroscopic spring; force is proportional to extension, which is in turn proportional to fluorescent signal.

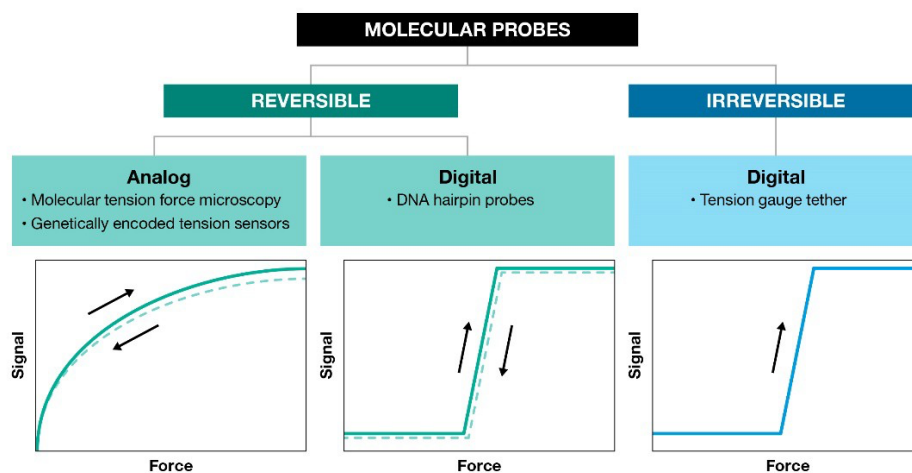


**Figure 7. Molecular sensor classifications.** Reprinted with permission from *Molecular Force Sensors*; Copyright 2022 American Chemical Society

In contrast to analog tension sensors, digital sensors are two-state sensors that are in a folded or unfolded state that is dependent on the applied force. Therefore, digital sensors adopt an on/off response and abruptly switch between states within a narrow range of applied force. Digital sensors provide more specific molecular quantification of cellular forces, precisely because of the threshold response that allows one to determine the absolute number of unfolded sensors in an ensemble. This seems counter-intuitive but is already a well-known phenomenon to physical chemists. For example, the temperature in an experiment can be determined simply by measuring

the ratio of molecules occupying an excited state in a two-state system with a known energy gap between the two states. In the absence of applied force, digital sensors are quenched and there is no observable fluorescent signal. However, each sensor that experiences force exceeding the threshold for unfolding leads to a constant amount of signal that is linearly proportional to the number of mechanical unfolding events. This allows one to perform ensemble fluorescence measurements and to use these measurements to determine the number of receptors applying a threshold force.

### *1.2.3 Analog surface immobilized tension sensors*

One class of synthetic tension sensor is the entropic spring-like sensor. These sensors consist of a ligand attached to a “spring” that is anchored to the surface. The spring is flanked by a FRET acceptor and donor and can report on integrin-mediated forces across the cell surface. Polymer extension is related to the magnitude of external force and FRET efficiency is proportional to the distance between the donor and acceptor. Taking advantage of these relationships, these sensors provide what is known as an analog response - extension and therefore fluorescence increase as a function of the magnitude of the externally applied forces. In other words, the more force a cell exerts, the brighter the signal.

While the later generations of these molecular tension force microscopy (MTFM) sensors can be classified as digital the first MTFM sensor was considered analog.<sup>(18)</sup> This sensor was used to map forces associated with uptake of the EGFR upon binding to its ligand and initially consisted of a PEG spring flanked by a FRET pair and functionalized with biotin for immobilization to a streptavidin surface (**Fig. 8a**). Using the WLC and the estimated extension

of the PEG linker from the FRET relationship, researchers were able to determine that EGFR receptors apply peak forces of approximately 4 pN.

A second iteration of MTFM PEG sensors utilized gold nanoparticles for immobilization and quenching and investigated the integrin force ranges associated with cell adhesion (**Fig. 8b**).<sup>(19)</sup> The quenching of gold nanoparticles follows nanometal surface energy transfer (NSET), improving the sensitivity of fluorescence measurements as compared to traditional FRET pairs. Combining the WLC relationship with NSET, this iteration of the MTFM PEG sensor was estimated to respond to 25 pN of force, extending the dynamic range of the original MTFM PEG sensor.

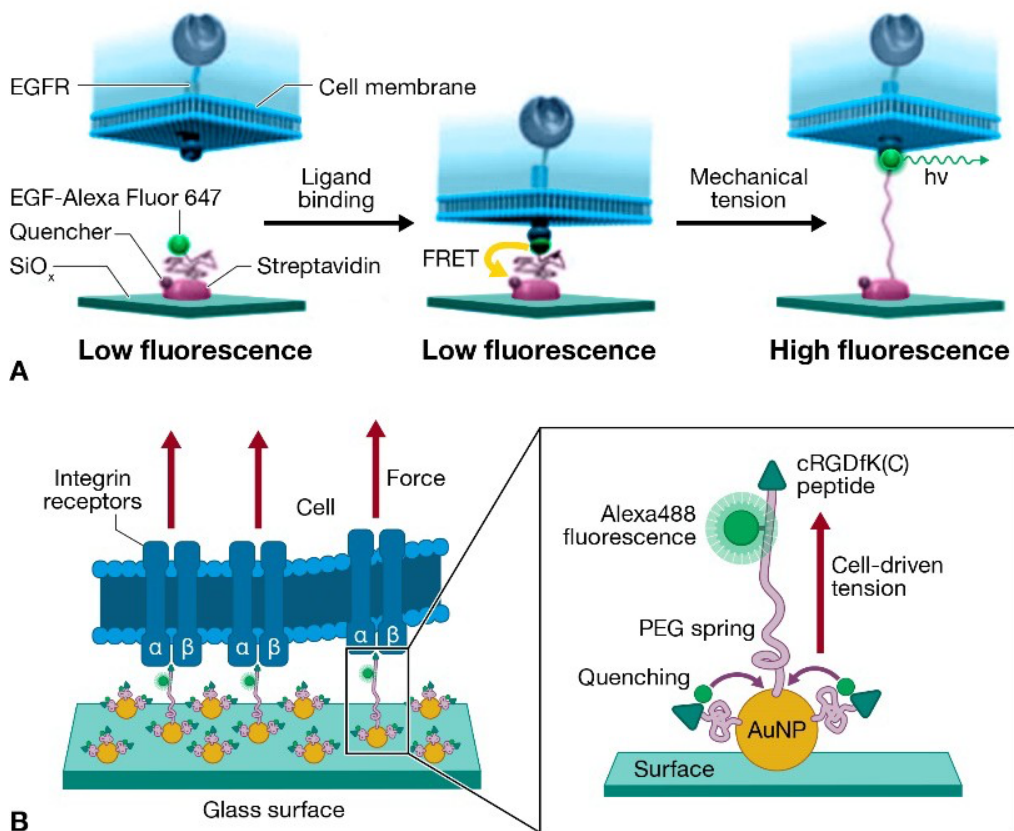


**Figure 8. Schemes of analog MTFM PEG sensors.** **a.** Streptavidin immobilized sensor used to measure forces associated with EGFR. A PEG spring is flanked by a fluorophore and quencher FRET pair, and is functionalized with EGF, a ligand for EGFR, and biotin for immobilization to a streptavidin functionalized glass surface. Following ligand binding, the cell exerts mechanical tension, extending the PEG linker, separating the fluorophore and quencher, resulting in an increase in fluorescence. **b.** Gold nanoparticle immobilized MTFM PEG sensors. A PEG spring is functionalized with a fluorophore, cRGDfK(C) peptide for cell ligand binding, and then immobilized to a gold nanoparticle coated surface. Gold nanoparticles quench fluorescence through NSET as opposed to FRET, resulting in a larger change in quenching efficiency as the probe is extended under force. As a result, gold nanoparticle immobilization improved the dynamic range of MTFM PEG sensors to 25 pN. Reprinted with permission from *Molecular Force Sensors*; Copyright 2022 American Chemical Society

#### 1.2.4 Digital surface immobilized tension sensors

Other classes of synthetic tension sensors can be classified as digital. Unlike analog sensors in which fluorescence increases with force, digital sensors have switch-like behavior and report on tension with an on-off mechanism. In other words, if a cell receptor exerts enough force to open the sensor, the fluorophore and quenchers are separated, resulting in an increase in fluorescence. This signal is not proportional to the amount of force being applied, however. Instead, the force tolerance of the probes can be tuned to provide more quantitative information on the amount of force being applied.

Nucleic acids have been used to construct digital molecular tension sensors such as the DNA hairpin sensor and the irreversible DNA sensors. The relatively low cost and ease of functionalization make DNA a highly attractive biomolecule for constructing these sensors and therefore there are several generations of these sensors. Duplexed and folded DNA and RNA oligonucleotide structures are also well-characterized and there is a substantial amount of work

characterizing the unfolding transitions of nucleic acids under mechanical load.

#### 1.2.4.1 DNA Hairpin Sensors

The digital DNA hairpin sensor pioneered by the Salaita lab consists of three DNA strands: anchor, ligand, and hairpin (**Fig. 9**). The anchor strand is immobilized to the surface and is functionalized with a quencher. The ligand strand is functionalized with a fluorophore and peptide or protein ligand specific to cell surface receptors. The hairpin strand is complementary to both the anchor and ligand strands and controls the  $F_{1/2}$  – the force that leads to a 50% probability of hairpin unfolding at equilibrium.

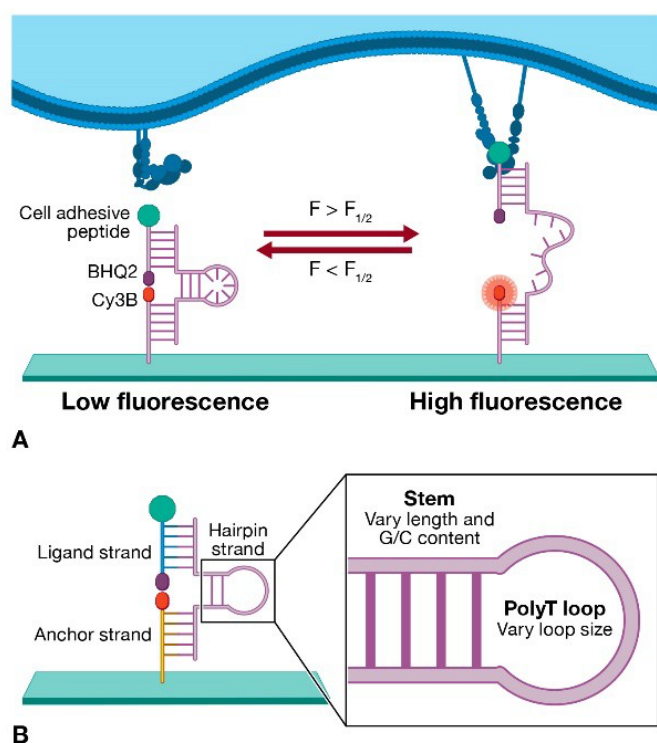


**Figure 9. Structure of DNA hairpin tension sensor. a.** The DNA hairpin is a reversible sensor anchored to a surface and functionalized with a ligand for cell adhesion. Upon a cell exerting force that exceeds the  $F_{1/2}$  of the sensor (the force that leads to a 50% probability of hairpin unfolding at equilibrium), the fluorophore and quencher are separated, resulting in an increase in fluorescence. **b.** The hairpin consists of an anchor strand for surface immobilization, a ligand strand for functionalization of a cell adhesive peptide, and the hairpin strand comprised of a stem and polyT loop. Reprinted with permission from *Molecular Force Sensors*; Copyright 2022 American Chemical Society

The  $F_{1/2}$  of hairpin sensors is tuned by the Guanine/Cytosine (G/C) nucleobase composition, length of the stem, and also by the size of the hairpin loop.(20) Specifically,  $\Delta G_{\text{unfolded}}$  is the free energy of hairpin folding, which is controlled by the length and the G/C content of the stem. Therefore, increasing the G/C content in the stem of the hairpin while keeping all other parameters constant will increase the  $F_{1/2}$  of the sensor because of the increased free energy of folding ( $\Delta G_{\text{unfolded}}$ ). Increasing the length of the loop will also modulate the  $F_{1/2}$  of the sensor. As previously mentioned, when ssDNA is stretched, it behaves as an entropic spring and can be modeled as a worm-like chain. Therefore, as the length of the loop is increased, the energetic cost of stretching is increased and the  $F_{1/2}$  decreases (Fig. 10). Using these principles, the  $F_{1/2}$  of hairpin sensors can be tuned spanning a measurable force range between  $\sim 5$  and 20 pN.(21)

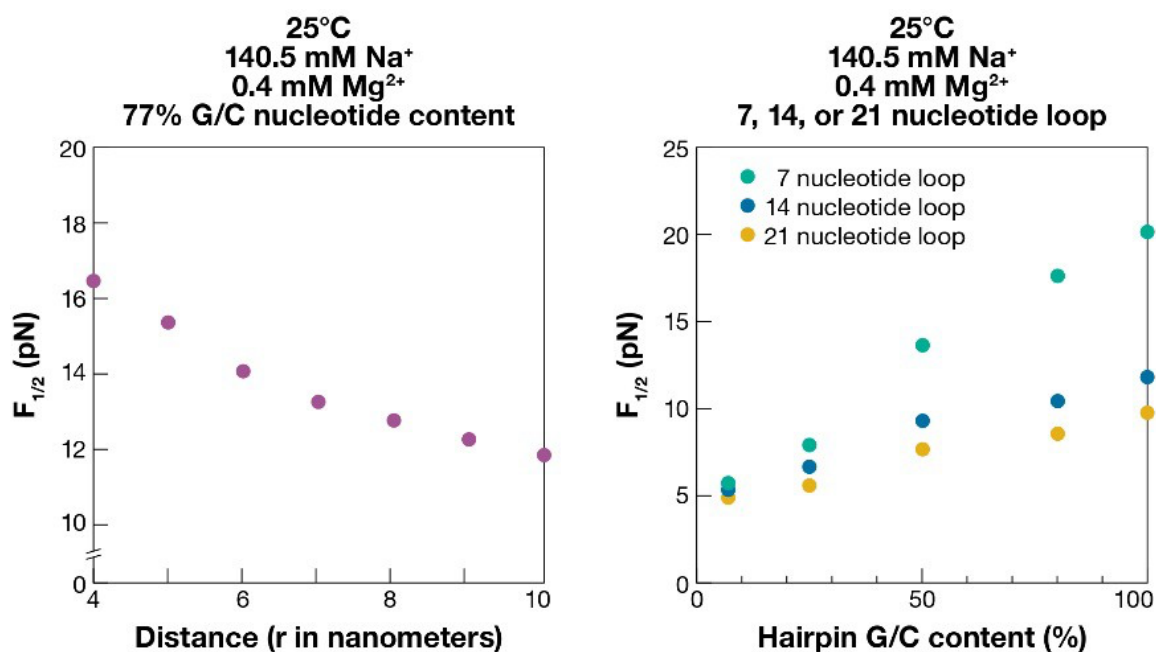


**Figure 10. Effects of G/C nucleobase content and loop size on the predicted  $F_{1/2}$  of hairpin tension sensors.** Reprinted with permission from *Molecular Force Sensors*; Copyright 2022 American Chemical Society

The DNA hairpin sensor engages single molecular receptors and therefore the signal intensity is linearly proportional to the number of molecules that exceed the unfolding force of the sensor. As a result, one can determine single receptor forces from within an ensemble measurement. Since these tension sensors incorporate only a single fluorophore per sensor, resolution is limited only by microscope optics, a vast improvement over traditional methods that have micrometer resolution. These sensors are surface immobilized using either non-covalent interactions such as biotin-streptavidin or using covalent attachment strategies such as copper click chemistry or thiol to gold. The desired fluorophore is attached typically by using an NHS ester and the ligand is covalently linked to the sensor using copper-mediated click chemistry.

In the first study using these sensors, the Salaita lab investigated how force is distributed within focal adhesions and found that in general, most engaged integrins exerted forces greater than or equal to 13.1 pN, and that focal adhesions near the cell edge preferentially open sensors with a higher  $F_{1/2}$ , suggesting that cells spread by sensing the stiffness of the substrate at the cell edge (**Fig. 11**). Subsequent studies by the Salaita lab have used these sensors to investigate platelet forces, the role of T-cell receptors in the immune system and podosome formation.(22)

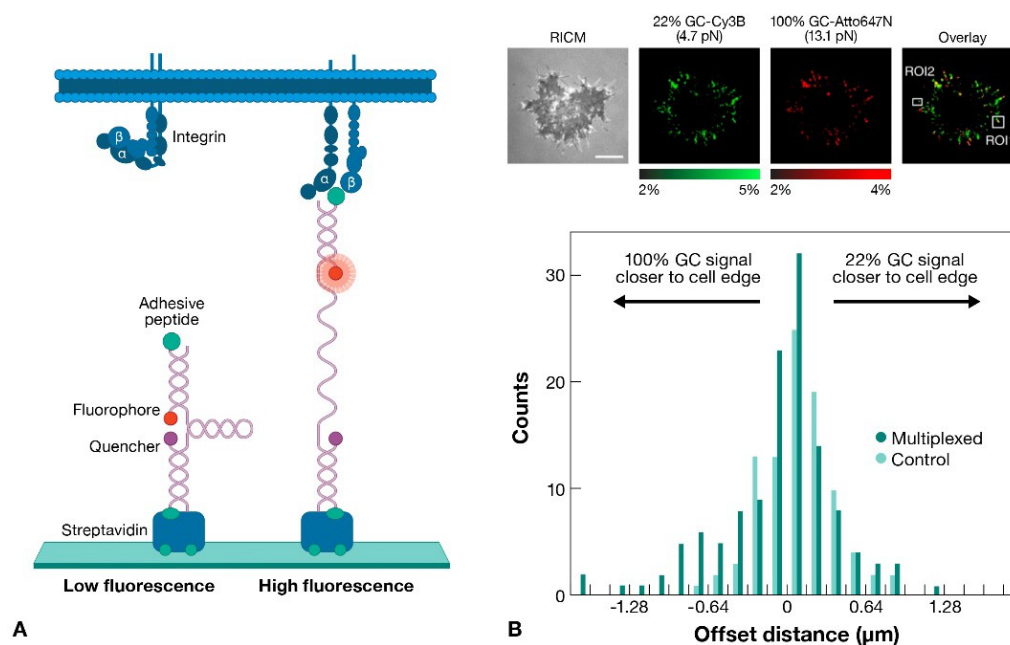


**Figure 11. Initial DNA hairpin design and use.** **a.** In the initial DNA hairpin design, the sensor consisted of three DNA strands: the anchor, ligand, and hairpin, and is functionalized with a biotin for surface immobilization and a peptide for cell adhesion. In this initial study, researchers used the sensor to study the role of integrin force in cell adhesion. **b.** By culturing cells on surfaces functionalized with hairpins with different  $F_{1/2}$  values (4.7 and 13.1 pN), the researchers determined that cells tend to exert more force at the cell edge, preferring to open the higher force sensor when given the choice between the 13.1 and 4.7 pN sensors. Reprinted with permission from *Molecular Force Sensors*; Copyright 2022 American Chemical Society

Coincident with the report of the three-strand design of the Salaita group was the report by Chen and colleagues describing a single polynucleic acid DNA hairpin tension sensor.<sup>(23)</sup> Similar to the original hairpin design, the strand has a fluorophore and quencher at the termini and is functionalized with a peptide for cell adhesion (**Fig. 12**). Using optical trapping, the labs of Steven Block, David Liu, and Christopher Chen calibrated the unfolding force of their sensors to range from 5.7 to 16.5 pN and studied the distribution of vinculin in mouse embryonic fibroblast cells. While this initial report provided insight into the different patterns of vinculin distribution in cells, there have been no known follow-up reports using this sensor. This is likely because of the synthetic challenge of generating this oligonucleotide with four chemical

modifications and strong secondary structure.

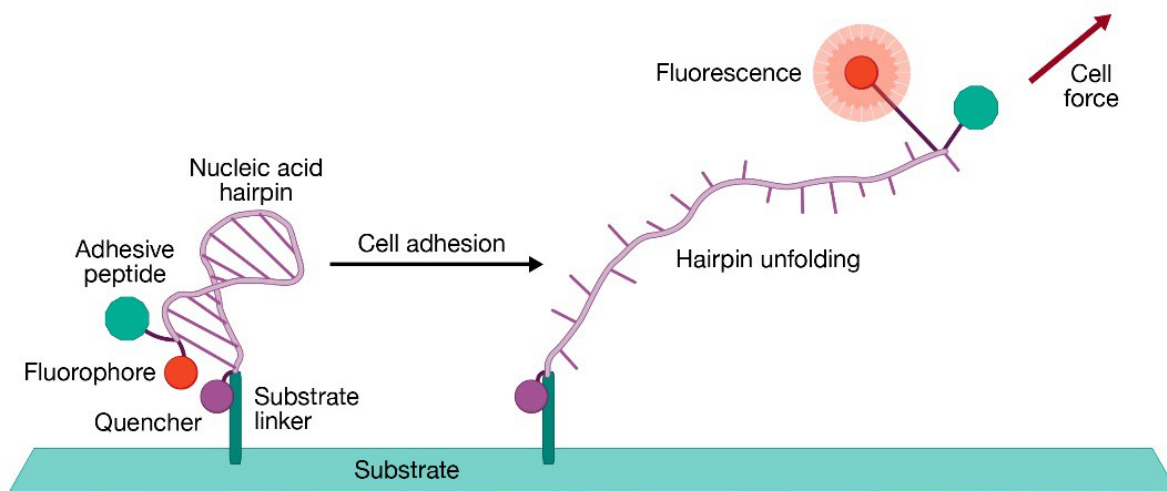


**Figure 12. Schematic of a single oligonucleotide hairpin.** Reprinted with permission from *Molecular Force Sensors*; Copyright 2022 American Chemical Society

#### 1.2.4.2 DNA Rupture Sensors

Another form of nucleic acid sensor is a DNA duplex that irreversibly ruptures in response to mechanical force. Mechanically induced rupture of DNA duplexes can be induced by “shearing” the sensor or “unzipping” the sensor (**Fig. 13**). Shearing occurs by stretching the duplex along its axis in order to induce dissociation. This is a high-force event compared to sensor unzipping, which occurs by stretching the sensor perpendicular to its axis.

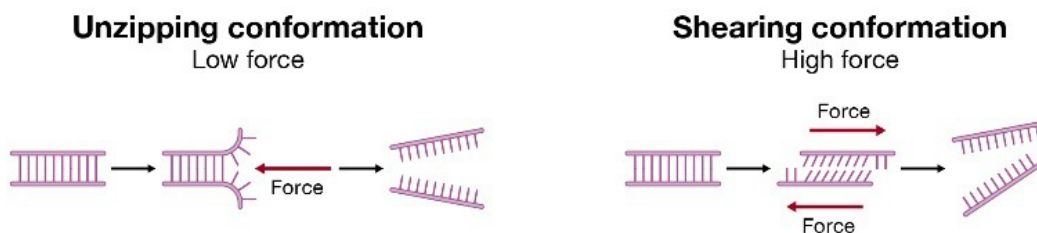


**Figure 13. Conformations of DNA rupture.** Reprinted with permission from *Molecular Force Sensors*; Copyright 2022 American Chemical Society

While shearing forces are correlated to length of the duplex, unzipping forces are relatively independent and primarily depend on the first few bases in the duplex. Importantly, one feature of DNA duplex rupture is the thermodynamic independence. The rupture force of DNA duplexes is dependent on the orientation of rupture rather than its melting temperature; therefore, two identical sequences can have drastically different rupture forces although they have identical melting temperatures and  $\Delta G$  values.

The rupture of these sensors has been measured by both force clamp experiments and force ramp experiments, and their behavior has been modelled extensively.(24-26) A widely used model is the deGennes model, in which the DNA duplex is modelled as a ladder.(27) Within a strand, springs hold the individual bases together while hydrogen bonding maintains the interaction between the two strands. This model assumes that when shearing force is applied to both ends of the duplex, the force is only propagated along the first few base pairs. Unlike the hairpin sensor where force is defined as the  $F_{1/2}$ , or the probability of the structure unfolding, the rupture force of duplexes is defined by their tension tolerance ( $T_{tol}$ ), the force required to mechanically melt 50% of the duplexes.  $T_{tol}$  can be expressed as:

$$T_{tol} = 2f_c [x^{-1} \tanh(x \frac{N}{2}) + 1]$$

The  $x$  term is used to describe the elasticity within a duplex and is defined as the square root of  $R$ , the spring constant of stretching the hydrogen bonds between base pairs in the duplex, over  $Q$ , the spring constant between bases within a strand.  $N$  is the number of base pairs that form

between the strand and  $f_c$  is defined as 3.9 pN, the force required to break a single base pair. Following this model, it is estimated that identical 21 base pair duplexes have a  $T_{tol}$  of approximately 56 pN in the shearing conformation, and 12 pN in the unzipping conformation.(17)

While this model can predict the relative rupture force of duplexes, it is worth noting that it considers neither sequence composition nor time of mechanical melting. Therefore, it does not consider variables such as G/C content or loading rate. However, although these models are an oversimplification of the biophysics of DNA rupture, experimental results have largely confirmed their validity as a useful approximation tool. Specifically, these approximations have been experimentally confirmed using magnetic tweezers and force ramping, in which researchers applied a constant force to the duplex and observed whether a rupture event occurred within 2 seconds.(28) If no rupture event took place, the force was increased and again, researchers observed whether the duplex ruptured. Therefore, the experimental results can be defined as the lowest constant force that ruptures the duplex within 2 seconds. Therefore, both the modeling and experimental data provide valuable insight into the biophysics of DNA duplex rupture and can be used to generate force estimates when designing molecular sensors.

The tension gauge tether (TGT) is a DNA rupture-based sensor that caps integrin forces at a particular threshold. The basic design of the TGT is a surface immobilized DNA duplex that is equipped with a peptide for cell recognition. This sensor exists in the low-force unzipping conformation and the high-force shearing conformation. The unzipping sensor ruptures when a cell exerts a  $T_{Tol}$  of 12 pN or greater on the sensor while the shearing sensor ruptures when a

cell exerts a  $T_{\text{Tot}}$  of 56 pN or greater on the sensor. These values were determined using magnetic tweezers and the force it took to rupture the duplexes after 2 seconds. In the initial experiments, TGT was used to investigate the Notch receptor, one of the most commonly activated signaling pathways in cancer.(29) The Notch receptor was not activated if the tension applied by the cell was greater than the  $T_{\text{Tot}}$  of the sensor, causing the duplex to rupture (**Fig. 14a**). However, if the cell exerted enough tension to pull, but not rupture the duplex, the receptor was activated, demonstrating the mechanosensitivity of the receptor (**Fig. 14b**).

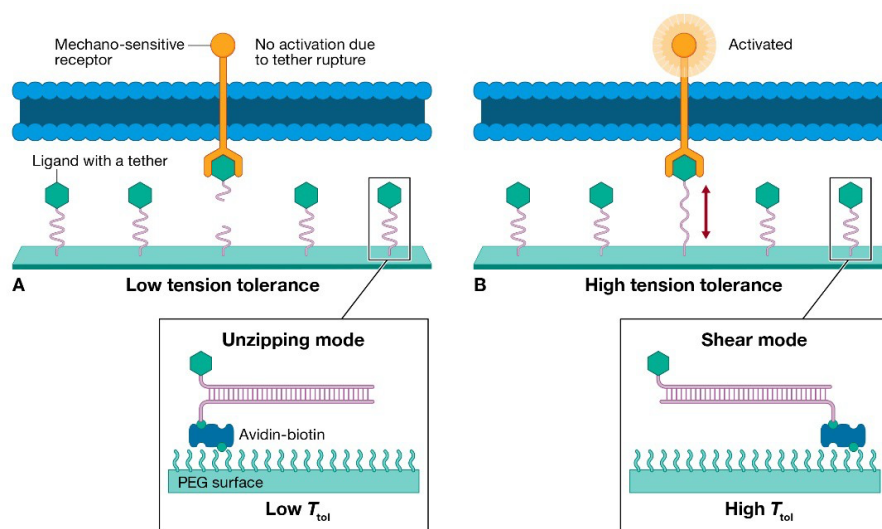


**Figure 14. Schematic of Tension Gauge Tether (TGT).** Reprinted with permission from *Molecular Force Sensors*; Copyright 2022 American Chemical Society

In another attempt to investigate the force requirement for Notch activation, the Ha lab modified their existing TGT into a “low tension gauge tether” (LTGT), also known as the Nano Yoyo.(30) In this design, the unzipping conformation of the TGT contained a long single-stranded region that was wound around the *E. coli* single-stranded binding protein (SSB) and unspooled at a force of approximately 4.2 pN at a loading rate of 500 nm/sec. Using this sensor, the researchers determined that greater than 4 pN of force is required for Notch activation, confirming their

previous results with the TGT that mechanical force is required for Notch activation and expanding the utility of the conventional TGT.

The TGT was later evolved into the integrative tension sensor (ITS).(31) The ITS is functionally identical to the TGT, but unlike the TGT, is functionalized with a fluorophore and quencher pair such that it can fluorescently report on cell tension. Specifically, when a cell exerts a tension exceeding the  $T_{To1}$  of the sensor, the duplex is ruptured, separating the fluorophore and quencher, resulting in a measurable increase in fluorescence. Like the previously mentioned TGT and hairpin probes, the ITS engages individual cell receptors. However, unlike the hairpin probes, rupture of these probes is irreversible. Therefore, fluorescence signal is accumulated over time and does not necessarily reflect “real-time” cell tension. Nevertheless, these sensors provide valuable information on the upper magnitude of forces generated by a cell. Using this sensor, researchers studied platelets and mapped their forces, ultimately finding that between 12 and 54 pN of force is required for initial adhesion and >54 pN of force is required for maturation and platelet contraction.

### **1.3 Limitations of existing force sensors**

Current force sensors are primarily constructed out of DNA and proteins, leaving them susceptible to degradation in the biological media and temperatures required for most biological assays. Specifically, studies have reported that the half-life of DNA is between 20-30 minutes when used in cell and tissue culture while the half-life of proteins in the presence of proteases is typically on the time scale of hours.(32) The stability of these biomolecules becomes even more relevant in the study of aggressive cell lines such as the study of cancer mechanics due to the high number of

degrading enzymes secreted by cancer cells.(33)

### *1.3.1 Biostability*

While significant advances have been made in nucleic acid technology for force sensing, there are several limitations that must be addressed. One limitation of most nucleic acid tension sensors, along with all DNA- or protein-based sensors, is their susceptibility to degradation in a cellular environment. This degradation presents a challenge when attempting to measure mechanical events over an extended time frame, and degradation can result in an increase in background fluorescence that obscures the tension signal. The Wang group has sought to overcome these limitations by incorporating peptide nucleic acids (PNA) into the ITS design.(34) PNA is a synthetic nucleic acid analog with a pseudo-peptide-like backbone.(35, 36) The oligo retains the ability to Franklin-Watson-Crick base- pair with other nucleic acids and is resistant to degradation by all known enzymes. Taking advantage of this feature, the Wang group created nuclease-resistant tension sensors in the form of PNA:DNA heteroduplexes. Using these sensors, the researchers were able to measure cellular traction forces with greater sensitivity due to the biostability of the sensors.

### *1.3.2 Real-time monitoring of integrin mediated forces > 19 pN*

Broadly surveying the two primary classes of synthetic tension probes, one is faced with distinct limitations. While reversible sensors report on real-time cell tension, they can only report on receptor forces  $\leq 19$  pN. Conversely, sensors that report on receptor forces as high as 56 pN irreversibly rupture, terminating cell mechanotransduction and providing a history of a cell's tension. In an attempt to address these individual limitations and create a "real-time" sensor

capable of reporting on receptor forces greater than 19 pN, the Liu lab synthesized a reversible shearing DNA-based tension probe (RSDTP).<sup>(37)</sup> These probes consist of two DNA strands that, when hybridized, form a stem-loop-like structure that unfolds in the shearing conformation, but is capable of refolding (**Fig. 15**). Using single molecule magnetic tweezers, the group found that in the shearing conformation, their probe had an unfolding force of 56 pN, expanding the measurable force range of “real-time” tension sensing. An important consideration with this probe however is the possibility for peeling of the quencher strand. Under force, the loop-containing strand is stretched to its contour length, disrupting the base stacking interactions and causing the quencher labeled strand to dehybridize. Once this dehybridization occurs, the probe is once again limited to a maximum force range of less than 19 pN.

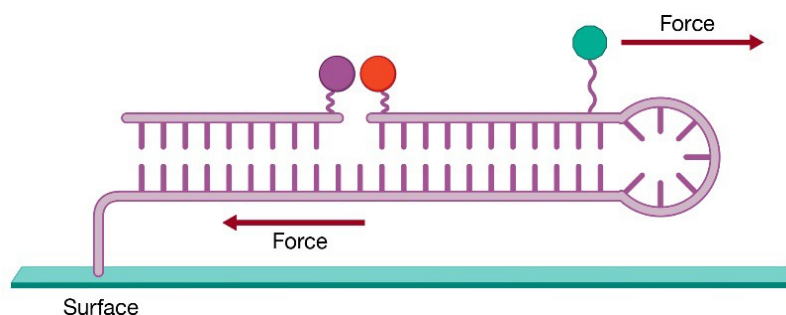


**Figure 15. Schematic of reversible shearing probe.** Reprinted with permission from *Molecular Force Sensors*; Copyright 2022 American Chemical Society

## 1.4 Dissertation scope and outline

DNA and peptide-based sensors are powerful tools for studying the role of integrin-mediated force in cell function. However, they face key limitations in their applications primarily due to the limits of their force thresholds, and their stability in biological settings. For example, to date, DNA-based probes have maximum force thresholds of  $\sim 60$  pN while peptide-based probes have maximum forces thresholds of  $\sim 110$  pN. Furthermore, both the scaffolds on which these probes are immobilized and the probes themselves are not thermostable and are susceptible to degradation by nucleases and proteases.

Limitations in force sensing technologies directly impact the questions one can ask regarding mechanobiology. For example, without robust immobilization scaffolds that are both chemically and biologically stable, it is impossible to measure cell forces over extended periods of time as scaffolds are either degraded by the biological medium and temperatures necessary for such analyses. Existing techniques to produce more robust scaffolds face other limitations such as poor functionalization densities or the introduction of exogenous reagents that impact biological processes. In **Chapter 2**, I describe characterizing the trans-cyclooctene and tetrazine iEDDA reaction for functionalization of glass substrates to measure cell tension. This iteration of a copper-free “click” reaction has a high on-rate, and produces densely functionalized, homogenous, and covalent substrates suitable for biological analyses.

Beyond immobilization strategies, current tension sensors are limited in their biostability and measurable force range. The majority of tension sensors are constructed from DNA or proteins, leaving them susceptible to nuclease and protease degradation. Furthermore, these sensors are

limited to measuring forces below  $\sim 100$  pN. In Chapter 3, I describe the synthesis and use of a new generation of tension probes constructed from peptide nucleic acids (PNA). PNA is a synthetic nucleic acid analogue that is resistant to enzyme degradation and has high thermostability. Using PNA:DNA and PNA:PNA duplexes, I have created force sensors that report on the upper level of integrin forces over several hours, revealing that cells exert forces in regimes not accessible using conventional DNA and protein based sensors.

Finally, in Chapter 4, I describe going beyond force threshold and measuring the ability of integrins to detect the molecular force extension curve of these ligands. Building a new generation of reversible molecular sensors, I demonstrate that integrins are not only responsive to differences in force thresholds but can detect the unique force-extension curves of their ligands. Specifically, cell adhesion receptors are sensitive to sudden perturbations in the resistive force required for forming cell adhesions. These perturbations result in downstream signaling effects, affecting mechanotransduction levels and overall cell function. Hence, these findings provide an additional level of characterization to the role integrins play in outside-in/inside-out signaling, revealing that in addition to actively detecting force threshold, integrins also detect and respond to the geometry of their ligands.

This body of work utilizes the principles of chemistry, physics, biology, and engineering and builds on the prior work in the fields of mechanochemistry and mechanobiology, adding to the molecular scale toolkits used by researchers to investigate the role of force in cell function.

## **CHAPTER 2: SURFACE TETHERING OF BIOMOLECULES USING THE REACTION BETWEEN TRANS-CYCLOOCTENE AND TETRAZINE**

### **2.1 Abstract**

Robust surface functionalization of biomolecules is critical to studying biological interfaces. Techniques must produce homogenous surfaces that withstand degradation at the elevated temperatures and medias required for biological assays. Today, one of the most commonly used techniques for surface tethering of biomolecules is the biotin/streptavidin interaction. However, this interaction is non-covalent, susceptible to degradation in biological media, and dissociates at elevated temperatures and under high force. Covalent methods of surface immobilization of biomolecules suffer from slow reaction rates or require the addition of reagents that are incompatible with biological measurements. Here, we describe the use of the trans-cyclooctene/tetrazine reaction to generate surfaces for tethering biomolecules. This reaction is in the family of “click reactions”, but is strain promoted and achieves a high on-rate without the addition of additional reagents. We demonstrate that this reaction produces homogenous and covalent surfaces at a rate similar to the rate of biotin/streptavidin functionalization. These surfaces have low levels of non-specific binding and are resistant to thermal dissociation and protease degradation. Finally, we demonstrate that because there is no degradation of the surface, the trans-cyclooctene/tetrazine reaction can be used to immobilize DNA force probes, increasing the time scales of cell force measurements compared to scale achievable using biotin/streptavidin surfaces.

## 2.2 Introduction

Functionalizing surfaces to study biological interfaces is essential to basic research. Surface tethering of biomolecules is necessary for a variety of assays including ELISA's, DNA and protein arrays, and biophysical studies. In ELISA'S, antibodies must be immobilized onto a solid support that is homogenously functionalized and readout is dramatically affected by inconsistent immobilization. Specifically, non-specific binding of the antigen to the surface can lead to false positive or negative results.(38) The effect of surface immobilization strategies is also well documented in work involving DNA and protein arrays with the optimal strategies involving covalent immobilization of the biomolecule to glass using click chemistry.(39, 40) Biophysical studies include creating scaffolds to study the role of force in cell function. These scaffolds are functionalized with nucleic acid-based sensors capable of reporting on the integrin mediated force fundamental to the understanding of forces relevant to cell biology.(22, 41-46) Surface immobilization strategies used in such applications must be able to withstand biologically relevant conditions such as a the presence of degrading enzymes and increased assay temperatures. Thus, there is a need to characterize surface functionalization strategies to ensure that they produce homogenous surfaces at time scales relevant for the assay being conducted and are robust in biologically relevant environments.(47-50)

While there are many functionalization techniques available, common methods for immobilizing biomolecules to solid supports include using non-covalent biotin/streptavidin (Biotin/STVD) or gold/thiol interactions, forming covalent bonds using copper-mediated, copper-free DBCO, or the reaction between maleimide and thiol (**Fig. 16a, b**).(17, 51-55) While each of these techniques confers some advantages in surface chemistry, there are several limitations that are problematic,

particularly in biological settings. For example, while the biotin-streptavidin interaction is one of the strongest non-covalent bonds known, it is susceptible to degradation by proteases and its off-rate is accelerated by the increased temperatures often required for biological studies.(56-58) Covalent bonds formed through techniques such as the copper-mediated click overcome the challenges associated with the off-rate of non-covalent bonds; however, the required copper catalyst can interact with or destroy the biomolecule of interest.(59) Other methods of covalent attachment such as the DBCO reaction suffer from on-rates of binding as slow as  $10^{-3} \text{ M}^{-1} \text{ sec}^{-1}$ , and bonds formed by the gold/thiol interaction are susceptible to force-induced dissociation as well as nucleophilic exchange with thiols.(60, 61) Hence, there are several variables one must address when designing surface immobilization strategies that can be used in a biological setting and there is a gap in the tools available to undertake robust biological studies that require surface functionalization.

The “ideal surface functionalization” would meet several criteria. The immobilization strategy would be covalent and use a reaction with a high  $k_{\text{on}}$  and low  $k_{\text{off}}$  (**Fig. 16c**). Specifically, the reaction rate would need to be sufficient to proceed at reasonable physiological conditions and with the low concentrations of reagents often used in biological measurements. The reaction would not employ catalysts or reagents that would perturb biological systems and would reliably produce homogenous surfaces. Additionally, one must consider the bioorthogonality of the molecule to ensure specific coupling to the surface, and minimal cross-reactivity with other biomolecules within the system. Finally, the surface immobilization strategy would not be susceptible to degradation by biologically relevant conditions that often include external force generation, enzymatic attack, and increased temperatures.

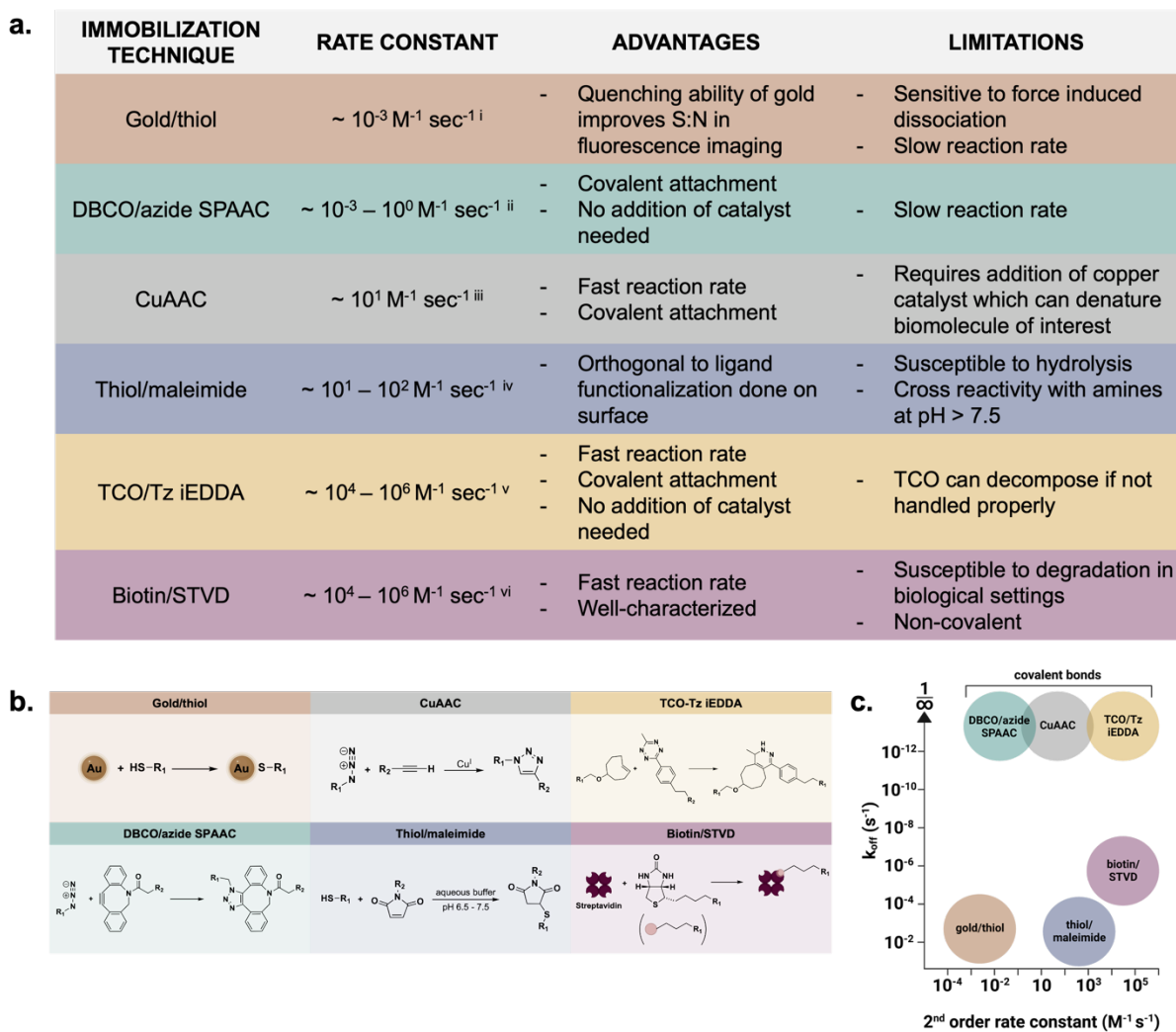


**Figure 16. Common techniques for surface immobilization of biomolecules.** a. Rate constants, advantages, and disadvantages of common surface immobilization strategies. i.(49, 50) particle size =  $3.2 \pm 0.7$  nm,  $T \cong 25$  °C; ii.(62) physiological conditions ( $T \cong 25$  °C,  $\text{pH} \cong 7.6$ ); iii.(63) 50  $\mu\text{M}$  Cu(I), 5 mM NaAsc,  $T = 25 \pm 1$  °C,  $\text{pH} = 7.6 \pm 0.02$ ; iv.(64)  $T = 25$  °C,  $\text{pH} = 7.4$ ; v.(65)  $T = 25 \pm 0.5$  °C; vi.(58, 66)  $\text{pH} = 8.0$ ,  $T \cong 25$  °C) ten-fold excess of dienophile b. Reaction schemes for common surface immobilization strategies for biomolecules. c. Rate constants vs  $k_{\text{off}}$  rates for common techniques used for surfaces immobilization for biomolecules.

To overcome the limitations of the aforementioned immobilization strategies, we characterize the use of the tetrazine (Tz) and trans-Cyclooctene (TCO) reaction for immobilization of biomolecules onto a solid support. First reported in 2008, the reaction has become more widely used in recent years due to increased accessibility and advances in reagent synthesis.(67) The inverse electron demand Diels-Alder (iEDDA) reaction between Tz and TCO falls in the class of copper-free “click reactions”. The reaction between TCO and Tz reaction is unique in that it has a reported on-rate of  $10^3 - 10^6 \text{ M}^{-1} \text{ sec}^{-1}$  without the addition of exogenous reagents, and produces a stable covalent bond.(68, 69) Notably, the TCO/Tz iEDDA reaction has been used to tether biomolecules to surfaces, notably improving the sensitivity of ELISA techniques, and improving the kinetics and chemoselectivity of DNA microarrays.(70, 71)

Here, we characterize the use of the TCO and Tz iEDDA reaction for tethering oligonucleotides to a glass scaffold. We use TCO modified surfaces and Tz modified ligands to produce TCO/Tz iEDDA surfaces and compared our findings to streptavidin modified surfaces for immobilizing biotinylated ligands (Biotin/STVD surfaces). The biotin streptavidin linkage is one of the most commonly used surface tethering technique in the field and therefore a useful benchmark to compare the TCO/Tz iEDDA surfaces with.(72, 73) We found that Tz-modified oligonucleotides can be successfully immobilized onto TCO-modified surfaces with higher density and lower non-specific binding than is achieved with Biotin/STVD surfaces. We demonstrate that biotin labeled DNA and Tz labeled DNA bind to solid substrates with similar on-rates and that biomolecules immobilized onto Biotin/STVD surfaces are subject to protease and thermal induced dissociation while biomolecules immobilized onto TCO/Tz iEDDA surfaces are stable in biologically relevant conditions. Finally, we show that while both techniques can be used to immobilize DNA to a

surface used for visualizing the forces exerted by a cell, TCO/Tz iEDDA surfaces can be used to report on cell tension for > 4 hours while biotin/STVD surfaces begin to lose S:N resolution due to dissociation of fluorescent DNA from the surface, increasing background fluorescence and obscuring meaningful fluorescent signal.

## 2.3 Results

### 2.3.1 TCO/Tz iEDDA surfaces are more homogenous than Biotin/STVD surfaces

Similar protocols are used to prepare biotin and TCO modified glass surfaces (**Fig. 17a**). Glass slides are first washed and hydroxylated using a mixture of H<sub>2</sub>SO<sub>4</sub> and H<sub>2</sub>O<sub>2</sub>, known as piranha solution. Slides are then aminated with the addition of (3-Aminopropyl)triethoxysilane (APTES). Here, either a biotin-NHS reagent or a TCO-NHS reagent is added and allowed to incubate overnight, producing the functionalized surfaces. Following incubation in the NHS reagent biotin surfaces must first be blocked with a solution of bovine serum albumin (BSA) and incubated in streptavidin to allow a biotinylated molecule to bind. Surfaces functionalized with TCO do not require BSA blocking and Tz functionalized molecules can be directly conjugated to the surface.

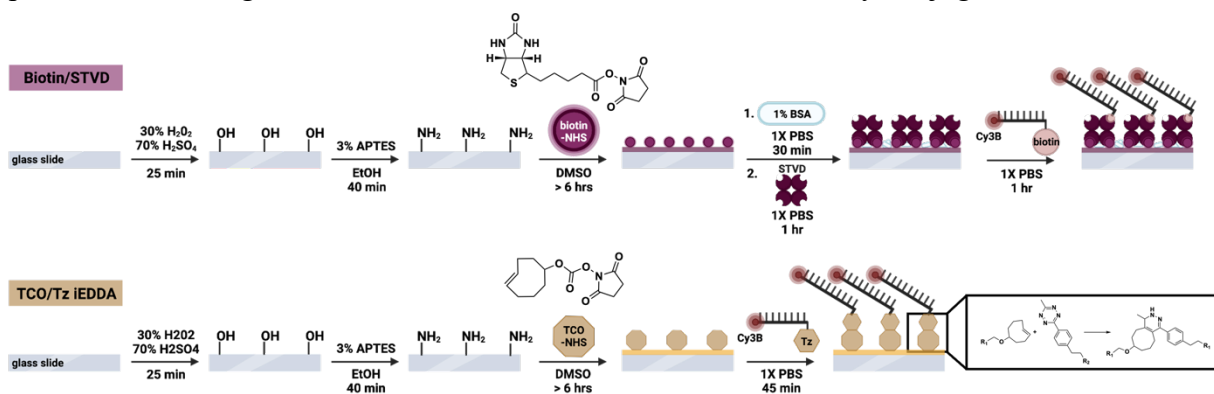


**Figure 17. Characterization of biotin and TCO coated glass surfaces.** Scheme detailing preparation of Biotin/STVD and TCO/Tz iEDDA surfaces. Glass slides are etched with piranha acid before being aminated and functionalized with either biotin or TCO via an NHS reagent. Before use, Biotin/STVD surfaces are blocked with BSA to prevent non-specific adhesion and functionalized with streptavidin, allowing the biotinylated biomolecule to bind. TCO/Tz iEDDA surfaces can be immediately functionalized with a Tz labelled biomolecule following functionalization with TCO.

We first validated that Biotin/STVD and TCO/Tz iEDDA surfaces had similar degrees of functionalization by adding Cy3B labeled DNA functionalized with either Tz or biotin and measuring the resulting fluorescence intensity of the surfaces (**Fig. 18a, A1, A2, Table A1**). We found that the 50% effective concentration ( $C_{\text{eff at 50\%}}$ ) of TCO/Tz iEDDA surfaces was  $9.26 \pm 0.9$  nM compared to the equilibrium constant ( $K_{\text{eq}}$ ) of  $10.48 \pm 1.0$  nM measured for biotin surfaces, suggesting that both Biotin/STVD and TCO/Tz iEDDA surfaces can be functionalized with biomolecules to a similar degree (**Fig. 2c**). Note also that TCO/Tz iEDDA surfaces are more homogenous and have a significantly lower coefficient of variation than Biotin/STVD surfaces (**Fig. 18b, A3**). Note also that TCO/Tz iEDDA surfaces are nearly 10-times more homogenous than biotin/STVD surfaces (**Fig. 18c**).

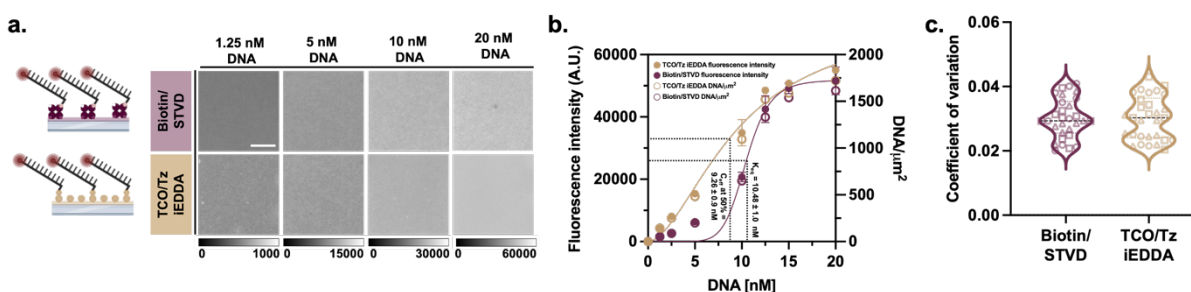


**Figure 18. TCO/Tz iEDDA surfaces are more densely functionalized and more homogenous than biotin/STVD surfaces.** **a.** Fluorescence images of biotin and TCO functionalized glass surfaces coated in Cy3B labelled DNA. Scale bar = 20  $\mu\text{m}$ . **b.** Binding curves of DNA binding to biotin/STVD and TCO/Tz iEDDA surfaces. Fluorescence and number of DNA/ $\mu\text{m}^2$  are reported as a function of DNA concentration. The measured equilibrium constant ( $K_{\text{eq}}$ ) for Biotin/STVD surfaces is  $10.49 \pm 1.0$  nM and the  $C_{\text{eff at 50\%}}$  (the concentration at which 50% of the surfaces is saturated) is  $9.26 \pm 0.9$  nM for TCO/Tz iEDDA surfaces. Biotin/STVD surfaces can be functionalized with  $1614 \pm 77$  Cy3B labelled DNA probes per  $\mu\text{m}^2$  while TCO/Tz iEDDA surfaces can be functionalized with  $1723 \pm 63$  Cy3B labelled DNA probes per  $\mu\text{m}^2$   $n=3$  surfaces, 10 regions per surface. **c.** Coefficient of variation of Biotin/STVD and TCO/Tz iEDDA surfaces reveals that Biotin/STVD surfaces are more heterogeneous than TCO/Tz iEDDA surfaces. Coefficient of variation was determined by dividing the standard deviation of a fluorescent ROI by the average fluorescence of the ROI.  $n = 3$  surfaces, 10 regions per surface,  $p < 0.0001$ .

We next measured the degree of non-specific binding that occurs on both surfaces by adding DNA with and without ligand to STVD and TCO functionalized glass slides and measuring the resulting fluorescence (**Fig. 19 a, b**). We found that even when BSA blocking is used, Biotin/STVD surfaces have nearly twice as much non-specific binding of biomolecules as TCO/Tz iEDDA. (**Fig. 19c**).

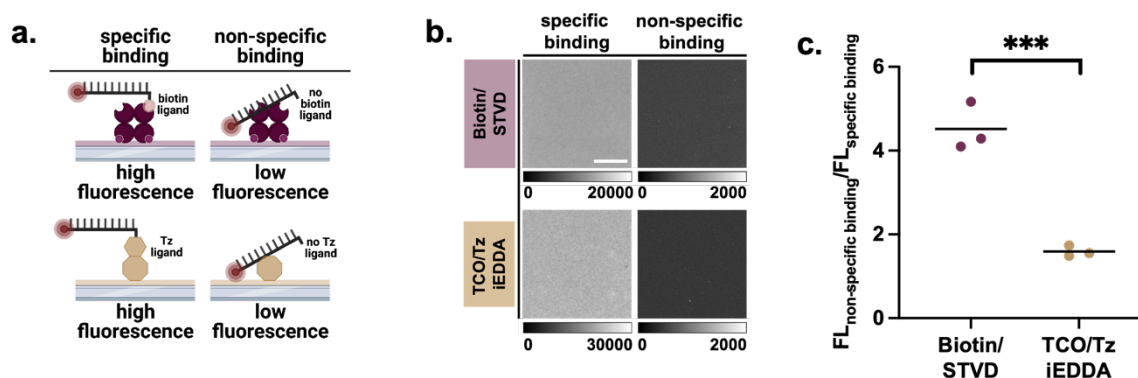


**Figure 19. TCO/Tz iEDDA surfaces have reduced levels of non-specific binding of biomolecules than biotin/STVD surfaces.** **a.** Scheme of measuring non-specific binding to biotin and TCO surfaces. Fluorescent DNA with and without biotin ligand is added to streptavidin coated biotin surfaces to measure specific binding to biotin surfaces. Fluorescent DNA with and without Tz ligand is added to TCO coated surfaces to measure specific binding to TCO surfaces. **b.** Fluorescence images of 10 nM Cy3B labelled DNA with and without ligand added to biotin and TCO surfaces. **c.** Quantification of non-specific binding of DNA to biotin and TCO surfaces. There is a significantly higher amount of non-specific binding of DNA to biotin coated surfaces than to TCO coated surfaces.  $n = 3$  surfaces, 10 regions imaged per surface.  $p = 0.001$ .

Next, we measured the on-rate of both the biotin/STVD and TCO/Tz iEDDA surfaces. Cy3B labeled with DNA functionalized with a biotin moiety was added to the Biotin/STVD surface in concentrations ranging from 0.1 to 10 nM (**Fig. 20a**). Images were collected over 90 minutes and corrected for background fluorescence and photobleaching (**Fig. 20b**). The linear regions of the fluorescence curves were plotted as a function of DNA molecules per  $\mu\text{m}^2$  (**Fig. 20c, Fig. A3**). Using pseudo-first-order kinetics, we calculated the  $k_{\text{reaction}}$  of DNA binding to biotin/STVD surfaces to be  $6.3 \times 10^6 \text{ M}^{-1} \text{ sec}^{-1}$ , consistent with previous literature reports (**Fig. 20d**).<sup>(58)</sup> Similar

protocols were followed for measuring the  $k_{\text{reaction}}$  of DNA binding to TCO/Tz iEDDA surfaces. DNA functionalized with a Tz moiety was added to the TCO/TZ iEDDA surface in concentrations ranging from 0.1 to 10 nM and images were collected over 90 minutes and corrected for background fluorescence and photobleaching (**Fig. 20e, f**). The linear regions of the fluorescence curves were plotted as a function of DNA molecules per  $\mu\text{m}^2$  and using pseudo-first-order kinetics, we calculated the  $k_{\text{reaction}}$  of DNA binding to TCO/Tz iEDDA surfaces as  $5.8 \times 10^6 \text{ M}^{-1} \text{ sec}^{-1}$ , consistent with previous literature reports (**Fig. 20g, h**).<sup>(69, 74)</sup> These similar on-rates highlight that when using the TCO/Tz iEDDA surfaces, one does not sacrifice the rapid kinetics of binding that can be achieved when using biotin/STVD surfaces.

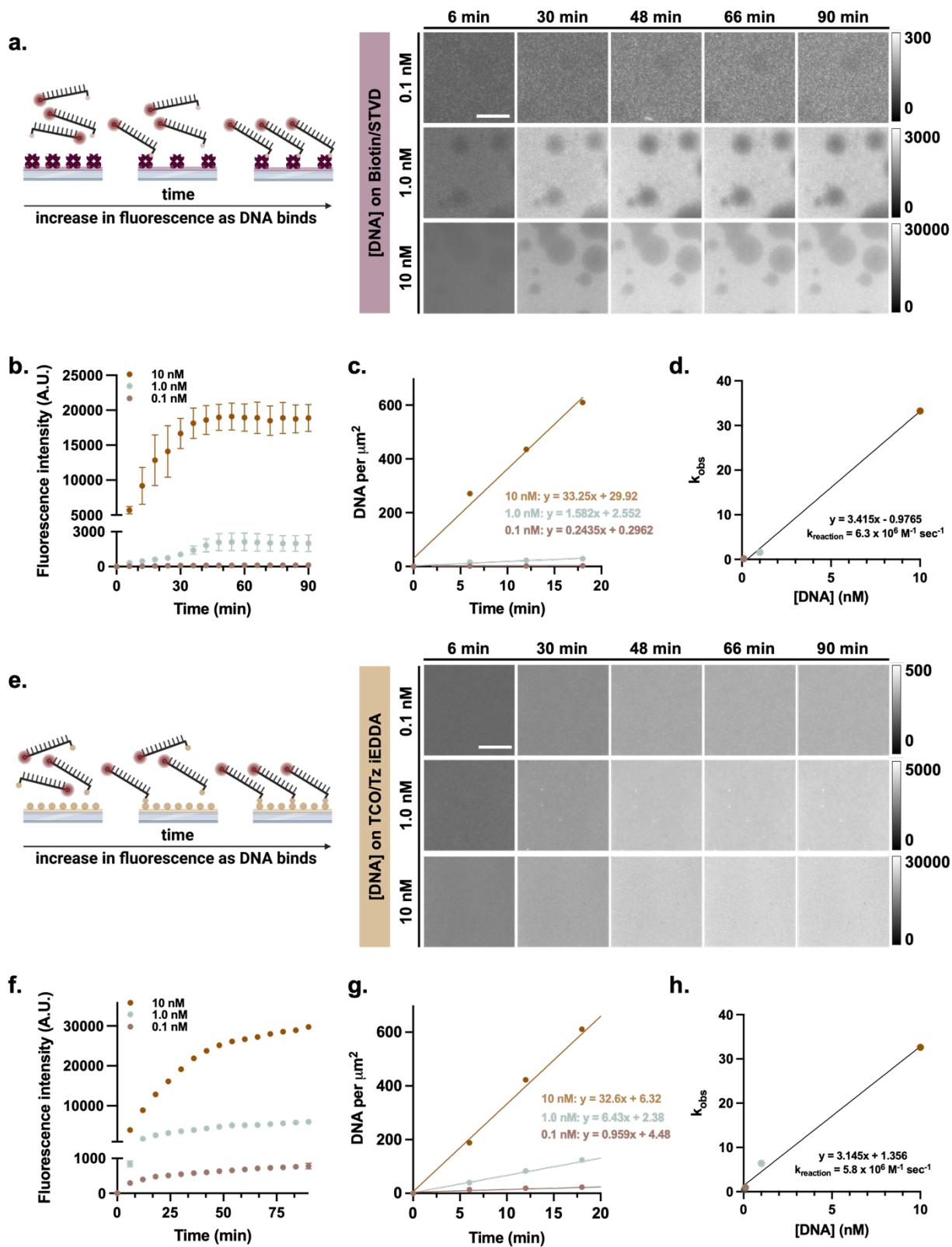


**Figure 20. Kinetics of DNA binding to Biotin/STVD and TCO/Tz iEDDA surfaces.** **a.** Fluorophore labeled DNA functionalized with biotin is added to Biotin/STVD surfaces and its binding recorded over time by measuring the increase in fluorescence of the surface. **b.** Fluorescence binding curves of 0.1, 1.0, and 10 nM Fluorophore labeled DNA functionalized with biotin to Biotin/STVD surfaces. Fluorescence was recorded for 90 minutes, and fluorescent images taken every 6 minutes. Reported values have been background subtracted and corrected for photobleaching.  $n = 3$  surfaces, 3 regions per surface. **c.** Linear region of fluorescence curves converted to DNA molecules bound per  $\mu\text{m}^2$  (**Fig. A3a, b**). **d.** The plot of  $k_{\text{obs}}$  vs concentration of DNA is used to calculate a  $k_{\text{reaction}}$  of  $6.3 \times 10^{-6} \text{ M}^{-1} \text{ sec}^{-1}$  for DNA binding to Biotin/STVD surfaces. **e.** Fluorophore labeled DNA functionalized with Tz is added to TCO/Tz iEDDA surfaces and its binding recorded over time by measuring the increase in fluorescence of the surface. **f.** Fluorescence binding curves of 0.1, 1.0, and 10 nM Fluorophore labeled DNA functionalized with Tz to TCO/Tz iEDDA surfaces. Fluorescence was recorded for 90 minutes, and fluorescent images taken every 6 minutes. Reported values have been background subtracted and corrected for photobleaching.  $n = 3$  surfaces, 3 regions per surface. **g.** Linear region of fluorescence curves converted to DNA molecules bound per  $\mu\text{m}^2$  (**Fig. A3c**). **h.** The plot of  $k_{\text{obs}}$  vs concentration of DNA is used to calculate a  $k_{\text{reaction}}$  of  $5.8 \times 10^{-6} \text{ M}^{-1} \text{ sec}^{-1}$  for DNA binding to TCO/Tz iEDDA surfaces.

### 2.3.2 TCO surfaces are more resistant to degradation than biotin surfaces

We next demonstrated that our surfaces are both biologically and thermally stable, filling a critical gap in common immobilization techniques. We first measured the stability of both biotin/STVD and TCO/Tz iEDDA surfaces at physiological temperatures relevant to biological applications. TCO-Tz is a covalent bond and therefore has a negligible off rate that is not accelerated by increased temperature. The biotin streptavidin interaction is non-covalent, and its off rate can be accelerated with increasing temperatures. To test the effect temperature would have on surface functionalization, we immobilized identical concentrations of fluorescently labeled DNA to both biotin/STVD and TCO/Tz iEDDA surfaces (**Fig. 21a**). We then measured the initial fluorescence intensity of the surfaces, as well as the intensity of the surfaces after being warmed to  $37^\circ\text{C}$  overnight, mimicking standard cell culture conditions (**Fig. 21b**). Indeed, we found that there was nearly a 70% decrease in fluorescence intensity of the non-covalent Biotin/STVD surfaces after 24 hours while there was not a significant difference in the fluorescence of the TCO/Tz iEDDA

surfaces, highlighting the thermal stability that TCO surfaces offer over biotin surfaces (**Fig. 21c**).

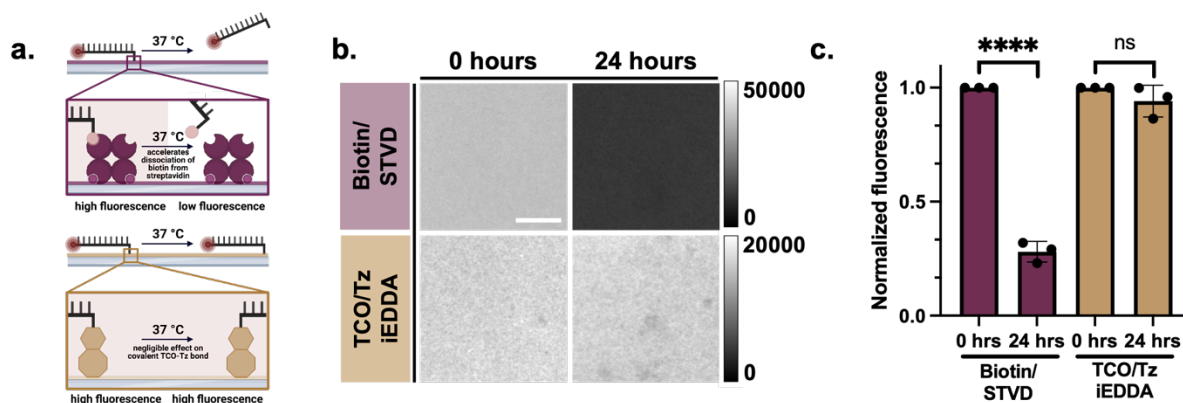


**Figure 21. TCO/Tz iEDDA surfaces are resistant to thermal degradation.** **a.** Experimental setup to measure thermal degradation resistance of Biotin/STVD and TCO/Tz iEDDA surfaces. Fluorophore labelled DNA is immobilized to either biotin or TCO coated surfaces and incubated at 37 °C for 24 hours. **b.** Fluorescence images of Biotin/STVD and TCO/Tz surfaces coated with fluorophore labelled DNA before and after 24 hour incubation at 37 °C. **c.** Quantification of fluorescence of Biotin/STVD and TCO/Tz iEDDA surfaces coated with fluorophore labelled DNA before and after 24 hour incubation at 37 °C. Fluorescence of Biotin/STVD surfaces significantly decreased after incubation while there was no significant change in fluorescence of TCO/Tz iEDDA surfaces.  $n = 3$  surfaces, 10 regions per surface. Biotin/STVD surfaces:  $p < 0.0001$ , TCO/Tz iEDDA surfaces:  $p = 0.2133$ .

Next, we tested the biological stability of Biotin/STVD surfaces compared to TCO/Tz iEDDA surfaces by measuring their susceptibility to protease degradation. Proteases are commonly secreted by cells and are enzymes which are responsible breaking peptide bonds in proteins, therefore the DNA should be left intact and any change in fluorescent signal can be attributed to cleavage of the bond between the DNA and surface. We again immobilized fluorescently labeled single stranded DNA to both biotin/STVD and TCO/Tz iEDDA surfaces before incubating the surfaces in trypsin, an enzyme that breaks down proteins (**Fig. 22a**). Following fluorescence measurements for 90 minutes, we observed that there was a 26% loss of fluorescent signal on the biotin/STVD surfaces compared to only 4% on the TCO/Tz iEDDA surfaces, demonstrating that the biotin/STVD interaction is unstable at the temperatures required for biological studies (**Fig.**

22b, c).

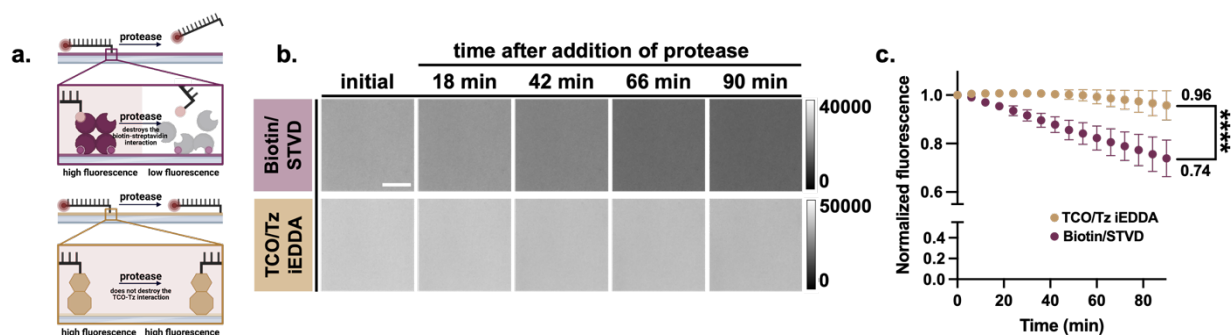


**Figure 22. TCO/Tz iEDDA surfaces are resistant to protease degradation.** **a.** Experimental setup to measure Biotin/STVD and TCO/Tz iEDDA surface resistance to protease degradation. Fluorophore labelled DNA is immobilized to either biotin or TCO coated surfaces and incubated in trypsin. **b.** Fluorescence images of Biotin/STVD and TCO/Tz iEDDA surfaces coated with fluorophore labelled DNA and incubated in trypsin for 90 minutes. **c.** Quantification of fluorescence over time of Biotin/STVD and TCO/Tz iEDDA surfaces coated with fluorophore labeled DNA and incubated in trypsin.  $n = 3$  surfaces, 10 regions per surface.  $p < 0.0001$ .

### 2.3.3 TCO surfaces are superior scaffolds for studying mechanotransduction

Highlighting the importance of degradation resistance of surfaces, we next used the Biotin/STVD and TCO/Tz iEDDA surfaces as scaffolds to measure the forces exerted by mouse embryonic fibroblasts (MEFs). MEFs were plated on surfaces coated with a DNA duplex force probe that reports on the accumulated force generated by a cell.<sup>(17, 31)</sup> The force probe consists of a DNA duplex immobilized to either a biotin/STVD or TCO/Tz iEDDA glass surface. The duplex is equipped with a cyclic RGDfK (cRGD) peptide specific for cell adhesion and a fluorophore and quencher pair. When sufficient cell force is applied by an integrin to the cRGD peptide, the duplex is ruptured separating the fluorophore and quencher, resulting in an increase in fluorescence that can be measured using conventional fluorescence microscopy (**Fig. 23a**). MEFs were cultured on Biotin/STVD and TCO/Tz iEDDA surfaces coated with fluorescent TGT'S and tension was measured after one and four hours (**Fig. 23b**). After both one and four hours, we did not observe a

significant difference in the spread area of MEFs on either Biotin/STVD or TCO/Tz iEDDA surfaces (**Fig. 23c**). After one hour, we observed that the signal: noise (S:N) of tension signal generated by MEFs on TCO/Tz iEDDA surfaces was significantly higher than the S:N of tension signal generated by MEFs on biotin/STVD surfaces (**Fig. 23d**). This difference was further amplified after four hours due to the dissociation of duplexes from the biotin/STVD surfaces at 37 °C, resulting in an increase in background fluorescence. DNA duplex force probes report on accumulated tension over time, therefore S:N increases on TCO/Tz iEDDA surfaces due to an increase in fluorescent tension signal generated by the cells that is not accompanied by an increase in background fluorescence.

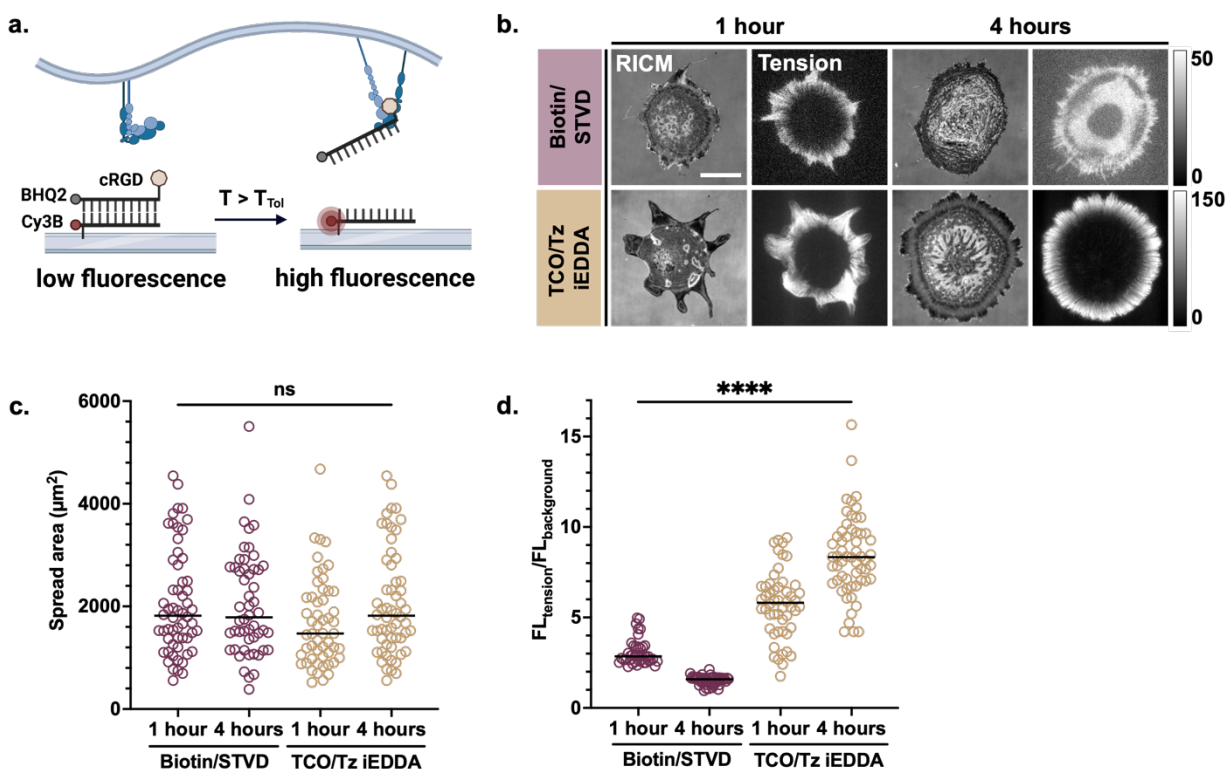


**Figure 23. Biotin/STVD and TCO/Tz iEDDA surfaces as scaffolds for measuring cell force. a.** Scheme of DNA fluorescent TGT's used for reporting on cell force exertion. In this study, fluorescent TGT's consist of a duplex in which the anchor strand is functionalized with a Cy3B fluorophore and either biotin or Tz. The ligand strand is functionalized with a BHQ2 quencher and cRGD peptide for cell adhesion. This duplex is then immobilized onto either Biotin/STVD or TCO/Tz iEDDA surfaces. Upon a cell exerting sufficient integrin mediated force through the cRGD peptide, the duplex is ruptured, separating the fluorophore and quencher, resulting in a measurable increase in fluorescence. **b.** Fluorescent tension signal generated by mouse embryonic fibroblasts (MEFs) cultured on TGT coated Biotin/STVD or TCO/Tz iEDDA surfaces for 1 hour. **c.** Spread area of MEFs on RS and RU probes. Spread area was measured by drawing a region of interest around platelets in the RICM channel.  $n = 3$  experiments, Biotin/STVD 1 hour: 58 cells, Biotin/STVD 4 hours: 52 cells, TCO/Tz iEDDA 1 hour: 53 cells, TCO/Tz iEDDA 4 hours: 58 cells, Biotin/STVD 1 hour:Biotin/STVD 4 hours  $p = 0.9192$  , Biotin/STVD 1 hour:TCO/Tz iEDDA 1 hour  $p = 0.0708$  , Biotin/STVD 4 hourS:TCO/Tz iEDDA 4 hours  $p = 0.9192$ , TCO/Tz iEDDA 1 hour:TCO/Tz iEDDA 4 hours  $p = 0.0708$  **d.** Signal to noise (S:N) of tension signal generated by cells cultured for 1 hour on fluorescent TGT's immobilized to biotin/STVD and TCO/Tz iEDDA surfaces defined as the fluorescence of tension signal ( $FL_{\text{tension}}$ ) divided by the local background fluorescence ( $FL_{\text{background}}$ ). S:N was significantly higher on TCO/Tz iEDDA surfaces compared to Biotin/STVD surfaces.  $n = 3$  experiments, Biotin/STVD 1 hour: 58 cells, Biotin/STVD 4 hours: 52 cells, TCO/Tz iEDDA 1 hour: 53 cells, TCO/Tz iEDDA 4 hours: 58 cells,  $p < 0.0001$ .

## 2.4 Discussion

Here, we have described using the TCO/Tz iEDDA reaction for functionalizing solid scaffolds and have highlighted several advantages of this functionalization strategy, particularly in a biological context. Using this reaction, one can functionalize glass surfaces with a homogenous layer of biomolecules that can be used in biological assays. Importantly, the  $k_{\text{reaction}}$  of immobilization of biomolecules to both Biotin/STVD and TCO/Tz iEDDA is nearly identical, and therefore there is not difference of efficiency in functionalizing TCO/Tz iEDDA surfaces relative to kinetics. However, it is important to note that the level of non-specific binding of biomolecules to TCO/Tz iEDDA surfaces is lower than the level of non-specific binding of biomolecules to Biotin/STVD surfaces. Therefore, the TCO/Tz iEDDA reaction produces surfaces that can be densely functionalized with a lower level of non-specific binding than Biotin/STVD surfaces.

Surfaces functionalized using the TCO/Tz iEDDA reaction are also more resistant to degradation than surfaces produced using the Biotin/STVD interaction. Specifically, unlike Biotin/STVD surfaces, surfaces functionalized using TCO/Tz iEDDA are resistant to thermal degradation and enzyme degradation that can occur at the conditions used for biologically relevant experiments. Finally, we demonstrate that TCO/Tz iEDDA surfaces are superior to Biotin/STVD surfaces when completing studies that rely on fluorescence. Specifically, MEFs cultured on fluorescent TGT's immobilized to TCO/Tz iEDDA surfaces generate have higher S:N than when cultured on fluorescent TGT's immobilized to Biotin/STVD surfaces, due to the degradation of the Biotin/STVD interaction at higher temperatures, and by the proteases secreted by the cells.

Taken together, we have demonstrated that the TCO/Tz iEDDA reaction is a superior method for producing substates used to study biological phenomena. The primary limitation that must be considered when using the TCO/Tz iEDDA reaction is stability of the reagents. Stability of Tz can be achieved by using methyltetrazine without sacrificing reaction rates or specificity of binding. It is possible for TCO to isomerize into the less reactive cis conformation, particularly when exposed to aqueous conditions. Therefore, it is important to store TCO functionalized scaffolds in an organic solvent such as DMSO until use. One final consideration when using the tetrazine is its solubility. Tz is very hydrophobic and therefore special care must be taken when functionalizing biomolecules to ensure that there is a sufficient amount of organic solvent present in the reaction buffer to maintain the solubility of the reagent. However, in our hands, upon functionalization of Tz to a biomolecule such as DNA, we did not observe any decrease in water solubility of the functionalized molecule. In summary, we have demonstrated that the TCO/Tz iEDDA reaction is a suitable addition to the toolkit of techniques used for surface tethering of biomolecules. Our

findings can be extended to other areas of surface chemistry, highlighting the strength of the TCO/Tz iEDDA reaction and the importance of considering the effect surface chemistry can have on data acquisition and analysis in biological and non-biological systems.

## CHAPTER 3. PNA TENSION PROBES EXPAND THE MEASURABLE FORCE RANGE OF NUCLEIC ACID INTEGRIN FORCE SENSING TECHNOLOGY

### 3.1 Abstract

Cells physically interact with their environment and respond to these stimuli through mechanotransduction, converting physical tension into biochemical signals that guide cell function. Mechanotransduction is critical for a variety of cell processes and has been implicated in the pathology and progression of a number of diseases. DNA and protein sensors that rupture or extend under force are widely used to measure cellular mechanoforces, offering high sensitivity and throughput without external perturbation of the cell. However, the composition of these probes make them susceptible to nuclease and protease degradation, significantly limiting the time scales they can report over. Furthermore, the inherent anionic structure of DNA polymers limits the mechanical rupture threshold of these probes. Peptide nucleic acids (PNAs) are an attractive alternative to address these problems. PNA is a synthetic DNA analog that retains its ability to form Watson-Crick-Franklin interactions, but is resistant to nuclease and protease degradation, and has a high affinity for its oligonucleotide binding partners, leading to increased mechanical stability. We demonstrate that by constructing nucleic acid rupture sensors out of PNA, we are able to measure integrin mediated forces in time and force regimes inaccessible using traditional DNA and protein-based sensors. Using PNA rupture sensors, we also improve the resolution of tension generated by aggressive cancer cell lines. Taken together, our results highlight a new class of molecular force sensors that expand the time and force range over which cell mechanics can be measured.

### 3.2 Introduction

As highlighted in **Chapter 1**, a major limitation of existing force sensing technologies is the threshold of forces on which they can report (**Fig. 24**). Genetically encoded tension sensors (GETS) and the PEG entropic spring report on forces  $< 20$  pN while DNA 2<sup>o</sup> structure and  $\beta$  sheet protein sensors are limited to upper thresholds of  $\sim 70 - 80$  pN. Specifically, the commonly used DNA-based tension gauge tether (TGT) is limited to an upper threshold of  $\sim 60$  pN of force.(17, 31) Importantly, there are currently no tools available to measure forces between 100 pN and 10 nN without external perturbation of the cell. This limitation is significant considering that mammalian cells have been reported to exert week-long traction forces in the nanonewton range.(75) Furthermore, many of these techniques are susceptible to degradation in biologically relevant environments. Both protein-based and DNA-based sensors are susceptible to enzymatic and thermal degradation and are therefore unsuitable for measuring cell mechanics over extended time frames. Together, these limitations present a significant barrier towards more comprehensive understanding of cell mechanics and mechanotransduction events, and new tools are needed to quantify higher cellular forces and resolve cell force in extended time frames.

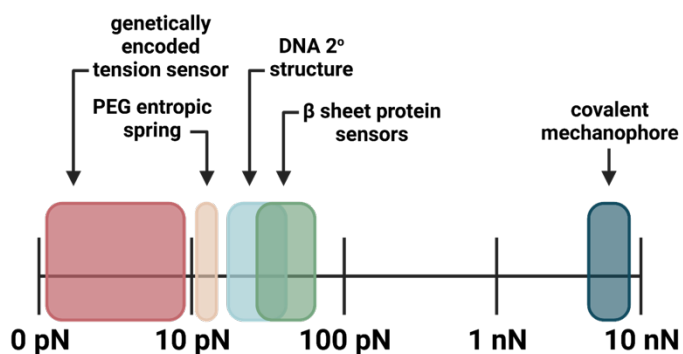


**Figure 14. Probe-based methods to measure cellular mechanotransduction events.** Current methods used to measure mechanotransduction events that do not involve an external perturbation of the cell are limited not only in their biostability, but in the range of forces they are able to reliably report on. As a result, there is not a reliable method to measure mechanical events with forces between 100 pN and 10 nN without applying a disruptive external force to the system. The force values represented here assume average bond lifetime of integrins.

### 3.2.1 Protein-based force sensors

Protein-based sensors are widely used in the study of mechanobiology in the form of genetically encoded tension sensors. There has been a long-standing interest in measuring the forces experienced by proteins within living cells, as it is known that cells can sense and transmit forces at molecular pN scales. Early studies of motor proteins using single molecule force spectroscopy showed that molecules such as kinesin, myosin, and dynein generate forces in the range of 1-10 pN, and hence it was suspected that force-sensing proteins experience forces in this pN magnitude regime.

Molecular forces on the order of 2-10 pN can drive conformational changes within proteins and hence regulate a host of biological processes including cytoskeletal rearrangement, protein binding, and integrin activation. (80-82). These molecular forces are critical to cellular function, yet measuring them remained a challenge prior to the development of genetically encoded tension sensors (GETS). GETS are protein-based and take advantage of the relationship between force-

extension and FRET. While a number of sensors that have been designed, each consists of the same basic construct. Fluorescent donor and acceptor proteins are designed to flank a flexible linker domain. Together, this construct serves as a tension sensing module and stretches and relaxes in response to changes in tension (**Fig. 25**). The construct is inserted into a protein of interest such that when the protein experiences tension, the linker extends, separating the fluorescent proteins, resulting in a change in FRET that can be measured by fluorescent microscopy.

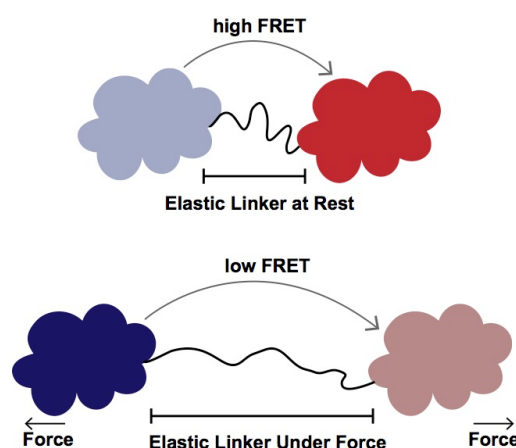


**Figure 25. Basic design of protein-based Genetically Encoded Tension Sensors (GETS).** Fluorescent protein FRET pairs are linked by a flexible linker that can stretch and relax in response to external tension. Reprinted with permission from *Molecular Force Sensors*; Copyright 2022 American Chemical Society

Challenges associated with this technique include identifying a flexible domain that can function as a spring and does not lead to misfolding and degradation of the protein of interest. Additionally, this spring domain must also match the FRET distances between the donor and acceptor. In other words, the flexible domain must bring the donor and acceptor in close proximity at rest but with the application of pN range forces, the domain must stretch to place the donor and acceptor at distances that exceed the FRET radius (often greater than 5 nm). Given that the magnitude of forces within cells is unknown, it is difficult to design appropriate probes without significant

amounts of empirical trial and error. The generation and subsequent characterization of GETS revolutionized the way one could measure intercellular tension. However, these protein-based sensors are limited to measuring intercellular forces below 10 pN and are not suitable for measuring integrin mediated forces modulated by the extracellular matrix.

Expanding the use of proteins in tension sensing beyond the genetically encoded tension sensor and into a sensor capable of reporting , the Salaita lab developed a sensor consisting of the I27 domain of titin (**Fig. 26**).<sup>(76)</sup> The sensor was flanked by a fluorophore and immobilized onto a gold nanoparticle that quenched fluorescence when the sensor was in its folded state. Using disulfide linkages and the known rates of disulfide reduction, the team calibrated the unfolding force of the sensor to  $110 \pm 15$  pN. Hence, these sensors were capable on reporting on high magnitude integrin-mediated forces. However, like all proteins, these sensors are susceptible to degradation in biological media. Furthermore the immobilization of these sensors to gold nanoparticles leaves them prone to force-induced dissociation as discussed in **Chapter 2**, limiting the force range that they can reliably report on.

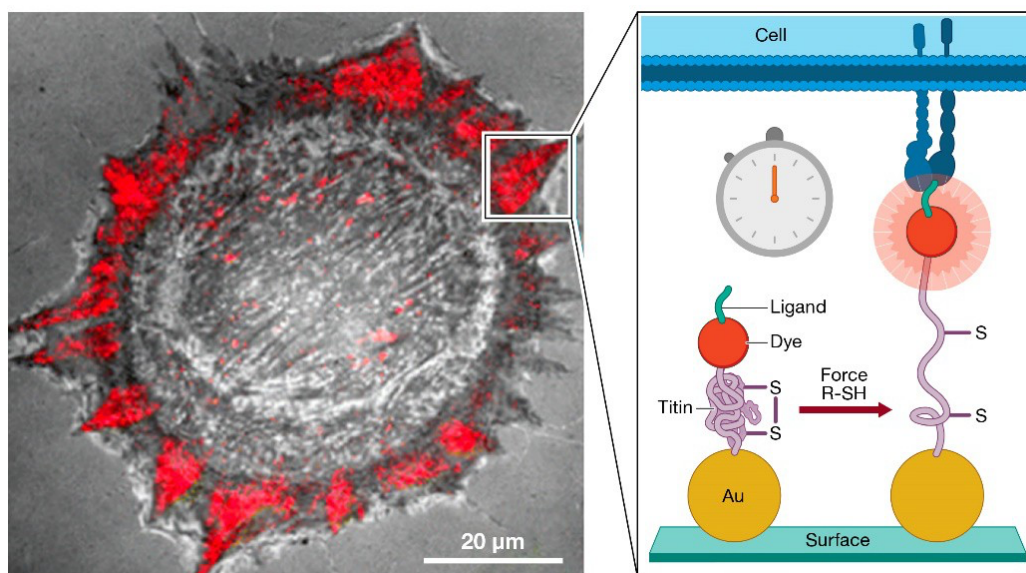


**Figure 26. Structure of the titin protein tension sensor.** The titin sensor, constructed from the I27 domain of the titin protein, was used to measure forces in focal adhesions and estimated to report on forces exceeding 110 pN. The force threshold of the sensor was determined by the rate at which the disulfide bridge in the sensor was reduced, resulting in unfolding of the sensor and increased fluorescence. Reprinted with permission from *Molecular Force Sensors*; Copyright 2022 American Chemical Society

### 3.2.2 Peptide nucleic acids (PNA)

Unnatural nucleic acids are alternatives to natural RNA and DNA that retain the ability to form Watson-Crick base pairs and store genetic information. These typically have modified backbone structures, altering their biophysical properties for biomaterial and nanotechnology applications. Several nucleic acid analogs have been developed, including locked and unlocked nucleic acids, threose nucleic acids, glycol nucleic acids, and peptide nucleic acids (**Fig. 27**). These modified structures often confer advantages on the nucleic acid structure such as increased thermostability and resistance to degradation in biological media.

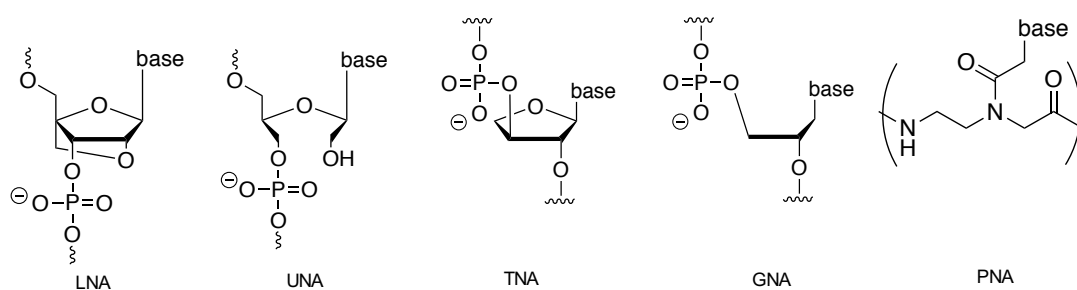


**Figure 27. Structures of synthetic nucleic acids.**

Peptide nucleic acids (PNA) are synthetic DNA analogs comprised of an unnatural amide backbone, endowing it with high nuclease and protease resistance. Additionally, the nonionic

backbone increases stability when hybridizing with itself or another oligonucleotide.(77) These unique properties position PNA as a promising candidate for use in therapeutics and diagnostic assays.(78)

### 3.2.3 Characterization of PNA

The structural properties of PNA have been extensively explored. The PNA amide backbone results in duplexes with unique hybridization patterns. While PNA forms Watson-Crick base pairs, the resulting helices are P-like, rather than traditional A and B form. (**Figure 28a**).<sup>(79)</sup> Additionally, the high specificity and unique hybridization properties of PNA enable unique binding mechanisms, including triplex formation and invasion.<sup>(80)</sup> The hybridization patterns, along with the unique binding modes results in duplexes with slightly different structural properties than DNA duplexes (**Figure 28b**).<sup>(81, 82)</sup>

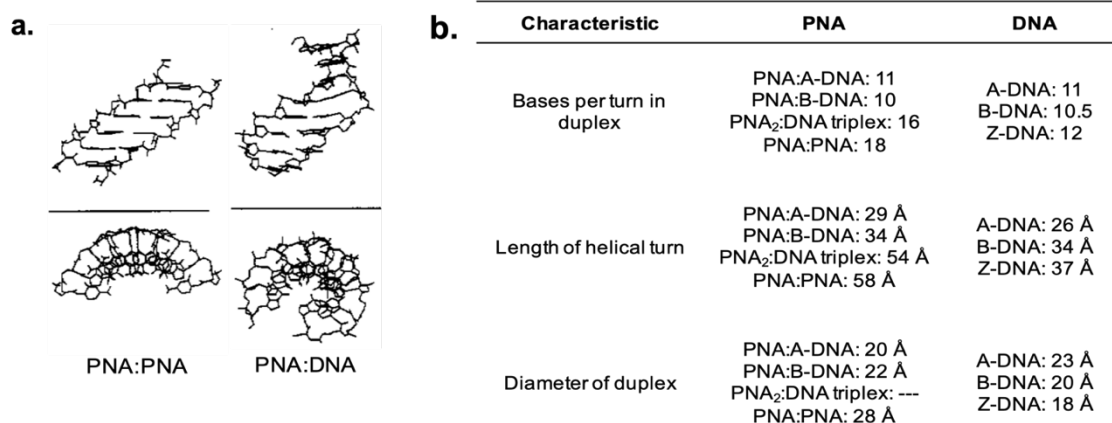


**Figure 28. Structural properties of peptide nucleic acids (PNA).** **a.** While PNA retains the ability to form Watson-Crick base pairs, the resulting duplexes have slightly different characteristics than natural DNA:DNA duplexes. **b.** Structural characteristics of PNA compared to DNA.

The relative stability of PNA has also been explored through melting temperature analysis, particularly when PNA is hybridized with DNA. On average, 10-mer PNA:DNA duplexes with 40% G/C content exhibit melting temperatures near 50 °C while 15-mer duplexes have melting temperatures near 70 °C.(83, 84) This is in contrast to DNA:DNA counterparts which have calculated melting temperatures of 22 °C and 43 °C under the same conditions. While PNA:PNA duplexes have been less characterized, one study found that 8-mer PNA:PNA with nearly 40% G/C content displayed melting temperatures of approximately 55 °C, while calculated DNA:DNA duplexes had a calculated melting temperature of 16°C.(85) Importantly, the affinity of PNA for its binding complements is higher than that of DNA, due to the lack of a backbone charge which can cause repulsion, and the pre-organized structure of PNA in solution.(86) Specifically, the binding constants of PNA are often on the order of magnitude of  $10^7$  while identical DNA counterparts have a binding constant on the order of  $10^5$ .(87)

Despite these analyses, characterization of PNA rupture force remains largely unexplored. Previous work has been limited to PNA:DNA and there are currently no reports of PNA:PNA duplex rupture forces. One report indicated that by AFM, a force of 148 pN was needed to rupture a poly-T 6-mer PNA with its complementary DNA. Corresponding DNA:DNA duplexes had a measured rupture force of only 35 pN.(88) In another study which probed miniPEG $\gamma$ -PNA-DNA using AFM, researchers found that the modified 10-mer PNA, when hybridized to a long DNA strand immobilized to a surface and AFM tip through a PEG linker, had a mean rupture force of  $65 \pm 15$  pN while the corresponding DNA:DNA setup had a mean rupture force of  $47 \pm 15$  pN.(89)

PNA:DNA duplexes have also been used as tension probes for measuring cell integrin forces. A previous study from the Wang lab successfully used PNA:DNA duplexes as tension probes, measuring the forces exerted by platelets, 3T3's, CHO-K1, HeLa, and MTC cells.(34) However, the scope of this work was limited to highlighting the biological stability of PNA:DNA duplexes, and the researchers did not explore the use of PNA:PNA for measuring the upper levels of integrin mediated force in cells.

Overall, while PNA:DNA duplexes have been moderately investigated, PNA:PNA duplexes remain only sparsely explored and to our knowledge, there are no reports of using PNA:PNA duplexes to study cellular mechanics. Here, we describe the synthesis and use of PNA:DNA and PNA:PNA rupture force sensors. We have generated these sensors in both shearing and unzipping conformations with the goal of extending the measurable force range of nucleic acid tension sensors beyond 60 pN. Using thermodynamic analysis, we demonstrate that PNA:DNA and PNA:PNA duplexes have lower values of  $\Delta G$  than DNA:DNA duplexes. We also demonstrate that unlike DNA- and protein-based force sensors, PNA force sensors are resistant to nuclease and protease degradation, enabling them as tools to report on cell forces over extended time frames. Importantly, PNA force sensors can report on forces generated by a variety of cell types as demonstrated here with fibroblasts, muscle cells, and cancer cells. Evidencing that PNA probes report on the upper levels of integrin forces, we show that while fibroblasts are not capable of opening a PNA:PNA force sensor in the shearing conformation, muscle cells are capable of rupturing the sensor after ~3 hours, suggesting that the sensors take a high magnitude force to be ruptured. Finally, we demonstrate the utility of PNA tension sensors in cancer cell force imaging. While DNA sensors are degraded rapidly by MDA-MB-231 cells, PNA force sensors remain intact

for longer than 5 hours, enabling force measurements over extended time frames.

### 3.3 Results

#### 3.3.1 Synthesis and design of PNA force sensors

PNA is a synthetic nucleic acid analogue with a pseudo-peptide like backbone (**Fig. 29a**). The PNA:DNA and PNA:PNA probes are comprised of 10-mer sequences with 40% G/C nucleobase content (**Table A2, Fig. A4 – A6**). The duplexes are synthesized in the high-force shearing and low-force unzipping conformations (**Fig. 29b, Fig. A7 – A14**) The shearing conformation is achieved by immobilizing the duplex onto the surface at the terminal opposite the cell adhesive peptide. As discussed in **Chapter 1**, shearing occurs by stretching the duplex along its axis in order to induce dissociation. This is a high-force event compared to probe unzipping, which occurs by stretching the sensor perpendicular to its axis. The probes are covalently functionalized with a Cy3B fluorophore and BHQ2 quencher, enabling the use of fluorescence as a readout for cell-mediated PNA unfolding and traction force. This force is applied through a cyclic RGD(fK) peptide covalently linked to the duplex using copper-mediated click chemistry. Furthermore, the probes are immobilized to the surfaces using the TCO/Tz iEDDA strategy discussed in **Chapter 2**. Hence, the probes are covalently anchored to the surfaces and only mechanical separation exceeding the  $T_{Tol}$  of the duplex leads to an increase in fluorescence. As a control, our PNA sensors were compared to conventional TGT force sensors. These sensors are comprised of 21-mer DNA:DNA duplexes and have a calibrated unzipping force of  $\sim 12$  pN and a calibrated shearing force of  $\sim 56$  pN. Hence, they serve as a useful control to compare our PNA-based sensors to when

estimating  $T_{\text{Tot}}$ .

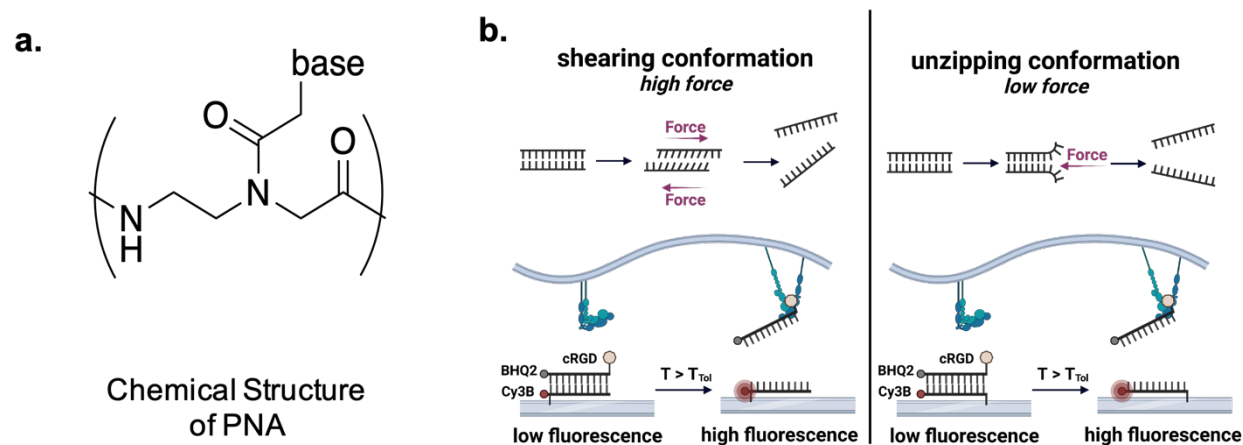


**Figure 29. Chemical structure of PNA and scheme of PNA force sensors.** **a.** Chemical structure of PNA. **b.** Scheme of shearing and unzipping constructs. Both the shearing and unzipping duplexes are covalently linked to a glass slide using the TCO/Tz iEDDA reaction. The shearing conformation is achieved by immobilizing the duplex onto the surface at the terminal opposite the cell adhesive peptide. Shearing occurs by stretching the duplex along its axis in order to induce dissociation. This is a high-force event compared to probe unzipping, which occurs by stretching the sensor perpendicular to its axis. The probes are covalently functionalized with a Cy3B fluorophore, BHQ2 quencher, and cyclic RGD(fK) peptide (cRGD). When a cell binds to the cRGD ligand and exerts a force exceeding the force tolerance of the duplex (when  $T > T_{\text{Tot}}$ ), the duplex is irreversibly ruptured, leading to a measurable increase in fluorescence.

### 3.3.1 Characterization of PNA force sensors

We first measured the  $\Delta H$ ,  $\Delta S$ , and  $\Delta G$  for the DNA:DNA, PNA:DNA, and PNA:PNA probes. In this study, the temperature-dependent fluorescence of Cy3B was measured from 25 to 100 °C, allowing us to detect probe dehybridization driven by increasing temperatures (**Fig. 30a**). The melting curves were used to generate a van't Hoff plot (**Fig. 30b**, **SI Note A1**).

The  $\Delta G$  ( $T = 298$  K) values for the DNA:DNA, PNA:DNA, and PNA:PNA were  $-20.7 \pm 2.1$ ,  $-26.5 \pm 3.7$ , and  $-25.5 \pm 2.8$  kcal mol<sup>-1</sup>, respectively (Fig. 30c).

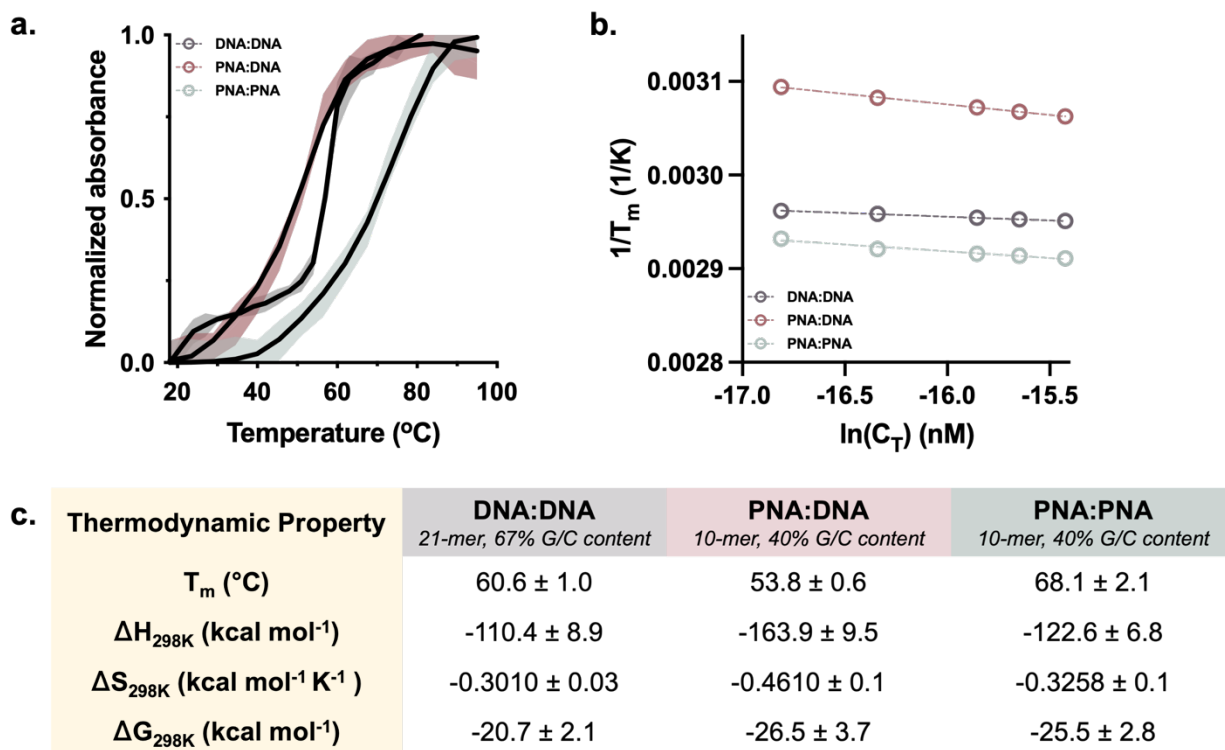
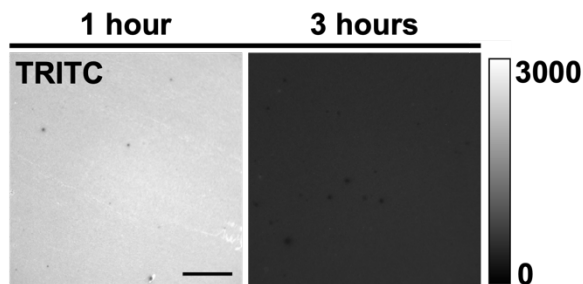
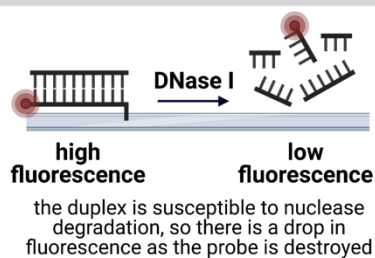


**Figure 30. Thermodynamic characterization of PNA- and DNA-based force sensors.** **a.** Temperature dependent DNA dehybridization analysis adapted from fluorescent melting curve for DNA:DNA, PNA:DNA, and PNA:PNA force sensors in 1X PBS solution. **b.** van't Hoff plot of DNA:DNA, PNA:DNA, and PNA:PNA generated from (a). **c.** Thermodynamic properties of DNA:DNA, PNA:DNA, and PNA:PNA force sensors as calculated from (b). Values were calculated for  $T = 298$  K.

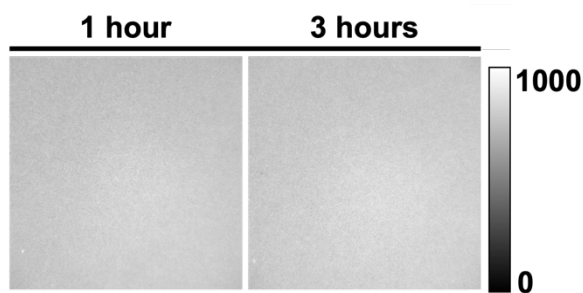
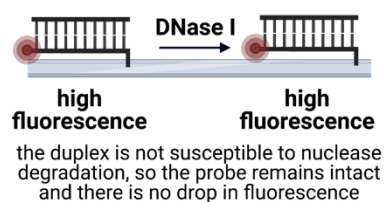
We next analyzed the stability of PNA force sensors in biologically relevant conditions. Specifically, we studied the resistance of PNA:DNA and PNA:PNA duplexes to enzyme degradation compared to commonly used DNA:DNA probes. DNA:DNA, PNA:DNA, and PNA:PNA duplexes were immobilized to a glass surface using the TCO/Tz iEDDA immobilization strategy discussed in **Chapter 2**. This immobilization strategy is covalent and

unsusceptible to thermal, chemical, and biological degradation. Therefore, any changes observed in functionalization of the surface is due to degradation of the duplexes. Probes were fluorescently labeled and therefore degradation could be measured by a decrease in fluorescence as probes are destroyed, releasing the fluorophore into solution (**Fig. 31a, b, c**). As expected, we observed rapid degradation of surfaces coated in DNA:DNA duplexes when the surfaces were exposed to the nuclease DNaseI and nearly 75% of fluorescent signal was lost within the first 30 minutes of analysis (**Fig. 31d**). Conversely, neither PNA:DNA nor PNA:PNA duplexes were destroyed by the enzyme and surfaces retained nearly 100% of their fluorescent signal over the course of the experiment. Importantly, although they possess an amide backbone, PNA:PNA duplexes were also found to be resistant to protease degradation with surfaces retaining nearly 100% of their fluorescent signal over three hours (**Fig. 31e, f**).

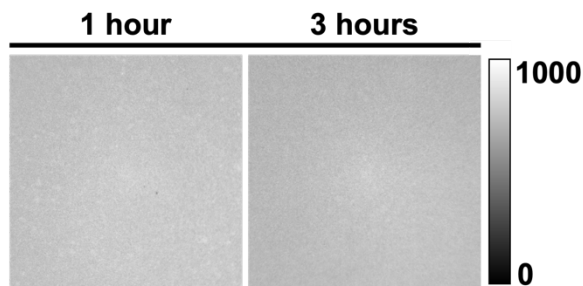
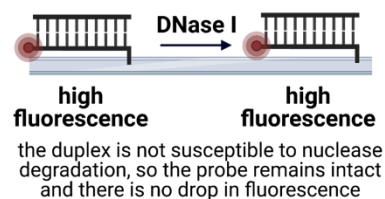
**a. DNA:DNA nuclease resistance**



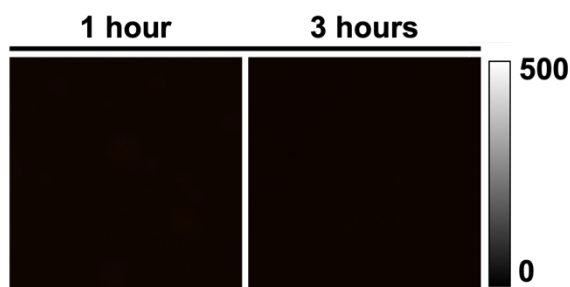
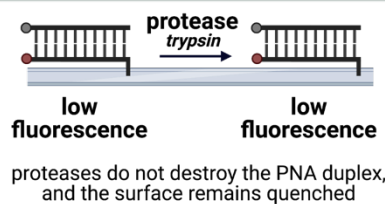
**b. PNA:DNA nuclease resistance**



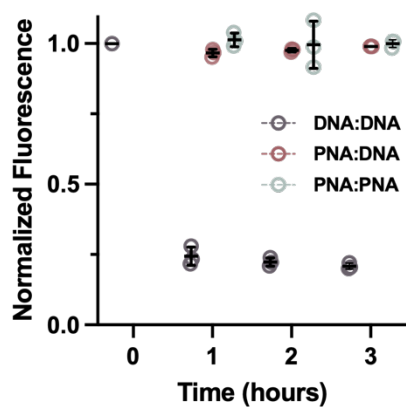
**c. PNA:PNA nuclease resistance**



**d. PNA: PNA protease resistance**



**e.**



**f.**

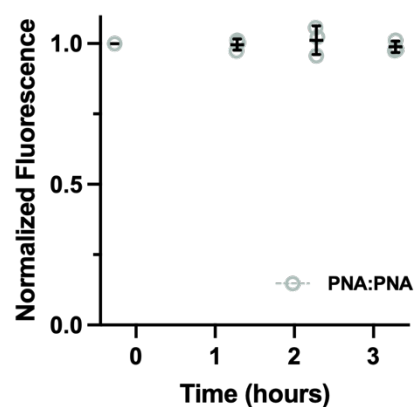


**Figure 31. PNA force sensors are resistant to nuclease and protease degradation.** **a.** Fluorescently labeled DNA:DNA duplexes were immobilized to a glass slide and exposed to DNaseI. The enzyme cleaved the duplexes, releasing the fluorophore from the surface, and there was an observable drop in fluorescence. **b.** Fluorescently labeled PNA:DNA duplexes were immobilized to a glass slide and exposed to DNaseI. The enzyme did not cleave the duplexes, and there was no observable drop in fluorescence. **c.** Fluorescently labeled PNA:PNA duplexes were immobilized to a glass slide and exposed to DNaseI. The enzyme did not cleave the duplexes, and there was no observable drop in fluorescence. **d.** Fluorophore and quencher labeled PNA:PNA duplexes were immobilized to a glass slide and exposed to the protease trypsin. The enzyme did not cleave the duplexes, and there was no observable increase in fluorescence. **e.** Quantification of DNA:DNA, PNA:DNA, and PNA:PNA fluorescence over time when exposed to DNaseI. There was a significant drop in fluorescence on DNA:DNA surfaces after 30 minutes but no significant decrease in fluorescence on PNA:DNA and PNA:PNA surfaces.  $n = 3$  surfaces, 10 regions per surface. **f.** Quantification of PNA:PNA fluorescence over time when exposed to trypsin. There was no significant increase in fluorescence over time indicating that the PNA:PNA duplexes were not degraded, keeping the fluorophore and quencher in close contact.  $n = 3$  surfaces, 10 regions per surface.

### 3.3.2 PNA sensors report on forces generated by fibroblasts

As an initial model, studied the behavior of NIH/3T3 fibroblasts on surfaces coated with DNA:DNA, PNA:DNA, and PNA:PNA sensors in the shearing and unzipping conformations. Fibroblasts are one of the best studied models for integrin mechanotransduction and their ability to generate large traction forces to mechanosense the ECM is well documented.(90, 91) 3T3s were cultured on DNA:DNA, PNA:DNA, and PNA:PNA sensors in the unzipping conformation (uDNA:DNA, uPNA:DNA, uPNA:PNA, respectively) and imaged 1, 3, and 5 hours after seeding to evaluate cell spread area and tension signal. (**Fig. 32a**). At 1, 3 and 5 hours, there were not significant differences in cell spread area (**Fig. 32b**). However, there was a significant difference in tension signal produced by 3T3s on all probes over all time points. Specifically, 3T3s on uDNA:DNA sensors produced higher tension signal than 3T3s on uPNA:DNA and uPNA:PNA sensors at all time points. Interestingly, the tension signal generated by 3T3s on uPNA:DNA and PNA:PNA sensors is significantly lower than the signal generated on DNA:DNA sensors, suggesting that PNA provides a level of mechanical stability to the sensors, increasing the  $T_{Tot}$

required to rupture the sensor (Fig. 32c).

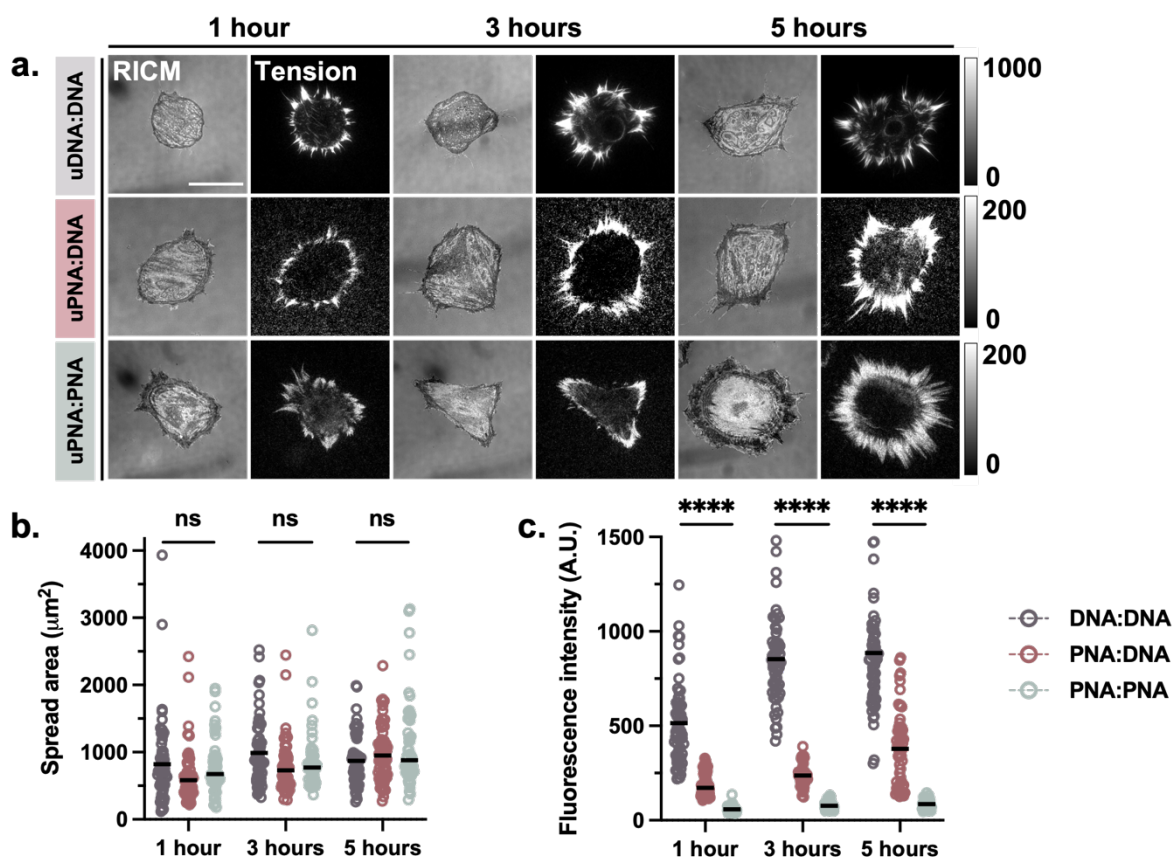


**Figure 32. PNA force sensors report on the forces generated by fibroblasts** **a.** RICM and fluorescent tension images of 3T3 cells cultured on uDNA:DNA, uPNA:DNA, and uPNA:PNA force sensors for 1, 3, and 5 hours. Scale bar, 100  $\mu\text{m}$ . **b.** Spread area of 3T3 cells cultured on uDNA:DNA, uPNA:DNA, and uPNA:PNA force sensors. Spread area was measured by drawing a region of interest around 3T3 cells in the RICM channel. (n = 3 experiments, 60 cells, uDNA:DNA:uPNA:DNA 1 hour p = 0.1946, 3 hours p = 0.0617, 5 hours p = 0.2998, uDNA:DNA:uPNA:PNA 1 hour p = 0.8199, 3 hours p = 0.2548, 5 hours p = 0.0591, uPNA:DNA:uPNA:PNA 1 hour p = 0.2968, 3 hours p = 0.7654, 5 hours p = 0.4863 **c.** Average fluorescence intensity generated by 3T3 cells cultured on uDNA:DNA, uPNA:DNA, and uPNA:PNA force sensors. Average fluorescence was determined by drawing a region of interest around the fluorescent signal in the TRITC channel. (n = 3 experiments, 60 cells, p < 0.0001 for all comparisons).

The difference is  $T_{Tot}$  of PNA and DNA force sensors particularly striking when 3T3s are cultured on sensors in the shearing conformation (sDNA:DNA, sPNA:DNA, sPNA:PNA). 3T3s were again cultured for 1, 3, and 5 hours on surfaces coated with sDNA:DNA, sPNA:DNA, and sPNA:PNA sensors. We did not observe a significant difference in cell spread area at any of the time points, indicating that the cells were well adhered to all surfaces (**Fig. 33a, b**). However, there was a significant difference in the tension signal generated by cells cultured on sPNA:PNA sensors compared to sDNA:DNA and sPNA:DNA sensors (**Fig. 33c**). Lack of fluorescent tension signal generated by 3T3s on sPNA:PNA probes provides further evidence that PNA:PNA duplexes are more mechanically stable than DNA duplexes and can therefore be used to study the upper level of integrin force.

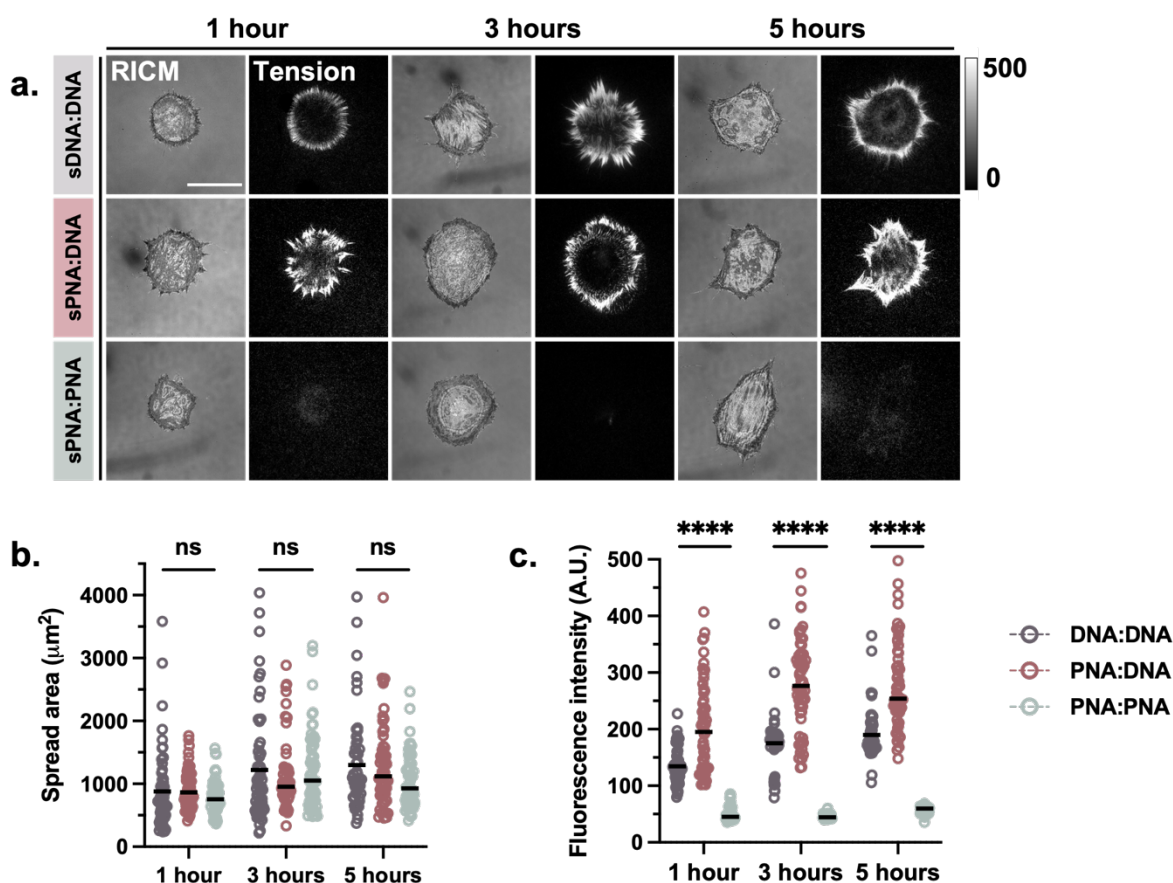


**Figure 33. Fibroblasts do not exert a  $T_{Tot}$  large enough to rupture sPNA:PNA force sensors.** **a.** RICM and fluorescent tension images of 3T3 cells cultured on sDNA:DNA, sPNA:DNA, and sPNA:PNA force sensors for 1, 3, and 5 hours. Scale bar, 100  $\mu\text{m}$ . **b.** Spread area of 3T3 cells cultured on sDNA:DNA, sPNA:DNA, and sPNA:PNA force sensors. Spread area was measured by drawing a region of interest around 3T3 cells in the RICM channel. (n = 3 experiments, 60 cells, sDNA:DNA:sPNA:DNA 1 hour p = 0.8684, 3 hours p = 0.6781, 5 hours p = 0.9942, sDNA:DNA:sPNA:PNA 1 hour p = 0.6286, 3 hours p = 0.9899, 5 hours p = 0.0847, sPNA:DNA:sPNA:PNA 1 hour p = 0.0756, 3 hours p = 0.7563, 5 hours p = 0.0554 **c.** Average fluorescence intensity generated by 3T3 cells cultured on sDNA:DNA, sPNA:DNA, and sPNA:PNA force sensors. Average fluorescence was determined by drawing a region of interest around the fluorescent signal in the TRITC channel. (n = 3 experiments, 60 cells, p < 0.0001 for all comparisons.

### 3.3.4 PNA sensors report on the upper levels of integrin force generated by muscle cells

To further test the hypothesis that sPNA:PNA sensors report in the upper level of integrin force in cells, we next cultured Human Airway Smooth Muscle Cells (HASMCs) on sDNA:DNA, sPNA:DNA, and sPNA:PNA sensors for 1, 3, and 5 hours. HASMCs are known to exert integrin mediated forces exceeding 100 pN, exceeding the range of 3T3s and making them a useful model to test the hypothesis that sPNA:PNA sensors report on a range of integrin forces inaccessible by sDNA:DNA sensors.

HASMCs were cultured on sDNA:DNA, sPNA:DNA, and sPNA:PNA sensors for 1, 3, and 5 hours (**Fig. 34a**). There were no significant differences in cell spread area, indicating that HASMCs were well adhered and spread on each of the three surfaces (**Fig. 34b**). Tension signal generated by 3T3s cultured on sDNA:DNA and sPNA:DNA sensors was again significantly higher than signal generated by 3T3s cultured on sPNA:PNA sensors (**Fig. 34c**). However, unlike surfaces in which 3T3s were cultured on shearing probes, HASMCs generated observable tension signal on sPNA:PNA probes after 3 hours, further evidencing that sPNA:PNA sensors can only be ruptured by high levels of force, and likely require a great force to open than 3T3s are capable of

exerting through their integrin receptors.

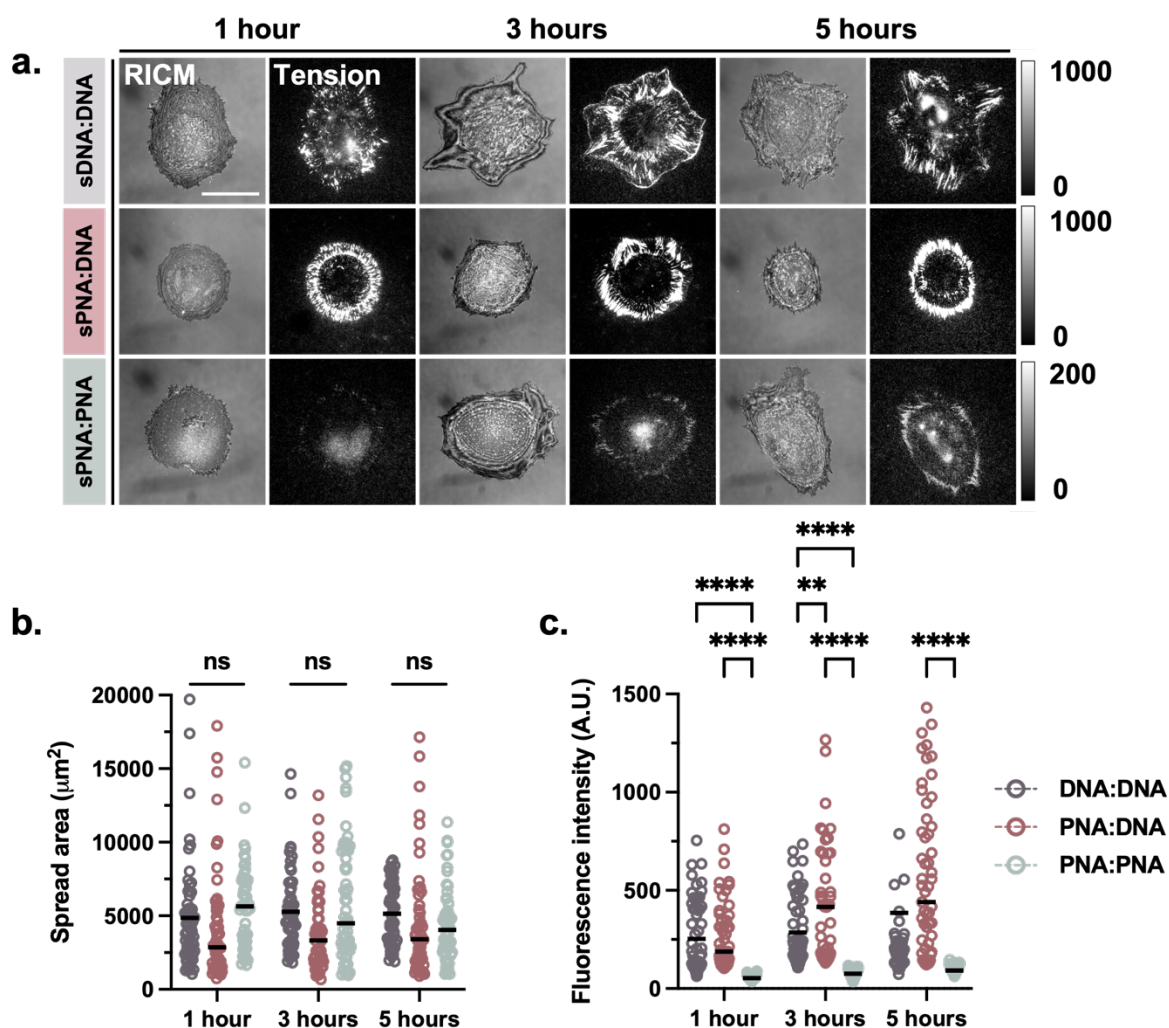


**Figure 34. PNA force sensors report on the upper levels of cell integrin force in muscle cells. a.** RICM and fluorescent tension images of HASMC's cultured on sDNA:DNA, sPNA:DNA, and sPNA:PNA force sensors for 1, 3, and 5 hours. Scale bar, 100  $\mu\text{m}$ . **b.** Spread area of HASMC's cultured on sDNA:DNA, sPNA:DNA, and sPNA:PNA force sensors. Spread area was measured by drawing a region of interest around HASMC's in the RICM channel. (n = 3 experiments, 60 cells, sDNA:DNA:sPNA:DNA 1 hour p = 0.5742, 3 hours p = 0.1096, 5 hours p = 0.6013, sDNA:DNA:sPNA:PNA 1 hour p = 0.4678, 3 hours p = 0.6859, 5 hours p = 0.1963, sPNA:DNA:sPNA:PNA 1 hour p = 0.0552, 3 hours p = 0.0513, 5 hours p = 0.9720) **c.** Average fluorescence intensity generated by HASMC's cultured on sDNA:DNA, sPNA:DNA, and sPNA:PNA force sensors. Average fluorescence was determined by drawing a region of interest around the fluorescent signal in the TRITC channel. (n = 3 experiments, 60 cells, sDNA:DNA:sPNA:DNA 1 hour p = 0.8402, 3 hours p = 0.0011, 5 hours p = 0.4694, sDNA:DNA:sPNA:PNA 1 hour p < 0.0001, 3 hours p < 0.0001, 5 hours p = 0.0567, sPNA:DNA:sPNA:PNA 1 hour p < 0.0001, 3 hours p < 0.0001, 5 hours p < 0.0001)

### *3.3.5 PNA sensors report on cancer cell mechanics with improved resolution over DNA sensors*

Finally, we next demonstrated the utility of degradation resistant force sensors by measuring the forces of the cancerous MDA-MB-231 cell line. Cancer cells are known to secrete proteases and nucleases within their environment, making their forces difficult to measure over extended time frames using conventional DNA and protein-based sensor designs. We cultured MDA-MB-231 cells on uDNA:DNA, uPNA:DNA, and uPNA:PNA sensors for 1, 3, and 5 hours and measured the spread area of the cells resulting fluorescent signal. As previously mentioned, significant degradation of DNA by nucleases happens in as little as 30 minutes. This presents a serious limitation in cancer cell imaging. Indeed, after 3 hours, it is evident that cells on uDNA:DNA surfaces have degraded the sensors on the surface, obscuring the tension signal (**Fig. 35a**). Interestingly, while the spread area of cells cultured on PNA duplexes increased over time, the spread area of cells cultured on DNA probes decreased, indicating that they had rapidly depleted their available ligand not only through mechanical dissociation, but also through degradation by nucleases (**Fig. 35b**). In contrast, cells cultured on uPNA:DNA and uPNA:PNA sensors could not destroy the duplexes, and therefore the cells increased in spread area over time due to their ability to continue to form adhesions to the surface. Notably, although the fluorescent tension signal generated by cells cultured on uPNA:DNA sensors is significantly higher than the signal generated on uDNA:DNA and uPNA:PNA sensors, it is difficult to discern if the fluorescent signal generated on uDNA:DNA sensors is due to mechanical separation of the duplex, or biological degradation (**Fig. 35c**).

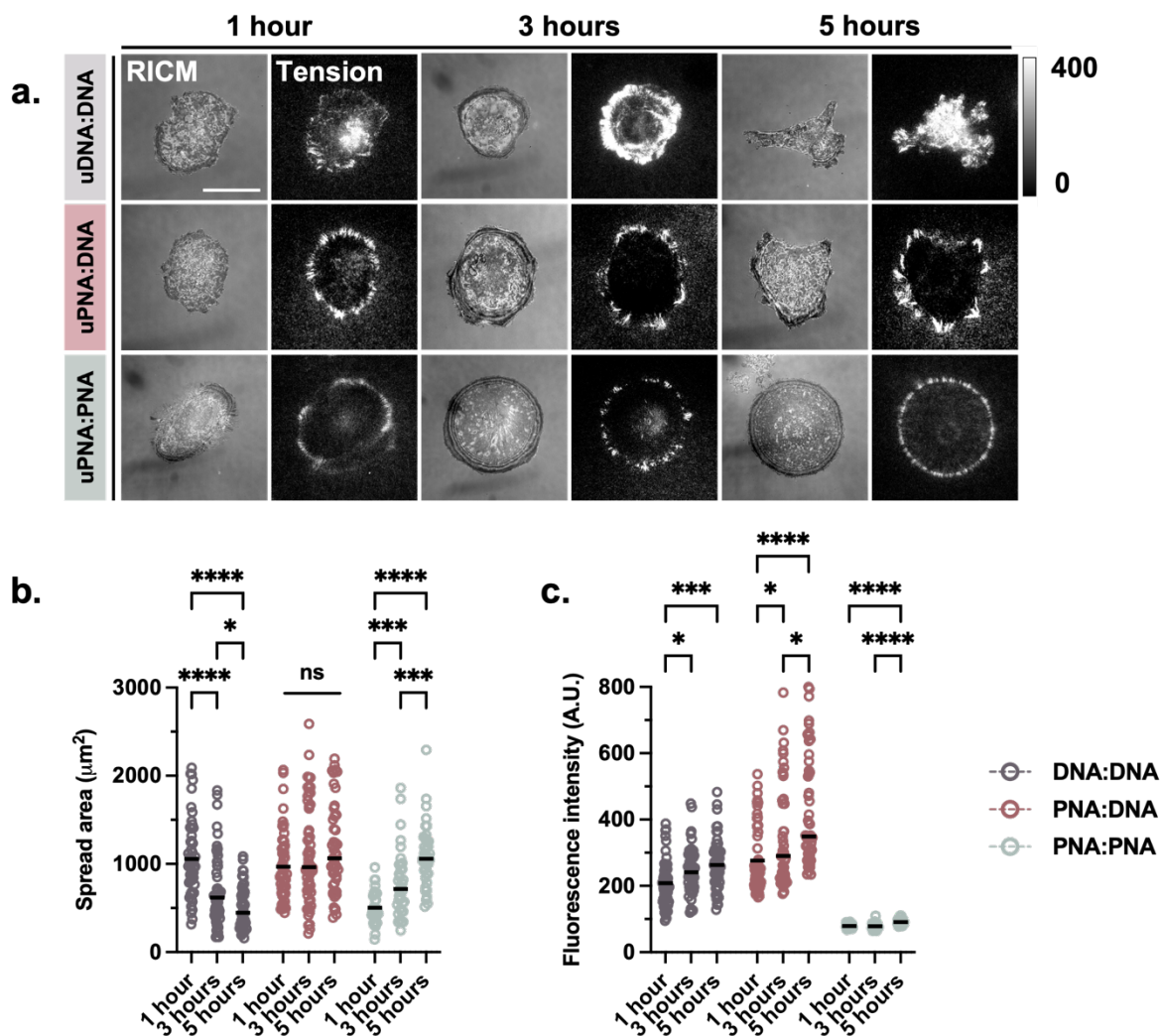


**Figure 35. PNA force sensors improve signal resolution of forces generated by cancer cells.** **a.** RICM and fluorescent tension images of MDA-MB-231 cells cultured on sDNA:DNA, sPNA:DNA, and sPNA:PNA force sensors for 1, 3, and 5 hours. Scale bar, 100  $\mu\text{m}$ . **b.** Spread area of MDA-MB-231 cells cultured on sDNA:DNA, sPNA:DNA, and sPNA:PNA force sensors. Spread area was measured by drawing a region of interest around MDA-MB-231 cells in the RICM channel. ( $n = 3$  experiments, 45 cells, sDNA:DNA:sPNA:DNA 1 hour  $p < 0.0001$ , 3 hours  $p = 0.3105$ , 5 hours  $p = 0.0006$ , sDNA:DNA:sPNA:PNA 1 hour  $p < 0.0001$ , 3 hours  $p = 0.0765$ , 5 hours  $p < 0.0001$ , sPNA:DNA:sPNA:PNA 1 hour  $p = 0.0142$ , 3 hours  $p = 0.7860$ , 5 hours  $p = 0.0009$ ) **c.** Average fluorescence intensity generated by MDA-MB-231 cells cultured on sDNA:DNA, sPNA:DNA, and sPNA:PNA force sensors. Average fluorescence was determined by drawing a region of interest around the fluorescent signal in the TRITC channel. ( $n = 3$  experiments, 45 cells, sDNA:DNA:sPNA:DNA 1 hour  $p = 0.0178$ , 3 hours  $p = 0.0242$ , 5 hours  $p = 0.9243$ , sDNA:DNA:sPNA:PNA 1 hour  $p = 0.0002$ , 3 hours  $p < 0.0001$ , 5 hours  $p < 0.0001$ , sPNA:DNA:sPNA:PNA 1 hour  $p < 0.3625$ , 3 hours  $p = 0.0243$ , 5 hours  $p < 0.0001$ )

### 3.4 Discussion

We have synthesized a new generation of PNA-based force sensors that are resistant to biological and thermal degradation and likely report on the upper levels of integrin forces. Previously reported protein- and DNA-based probes have two primary limitations. One is that they are susceptible to biological degradation in conditions relevant for cell imaging. Specifically, protein-based sensors are susceptible to degradation by proteases while DNA-based sensors are degraded by nucleases. This presents a significant limitation in imaging forces of cancer cells which are known to secrete proteases and nucleases into their environment. A second limitation of current force probing sensors is the force range on which they can measure. Current DNA-based probes can only report on forces  $< 60$  pN. However, the high association rate of PNA for other oligonucleotides combined with its thermostability make it a promising candidate for producing force sensors that report on the upper limits of cell integrin force. Importantly, in our design, PNA probes are covalently linked to the surface using the TCO/Tz iEDDA reaction. Hence, our ability to measure high magnitude forces is not limited by possible dissociation of the probes from the surface.

We have generated PNA:DNA and PNA:PNA force sensors in the unzipping and shearing conformations. PNA:DNA duplexes have a  $T_M$  of  $53.8 \pm 0.6$  °C and a  $\Delta G$  of  $-26.5 \pm 3.7$  kcal mol<sup>-1</sup> while PNA:PNA duplexes have a  $T_M$  of  $68.1 \pm 2.1$  °C and a  $\Delta G$  of  $-25.5 \pm 2.8$  kcal mol<sup>-1</sup>. As a control, these duplexes were compared to DNA:DNA duplexes that have a  $T_M$  of  $60.6 \pm 1.0$  °C and a  $\Delta G$  of  $-20.7 \pm 2.1$  kcal mol<sup>-1</sup>. We demonstrate that PNA probes are resistant to nuclease and protease degradation and therefore can be used in cell imaging applications over extended time

frames.

Using PNA force sensors, we have demonstrated that cell integrins likely exert peak forces  $\gg 60$  pN, and steady state forces  $> 60$  pN. 3T3 cells were capable of exerting forces greater than the  $T_{Tol}$  of the uPNA:DNA, uPNA:PNA, and sPNA:DNA force sensors. However, they were incapable of exerting forces exceeding the  $T_{Tol}$  of the sPNA:PNA duplexes, suggesting that these sensors report on an upper level of integrin force that 3T3s cannot achieve. HASMCs, a cell line known to exert forces  $> 100$  pN were capable of exerting forces greater than the  $T_{Tol}$  of both sPNA:DNA and sPNA:PNA sensors, providing further evidence that the  $T_{Tol}$  of PNA-based force sensors is greater than the  $T_{Tol}$  of DNA-based force sensors.

Ongoing work is underway to model the exact shearing and unfolding behavior of PNA-based sensors to determine the  $T_{Tol}$  of the sensors discussed here. However, we can arrive at our estimation of  $T_{Tol}$  using prior calibration data of the TGT. The  $T_{Tol}$  of the DNA:DNA duplexes used in this work has been calibrated in previous works. The uDNA:DNA sensor is known to have an unzipping force of  $\sim 12$  pN while the sDNA:DNA sensor is known to have a rupture force of  $\sim 56$  pN. It is important to note that calibration of sensors and the force threshold values they reveal are not absolute. Such measurements are time and loading rate dependent and therefore will vary based on experimental conditions. However, the values presented here are calculated using an average bond lifetime of integrins and are therefore relevant to the work described. Hence, these values of TGT unzipping and shearing provide useful context when estimating the force threshold of our PNA force sensors.

Finally, we demonstrated the utility of a biostable force sensor by measuring the tension signal

generated by the cancer cell line MDA-MB-231 on DNA- vs PNA-based force sensors. As expected, signal resolution was lost on the DNA-based sensors in as little as 3 hours and was indistinguishable from the fluorescence resulting from degradation of the probes after 5 hours. The degradation of the probe also impacted cell adhesion, and spread area of MDA-MB-231 cells on uDNA:DNA sensors significantly decreased over time due to degradation of ligand. However, tension signal remained discernable on both uPNA:DNA and uPNA:PNA force sensors, highlighting the importance of using such sensors to measure tension of aggressive and destructive cell lines.

## CHAPTER 4. CELL ADHESION RECEPTORS DETECT THE MOLECULAR FORCE EXTENSION CURVE OF THEIR LIGANDS

*Adapted from Bender, R. L., Ogasawara, H., et al. "Cell adhesion receptors detect the molecular force extension curve of their ligands"*

### 4.1 Abstract

Integrin receptors transduce the mechanical properties of the extracellular matrix. Past studies using DNA probes showed that integrins sense the magnitude of ligand forces with pN resolution. An open question is whether integrin receptors not only sense force magnitude, but also sense the force-extension trajectory of their ligands. The challenge in addressing this question pertains to the lack of molecular probes that can control force-extension trajectories independently of initial and final states of the probe. To address this limitation, we synthesized two DNA probes that are thermodynamically identical in their initial folded and final unfolded states but follow different force-extension trajectories to reach their final unfolded ssDNA states. As fibroblasts mechanically open the RS probe, they experience an abrupt disruption in their mechanical input upon shearing of the probe, and do not regain substantial mechanical input until the probe has been fully extended. This is reflected in their markers of mechanotransduction such as reduced stress fiber formation, reduced nuclear YAP localization, increased focal adhesion turnover, and reduced integrin activation. In contrast, when presented with RU probes, fibroblasts do not experience an abrupt change in their mechanical input and therefore have elevated markers of mechanotransduction. Simulations support our experimental data and suggest that integrins form a molecular clutch that is sensitive to the geometry of the ligand. This demonstrates that integrin receptors within focal adhesions sense the molecular force-extension trajectory of their ligands and are sensitive to abrupt changes in these trajectories.

## 4.2 Introduction

### *4.2.1 Design of Molecular Sensors*

In addition to rupture sensors that were discussed in **Chapter 3**, another class of sensors relies on the unfolding, rather than rupture of nucleic acids. These sensors unfold and re-fold in response to cell force and measure the “real-time” force generated by a cell. When designing such sensors, it is important to consider the force-extension behavior of the sensor, both in how it affects readout, and in how the extensibility may be used to modulate cell response.

The extension of molecules and polymers under force is radically different from the extendibility of macroscale springs. Indeed, some molecules will display switch-like behavior (such as DNA or folded proteins) and will only extend within a narrow range of forces. In other words, they remain folded until undergoing a sharp transition into their extended or unfolded state. However, other molecules, (such as polymers of ethylene glycol) will gradually extend as the applied force increases until the polymer nears its full length.

Design of molecular force sensors draws heavily on the principles of polymer force extension, and the behavior of fluorescent molecules. Polymer force extension describes the behavior of macromolecules at rest and when an external force is applied. Application of force allows polymers to exist outside of their optimal energy conformations. Hence, when designing molecular tension sensors, it is important to know the optimal energy conformations of the polymer being used and whether the force generated by the receptor of interest is sufficient to drive the necessary conformational change (extension) of the probe.

Force sensors for mechanobiology are designed to detect conformational changes in macromolecules rather than covalent bond rupture. Synthetic and biological polymers have all been employed as the “spring element” in molecular tension sensors. In this context, the word “spring” does not suggest that sensors behave as ideal Hookean springs that linearly extend as the force increases, but rather conveys the qualitative notion that the two ends of the molecule will become separated with force.

Like a rubber band, polymers are subject to tension as they are stretched. Polymer stretching and the accompanying forces can also be thought of in terms of the energy associated with their conformational changes (**Fig. 36**) (22). The relationship between the extensibility of a polymer and the force it experiences depends on how the polymer finds balance between its entropy and the molecule’s optimal energy conformation (23). Entropy implies inherent disorder; therefore, in irreversible processes, entropy is always increasing. However, reversible systems aim to reduce their entropy by existing in the lowest possible energy conformations. This is counterintuitive to the second law of thermodynamics, which states that entropy can never decrease. Hence, reversible systems must maintain “zero-sum” entropy.

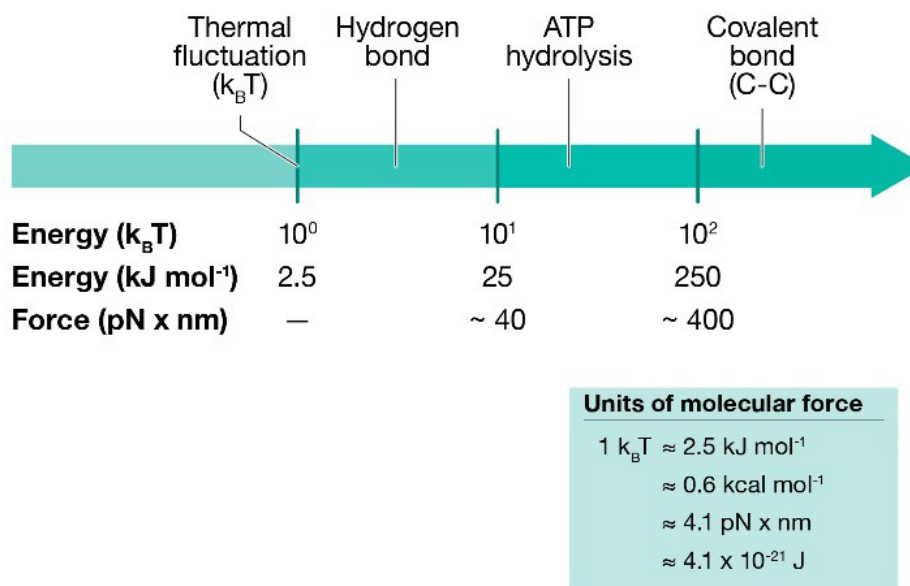


**Figure 36. Converting between force and energy.** Reprinted with permission from *Molecular Force Sensors*; Copyright 2022 American Chemical Society

Similar concepts exist in reversible molecular force sensors. The lowest energy conformations are achieved when force sensors are in their folded states. However, the application of force from a cell is sufficient to overcome the entropic barrier to unfolding, making these sensors highly effective tools for reporting on the receptor-mediated forces exerted by the cell. The principles of polymer force extension also have implications when designing the readout for molecular force sensors. Understanding the properties of polymer extension is critical to developing sensors that maximize this observable fluorescent signal.

#### 4.2.2 Modeling Polymer Behavior: Force-Extension Graphs

Force-extension graphs are used to describe the behavior of the polymer under tension and arise from the loss of entropy that a polymer experiences as it is extended (24). These graphs plot the force versus extension, and therefore the slope of the linear region of the curve represents the

stiffness of a polymer in the form of the spring constant. The lower the slope, the lower the spring constant and therefore the lower the stiffness of the polymer. Hence, under low levels of force, a polymer behaves similarly to an entropic spring - as the chain is stretched, the number of conformations a polymer can assume decreases and thus, entropy decreases (25). The external mechanical work that is applied to the sensor is stored in the polymer in the form of reduced entropic freedom.

In addition to providing information regarding the stiffness of a polymer, force extension curves can be used to estimate the energy stored in a polymer as it undergoes extension (**Fig. 37**). Just as when one stretches a rubber band, as more force is applied, it stretches further, and the energy stored in the rubber band increases until it can't be stretched any further. Continuing to stretch the rubber band will result in it becoming fully extended, or in the case of a molecule, reaching its full contour length. As previously mentioned, as the polymer is stretched, the conformations it can adopt or degrees of freedom the individual bonds have decreases. Therefore, the driving force of polymer behavior changes from entropy to enthalpy.

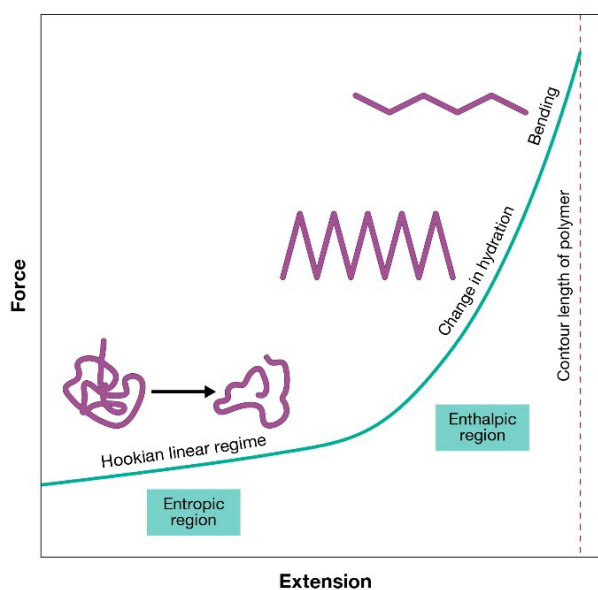


**Figure 37. Model of a force extension curve.** As polymers are stretched, they travel through several transitions. First, a well-solvated polymer at rest exists in its lowest energy conformation. Upon application of force, the polymer is pulled out of its lowest energy conformation and begins to stretch. As the polymer approaches its full contour length the number of conformations it can assume is reduced as the degrees of freedom each bond has become more limited. As a result, its extension becomes controlled by enthalpy rather than entropy. Reprinted with permission from *Molecular Force Sensors*; Copyright 2022 American Chemical Society

#### 4.2.3 Polymer Force-Extension Behaviors

The shape of the force-extension plot for any given macromolecule can be very complex and difficult to predict *a priori*. Tension sensors that use different types of spring elements, like proteins, peptides, nucleic acids, and synthetic polymers, will extend or rupture in response to the force differently according to their chemical and physical structure. Despite the complexity of trying to predict and measure the force-extension plot for any given macromolecule, there are some general classes of behaviors for idealized polymer systems that are useful to frame the discussion.

For example, consider a well-solvated polymer with minimal intramolecular interactions (no secondary structure). At rest, the polymer will adopt random conformations in solution – akin to cooked spaghetti in boiling water. The energetic cost of mechanically stretching this polymer will be relatively low, and the applied forces simply limit the entropic freedom of the polymer. Hence, this type of polymer is described as an entropic spring. In fact, entropic-spring behavior was the inspiration for the earliest synthetic molecular tension sensors used to study mechanobiology and the first example of a calibrated genetically encoded tension sensor (TSMoD) developed by Martin Schwartz and colleagues (27). This tension sensor consisted of a flagelliform linker sequence polymer flanked by fluorophores. As a cell exerted mechanical force on this sensor, the linker was extended, and the fluorophore was moved out of the

proximity of the quencher, resulting in a measurable increase in fluorescence.

A second class of polymer force-extension is one that is again well solvated but now has significant intramolecular interactions that drive the formation of secondary (and sometimes tertiary) structure. Examples of these types of polymers are DNA duplexes and hairpins as well as proteins. Because these structures are folded in defined 3D structures and their unfolding is highly cooperative, the force-extension plots tend to show abrupt changes in extension in response to a narrow range of externally applied forces. However, and perhaps counterintuitively, this switch-like extension behavior is very useful for constructing tension sensors.

A final class of polymer force extension behavior is one for polymers that are not well solvated and are therefore difficult to extend, such as polystyrene in an aqueous solution. Interactions between the hydrophobic backbone and aromatic groups with the water solvent are highly unfavorable, so the force to extend the polymer is very large. While the synthesis of tension sensors engineered using hydrophobic polymers is feasible, such sensors would be impractical for studying force in living systems, as the forces required for extension exceed the molecular forces employed in biology and the hydrophobicity of the polymer may also perturb the cell membrane.

#### *4.2.4 Worm-like chain model*

The worm-like chain (WLC) model describes deformations of relatively stiff biological macromolecules including proteins and DNA and is therefore the model most relevant to designing

and understanding the behavior of molecular tension sensors (**Fig. 38**) (34-37).

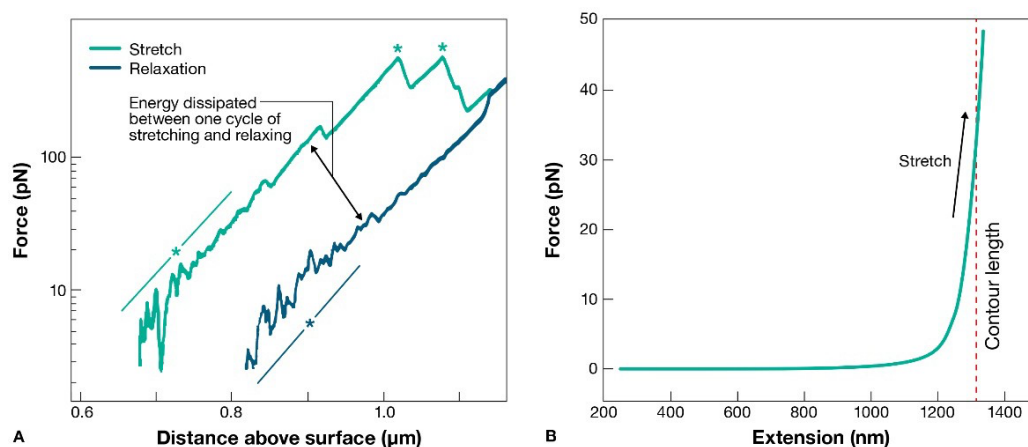


**Figure 38 Extension behavior of protein and DNA.** **a.** Force extension behavior of the spider silk protein used in the genetically encoded tension sensors. Force increases exponentially as spider silk protein is extended. The “saw-tooth” patterns, as indicated by the red and blue asterisks, indicate the bond rupture events that occur as the peptide is elongated. As the bonds are broken, new peptide length is revealed, reducing the overall tension on the peptide (hence the repeated drops in force). **b.** Force extension behavior of single-stranded DNA. Force increases as the DNA is stretched towards its contour length. Reprinted with permission from *Molecular Force Sensors*; Copyright 2022 American Chemical Society

The WLC represents an inextensible polymer, a polymer that has uniform distribution of stiffness along its entire length, and whose behavior is driven by thermal fluctuations. Unlike the freely jointed chain model, which divides the polymer chain into defined linear segments and determines mean end-to-end distance of the polymer as a sum of freely rotating vectors (**Fig. 39a**), the WLC models the curvature of the chain and integrates the tangent along the length of the polymer to account for the polymer’s inherent flexibility (**Fig. 39b**). More simply put, in contrast to an ideal chain, which is only flexible between defined rigid segments, this model assumes a continuously flexible rod that is stiff over short distances and flexible over longer distances.

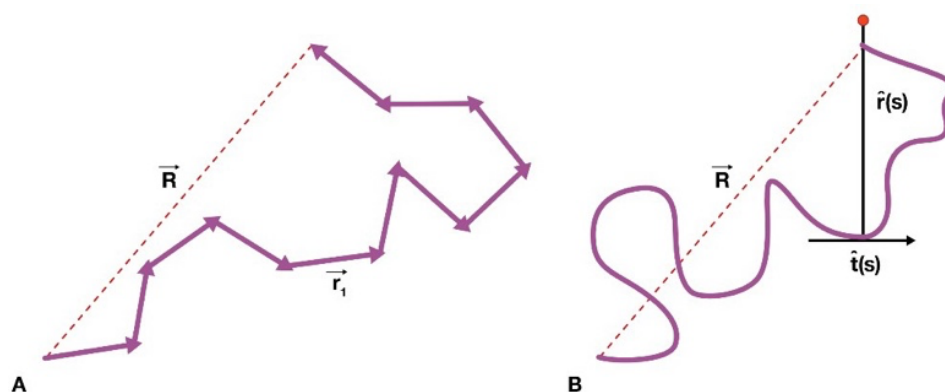


**Figure 39. Models of ideal chains and worm-like chains.** **a.** Model of ideal chain. **b.** Model of worm-like chain. Reprinted with permission from *Molecular Force Sensors*; Copyright 2022 American Chemical Society

At low forces, the standard extension and force relationship described by Hooke's law is observed. However, as the polymer approaches its full contour length, the extension is no longer linear and the difference between the end-to-end extension and total contour length approaches zero. This behavior can be modeled using force-extension graphs and is important to consider when designing tension sensors and analyzing a cell's response to the unfolding trajectory of the probe.

#### 4.2.5 Molecular Springs with Secondary Structure

Molecular tension sensors using entropic spring polymers that are well described by the WLC model are very sensitive to low values of mechanical forces. This statement would seem obvious as the resistive forces to extension are driven by entropy and are therefore very low (less than 10 pN) for well-solvated polymers. Interestingly, multiple reports, including work by the Salaita and Ha labs, demonstrated that forces transmitted through adhesion receptors, such as integrins, exceed 10 pN, sparking broad interest in generating tension sensors that can report on forces of greater

magnitudes (42, 43). This desire to employ molecular springs with a greater effective stiffness led to the development of polymer spring elements that include a stable secondary structure. Examples include proteins, DNA hairpin loops, and molecular sensors that irreversibly dissociate upon experiencing thresholds of force.

As previously mentioned, molecular sensors are defined by their force-extension curves and can be classified as reversible or irreversible, as well as analog or digital. Reversible sensors, such as DNA hairpin and protein-based sensors, are polymers that can return to their original shape and length after being extended. Irreversible sensors, such as the tension gauge tether (TGT), do not return to their original structure after rupture. Reversible and irreversible sensors can be further categorized into analog or digital sensors. Analog techniques produce a signal that increases with the amount of force being applied. In contrast, digital sensors such as the hairpin sensor or TGT use an “on or off” mechanism. Once a sufficient amount of force is applied, a signal is turned on. In the case of the reversible hairpin sensor, this signal can be turned off once the force is removed; however, in irreversible sensors such as the TGT, the signal cannot be turned off.

#### *4.2.6 How Forces Influence the Kinetics and Thermodynamics of Unfolding*

The mechanical properties of peptides and DNA nanostructures have been extensively studied (44, 45). **Figure 40** shows a highly idealized two-state representation of the unfolding energy landscape for a given biomolecule such as a protein or nucleic acid. At equilibrium with no externally applied force (orange line), the folded state A is lower in energy compared to the unfolded state B. These two states are separated by an energy barrier  $G^\ddagger$  that must be overcome in order for the molecule to reach the unfolded state B (46). The application of a constant

external force ( $F$ ) modifies this idealized free energy diagram by a value proportional to its extension ( $\Delta x$ ). One way to describe how the energy diagram changes under force is to say that external  $F$  “tilts” the energy diagram by a linear value of  $F\Delta x$  that stabilizes the extended unfolded conformation of the molecule.

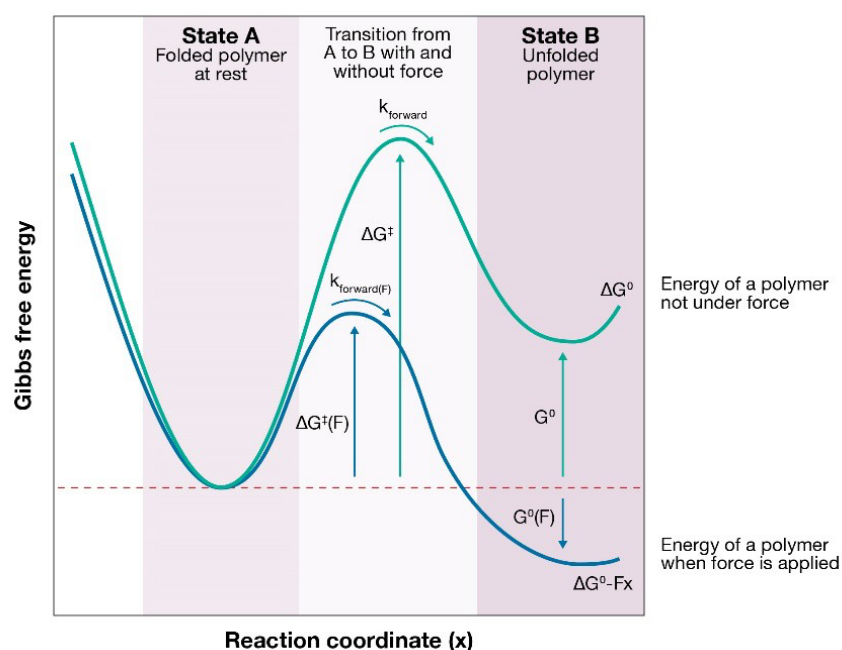


**Figure 40. Reaction coordinate diagram of two-state model of polymer unfolding.** Polymers adopt their lowest energy conformation at rest (State A). Unfolding of a polymer is energetically unfavorable, hence the increase in energy required for the polymer to transition between State A and the unfolded State B. Application of an external force lowers the energy barrier needed for this transition to occur and lowers the energy of the polymer in its unfolded state, making the unfolded structure the more energetically favorable conformation. Without external force, State B is higher energy than State A, and therefore an energetically unfavorable conformation. Reprinted with permission from *Molecular Force Sensors*; Copyright 2022 American Chemical Society

The free energy change increases linearly as a function of  $\Delta x$ . Thus, the equilibrium free energy at any given reaction coordinate and the equilibrium distribution ( $K_{eq}$ ) between state A and B will be modified, by the applied  $F$  as follows:

$$\Delta G^\circ - F\Delta x = -RT \ln(K_{eq}(F))$$

Therefore, the applied force will exponentially increase the equilibrium population of unfolded molecules. Interestingly, based on this thermodynamic relation, one can use this relation to estimate the applied force by measuring the distribution of tension sensors that are unfolded and assuming equilibrium conditions. Notably, because the structures do not re-fold, one cannot simply use this relation to estimate the applied force for irreversible processes such as the denaturation of a DNA duplex that occurs in the TGT or for situations where the system is not at equilibrium.

In terms of unfolding rates (kinetics), the free energy of the transition state ( $G^\ddagger$ ) will also be modified and hence will accelerate the rate of unfolding the molecule into state B. Almost four decades ago, George Bell derived a simple relation to predict the acceleration in reaction kinetics under the application of external  $F$ , which is described as the Bell model:

$$k_{forward(F)} = k_{forward(F=0)} \exp\left(\frac{F\Delta x}{k_b T}\right)$$

where  $k_{forward(F=0)}$  represents the rate of the forward reaction when  $F = 0$  and  $\Delta x$  is the distance to the transition state. In principle, external forces exponentially accelerate the rates of reactions, as well as the equilibrium position of the unfolded species, and this is in part why MTFM sensors comprised of folded nucleic acids and proteins display a digital-like response to forces where unfolding is observed within a narrow range of ~2-3 pN values.

In practice however, unfolding of the vast majority of biomolecules cannot be described using an ideal two-state model. Instead, most biomolecules show much more complex energy

landscapes for folding and extensive efforts both in theory and experimentation have been devoted to predicting and, in some cases, directly measuring these processes. Often, single molecule force spectroscopy technologies such as atomic force microscopy (AFM), magnetic tweezers, and optical tweezers are used to achieve this goal (47-49). These foundational studies are the metaphorical “shoulders of giants” that the mechanochemistry and mechanobiology areas are standing on, which allow us to calibrate and estimate the applied forces using molecular tension sensors.

#### *4.2.7 Mechanotransduction depends on outside-in and inside-out signaling*

As discussed in **Chapter, 1**, integrin receptors are heterodimeric transmembrane proteins responsible for linking the internal cytoskeleton of the cell with the outside extracellular matrix (ECM).(92, 93) Because integrins transmit cell-generated forces to the ECM, it is not surprising that this class of receptors are mechanotransducers. For example, binding of talin to the cytoplasmic tail of integrins leads to “inside-out” activation and involves a conformational shift of the integrin to the open extended state that has a ~ 1000 fold enhancement in affinity toward the ECM.(94-97) Conversely, “outside-in” signaling requires that integrins bind clustered and mechanically stable ECM ligands that resist traction forces of tens of piconewtons (pNs) per molecule to trigger activation.(98) Integrins also adjust the applied forces transmitted by the cell to the ECM ligands in response to the mechanical properties of the ECM itself. (99-102) This is illustrated by experiments showing that cells cultured on stiff polyacrylamide gels generate greater traction forces than cells cultured on soft gels.(103, 104) Cells also test ECM rigidity with high spatial resolution as evidenced by their transient deflection of 500 nm PDMS micropillars.(105) Integrin mechanosensing at molecular scales has been studied using a suite of nucleic acid probes

that include DNA duplexes that rupture at specific mechanical thresholds.(106) These probes can be designed in unzipping and shearing conformations with differential force thresholds of rupture, estimated at  $\sim 12$  and  $\sim 56$  pN, respectively, assuming a 2 second force duration. These probes are useful in manipulating the maximum integrin tension and recording the ensuing cell signaling state.(107-111) Indeed, previous studies indicated that  $> 43$  pN forces are required for initial cell adhesion.(106, 112) Because DNA duplex probes rupture, mechanotransduction is terminated and hence such probes are poorly suited for measurement of forces. Recently, the Liu group constructed a DNA-based reversible shearing probe in an attempt to overcome this limitation.(113) Using this reversible probe and other innovative tension sensor designs a more clear description of the forces associated with integrin activation have emerged indicating that  $F > 56$  pN are central to focal adhesion maturation. (102, 114-116)

#### *4.2.8 Integrins detect the force-extension curve of their ligands*

Interestingly, other studies have suggested that mechanosensor proteins not only detect and transduce force magnitude but also the force-extension history upon engaging the ligand.(117, 118) For example, mechanical strain of integrin-ligand bonds leads to their reinforcement which is described as catch-bond behavior.(119-121) Integrin-ligand bonds also respond to pN mechanical cycling by transitioning to a long-lived binding state to their ligands.(122) Therefore, an emerging fundamental question in the field is whether integrins detect the molecular force-extension behavior of ECM ligands in addition to the magnitude of resistive force applied by the ECM. Addressing this question poses an experimental challenge as it requires developing a set of DNA probes that are thermodynamically identical in their initial folded and final unfolded states but follow different force-extension pathways to reach their fully extended ssDNA states. In other

words, current probes only measure and manipulate force magnitude and cannot manipulate the force-extension trajectory of the adhesion ligand. (115, 123, 124)

To address this challenge, we generated two DNA probes that have identical nucleobase composition but fold into unique secondary structures. The reversible unzipping (RU) probe adopts a classic stem-loop hairpin while the reversible shearing (RS) probe was synthesized to fold into a knotted structure using a 3'-3' linkage (**Fig. 41a**). Because the nucleobase composition is identical, both DNA probes display identical values of  $\Delta G_{\text{unfolding}}$  and therefore identical  $F_{\text{eq}}$  values (the equilibrium force that leads to a 50% probability of unfolding) (**Fig. 41b**). Yet, under mechanical force, the probes follow different pathways to unfold to their fully extended states, allowing us to use them to manipulate the force-extension trajectory of adhesion ligands. Specifically, these probes were designed to test if adhesion receptors are sensitive to sudden drops in resistive force when pulling on their ligands. Cells cultured on RU probes will not form focal adhesions until the probe is fully extended while cells cultured on RS probes can form focal adhesions prior to rupturing the probe. However, upon rupture of the probe, the resistive forces required for cells to maintain stable adhesions is disrupted. We were curious if this abrupt change in resistive force

could be detected by cell adhesion molecules.

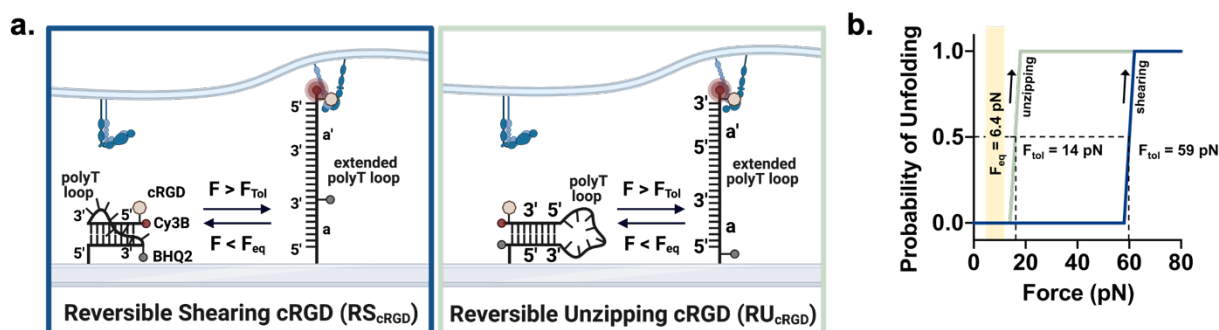


**Figure 41. Design and characterization of RS and RU probes.** **a.** Scheme depicting RS and RU probes immobilized on a glass surface. **b.** Probability of RS and RU probe unfolding at increasing force. The  $F_{Tol}$  of the RS and RU probe is 59 pN and 14 pN, respectively.

Following synthesis, we performed van't Hoff analysis and confirmed that RS and RU probes have similar thermodynamic parameters for thermal melting, indicating that the  $F_{eq}$  is identical for both probes at 7.2 pN, in good agreement with the NUPAK estimation of 6.4 pN. In contrast, the force tolerance ( $F_{tol}$ ), which we define as the peak force required to overcome the barrier to unfolding, was 59 pN and 14 pN for RS and RU probes, respectively, as determined by coarse grain (oxDNA) modeling. We found that mouse platelet integrins mechanically unfold the RU probes but do not open the RS probes, confirming the different  $F_{tol}$  values of the probes. In contrast, fibroblast integrins unfolded both the RS and RU probes to similar levels after 1 hour of being seeded on the probes. Interestingly however, fibroblasts on the RS and RU probes had dramatically different levels of mechanotransduction. Counterintuitively, compared to fibroblasts on RS probes, fibroblasts on RU probes displayed an increase in mechanotransduction markers such as nuclear YAP localization, actin stress fiber formation, fibronectin secretion, and integrin activation. Measurement of focal adhesion turnover further confirmed these findings, revealing that

fibroblasts cultured on RU probes have less focal adhesion turnover than fibroblasts cultured on RS probes, demonstrating that fibroblasts on RU probes form more stable focal adhesions. We hypothesized that our findings were due to the abrupt drop in force that occurs during shearing of the RS probe, perturbing mechanotransduction. To confirm this hypothesis, we generated probes that follow identical force extension curve of the RS probe but prevent the abrupt drop in force. We observed that when this abrupt change in force is prevented, fibroblasts on RS probes have similar mechanotransduction levels as fibroblasts on RU probes, suggesting that the previously observed difference were due to this abrupt change in force upon probe shearing. These results are further supported by molecular clutch model simulations which suggest that integrin ligand binding is dependent on the molecular force extension curve of ligands. These simulations are further supported by our experimental data which demonstrates that integrins bound to RU probes more readily access the fully extended probe and the force regimes necessary for enhanced mechanotransduction. Taken together, our experimental results combined with our simulations show that integrin adhesion receptors transduce the molecular force-extension curves of their ligands and the abrupt drop in force during extension of RS probes hinders mechanotransduction.

## 4.3 Results

### *4.3.1 Synthesis and design of reversible probes*

The RS and RU probes are comprised of self-complementary DNA sequences linked by a 30 nt polyT spacer and covalently anchored to a surface. The RU probe is a conventional 3'–5' polynucleic acid that forms a hairpin, while the RS probe is designed with an identical sequence but incorporating a 3'–3' linkage. We covalently functionalized the RS and RU probes with a Cy3B fluorophore and BHQ2 quencher, enabling the use of fluorescence as a readout for cell-

mediated DNA unfolding and traction force. Given that the probe design is completely covalent in nature, only mechanical separation exceeding the  $F_{\text{tol}}$  of the probe leads to an increase in fluorescence.

The RS and RU probes required the introduction of two chromophores, a peptide, and a tetrazine moiety to drive an inverse electron demand Diels-Alder reaction for surface immobilization. Moreover, the 3'-3' linkage of the RS probe is not accessible by enzymatic or solid-phase synthesis. Hence, a multistep strategy was required to generate the constructs which were synthesized as shown in **Fig. 42** and **Scheme A1**. The RU probe and the top strand of the RS probe were first covalently conjugated to the fluorophore labelled ligand using a copper-mediated click reaction (CUAAC), then functionalized with an azide using an NHS ester reaction. Similarly, CUAAC was used to functionalize the quencher-labelled bottom strand with a tetrazine moiety used for surface attachment to the trans-cyclooctene surface, and then functionalized with an azide using an NHS ester reaction. The azide on the unzipping probe was used to functionalize the DNA with the quencher-tetrazine moiety via CUAAC. The azide-functionalized 3' ends of the top and bottom strands of the RS probe were covalently attached to each other using subsequent strain-promoted click reactions with a homobifunctional DBCO linker. The final products were purified using HPLC and validated by ESI-MS (**Fig. A16** and **A17**).

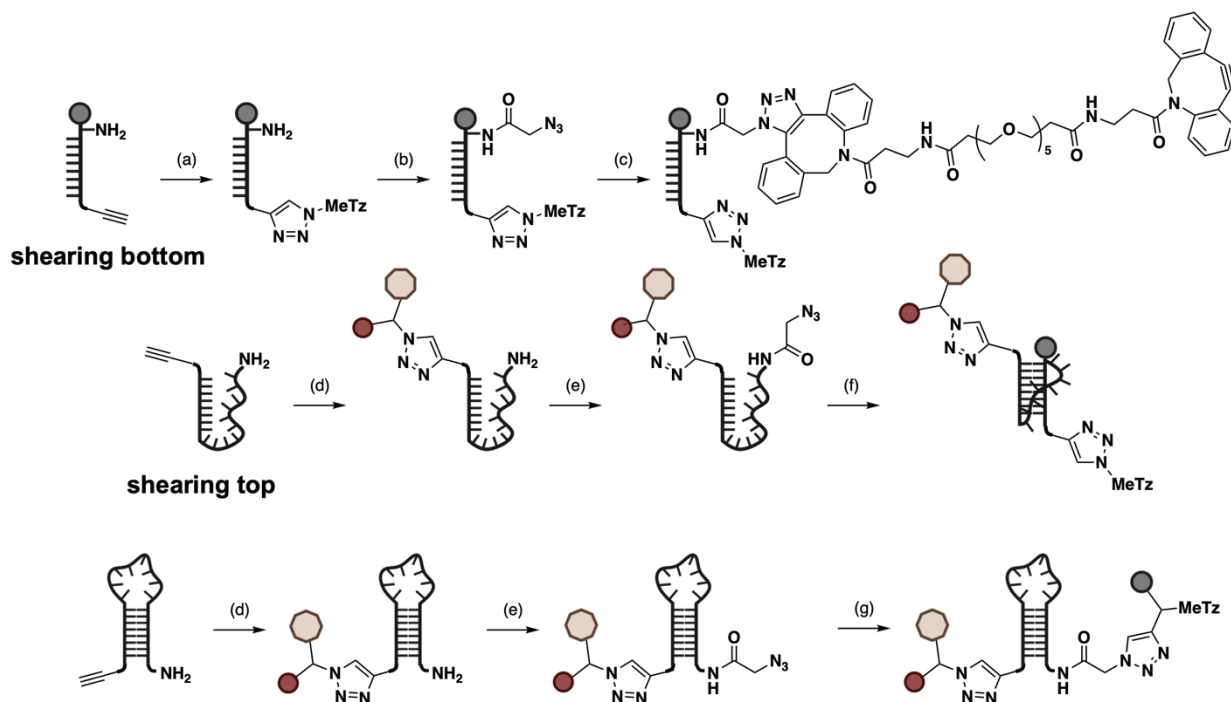


**Figure 42. Synthesis of RS and RU probes.** Scheme depicting synthesis of RS and RU probes. i) methyltetrazine-PEG<sub>4</sub>-azide, CuSO<sub>4</sub>, THPTA, sodium ascorbate in 40% of DMSO and 60% of water at 50°C for one hour. ii) Azido-NHS ester in aqueous solution of 0.1M sodium bicarbonate and 1X PBS with 20% DMSO at room temperature (r.t.) for one hour. iii) DBCO-PEG<sub>5</sub>-DBCO in 50% of water and 50% of DMSO at r.t. for 1 hour. iv) cRGD-Cy3B-N<sub>3</sub>, CuSO<sub>4</sub>, THPTA, sodium ascorbate in 40% of DMSO and 60% of water at 50°C for one hour. v) MeTz-BHQ2-alkyne, CuSO<sub>4</sub>, THPTA, sodium ascorbate in 60% of DMSO and 40% of water at 50°C for one hour. vi) RS-bottom-DBCO in water at r.t. for 4 hours.

#### 4.3.2 RU and RS probes have identical $\Delta G$ 's of unfolding but differ in their molecular extension curves

We next measured the  $\Delta G$  of folding for the RU and RS probes. In this study, the temperature-dependent fluorescence of Cy3B was measured from 37 to 95 °C, allowing us to detect probe unfolding driven by increasing temperatures. The melting curves were used to generate a van't Hoff plot (Fig. A18, Table A3, A4, SI Note A2).<sup>(125)</sup> As we expected, the thermodynamic

parameters of the RS and RU probes were similar. Specifically, the  $\Delta G_{\text{folding}}$  ( $T = 37\text{ }^{\circ}\text{C}$ ) for the RS and RU probes were  $-17.2 \pm 0.4$  and  $-17.3 \pm 0.6$  kcal mol<sup>-1</sup>, respectively (**Fig. 43a**). These values were then used to infer the  $F_{\text{eq}}$  for the RS and RU probes.(126, 127)

Next, using a detailed coarse-grained DNA model (oxDNA) we simulated force extension curves for the reversible probes (**Fig. 43b**). The dissociation behavior observed for the probes was similar to the behavior observed for corresponding DNA duplex unzipping and shearing (**Fig. A19**). While the RU probe required low levels of force to unfold ( $F_{\text{tol}} \sim 14$  pN), the RS probe required  $\sim 59$  pN of force to dissociate. In both the RU and RS probes, we observed a “two-state” mechanism of unfolding in which the probe’s  $F_{\text{tol}}$  is required for initial unzipping or shearing and is followed by an approximately 25 nm extension of the probe which occurs at a significantly lower force than the probe’s  $F_{\text{tol}}$ . As the probes reach full extension, the amount of force the probes can withstand increases into the nN range due to their covalent linkage which prevents rupture.

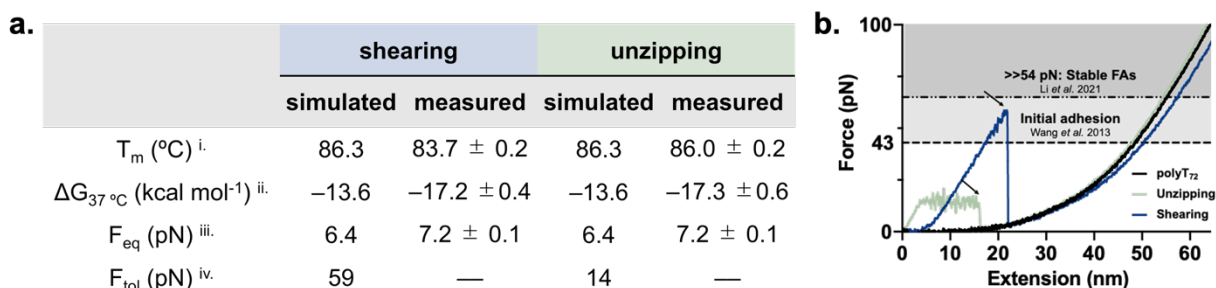


**Figure 43. Thermodynamic parameters of RS and RU probes.** **a.** Thermodynamic properties, equilibrium force, and force tolerance of RS and RU probes. i.  $T_m$  were measured experimentally in 1X PBS at 10 nM. ii.  $\Delta G$  values were calculated from fluorescent melting curve (see **SI note 1**) iii.  $F_{\text{eq}}$  values were calculated based on  $\Delta G$ . (ref) iv.  $F_{\text{tol}}$  values were simulated using oxDNA software (see **SI note 2**) **b.** Force-extension curve of RS and RU probes superimposed on the force extension curve of a 72 nucleotide polyT DNA strand. Arrows on the graph indicate force induced dissociation of the duplexes, either by shearing or unzipping. The graph also indicates the force threshold required for initial cell adhesion ( $> 43$  pN) and focal adhesion formation ( $>> 54$  pN).

#### 4.3.3 Platelet integrin forces unfold RU but not RS probes

As an initial model, we first cultured platelets on RS and RU probes functionalized with the ligand cyclic RGDfK, a cell adhesive peptide (denoted as  $\text{RS}_{\text{cRGD}}$  and  $\text{RU}_{\text{cRGD}}$ ). Platelets are a useful model to experimentally support our  $F_{\text{tol}}$  simulation because of their inability to generate the forces required to open the  $\text{RS}_{\text{cRGD}}$  probe. (126, 128-132) Platelets were cultured on  $\text{RS}_{\text{cRGD}}$  and  $\text{RU}_{\text{cRGD}}$  probes for 1 hour before activation with 10  $\mu\text{M}$  ADP for 10 minutes (**Fig. 44a**). Upon activation, platelets rapidly adhered to the surface and generated molecular traction forces. The spread area of platelets cultured on  $\text{RU}_{\text{cRGD}}$  and  $\text{RS}_{\text{cRGD}}$  probes was similar; however, platelets cultured on  $\text{RU}_{\text{cRGD}}$  probes generated nearly 50-times the amount of fluorescent tension signal compared to platelets cultured on  $\text{RS}_{\text{cRGD}}$  probes. (**Fig. 44b, c**). Consistent with the data obtained from oxDNA modeling, this result demonstrates that higher forces are required to unfold  $\text{RS}_{\text{cRGD}}$  than the  $\text{RU}_{\text{cRGD}}$

probes.

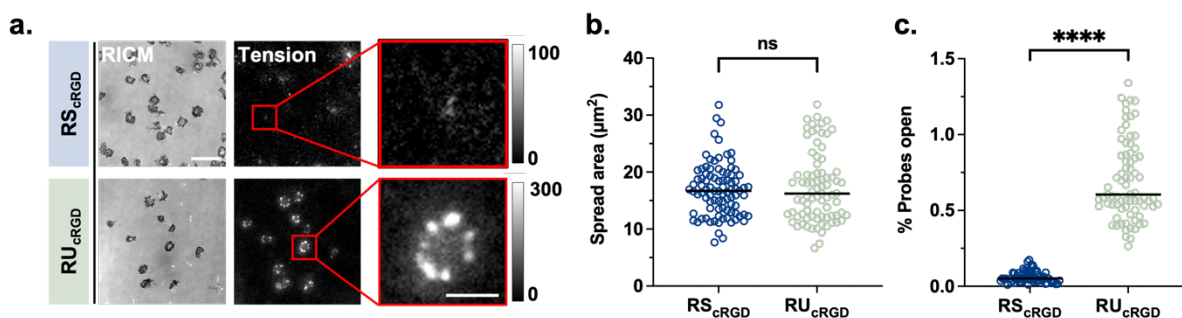


**Figure 44. Mouse platelets exert sufficient force to open RU<sub>cRGD</sub> probes.** **a.** RICM and fluorescent tension images of mouse platelets plated on RS and RU probes. Scale bar, 2 μm. **b.** Spread area of mouse platelets on RS and RU probes. Spread area was measured by drawing a region of interest around platelets in the RICM channel. (n = 3 experiments, RS = 90 cells, RU = 81 cells; p = 0.5889). **c.** Percent of RS and RU probes opened by mouse platelets. Percent of probes open was determined by dividing the fluorescent tension signal by the fluorescence value of an unquenched surface. (n = 3 experiments, RS = 72 cells, RU = 77 cells; p < 0.0001).

#### 4.3.4 Fibroblast integrins unfold RS and RU probes in a time-dependent fashion

We next studied the behavior of mouse embryonic fibroblasts (MEFs) stably expressing GFP vinculin (MEF-GFP-vinculin) on surfaces coated with RS<sub>cRGD</sub> and RU<sub>cRGD</sub> probes. Fibroblasts are one of the best studied models for integrin mechanotransduction and their ability to generate large traction forces to mechanosense the ECM is well documented.<sup>(133)</sup> MEFs were imaged 1 hour after seeding to evaluate cell spread area, tension signal, and GFP-vinculin signal (**Fig. 445a, A20**). At 1 hour, there was not a significant difference in tension signal produced by cells on RS<sub>cRGD</sub> and RU<sub>cRGD</sub> probes (**Fig. 45b**). Unlike platelets, MEFs open both the RS<sub>cRGD</sub> and RU<sub>cRGD</sub> probes, which indicates that integrin-RGD forces transmitted within focal adhesions are sufficient to mediate shearing of the RS<sub>cRGD</sub> probes (Fig). We next confirmed that probes are reversible and rapidly refold (~ 1-2 min) upon termination of the cytoskeleton generated forces by treating cells

with Latrunculin B, a disruptor of actin polymerization (**Fig. A21**).(134) Interestingly, fibroblasts on  $RS_{cRGD}$  probes had a smaller spread area than fibroblasts on  $RU_{cRGD}$  probes, implying that the different probe extension pathways had an effect on cell adhesion (**Fig. 45c**). It is important to note that while there are differences in adhesion area in MEFs cultured on  $RS_{cRGD}$  and  $RU_{cRGD}$  probes, there is no difference in adhesion area in MEFs cultured on  $RU_{cRGD}$  probes and a fibronectin coated surface, suggesting that simply culturing cells on a probe coated surfaces do not alter cell biology (**Fig. A22**). To further explore the effects  $RS_{cRGD}$  and  $RU_{cRGD}$  probes have on fibroblast biology, we next analyzed several key mechanotransduction markers.

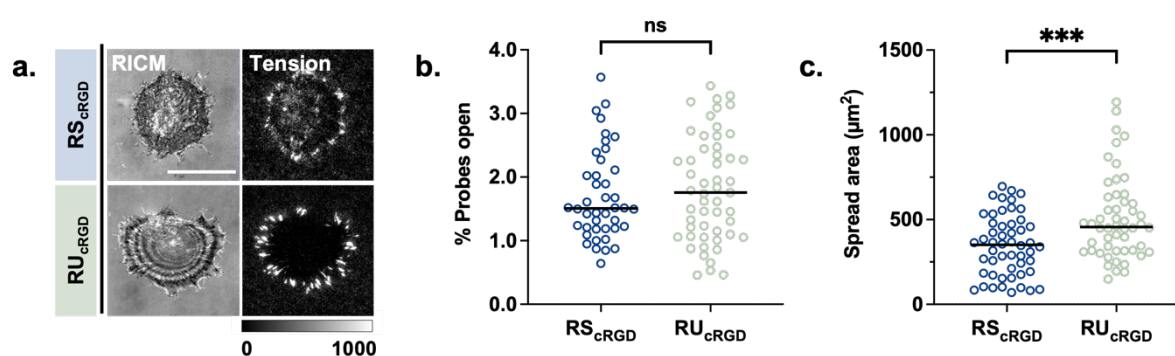


**Figure 45. Mouse embryonic fibroblasts (MEFs) respond to  $RS_{cRGD}$  and  $RU_{cRGD}$  probes differently.** **a.** RICM and fluorescent tension images of MEFs plated on  $RS_{cRGD}$  and  $RU_{cRGD}$  probes. **b.** Plots showing %probes open for  $RS_{cRGD}$  and  $RU_{cRGD}$  surfaces. Probes open % was determined by normalizing the tension signal against that of an unquenched surface ( $n = 3$  experiments, 1 hour:  $RS_{cRGD} = 52$  cells,  $RU_{cRGD} = 53$  cells,  $p = 0.2106$ , 3 hours:  $RS_{cRGD} = 52$  cells,  $RU_{cRGD} = 50$  cells,  $p < 0.0001$ ). **c.** Spread area of MEFs on  $RS_{cRGD}$  and  $RU_{cRGD}$  probes ( $n = 3$  experiments, 1 hour:  $RS_{cRGD} = 80$  cells,  $RU_{cRGD} = 68$  cells,  $p = 0.2106$ , 3 hours:  $RS_{cRGD} = 100$  cells,  $RU_{cRGD} = 85$  cells,  $p < 0.0001$ ).

#### *4.3.5 Fibroblasts show enhanced mechanical signal when cultured on RU<sub>cRGD</sub> probes compared to RS<sub>cRGD</sub> probes*

We investigated Yes-associated protein (YAP) nuclear translocation, actin stress fiber formation, fibronectin production, and integrin activation levels as validated markers of cellular mechanotransduction.<sup>(135, 136)</sup> YAP, a transcription co-activator, localizes to the nucleus of cells in response to mechanical signaling (**Fig. 46a**). Cells were allowed to spread for 1 hour on RS<sub>cRGD</sub> and RU<sub>cRGD</sub> surfaces before fixing and immunostaining for YAP (**Fig. 46b**). We found that after 1 hour, there was a significantly higher amount of YAP localized to the nucleus of cells cultured on RU<sub>cRGD</sub> probes (**Fig. 46c**). These results are further validated by the observed formation of actin stress fibers. Circular actin is associated with early cell adhesion while the progression through radial to linear actin patterns develops as a cell forms stable adhesions to its substrate (**Fig. A23a**). Cells were cultured on RS<sub>cRGD</sub> and RU<sub>cRGD</sub> probes for 1 hour before being stained with SiR-actin. Subsequent image analysis revealed that cells cultured on RU<sub>cRGD</sub> probes formed greater levels of actin stress fibers compared to cells cultured on RS<sub>cRGD</sub> probes (**Fig. A23b**). Actin patterns were further classified as either circular, radial, or linear. Actin in cells cultured on RS<sub>cRGD</sub> probes tended to be in the radial form while actin in cells cultured on RU<sub>cRGD</sub> probes was in the linear form (**Fig. A23c**). As a control, we cultured fibroblasts on conventional > 56 pN DNA rupture probes that terminate the mechanical signaling pathways upon rupture. Indeed, cells on these surfaces showed lower levels of nuclear YAP and minimal stress fiber formation (**Fig. A23d**). These findings demonstrate that cells cultured on RU<sub>cRGD</sub> probes are more mechanically active than cells cultured on RS<sub>cRGD</sub> probes. Importantly, results with conventional DNA rupture probes highlight that our observations are not due to the differences in force tolerance of the probes, but rather the

differences in the molecular force extension curves.

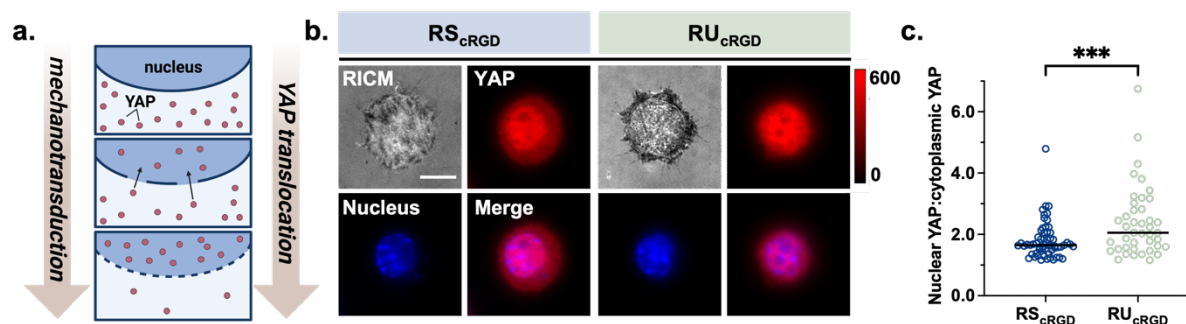


**Figure 46. Nuclear:cytoplasmic YAP is greater in MEFs cultured on RU<sub>cRGD</sub> probes.** **a.** Scheme showing that as cell mechanotransduction increases, nuclear levels of YAP increase. **b.** RICM, YAP, and nuclear staining (DAPI) images for MEF cultured on RS<sub>cRGD</sub> and RU<sub>cRGD</sub> probes for 1 hour. **c.** Ratio of nuclear to cytoplasmic YAP in MEFs plated on RS<sub>cRGD</sub> and RU<sub>cRGD</sub> probes at 1 hour ( $n = 3$  experiments, RS = 59 cells, RU = 42 cells,  $p = 0.0036$ ).

Fibronectin is one of the primary components of the ECM and fibronectin secretion is associated with increased mechanotransduction (**Fig. 47**).<sup>(137)</sup> We next immunostained fibronectin secreted by fibroblasts on RS<sub>cRGD</sub> and RU<sub>cRGD</sub> surfaces (**Fig. 47**). Consistent with our observations of stress fiber formation and nuclear YAP localization, we found that cells cultured on RU<sub>cRGD</sub> probes produced a greater amount of fibronectin than cells on RS<sub>cRGD</sub> probes further confirming that fibroblasts on RU<sub>cRGD</sub> surfaces are more mechanically active than cells on RS<sub>cRGD</sub> surfaces (**Fig. 47**).

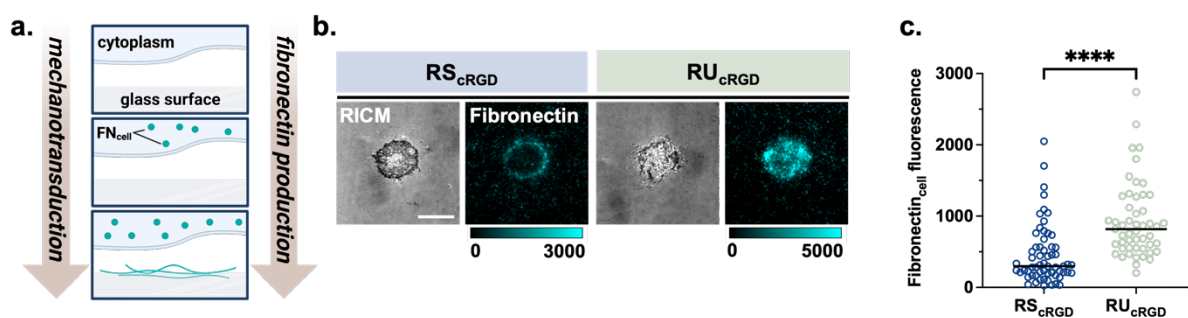


**Figure 47. Fibronectin production is greater in MEFs cultured on RU<sub>cRGD</sub> probes.** **a.** Scheme showing that as mechanotransduction increases the amount of fibronectin produced by cells increases. **b.** RICM and fibronectin staining images for MEFs seeded on RS<sub>cRGD</sub> and RU<sub>cRGD</sub> surfaces for 1 hour. Fibronectin was immunostained and measured using epifluorescence. **c.** Plot quantifying fibronectin generated by cells and deposited onto the surface at 1 hour ( $n = 3$  experiments, RS<sub>cRGD</sub> = 61 cells, RU<sub>cRGD</sub> = 51 cells,  $p < 0.0001$ ).

Finally, we quantified active integrins on cells cultured on RS<sub>cRGD</sub> and RU<sub>cRGD</sub> probes using immunostaining methods (Fig. 48a, b, c). Specifically, we immunostained integrin  $\beta 1$  in the active conformation using the 9EG7 antibody.(138) Indeed, we found that cells cultured on RU<sub>cRGD</sub> probes had a significantly higher number of integrins in the active conformation, aligning with our earlier results and providing evidence that the observed increases in mechanotransduction were driven by the unique force extension curves of the RS<sub>cRGD</sub> and RU<sub>cRGD</sub> probes. Further evidencing these results, MEFs cultured on RU<sub>cRGD</sub> probes also retrieved significantly more fibronectin from solution (Fig. 48 d, e, f). As a control, we confirmed that the increase in integrin activation levels was not simply due to an increase in the total number of integrins in cells on RU<sub>cRGD</sub> probes vs RS<sub>cRGD</sub> probes (Fig. A25). These results confirmed that the relative total number of integrins on cells on RU<sub>cRGD</sub> and RS<sub>cRGD</sub> probes is the same; further validating the conclusion that the level of

mechanotransduction is higher in fibroblasts cultured on  $RU_{cRGD}$  probes than  $RS_{cRGD}$  probes.

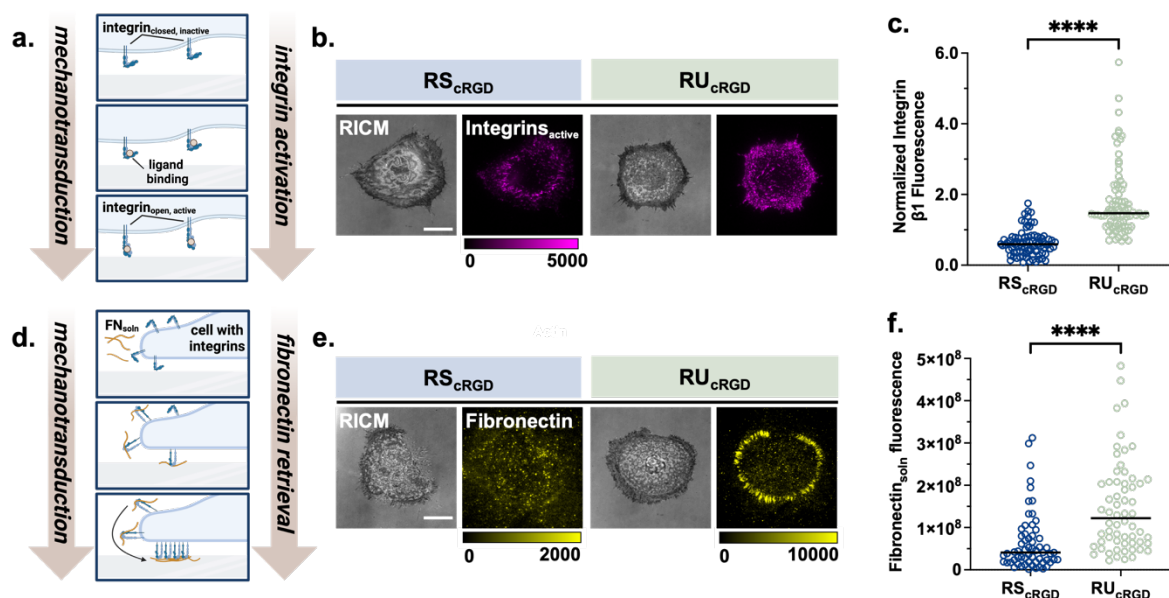


**Figure 48. Integrin activation is greater in MEFs cultured on  $RU_{cRGD}$  probes.** **a.** Scheme showing that as mechanotransduction increases, integrin activation increases. **b.** RICM and immunostained integrin  $\beta 1$  in the active conformation of MEF cells cultured on  $RS$  and  $RU$  probes for 1 hour. **c.** Plot quantifying integrin  $\beta 1$  in the active conformation at 1 hour. ( $n = 3$  experiments, 66 cells,  $p < 0.0001$ ) **d.** Scheme showing that as mechanotransduction increases, fibronectin deposition increases. **e.** RICM and fluorescently labeled fibronectin deposited by MEF cells cultured on  $RS_{cRGD}$  and  $RU_{cRGD}$  probes for 1 hour. **f.** Plot quantifying fibronectin retrieved from solution and deposited onto the surface by MEF cells. ( $n = 3$  experiments, 59 cells,  $p < 0.0001$ )

#### 4.3.6 Focal adhesions have lower turnover rates in fibroblasts cultured on $RU_{cRGD}$ probes compared to $RS_{cRGD}$ probes

Previous literature demonstrates that as integrin activation levels increase, integrin turnover rates decrease.<sup>(139)</sup> To test if the observed increase of mechanotransduction markers in fibroblasts on  $RU_{cRGD}$  probes was accompanied by a decrease in focal adhesion turnover rates, we measured recovery of tension signal, paxillin, and integrin  $\beta 3$ . To measure the recovery of tension signal, we

photobleached open probes under the fibroblasts and measured the time it took for fluorescence to recover. In this experiment we selectively photobleached probes unfolded under tension, as the fluorophores in the folded probes are quenched and photo-protected from bleaching. Thus, the recovery of tension signal indicates integrin turnover - either through recruitment of new integrins or rebinding of existing integrins to fresh probe sites. Cells cultured on RS<sub>cRGD</sub> probes began to recover their fluorescent signal in < 2 minutes while cells cultured on RU<sub>cRGD</sub> probes took ≥ 10 minutes to begin to recover their fluorescent signal (**Fig. 49**).

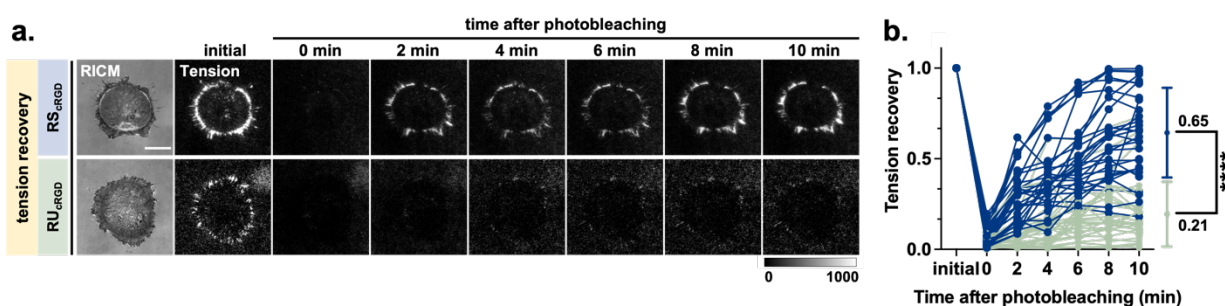


**Figure 49. Tension turnover is higher in MEFs cultured on RS<sub>cRGD</sub> probes.** **a.** Time dependent fluorescent tension signal recovery. **b.** Following bleaching of observable fluorescent signal, recovery of signal was determined by measuring the fluorescent signal within a region of interest over time. There was a significant difference in the fluorescent tension signal recovered on RS and RU probes. Fibroblasts cultured on RS<sub>cRGD</sub> probes recovered 65% of their initial fluorescence while fibroblasts cultured on RU<sub>cRGD</sub> probes recovered 21% of their fluorescence (n = 3 experiments, 15 cells, 30 regions of interest, p < 0.0001)

We next quantified turnover of paxillin and integrin  $\beta 3$ . Following transfection with either GFP-paxillin or GFP-integrin  $\beta 3$ , fibroblasts were allowed to spread on RS<sub>cRGD</sub> or RU<sub>cRGD</sub> surfaces for 1 hour. GFP signal that was accompanied by tension signal was photobleached and signal recovery was measured for 10 minutes. In line with our tension recovery results, we observed that both paxillin and integrin  $\beta 3$  signal recovered to a higher degree in fibroblasts on RS<sub>cRGD</sub> probes than RU<sub>cRGD</sub> probes. Fibroblasts cultured on RS<sub>cRGD</sub> surfaces recovered 81% of their paxillin signal

while fibroblasts cultured on  $RU_{cRGD}$  surfaces recovered only 59% of their paxillin signal (**Fig. 50 a, b**). Similarly, fibroblasts cultured on  $RS_{cRGD}$  surfaces recovered 55% of their integrin  $\beta 3$  signal while fibroblasts cultured on  $RU_{cRGD}$  surfaces recovered only 37% of their integrin  $\beta 3$  signal (**Fig. 50 c, d**). These results demonstrate that focal adhesion turnover rate is higher in fibroblasts cultured on  $RS_{cRGD}$  probes, corroborates the conclusion that integrin mechanotransduction is enhanced on  $RU_{cRGD}$  probes compared to that of  $RS_{cRGD}$  probes.

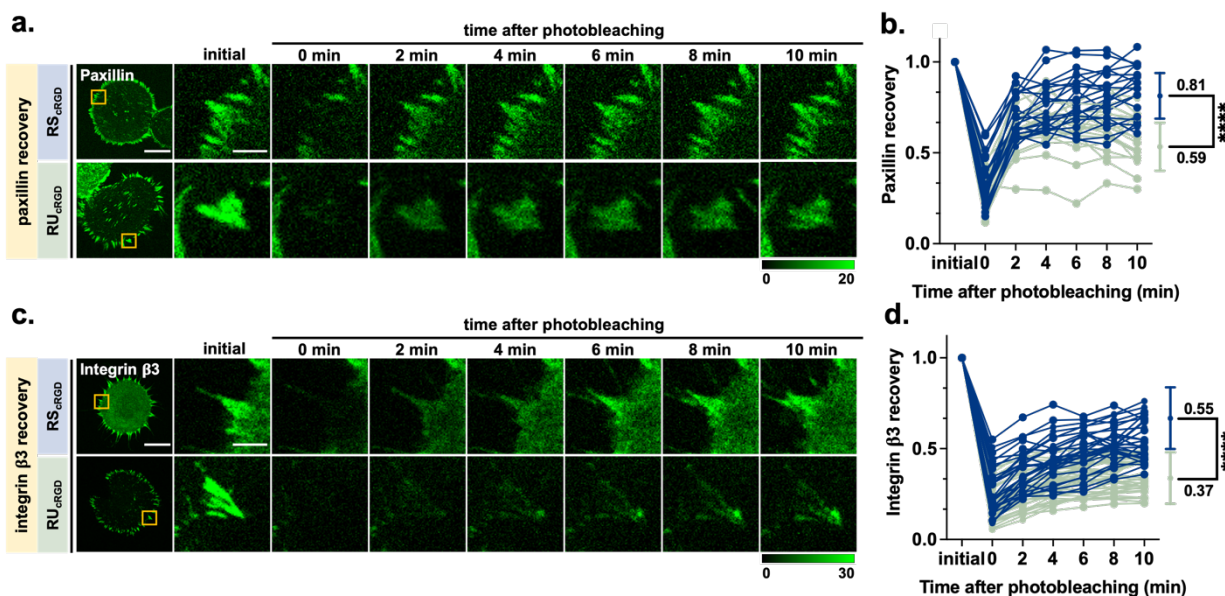


**Figure 50. Focal adhesion turnover is higher in MEFs cultured on  $RS_{cRGD}$  probes.** **a.** Time dependent fluorescent paxillin recovery. **b.** Following bleaching of observable fluorescent signal, recovery of signal was determined by measuring the fluorescent signal within a region of interest over time. There was a significant difference in the fluorescent paxillin signal recovered on  $RS_{cRGD}$  and  $RU_{cRGD}$  probes. Fibroblasts plated on  $RS_{cRGD}$  probes recovered 81% of their initial paxillin fluorescence while fibroblasts plated on  $RU_{cRGD}$  probes recovered 59% of their initial paxillin fluorescence. ( $n = 3$  experiments,  $RS_{cRGD} = 15$  cells, 36 regions of interest,  $RU_{cRGD} = 16$  cells, 34 regions of interest,  $p < 0.0001$ ) **c.** Time dependent fluorescent integrin  $\beta 3$  recovery. **d.** Following bleaching of observable fluorescent signal, recovery of signal was determined by measuring the fluorescent signal within a region of interest over time. There was a significant difference in the fluorescent integrin  $\beta 3$  signal recovered on  $RS_{cRGD}$  and  $RU_{cRGD}$  probes. Fibroblasts plated on  $RS_{cRGD}$  probes recovered 55% of their initial fluorescent integrin  $\beta 3$  signal while fibroblasts plated on  $RU$  probes recovered 37% of their initial fluorescent integrin  $\beta 3$  signal. ( $n = 3$  experiments,  $RS_{cRGD} = 17$  cells, 51 regions of interest,  $RU_{cRGD} = 15$  cells, 44 regions of interest  $p < 0.0001$ ). Fluorescent regions were determined in a using the ROI generated in the RICM channel. Fluorescent regions in c and e were selected in the fluorescent channel (3 regions per cell). Scale bars, 5  $\mu$ m.

#### 4.4 Discussion

It is important to note that the differences we observed in the platelets cultured on  $RS_{cRGD}$  and  $RU_{cRGD}$  probes were not caused by the density or the accessibility of the ligand on the surface. We validated that the  $RS_{cRGD}$  and  $RU_{cRGD}$  probe surface density was similar by confirming that the fluorescence of unquenched surfaces was the same, indicating that a similar amount of ligand is immobilized (**Fig A26**). Furthermore, as estimated by the duplex length and degree of freedom around the ligand, the radius of gyration of the ligand on the  $RS_{cRGD}$  probes is  $\sim 7$  nm, while the radius of ligand gyration on the  $RU_{cRGD}$  probes is  $\sim 2$  nm, given the different location of ligand with respect to the location of surface attachment. Therefore, the ligand on the  $RS_{cRGD}$  probe is not less accessible than the ligand on the  $RU_{cRGD}$  probe.

We have synthesized two completely covalent DNA-based probes capable of reporting on cell traction forces in real-time and measuring cell response to unique force extension curves of their ligands. Previously reported DNA-based probes have two primary limitations. One is that they rely on non-covalent interactions, such as biotin-streptavidin, and labile bonds such as thiol-maleimide and thiol-Au interactions, to anchor the probe to the surface which can lead to spontaneous probe dissociation.(140, 141) Both thiol-maleimide and thiol-Au bonds are particularly labile in cell media which contains mM concentrations of thiols and reducing agents that drive exchange reactions. Our probes are covalently anchored to the surface using a non-exchangeable TCO-Tz bond and are synthesized using covalent chemical conjugation. Second, DNA hairpin probes cannot measure real-time cell mechanical events with peak forces exceeding 19 pN. While the reversible shearing probes reported by Liu et al. address this limitation, these probes use hybridization to introduce the quencher, and hence under sufficient force the quencher labelled strand will undergo irreversible “peeling” or denaturation (**Fig. A27**).(142, 143) We have

synthesized these probes in the unzipping and shearing conformation, with the shearing conformation containing a novel 3'-3' linkage that is not accessible using enzymatic or conventional solid-phase phosphoramidite chemistry. Our probes are thermodynamically identical but have unique force thresholds and pathways of unfolding which we have demonstrated with modeling and experimental data.

The RS probe reversibly unfolds at  $\sim 59$  pN while the RU probe reversibly unfolds at  $\sim 14$  pN. Following the unfolding of each duplex, the probes follow the worm-like chain (WLC) model as they are extended. Thus, given the force thresholds of the probes and their previously identified relationship to cell adhesion, the cells cultured on the shearing probe form initial adhesions before dissociating the duplex while cells cultured on the unzipping probe must dissociate their duplex prior to forming initial adhesions. Full extension of both the RS and RU probe structures results in a mechanically robust ligand with a force rupture threshold in the nN range and thus facilitating maturation of focal adhesions to similar levels. It is important to note that the RS and RU probe each follow a unique force-extension curve as they approach full extension. Therefore, we investigated if the pathways of ligand-force-extension affect the pathways of mechanotransduction in fibroblasts and, if in the absence of thermodynamic differences, the geometry and subsequent kinetic behavior of a probe controls cell response.

MEF cells were capable of exerting forces greater than the  $F_{eq}$  of both the RS and RU probes. However, between 1 and 3 hours, the average tension signal generated by cells on RU probes decreased by nearly 60%, a surprising result considering there was no measurable decrease in their focal adhesion formation. This was accompanied by increases in other markers of mechanotransduction, specifically, an increase in actin stress fiber formation, nuclear YAP

localization, and fibronectin production. Cells cultured on RU probes also had a significantly higher number of  $\beta 1$  integrins in the active conformation, as well as lower integrin turnover compared to cells cultured on RS probes. As we described earlier, the differences we observed in the cells cultured on RS and RU probes were not caused by either the density or the accessibility of the ligand on the surface.

Using RS and RU probes, we have uncovered a unique biological feature of adhesion receptors. Our results suggest that adhesion receptors are not only able to detect the relative force thresholds of their ligands but also their unique force-extension curves. Indeed, prior work has demonstrated that integrins are sensitive to more than just the magnitude of force being applied.(144) For example, it is known that integrin activation is also sensitive to the force loading history and the direction of force.(145, 146) Furthermore, integrin activation is known to mediate mechanotransduction within the cell, which in turn influences integrin activation on the outside of the cell, highlighting the relationship between extracellular and intracellular signaling.(121, 147, 148)

Previous work has demonstrated that cells require  $\sim 43$  pN of force to form initial adhesions and greater than 56 pN of force to form stable focal adhesions. Due to the nature of unfolding of the RS and RU probes, cells cultured on these probes reach these force thresholds by different mechanisms. The  $F_{tol}$  of the RS probe is  $\sim 59$  pN while the  $F_{tol}$  of the RU probe is  $\sim 14$  pN, assuming a loading rate consistent with that used for modeling. Hence, cells can form initial adhesions on the RS probe before the DNA duplex is sheared (**Fig. 51a**). However, after the probe is sheared, the probe unfolds, dropping the force to zero and causing a disruption in mechanotransduction that significantly affects focal adhesion maturation. Conversely, cells on RU

probes cannot form initial adhesions until the probe is fully extended (Fig. 51b). Therefore, there is no disruption in mechanotransduction as the adhesions mature, possibly explaining the increased markers of mechanotransduction.

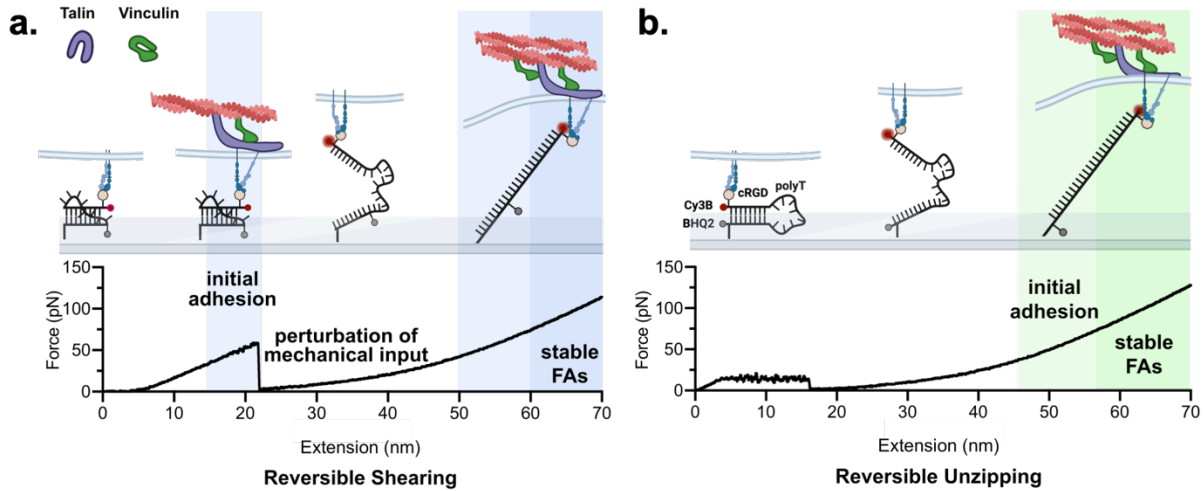


**Figure 51. The force extension trajectory of RS probes perturbs mechanotransduction. a.** Force extension behavior of RS probes as it relates to focal adhesion complex formation. The rupture of the DNA duplex in the RS probe requires  $> 59$  pN of force therefore cells on RS probes form initial adhesions as they begin to pull on the probe. Following rupture of the duplex, the resistive force from the probe on the integrin drops to zero, terminating mechanical input. The integrin then fully extends the probe to its contour length, at which point the resistive force is  $\gg 56$  pN, and therefore sufficient force for the cell to form stable focal adhesions. **b.** Force extension behavior of RU probes as it relates to focal adhesion complex formation. The rupture of the DNA duplex in the RU probe requires only 14 pN of force therefore cells on RU probes cannot form initial adhesions until the integrin has fully extended the probe to its contour length. Therefore, there is no disruption in mechanical input as the probe is unfolded.

To confirm that our findings were due to the difference in probe unfolding pathways, rather than the ramping rate of resistive force between the integrin and peptide, we cultured fibroblasts on surfaces functionalized with a 9-mer poly-T DNA strand functionalized with a cRGD peptide (T9<sub>cRGD</sub>) (Fig. 52a).  $\alpha$ xDNA simulations revealed that the initial force ramping rate of T9<sub>cRGD</sub> was similar to that of RS<sub>cRGD</sub>. However, the probe has no secondary structure and therefore does not

cause an abrupt change in resistive force. We observed that cell spread area, nuclear YAP translocation and active integrin levels were significantly higher in fibroblasts cultured on T9<sub>cRGD</sub> compared to RS<sub>cRGD</sub> but similar to fibroblasts cultured on RU<sub>cRGD</sub> probes (**Fig. 52b, c, A29**).

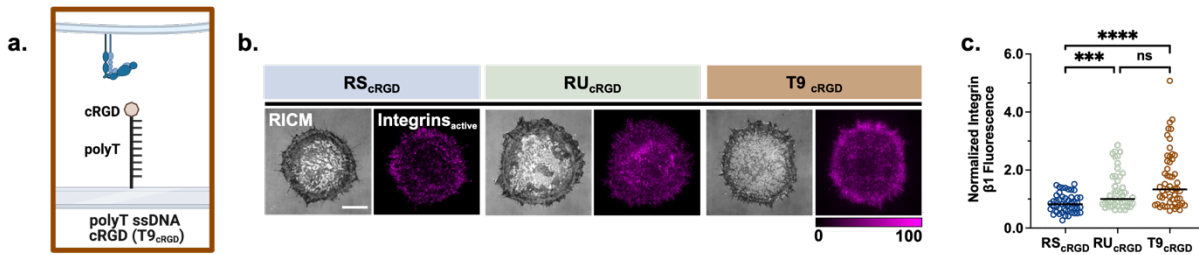


**Figure 52. Integrin activation is greatest in MEFs cultured on T9<sub>cRGD</sub> probes.** **a.** Scheme of 9 nucleotide thymine DNA strand immobilized to the surface and functionalized with cRGD. **b.** Immunostained integrin  $\beta 1$  in the active conformation of MEF cells cultured on RS<sub>cRGD</sub>, RU<sub>cRGD</sub>, and polyT ssDNA<sub>cRGD</sub> probes for 1 hour. **c.** Plot quantifying integrin  $\beta 1$  in the active conformation at 1 hour. (n = 3 experiments, RS<sub>cRGD</sub> = 50 cells, RU<sub>cRGD</sub> = 47 cells, T9<sub>cRGD</sub> = 55 cells, RS<sub>cRGD</sub>:RU<sub>cRGD</sub> : p = 0.001, RS<sub>cRGD</sub>:T9<sub>cRGD</sub> : p < 0.0001, RU<sub>cRGD</sub>:T9<sub>cRGD</sub> p = 0.0539) **n.** Plot quantifying cell spread area at 1 hour. (n = 3 experiments, RS<sub>cRGD</sub> = 52 cells, RU<sub>cRGD</sub> = 47 cells, T9<sub>cRGD</sub> = 50 cells, RS<sub>cRGD</sub>:RU<sub>cRGD</sub> : p = 0.00197, RS<sub>cRGD</sub>:T9<sub>cRGD</sub> p = 0.0002, RU<sub>cRGD</sub>:T9<sub>cRGD</sub> p = 0.0861)

Previous work suggests that integrin focal adhesion complexes work as a molecular clutch. This is defined as a coupling between actin retrograde flow and forward movement of the cell mediated by integrins and the focal adhesion complex.(149) This is a useful model for analyzing the role of external stimuli in cell response.(150) We have adapted this model to simulate the response of molecular clutches to ligands with different force extension curves (**Fig. 53a**). As we hypothesized using the model in **Fig. 51a**, the integrins that bind to RU<sub>cRGD</sub> probes experience forces > 60 pN nearly 3-times as often as integrins that bind to the RS<sub>cRGD</sub> probes (**Fig. 53b**). Validating this model, integrins that bind to the T9 probe experience forces > 60 pN much more often than integrins on both the RS<sub>cRGD</sub> and RU<sub>cRGD</sub> probes. This model was also used to predict molecular

clutches between integrins and linear RGD (GRGDS). GRGDS has an affinity for integrin  $\alpha_v\beta_3$  that is 10-times lower than the affinity that cRGD has for the integrin. As a result of this low affinity, the molecular clutches between integrins and GRGDS are capped at a lower magnitude ( $\sim 20$  pN) (**Fig. 53c**).

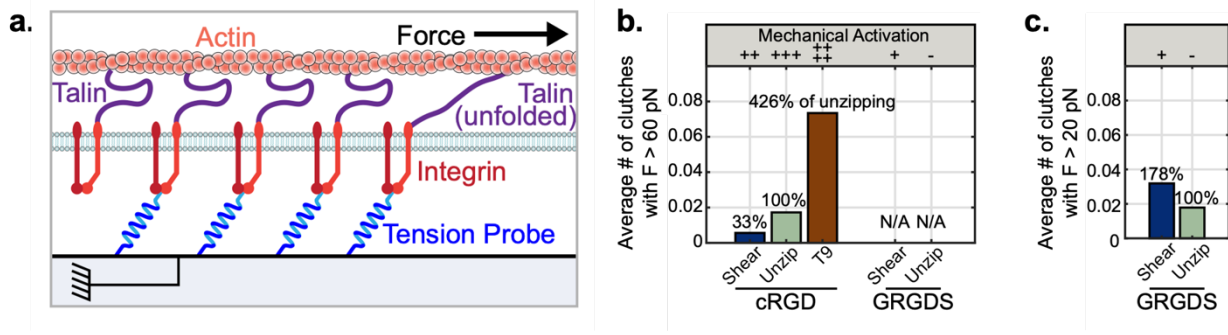


**Figure 53. Molecular clutch modeling reveals cells form more active clutches on  $RU_{cRGD}$  probes than  $RS_{cRGD}$  probes.** **a.** Scheme of the molecular clutch. **b.** Simulations reveal that cells cultured on  $RU_{cRGD}$  probes form more clutches exceeding 60 pN than cells cultured on  $RS_{cRGD}$  probes. **c.** Simulations reveal that cells cultured on  $RS_{GRGDS}$  probes form more clutches exceeding 20 pN than cells cultured on  $RU_{GRGDS}$  probes.

To confirm the clutch model, we synthesized  $RS_{GRGDS}$  and  $RU_{GRGDS}$  probes that eliminated the drop in resistive force and therefore perturbation of mechanical input experienced by cells cultured on  $RS_{cRGD}$  probes (**Fig. 54a, b**). While common techniques to dampen the forces exerted by cells include adding cytoskeletal inhibitors or drug treatments, we wanted to explore the role of force in modulating mechanotransduction and therefore wanted to avoid exogenous changes to the cell biology. Unlike on the  $RU_{GRGDS}$  probe, integrins cannot exert a large enough force on the GRGDS peptide to unfold the  $RS_{GRGDS}$  probe (**Fig. 54c, d**). Because there is no abrupt drop in resistive force, one would expect that there would be no difference in mechanotransduction markers observed in fibroblasts cultured on both the  $RS_{GRGDS}$  and  $RU_{GRGDS}$  probes. Indeed, we observed

that there was not a significant difference in cell spread area or active integrin  $\beta 1$  levels in fibroblasts cultured on  $RS_{GRGDS}$  and  $RU_{GRGDS}$  probes (Fig. 54e, f, A28). Additionally, we observed nuclear localization of YAP in fibroblasts cultured on  $RS_{GRGDS}$  was slightly higher than in fibroblasts cultured on  $RU_{GRGDS}$ , a reversal of the trend observed in fibroblasts cultured on  $RS_{cRGD}$  and  $RU_{cRGD}$  probes (Fig. A30). This demonstrates that when unfolding of, but not binding to the  $RS_{GRGDS}$  probe is prevented, there is no dampening of mechanotransduction since there is no abrupt change in resistive force perturbing mechanical input.

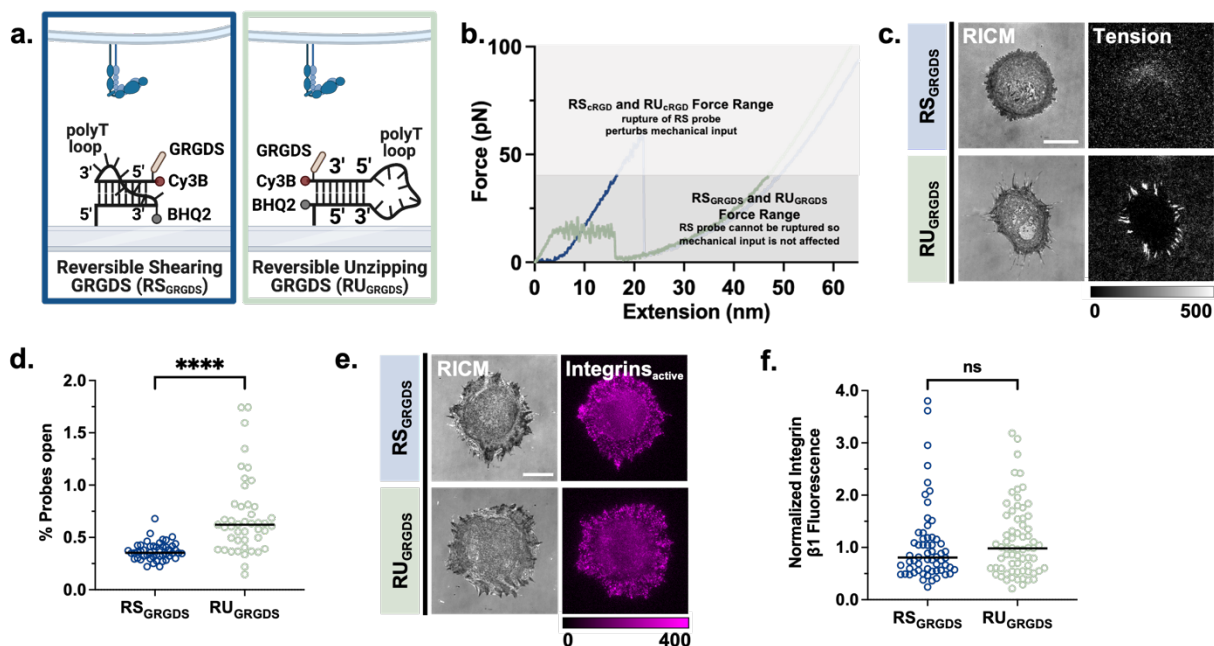


**Figure 54. Changes in mechanotransduction are not due to a difference in force ramping rate on RS and RU probes. a.** Scheme of RS and RU probes functionalized with linear RGD (GRGDS), denoted as  $RS_{GRGDS}$  and  $RU_{GRGDS}$ . **b.** Force extension behavior of  $RS_{cRGD}$  and  $RU_{cRGD}$  probes compared with force extension behavior of  $RS_{GRGDS}$  and  $RU_{GRGDS}$  probes. Integrin affinity for GRGDS is much lower than for cRGD. Hence the integrin does not stay bound to the peptide long enough to generate the force required to rupture the RS probe, preventing perturbation of mechanical input. **c.** RICM and fluorescent tension images of MEF cells cultured on  $RS_{GRGDS}$  and  $RU_{GRGDS}$  probes for 1 hour. **d.** Plot quantifying % probes open for  $RS_{GRGDS}$  and  $RU_{GRGDS}$  surfaces. Probes open % was determined by normalizing the tension signal against that of an unquenched surface ( $n = 3$  experiments,  $RS_{GRGDS} = 48$  cells,  $RU_{GRGDS} = 45$  cells,  $p < 0.0001$ ). **e.** Immunostained integrin b1 in the active conformation of MEF cells cultured on  $RS_{cRGD}$  and  $RU_{cRGD}$  probes for 1 hour. **f.** Plot quantifying integrin b1 in the active conformation at 1 hour. ( $n = 3$  experiments,  $RS = 70$  cells,  $RU = 68$  cells,  $p = 0.4592$ )

In conclusion, we have shown that adhesion receptors detect abrupt changes in resistive force and are sensitive to the molecular force extension curves of their ligands. Although the current probe design does not provide an absolute measure of force lifetimes, future iterations of these probes may address this area. Moreover, we show that cell adhesion receptors can detect the molecular force extension curve of their ligand. Previous work focused on cell adhesion receptor sensitivity to only the force threshold of their ligands. Our work indicates that it is not only the force threshold of ligands that controls cell mechanics, but also the unique force-extension curves that these ligands follow. Therefore, further work is necessary to elucidate the exact nature of the receptor-ligand interaction.

## CHAPTER 5. CONCLUSIONS AND FUTURE OUTLOOK

*Adapted from Bender, R. L., Salaita, K. "Molecular Force Sensors", 2022, ACS In Focus*

### 5.1 Summary of Advances

The field of molecular force sensor development lies at the intersection of chemistry, physics, and biology. As discussed in **Chapter 1**, there is a complex relationship between the internal workings of a cell and the extracellular environment. External mechanical cues are mediated by receptors in the cell membrane which guide intercellular response and cell function. Throughout this thesis, I have summarized work encompassing the development of scaffolds and tension sensors for reporting on cell mechanotransduction. I have also provided an overview of the foundational principles of molecular force sensor development and have highlighted examples of how these sensors are used in the study of cell mechanics. **Chapter 2** discussed the role that scaffolds play in the study of cell mechanotransduction and detailed work surrounding characterizing and utilizing the TCO/Tz iEDDA reaction to produce robust scaffolds for measuring cell mechanotransduction events. These scaffolds have several advantages over the commonly used Biotin/STVD scaffolds, primarily that they are completely covalent and resistant to degradation in conditions used for biological analyses. These findings are particularly relevant when designing general strategies to immobilize biomolecules and have particular relevance when designing studies using molecular force sensors. Indeed, our TCO/Tz iEDDA surfaces provide a scaffold in which molecular force sensors can be used to measure integrin-mediated forces in time and force regimes that were previously inaccessible.

Utilizing the new surfaces described in **Chapter 2**, **Chapter 3** discussed a new generation of PNA-based tension sensors for measuring cell forces that are high in magnitude and occur over extended time frames. PNA is highly thermostable and resistant to enzymatic degradation. Interestingly, PNA also has a high affinity for its binding complement and our hypothesis was that these variables would enable PNA with higher mechanical stability than DNA, and therefore require a higher force to undergo mechanical separation. We demonstrated successful synthesis of PNA rupture force sensors in both the low force unzipping and high force shearing conformations. These force sensors were resistant to nuclease and protease degradation, and therefore increased the S:N of tension imaging of aggressive cancer cells that secrete nucleases and proteases into their environment. We also demonstrated that PNA:PNA duplexes in the shearing conformation (sPNA:PNA) likely report on the upper levels of integrin forces and may provide insight to the upper magnitudes of force that cell adhesion receptors can exert. Future work with these sensors would include simulating the rupture of such duplexes in order to estimate the forces required for mechanical separation. In addition, the sensors described in this work are irreversible and therefore only provide a history of a cell's mechanical activity. However, by using PNA to construct "real time" hairpin sensors, one could also extend the time range over which integrin mediated force can be measured.

Finally, previous work has largely been focused on the effect force threshold and substrate stiffness has on cell function. However, we hypothesized that in addition to force threshold, cells are capable of **Chapter 4** discussed the principles of force-extension behavior of polymers and our hypothesis that this behavior can be transduced by adhesion receptors, leading to our generation of a class of sensors capable of measuring the response of cell adhesion receptors to

not only force threshold, but the unique force extension curves of their ligands. We developed these sensors to test our hypothesis that in addition to force threshold, cell integrins also detect the molecular force extension curve of their ligands. Our work revealed that mechanotransduction levels were reduced in cells cultured on reversible shearing probes due to the sudden drop in resistive force that occurs as the sensors are sheared prior to extension. Clutch model simulations support our experimental findings and further experiments confirmed that our findings were due to a difference in extension trajectories of shearing and unzipping probes rather than a force ramp rate between the integrin and ligand, demonstrating that cells are capable of detecting and transducing the force extension curve of their ligands. These findings have wide reaching applications in the study of how cells interact with the extracellular matrix, particularly when considering the role fibronectin fibril extension plays in the role of cell adhesion and function.(151, 152)

### *5.1.1 Discussion of biological limitations*

While our work describes the development of new tools to measure adhesion forces of cells, it is worth noting that these biological systems have some limitations. The primary limitation of the work described here is that our observations are made on studies completed on solid glass scaffolds. While the tension probe interface provides some level of responsiveness of the surface compared to the glass substrate alone, the actual extracellular matrix is much less rigid and much more biophysically complex. In addition, our work largely relies on the use of the cRGD ligands, biasing our sensors to  $\beta 3$  integrins. Finally, it is also worth noting that one marker of mechanotransduction is increased fibronectin production and fibronectin retrieval from solution. As fibronectin is deposited onto our surfaces, it directly competes with tension probes for integrin

access, obscuring tension signal, and increasing mechanotransduction of the cells binding to the fibronectin coated surface. Therefore, it is important to consider the role fibronectin may play in the mechanotransduction levels of cells cultured on force sensor coated substrates.

## **5.2 Outstanding questions and directions in developing nucleic acid nanotechnology for mechanobiology applications**

Advances in force sensing technologies have helped elucidate many features of integrin mediated mechanotransduction. Specifically, our work has added to the knowledge surrounding force threshold and force extension sensitivity of integrins. However, there are several outstanding questions that require further investigation. For example, while our results suggest that PNA force sensors can report on the upper levels of integrin generated force, the actual force threshold is unknown. Previous studies on rupture force have been limited to PNA:DNA duplexes and to our knowledge there are no reports regarding the rupture force of PNA:PNA duplexes. Previous studies on the rupture force of a 10-mer PNA:DNA duplex report a rupture force of  $65 \pm 15$  pN (loading rate = 4641 pN/sec) while another study reports the rupture of a 6-mer PNA:DNA duplex to occur at 148 pN (loading rate =  $10^5$  pN/sec).(88, 89) It is important to note that these values are loading rate dependent, accounting for their differences. Current limitations in single molecule force spectroscopy such as the need for DNA handles or the use of non-covalent immobilization strategies make it difficult to experimentally determine the rupture force of PNA:PNA duplexes, particularly in the shearing conformation. However, ongoing work in the Salaita lab is focused on producing simulated values that appropriately estimate the rupture force of PNA:PNA in the context of integrin mediated force.

Further investigation is also needed to better understand the role force extension curves play in integrin mediated mechanotransduction and there are several questions remaining. For example, previous studies have shown that fibronectin unfolding in the cell matrix is regulated by cytoskeletal tension, suggesting that cell-generated force maintains the conformation of fibronectin.(153) However, further studies are needed to better understand the cellular components that regulate this sensitivity to molecular force extension. Using the force sensors described in the work along with single molecule imaging techniques, it would be possible to screen subcellular structures to help elucidate their individual responses to changes in molecular force extension. For example, what are the differences in roles of integrins  $\beta 1$  and  $\beta 3$  in transducing molecular force extension? It is known that increases in mechanotransduction activate integrin  $\beta 1$  but not integrin  $\beta 3$ .(154) As previously mentioned, our studies use the cRGD ligand and are therefore biased towards the  $\beta 3$  ligand. Therefore, further work is needed to better elucidate the role of  $\beta 1$  in response to sudden perturbation of mechanical activation and one could employ single molecule imaging to visualize the turnover and exchange between integrins  $\beta 1$  and  $\beta 3$ . Furthermore, it is worth noting that our experiments in **Chapter 4** were completed with fibroblasts. The response of cells to unique force extension curves likely varies between cell types, and further investigation is needed to understand if our findings are universal, or if each class of cell has their own unique response pathway to transduce force extension curves.

### **5.3 Areas of exploration in mechanobiology**

There are many unanswered questions that remain in the field of mechanobiology. Outside of the focus of this specific work but broadly in the field of mechanobiology, a number of biological questions remain unanswered, including the role of mechanics in intercellular interactions, disease

progression, and immune system response. For example, how to ultra-high resistive forces affect cell development and function? And could our findings regarding the role of force extension behavior in mechanotransduction be used to better understand the role of fibronectin in cell adhesion? The number of outstanding questions grows even more considering that the current work is largely focused on studying mammalian cells. There is growing evidence to suggest that other kingdoms of life also respond to mechanical forces. For example, plants respond to force that drives root and stem growth and the opening of stomata in leaves, yet the way these mechanical signals are processed is unknown (163, 164). Bacteria also rely on mechanics for movement and biofilms are known to withstand nN levels of force (165, 166). Interestingly, adhesion of bacteria often increases in the presence of shear flow, suggesting that their adhesion is dependent on force (167). Yet the mechanisms for such behavior are still not entirely understood, particularly given the differences observed in different species of bacteria. Understanding the molecular factors responsible for this behavior would aid in our understanding and prevention of bacterial resistance. Furthermore, it is important to note that the examples provided throughout this e-book are done largely on planar substrates and measure cell interactions on solid substrates. In reality, cells exist in soft environments and experience force in all directions. Therefore, there is an ongoing need to develop systems capable of accurately mimicking a cell's natural environment.

Perhaps the ultimate goal for these sensors is to apply them in a clinical setting. Similar to the use of biopsies and blood tests, is it possible to analyze a cell's mechanical profile to diagnose disease? For example, one of the most commonly used methods for cancer screening involves detecting the presence of a tumor with different physical properties than the surrounding soft tissue. Hence, using the different mechanical properties of tumor cells for molecular diagnostics

may be powerful in diagnosing cancer earlier. Following diagnosis, could the cell's mechanics then be used to guide targeted drug therapy? In other words, if diseased cells have a unique mechanical profile, can we design drug delivery systems that are only activated by that profile?

As researchers attempt to answer these questions, the field of molecular force sensors will continue to evolve and researchers will continue to develop sensors to reach higher force thresholds with greater sensitivity, design new microscopy- and non-microscopy-based readout methods and create new scaffolds to better mimic the cellular environment.

## APPENDIX A: SUPPORTING INFORMATION

### A.1 Surface tethering of biomolecules using the reaction between trans-cyclooctene and tetrazine

#### A.1.1 Materials

##### Oligonucleotides

All custom synthesized oligonucleotides were purchased from Integrated DNA Technologies (Coralville, IA). **Table A1** and **Figure A1** includes the sequences and information of chemical modifications for all purchased oligonucleotides used in this work.

##### Reagents

Cy3B-NHS ester (PA63101) was acquired from GE Healthcare Life Sciences. Cyclo[Arg-Gly-Asp-d-Phe-Lys(PEG-PEG)] (PCI-3696-PI), elsewhere abbreviated as cRGD, was acquired from Vivitide. (3-Aminopropyl)triethoxysilane (APTES, 440140, 99% purity), (+)-sodium L-ascorbate (A4034-100G), anhydrous dimethylsulfoxide (DMSO, MX1457-7) methanol (34860-4L-R), and trifluoroacetic acid (TFA, TX1276-7) were purchased from Millipore Sigma. Methyltetrazine-PEG4-azide (1012, >95% purity) and tris-hydroxypropyltriazolylmethylamine (THPTA, 1010-100) was purchased from Click Chemistry Tools. BHQ-2 succinimidyl ester (BHQ2-NHS BHQ-2000S-5) was purchased from Biosearch™ Technologies. Azido-NHS (BP-22467, 95% purity) and TCO-NHS (BP-22417, 95% purity) were purchased from BroadPharm. Triethylamine Acetate (TEAA, 2.0 M) solution was purchased from Glen Research. All other chemicals (unless otherwise stated) were purchased from Millipore Sigma and used without purification. All buffers were prepared with 18.2 MΩ MilliQ water.

### *A.1.2 Equipment*

The major equipment that was used in this study includes Barnstead nanopure water purifying system (Thermo Fisher), high-performance liquid chromatography 1100 (Agilent) with AdvanceBio Oligonucleotide C18 column (653950-702, 4.6 x 150 mm, 2.7  $\mu$ m) (Agilent), Electrospray ionization mass spectrometer (ESI-MS) (LTQ Orbitrap Velos, Thermo Fischer Scientific), LightCycler 96 qPCR instrument (Roche), Nikon Eclipse Ti microscope (Nikon), and a T100 thermocycler (Bio-Rad).

### **A.1.3 Methods**

#### *A.1.3.1 Synthesis of tension probes*

*Dye and tetrazine labeled bottom strand:* Amine and alkyne modified bottom strand (20 nmol) was mixed with excess Cy3B NHS ester (50  $\mu$ g) in DMSO and allowed to react in an aqueous solution containing 10 % 10X PBS overnight at room temperature to generate **Product 1**. The mixture was purified using P2 gel filtration and reverse-phase HPLC (AdvancedBio Oligonucleotides, Agilent, 4.6  $\mu$ m~ 150 mm, solvent A: 0.1 M TEAA, solvent B: acetonitrile; starting condition: 90% A + 10% B, 1% per min gradient B, flow rate: 0.5 mL/min, (**Fig. A2a**). Following concentration, the alkyne and Cy3B labeled DNA was reacted with methyltetrazine-PEG4-azide using CuAAC to generate **Product 2**. Briefly, 1 mg of methyltetrazine-PEG4-azide was dissolved in 20  $\mu$ L of 1:4 dimethylsulfoxide/H<sub>2</sub>O and warmed to 50 °C. The copper catalyst solution was prepared in a separate tube by combining, in the following order, 20 mM CuSO<sub>4</sub> (2  $\mu$ L), 50 mM THPTA (4  $\mu$ L), and 50 mM ascorbic acid (2  $\mu$ L). The reaction mixture was added to

the Cy3B labeled DNA in 10  $\mu$ L 18.2 M $\Omega$  MilliQ water and warmed to 50  $^{\circ}$ C. Once warmed, the solution was added to the methyltetrazine-PEG4-azide with dropwise addition of dimethylsulfoxide to maintain solubility. The reaction proceeded at 50  $^{\circ}$ C for 1.5 h, and the resulting product was purified using P2 gel filtration and reverse-phase HPLC (AdvancedBio Oligonucleotides, Agilent, 4.6  $\text{\AA}$ ~ 150 mm, solvent A: 0.1 M TEAA, solvent B: acetonitrile; starting condition: 90% A + 10% B, 1% per min gradient B, flow rate: 0.5 mL/min (**Fig A2b**).

Dye and biotin labeled bottom strand: Amine and biotin modified bottom strand (20 nmol) was mixed with excess Cy3B NHS ester (50  $\mu$ g) in DMSO and allowed to react in an aqueous solution containing 10 % 10X PBS overnight at room temperature to generate **Product 3**. The mixture was purified using P2 gel filtration and reverse-phase HPLC (AdvancedBio Oligonucleotides, Agilent, 4.6  $\text{\AA}$ ~ 150 mm, solvent A: 0.1 M TEAA, solvent B: acetonitrile; starting condition: 90% A + 10% B, 1% per min gradient B, flow rate: 0.5 mL/min (**Fig. A2c**).

Ligand labeled top strand: 100 nmol of c(RGDfK)-PEG2-PEG2-NH<sub>2</sub> was reacted with an excess amount of NHS-azide in DMSO overnight to generate **Product 4**. cRGD-N<sub>3</sub> was purified via reverse-phase HPLC (Grace Alltech column, 4.6  $\text{\AA}$ ~ 250 mm, solvent A: 0.05% TFA in 18.2 M $\Omega$  MilliQ water, solvent B: 0.05% TFA in acetonitrile; starting condition: 90% A + 10% B, 1% per min gradient B, flow rate 1 mL/min (**Fig. A2d**)). Following concentration, the resulting azide functionalized cRGD was ligated to the alkyne and BHQ2 modified top strand using CuAAC to generate Product 21. Briefly, 10 nmol alkyne-labeled DNA in 18.2 M $\Omega$  MilliQ water was added to azide labelled c(RGDfK)-PEG2-PEG2-NH<sub>2</sub>). The copper catalyst solution was prepared in a separate tube by combining, in the following order, 20 mM CuSO<sub>4</sub> (2  $\mu$ L), 50 mM THPTA (4  $\mu$ L), and 50 mM ascorbic acid (2  $\mu$ L). The mixture was then added to the solution containing DNA and

peptide and reacted at room temperature for 2 hours. The resulting product was purified using P2 gel filtration and reverse-phase HPLC (AdvancedBio Oligonucleotides, Agilent, 4.6 Å~ 150 mm, 9 solvent A: 0.1 M TEAA, solvent B: acetonitrile; starting condition: 90% A + 10% B, 1% per min gradient B, flow rate: 0.5 mL/min (**Fig. A2e**).

#### *A.1.3.2 Surface Preparation*

Glass coverslips (#2 thickness, 25 mm diameter) were sequentially sonicated for 5 minutes in 18.2 MΩ MilliQ water and 200 proof ethanol. The coverslips were then dried in an oven (~110 °C) before immersing in freshly prepared piranha solution (3:1 H<sub>2</sub>SO<sub>4</sub> : H<sub>2</sub>O<sub>2</sub>) for 25 minutes. **(CAUTION: Piranha solution is highly reactive and explodes upon contact with organic solutions.)** Surfaces were then washed in 6 washes MilliQ water, followed by 3 washes ethanol. Surfaces were placed in a fourth wash of ethanol to which 3% of APTES was added for a 40-minute incubation. Following incubation, surfaces were washed in 3 washes ethanol and then baked in an oven (~110 °C) for 1 hour. A 4 mg/mL solution of trans Cyclooctene NHS ester in DMSO was then added to each surface and incubated for ≥ 12 hours. Surfaces were stored at room temperature and used within 6 weeks of preparation. Prior to usage, surfaces were washed in one wash ethanol before being placed into chambers.

#### *A.1.3.4 DNA Hybridization*

DNA oligonucleotides were hybridized at 200 nM in a 0.2 mL Thermowell tube. DNA was heated to 90 °C and then cooled at a rate of 1.3 °C min<sup>-1</sup> to 25 °C.

#### *A.1.3.5 Imaging Chamber Assembly*

Before imaging, coverslips were placed into imaging chambers and washed with 5 mL 1X PBS. Surfaces were then incubated with 20 nM DNA probe solutions in 1X PBS (1 mL) for 1 hour and washed with 5 mL 1X PBS. In experiments that did not use cells, surfaces were imaged in 1X PBS (1 mL). In experiments using cells, slides were washed and imaged in cell media (DMEM Media, A1896701, Thermo-Fisher).

#### *A.1.3.6 Cell Culture*

MEF WT cells were cultured according to American Type Culture Collection (ATCC) guidelines. Briefly, cells were cultured in DMEM supplemented with penicillin/streptomycin and 10% fetal bovine serum (v/v). Cells were passaged every 3 days as required.

#### *A.1.3.7 Image Acquisition and Analysis*

Fluorescent images were acquired using TRITC epifluorescence. CCD background fluorescence was subtracted from images and all analysis was completed in ImageJ.

*Functionalization characterization:* 50  $\mu$ L of solutions of Cy3B labeled DNA functionalized with either biotin or Tz and ranging in concentrations from 1.25 nM to 20 nM was added to surfaces immobilized in imaging chambers containing 950  $\mu$ L 1X PBS. DNA was allowed to incubate on the surface at room temperature for 1 hour. Surfaces were then rinsed with 5 mL 1X PBS before imaging (surfaces were left in 1 mL of 1X PBS for imaging). Coefficient of variation was determined by dividing the standard deviation of the fluorescence of a region of a surface by the average fluorescence of the region.

*Specific binding analysis:* 50  $\mu\text{L}$  of a 20 nM solution of Cy3B labeled DNA either unfunctionalized or functionalized with a biotin or Tz added to surfaces immobilized in imaging chambers containing 950  $\mu\text{L}$  1X PBS. DNA was allowed to incubate on the surface at room temperature for 1 hour. Surfaces were then rinsed with 5 mL 1X PBS before imaging (surfaces were left in 1 mL of 1X PBS for imaging). Fluorescence images were taken after 1 hour and degree of non-specific binding was determined by dividing the surface fluorescence of non-specific binding (Cy3B labeled DNA without a biotin or Tz ligand) by the surface fluorescence of specific binding (Cy3B labeled DNA functionalized with a biotin or Tz ligand).

*Thermal stability:* 50  $\mu\text{L}$  of a 20 nM solution of Cy3B labeled DNA functionalized with either biotin or Tz was added to surfaces immobilized in imaging chambers containing 950  $\mu\text{L}$  1X PBS. DNA was allowed to incubate on the surface at room temperature for 1 hour. Surfaces were then rinsed with 5 mL 1X PBS before taking initial images (surfaces were left in 1 mL of 1X PBS for imaging). Surfaces were incubated at 37  $^{\circ}\text{C}$  overnight and fluorescence images were taken after 24 hours.

*Protease resistance:* 50  $\mu\text{L}$  of a 20 nM solution of Cy3B labeled DNA functionalized with either biotin or Tz was added to surfaces immobilized in imaging chambers containing 950  $\mu\text{L}$  1X PBS. DNA was allowed to incubate on the surface at room temperature for 1 hour. Surfaces were then rinsed with 5 mL 1X PBS before taking initial images (surfaces were left in 1 mL of 1X PBS for imaging). 100  $\mu\text{L}$  of a pre-warmed solution of trypsin was then added to each surface and fluorescent images were acquired every 6 minutes for 90 minutes.

*On-rate:* Cy3B labeled DNA was added to surfaces in increasing concentrations ranging from 0.10 nM to 10 nM. Imaging exposure time was modified for each concentration to allow for signal detection and no gain was used. Exposure times for the varying concentrations of DNA were as follows: 0.1 nM = 1 sec exposure, 1 nM = 100 msec exposure, 10 nM = 10 msec exposure. Prior to measuring the  $k_{on}$  of Biotin/STVD surfaces, chambers were blocked in a saturated solution of BSA to prevent non-specific adhesion of biotin functionalized DNA to the sides of the chamber. Following image acquisitions, regions of the surface that had not been imaged during data acquisitions were imaged and quantified to correct for photobleaching.

Fluorescence plots were normalized for photobleaching and exposure time and converted to probes of DNA bound per  $\mu\text{m}^2$  and the linear regions of each curve was plotted over time. The slopes of the resulting linear fits were then used to determine the  $k_{reaction}$  for Biotin/STVD and TCO/Tz surfaces.

*Cell imaging:* Before imaging, coverslips were placed into imaging chambers and washed with 5 mL 1X PBS. Surfaces were then incubated with 20 nM DNA probe solutions in 1X PBS (1 mL) for 1 hour and washed with 5 mL 1X PBS. Slides were then washed with cell imaging media (DMEM Media, A1896701, Thermo-Fisher) and left in a remaining 1 mL of media for cell imaging experiments. 20,000 MEFs were added to each surface and allowed to incubate at 37 °C for 1 hour prior to imaging. Cells were imaged in RICM to confirm cell adhesion, and TRITC to determine fluorescent signal. Average fluorescence is measured by drawing a region of interest (ROI) around the fluorescent signal in the TRITC channel. Cell fluorescence is reported as S:N which is determined by dividing the fluorescence generated by the cell by the average background fluorescence.

## A.1.5 Figures, tables, and schemes

Name	Sequence (5' to 3')
TGT top	CAC AGC ACG GAG GCA CGA CAC //5OctdU//3BHQ_2
ssDNA and TGT bottom: TCO/Tz iEDDA surface	/5AmMC6/GTG TCG TGC CTC CGT GCT GTG /35OctdU/
ssDNA and TGT bottom: biotin/STVD surface	/5AmMC6/GTG TCG TGC CTC CGT GCT GTG /3bio/

3BHQ\_2 = BHQ2 ligated to 3' terminus. i5OctdU = alkyne linked internally within the DNA sequence. 5AmMC6 = 5' terminal amine. 35OctdU = 3' terminal alkyne

**Table A1: Oligonucleotide sequences and chemical structures of modifications used in Chapter 2.**

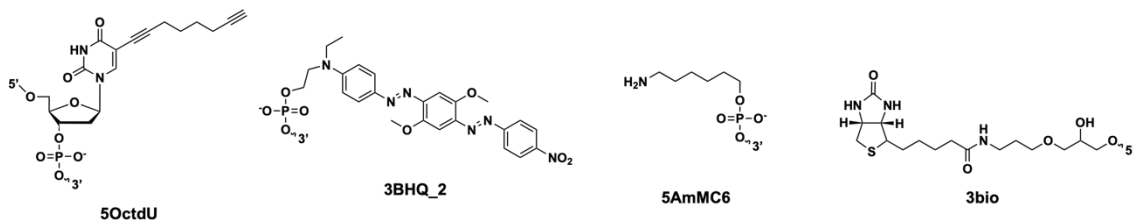


**Figure A1. Chemical structures of modifications used in Chapter 2.**

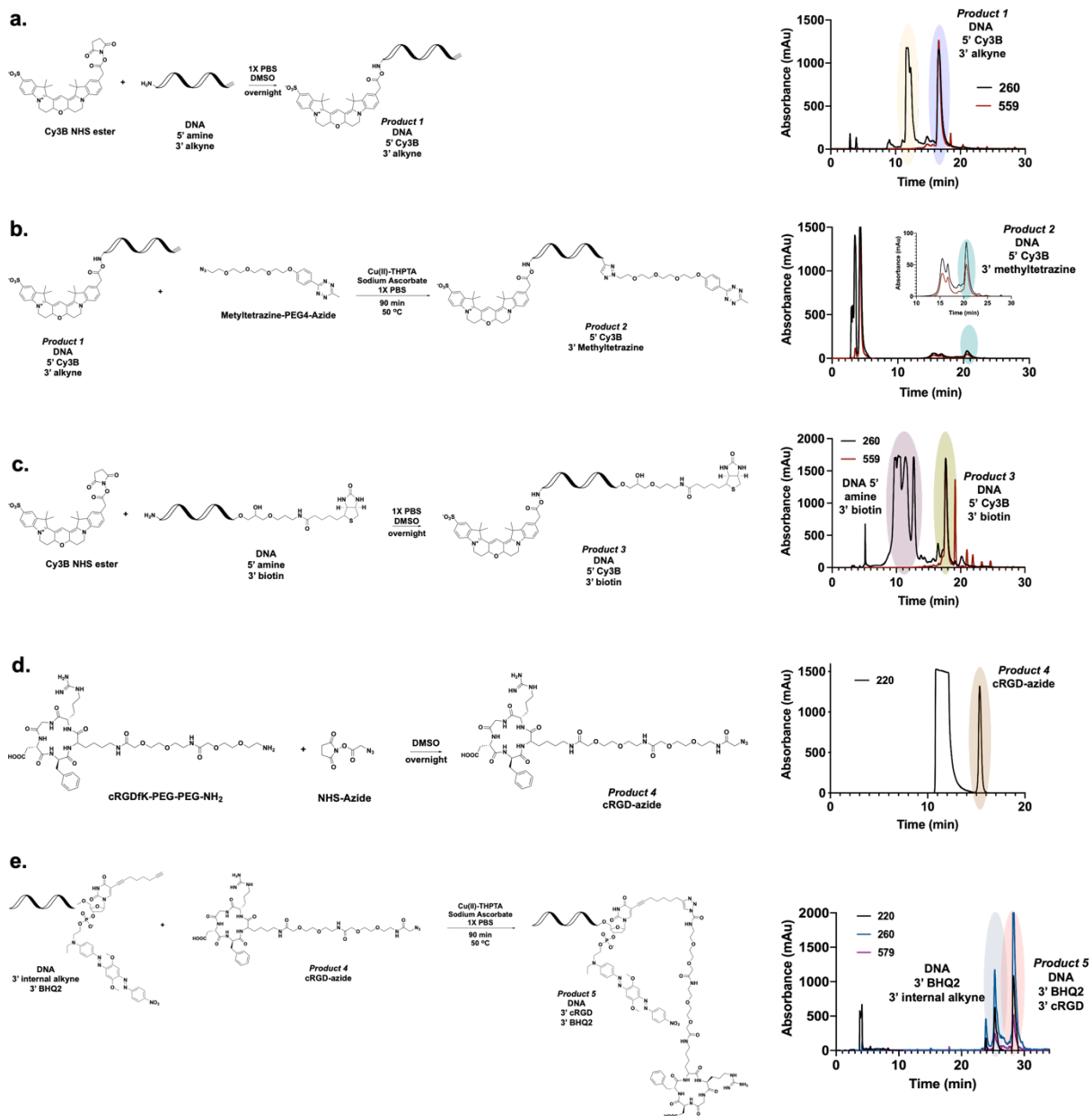


**Figure A2: HPLC characterization of DNA used in Chapter 2.** **a.** Schematic and HPLC chromatogram showing coupling of Cy3B-NHS to DNA to generate Product 1. **b.** Schematic and HPLC chromatogram showing alkyne-azide cycloaddition reaction to conjugate tetrazine to Product 1, generating Product 2. **c.** Schematic and HPLC chromatogram showing coupling of Cy3B to biotin labeled DNA to generate Product 3. **d.** Schematic and HPLC chromatogram showing the coupling between NHS-N<sub>3</sub> and cRGD-PEG-PEG-NH<sub>2</sub> to form cRGD-PEG-PEG-N<sub>3</sub> (Product 4). **e.** Schematic and HPLC chromatogram showing alkyne-azide cycloaddition to conjugate product 4 to BHQ2 labeled DNA, generating Product 5. *DNA purification: 0.5 mL/min flow rate; Solvent A: 0.1M TEAA, Solvent B: acetonitrile; starting condition: 90% A + 10 % B, 0.5%/min gradient B. Peptide purification: 1mL/min flow rate: Solvent A: nanopure water + 0.05% TFA, Solvent B: acetonitrile + 0.05% TFA; starting condition: 90% A + 10 % B, 1%/min gradient.*

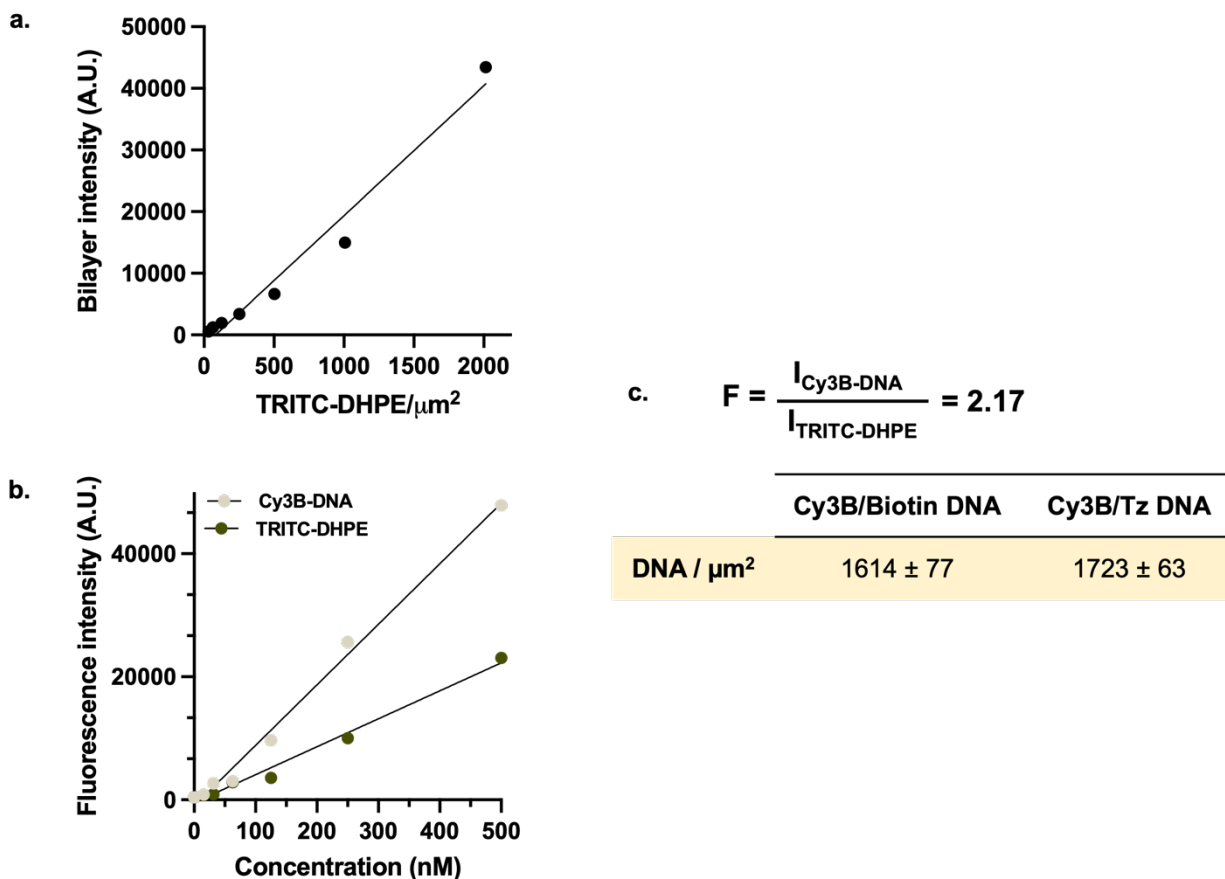


**Figure A3: Calibration curve used for determining molecular density of probes.** **a.** Calibration curve relating the fluorescence intensity of TRITC-DHPE – doped bilayers as a function of TRITC-DHPE density. **b.** Fluorescence calibration curves for Cy3B DNA and TRITC-DHPE as a function of concentration. **c.** An F factor, used to relate the fluorescence of TRITC-DHPE to Cy3B labeled DNA, was calculated by comparing the slope of the calibration curve for TRITC-DHPE against the slope of the calibration curve for the Cy3B labeled DNA. Using the F factor, we determined the molecular density of Cy3B/biotin labeled DNA and Cy3B/Tz labeled DNA to be  $1614 \pm 77$  and  $1723 \pm 63$  DNA strands per  $\mu\text{m}^2$ . Error signifies the SD (standard deviation) from three individual replicates.

## A.2 PNA tension probes expand the measurable force range of nucleic acid integrin force sensing technology

### A.2.1 Materials

#### Oligonucleotides

All custom synthesized DNA oligonucleotides were purchased from Integrated DNA Technologies (Coralville, IA) and then transformed into tension probes. PNA oligonucleotides were synthesized from commercially available monomers. **Table A2** and **Figure A4** includes the sequences and information of chemical modifications for all oligonucleotides used in this work.

#### Reagents

Cy3B-NHS ester (PA63101) was acquired from GE Healthcare Life Sciences. Cyclo[Arg-Gly-Asp-d-Phe-Lys(PEG-PEG)] (PCI-3696-PI), elsewhere abbreviated as cRGD, was acquired from Vivitide. (3-Aminopropyl)triethoxysilane (APTES, 440140, 99% purity), sulfuric acid (SX1244), *N,N*-diisopropylethylamine (*i*Pr<sub>2</sub>EtN, 387649-100ML), sodium bicarbonate (S6014-500G), (+)-sodium L-ascorbate (A4034-100G), anhydrous methylsulfoxide (DMSO, MX1457-7), trifluoroacetic acid (TFA, TX1276-7) was purchased from Millipore Sigma. Fmoc-protected-L-amino acids and nucleobases were purchased from ChemImpex. N(ε)-BHQ2-FMOC Lys OH, BHQ2-5042-100 was purchased from Biosearch Technologies. Methyltetrazine-PEG4-Amine (1012, >95% purity) and tris-hydroxypropyltriazolylmethylamine (THPTA, 1010-100) was purchased from Click Chemistry Tools. TCO-NHS (BP-22417, 95% purity) was purchased from BroadPharm. Dichloromethane (DCM, D143-4) was purchased from Fisher Chemicals. Cupric sulfate, 5-hydrate (CuSO<sub>4</sub>•5H<sub>2</sub>O, 4844) was purchased from Mallinckrodt chemicals. All other

chemicals (unless otherwise stated) were purchased from Millipore Sigma and used without purification. All buffers were prepared with 18.2 M $\Omega$  MilliQ water.

### **A.2.2 Equipment**

The major equipment that was used in this study includes Biotage SP Wave semiautomatic peptide synthesizer, Barnstead nanopure water purifying system (Thermo Fisher), high-performance liquid chromatography 1100 (Agilent) with AdvanceBio Oligonucleotide C18 column (653950-702, 4.6 x 150 mm, 2.7  $\mu$ m) (Agilent), Electrospray ionization mass spectrometer (ESI-MS) (LTQ Orbitrap Velos, Thermo Fischer Scientific), LightCycler 96 qPCR instrument (Roche), and a Nikon Eclipse Ti microscope (Nikon), T100 thermocycler (Bio-Rad).

### **A.2.3 Methods**

#### *A.2.3.1 PNA oligomer synthesis*

Synthesis began by downloading 50 mg of a rink amide MBHA resin (0.52 mmol/g) with 5  $\mu$ mol of the first Fmoc PNA monomer or Fmoc-Glu(Boc)-OH using HATU (1.2 equiv), DIPEA (1.2 equiv), and 2,6-lutidine (1.2 equiv) in 200  $\mu$ L dry NMP for 1 h at room temperature followed by 1 h of capping using a solution of 9% acetic anhydride/13% 2,6-lutidine in DMF. Successive couplings were performed using microwave assistance at 75  $^{\circ}$ C for 6 min with Fmoc PNA monomer (5 equiv), HATU (5eq), DIPEA (5 equiv), and 2,6-lutidine (5 equiv) in 400  $\mu$ L dry NMP. After coupling, capping (2  $\times$  5 min with 1 mL capping solution), washing (3  $\times$  1.1 mL DMF, 3  $\times$  1.1 mL DCM, then 3  $\times$  1.1 mL DMF), deprotection (3  $\times$  2 min with 1 mL 25% piperidine/ DMF), and washing (same as previous) completed a coupling cycle. Upon completion of synthesis,

cleavage was performed twice using 500  $\mu$ L of cleavage solution (95% TFA/2.5% triisopropylsilane/2.5% H<sub>2</sub>O) for 1 h.

Crude oligomers were collected by ether precipitation and purified by reverse-phase HPLC using an Agilent Eclipse XDB-C18 5  $\mu$ m, 9.4  $\times$  250 mm column at 60  $^{\circ}$ C with a flow rate of 2 mL/min, monitored at 260 nm using a linear gradient (10–40%) of 0.1% TFA/acetonitrile in 0.1% TFA/water. Identity was confirmed by ESI-TOF mass spectrometry.

#### *A.2.3.2. Tension probe synthesis*

100 nmol of c(RGDfK)-PEG<sub>2</sub>-PEG<sub>2</sub>-NH<sub>2</sub> was reacted with an excess amount of NHS-azide in DMSO overnight to generate **Product 1**. cRGD-N<sub>3</sub> was purified via reverse-phase HPLC (Grace Alltech column, 4.6  $\times$  250 mm, solvent A: 0.05% TFA in 18.2 M $\Omega$  MilliQ water, solvent B: 0.05% TFA in acetonitrile; starting condition: 90% A + 10% B, 1% per min gradient B, flow rate 1 mL/min, **Fig. A7**). Following concentration, using CuAAC chemistry, the resulting azide functionalized cRGD was either functionalized with methyltetrazine to generate **Product 2**, or ligated to DNA to generate **Products 3 and 4**. Briefly, 10 nmol alkyne-labeled tetrazine/ DNA in 18.2 M $\Omega$  MilliQ water was added to azide labelled c(RGDfK)-PEG<sub>2</sub>-PEG<sub>2</sub>-NH<sub>2</sub>). The copper catalyst solution was prepared in a separate tube by combining, in the following order, 20 mM CuSO<sub>4</sub> (2  $\mu$ L), 50 mM THPTA (4  $\mu$ L), and 50 mM ascorbic acid (2  $\mu$ L). The mixture was then added to the solution containing DNA and peptide and reacted at room temperature for 2 hours. The resulting oligonucleotide products were purified using P2 gel filtration and reverse-phase HPLC (AdvancedBio Oligonucleotides, Agilent, 4.6  $\times$  150 mm, solvent A: 0.1 M TEAA, solvent B: acetonitrile; starting condition: 90% A + 10% B, 1% per min gradient B, flow rate: 0.5 mL/min,

**Fig. A9).**

Amine and alkyne modified PNA and DNA bottom strands (20 nmol) were mixed with excess Cy3B NHS ester (50  $\mu$ g) in DMSO and allowed to react in an aqueous solution containing 10 % 10X PBS overnight at room temperature to generate **Product 5** and the precursors to **Product 9** and **Product 10**. The mixture was purified using P2 gel filtration and reverse-phase HPLC (AdvancedBio Oligonucleotides, Agilent, 4.6  $\times$  150 mm, solvent A: 0.1 M TEAA, solvent B: acetonitrile; starting condition: 90% A + 10% B, 1% per min gradient B, flow rate: 0.5 mL/min.). Following concentration, the alkyne and Cy3B labeled PNA and DNA were reacted with methyltetrazine-PEG<sub>4</sub>-azide using CuAAC to generate **Product 6**, **Product 9**, and **Product 10**. Briefly, 1 mg of methyltetrazine-PEG<sub>4</sub>-azide was dissolved in 20  $\mu$ l of 1:4 dimethylsulfoxide/H<sub>2</sub>O and warmed to 50 °C. The copper catalyst solution was prepared in a separate tube by combining, in the following order, 20 mM CuSO<sub>4</sub> (2  $\mu$ L), 50 mM THPTA (4  $\mu$ L), and 50 mM ascorbic acid (2  $\mu$ L). The reaction mixture was added to the Cy3B labeled DNA in 10  $\mu$ L 18.2 M $\Omega$  MilliQ water and warmed to 50 °C. Once warmed, the solution was added to the methyltetrazine-PEG<sub>4</sub>-azide with dropwise addition of dimethylsulfoxide to maintain solubility. The reaction proceeded at 50 °C for 1.5 h, and the resulting product was purified using P2 gel filtration and reverse-phase HPLC (AdvancedBio Oligonucleotides, Agilent, 4.6  $\times$  150 mm, solvent A: 0.1 M TEAA, solvent B: acetonitrile; starting condition: 90% A + 10% B, 1% per min gradient B, flow rate: 0.5 mL/min, **Fig. A9, A13, A14**).

Amine and BHQ2 labeled PNA top strands were reacted overnight with an excess of TCO NHS ester to generate **Product 7**. The resulting product was purified using P2 gel filtration and reverse-

phase HPLC (AdvancedBio Oligonucleotides, Agilent,  $4.6 \times 150$  mm, solvent A: 0.1 M TEAA, solvent B: acetonitrile; starting condition: 90% A + 10% B, 1% per min gradient B, flow rate: 0.5 mL/min, **Fig. A11**). Following concentration, **Product 7** was then reacted with **Product 2** in DMSO overnight to generate **Product 8**. The resulting product was purified using P2 gel filtration and reverse-phase HPLC (AdvancedBio Oligonucleotides, Agilent,  $4.6 \times 150$  mm, solvent A: 0.1 M TEAA, solvent B: acetonitrile; starting condition: 90% A + 10% B, 1% per min gradient B, flow rate: 0.5 mL/min, **Fig. A11, A12**).

#### *A.2.3.3 Surface preparation*

Surface preparation was modified from previously published protocols. Glass coverslips (#2 thickness, 25 mm diameter) were sequentially sonicated for 5 minutes in 18.2 M $\Omega$  MilliQ water and 200 proof ethanol. The coverslips were then dried in an oven ( $\sim 110$  °C) before immersing in freshly prepared piranha solution (3:1 H<sub>2</sub>SO<sub>4</sub> : H<sub>2</sub>O<sub>2</sub>) for 25 minutes. (**CAUTION: Piranha solution is highly reactive and explodes upon contact with organic solutions.**) Surfaces were then washed in 6 washes MilliQ water, followed by 3 washes ethanol. Surfaces were placed in a fourth wash of ethanol to which 3% of APTES was added for a 40-minute incubation. Following incubation, surfaces were washed in 3 washes ethanol and then baked in an oven ( $\sim 110$  °C) for 1 hour. A 4 mg/mL solution of trans-Cyclooctene NHS ester in DMSO was then added to each surface and incubated for  $\geq 12$  hours. Surfaces were stored at room temperature and used within 6 weeks of preparation.

#### *A.2.3.4 DNA hybridization*

Oligonucleotides were hybridized at 200 nM in a 0.2 mL Thermowell tube. DNA was heated to 90 °C and then cooled at a rate of 1.3 °C min<sup>-1</sup> to 25 °C.

#### *A.2.3.5 Imaging chamber assembly*

Before imaging, functionalized coverslips were placed into imaging chambers and washed with 5 mL 1X PBS. Surfaces were then incubated with 20 nM DNA probe solutions in 1X PBS (1 mL) for 1 hour and washed with 5 mL 1X PBS. Slides were then washed with cell imaging media (Tyrode's buffer for platelets, FluoroBrite DMEM Media, A1896701, Thermo-Fisher for fibroblast experiments) before plating cells.

#### *A.2.3.6 Cell culture*

3T3, HASM, and MDA-MB-231 cells were cultured according to American Type Culture Collection (ATCC) guidelines. Briefly, cells were cultured in DMEM supplemented with penicillin/ streptomycin and 10% fetal bovine serum (v/v). Media for HASMC's also included non-essential amino acids. Cells were passaged every 2–3 days as required.

#### *A.2.3.7 Image acquisition and analysis*

Fluorescent images were acquired using TRITC epifluorescence (tension. Epifluorescence images were locally background subtracted and all analysis was completed in ImageJ. Average fluorescence is measured by drawing a region of interest (ROI) around the fluorescent signal in the TRITC channel.

### A.2.8 Note 1– van't hoff analysis of PNA duplexes

Thermal melting curves were done using 100  $\mu\text{L}$  solutions of DNA:DNA, PNA:DNA, and PNA:PNA duplexes at 25, 40, 65, 80, and 100 nM in 1X PBS. The probe solutions were heated to 95  $^{\circ}\text{C}$  for 3 minutes and then cooled at a rate of 1.3  $^{\circ}\text{C min}^{-1}$  to 25  $^{\circ}\text{C}$  to hybridize. The solutions were then transferred to the 12 wells of a qPCR plate in 20  $\mu\text{L}$  each for three individual measurements for a condition. Using a qPCR instrument (LightCycler 96), the plate was incubated at 25  $^{\circ}\text{C}$  for 5 min and then heated to 95  $^{\circ}\text{C}$  over 1900 seconds with Cy3B fluorescent measurements.

Because the thermodynamic equilibrium of DNA folded structure is an intramolecular transition, their thermodynamic parameters, including  $\Delta G$ ,  $\Delta H$ , and  $\Delta S$ , are concentration-independent.(125) Thus, the probe's van't Hoff equation for thermodynamic analysis can be adopt from the definition of Gibbs free energy equation.

$$\Delta G = \Delta H - T\Delta S = RT \ln K_a \quad (\text{eq1})$$

Where  $K_a$  is the equilibrium constant of probe transition, R is gas constant (1.9872 cal/K•mol), and T is the temperature in Kelvin (0  $^{\circ}\text{C}$  = 273.15 K).

As a result of the equation transformation,

$$\ln C_T = \frac{\Delta H}{R} \frac{1}{T} - \frac{\Delta S}{R} \quad (\text{eq 2})$$

## A.2.9. Figures, tables, and schemes

Name	Sequence (5'/N to 3'/C)
sDNA top	CAC AGC ACG GAG GCA CGA CAC /i5OctdU//3BHQ_2
uDNA top	/55OctdU/CAC AGC ACG GAG GCA CGA CAC/3BHQ_2/
u/sDNA bottom	/5AmMC6/GTG TCG TGC CTC CGT GCT GTG /55OctdU/
u/sPNA top	Glu <sup>-</sup> /GTA GAT CAC T/Glu <sup>-</sup> /BHQ2
sPNA bottom	alkyne/AGT GAT CTA C/3MeK <sup>+</sup>
uPNA bottom	3MeK <sup>+</sup> /AGT GAT CTA C/alkyne

\3BHQ\_2 = BHQ2 ligated to 3' terminus. i5OctdU = alkyne linked internally within the DNA sequence. 5AmMC6 = 5' terminal amine. 35OctdU = 3' terminal alkyne. 3MeK<sup>+</sup> = trimethyl-lysine linked to the terminus of the PNA sequence.

Table A2. Oligonucleotides used in Chapter 3.

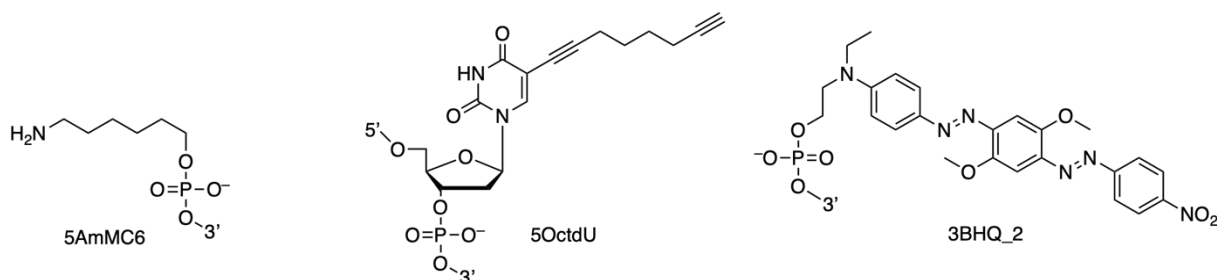


Figure A4. Chemical structures of oligo modifications used in Chapter 3.

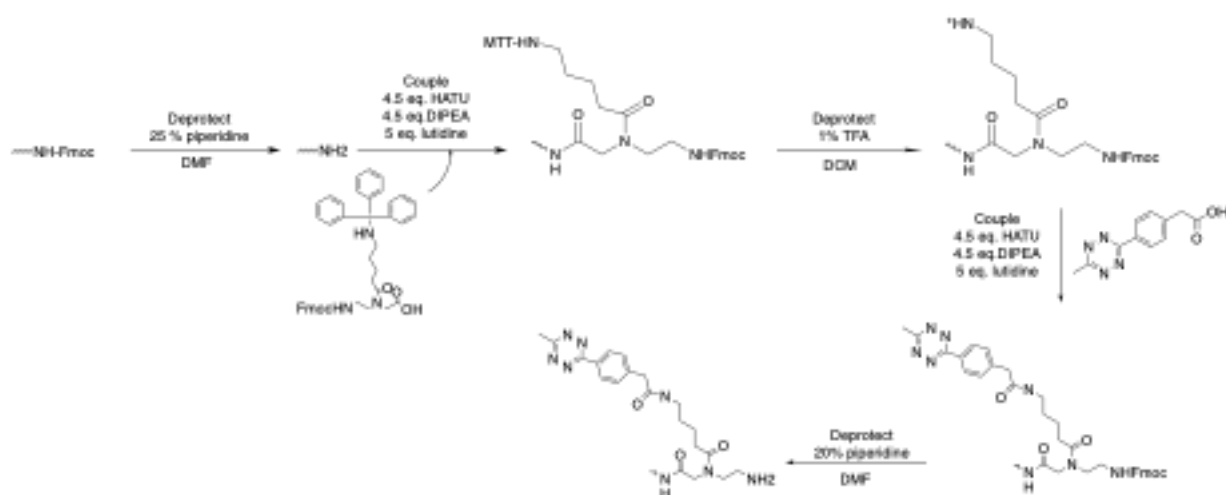
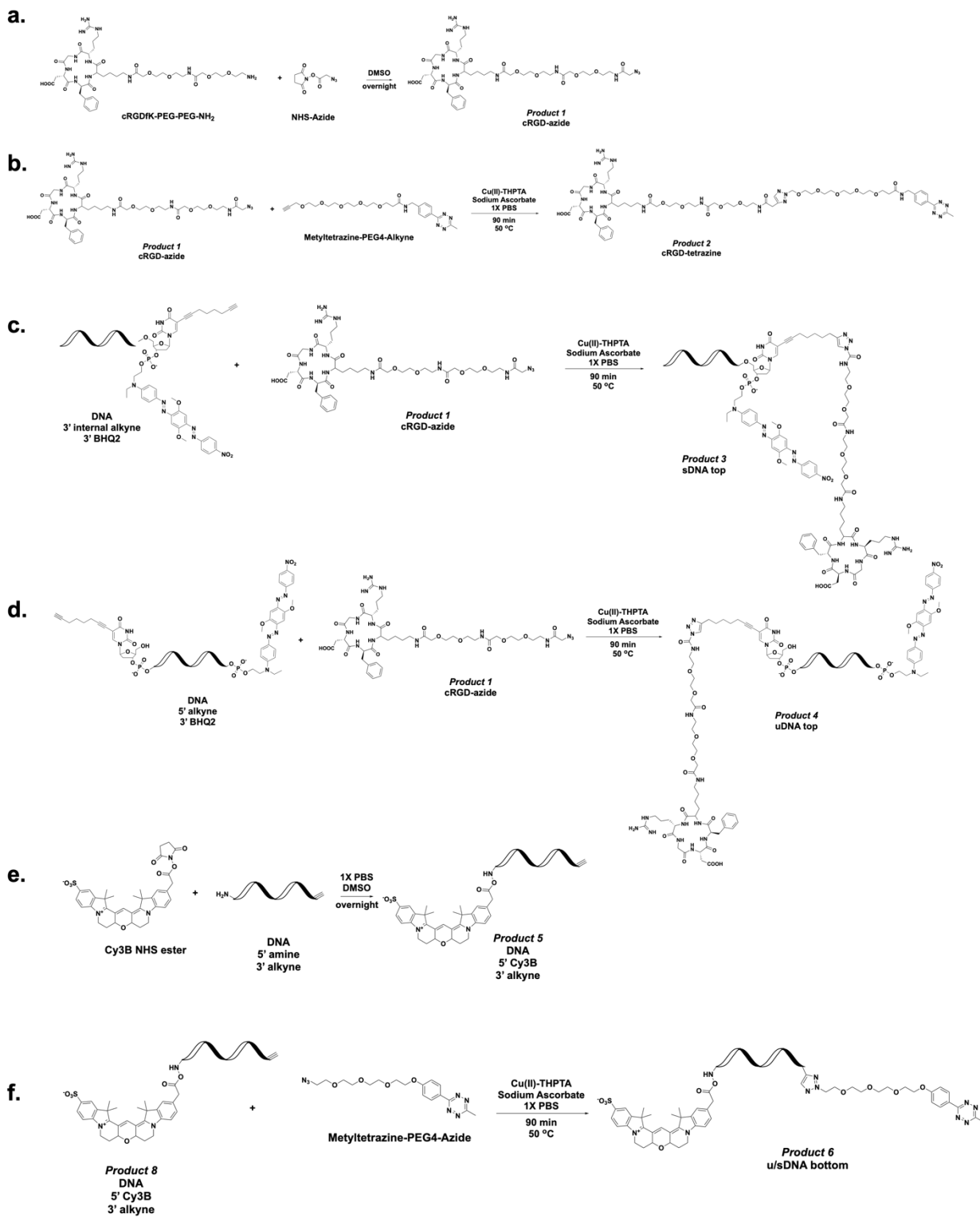
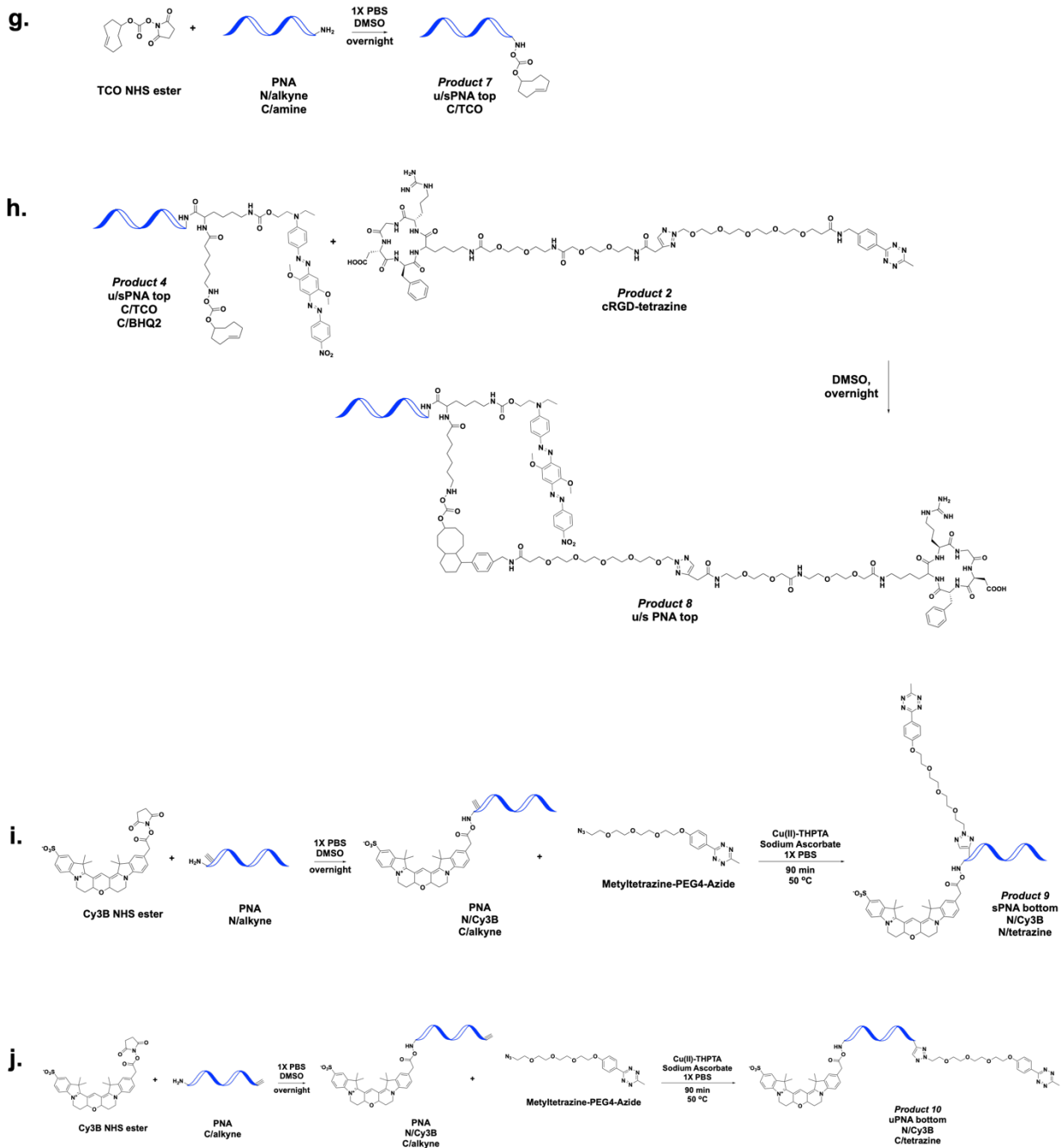
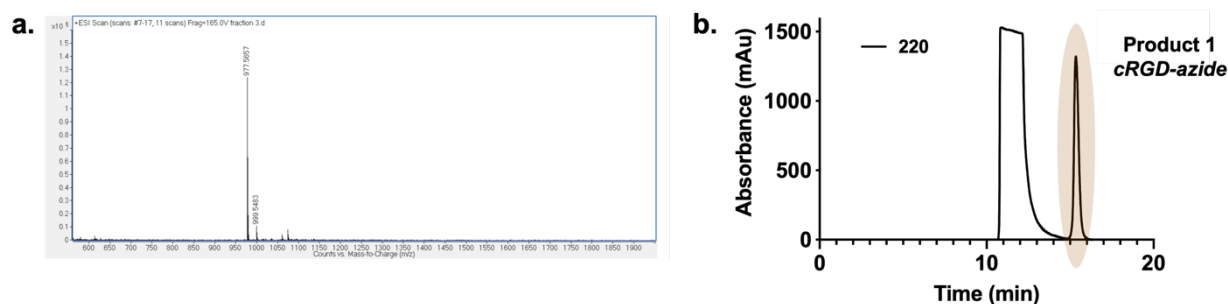


Figure A5. General synthetic scheme for PNA oligomers.





**Figure A6. Synthesis of PNA and DNA force sensors.** **a.** Schematic showing the coupling between NHS-N<sub>3</sub> and cRGD-PEG-PEG-NH<sub>2</sub> to form cRGD-PEG-PEG-N<sub>3</sub> (**Product 1**). **b.** Schematic showing the alkyne-azide cycloaddition reaction to conjugate tetrazine to **Product 1**, generating **Product 2**. **c.** Schematic showing the coupling of **Product 1** to DNA 3' internal alkyne 3'BHQ2 to generate sDNA top (**Product 3**). **d.** Schematic showing the coupling of **Product 1** to DNA 5' alkyne 3'BHQ2 to generate uDNA top (**Product 4**). **e.** Schematic showing coupling of Cy3B-NHS to DNA to generate **Product 5**. **f.** Schematic showing alkyne-azide cycloaddition reaction to conjugate tetrazine to **Product 5**, generating u/sDNA bottom (**Product 6**). **g.** Schematic showing the coupling between NHS-TCO and PNA (N/alkyne C/amine) to generate u/sPNA top TCO (**Product 7**). **h.** Schematic showing the alkyne-azide cycloaddition reaction to conjugate cRGD to generate u/sPNA top (**Product 8**). **i.** Schematic showing the coupling between Cy3B-NHS and methyltetrazine-azide to PNA to generate sPNA bottom (**Product 9**). **j.** Schematic showing the coupling between Cy3B-NHS and methyltetrazine-azide to PNA to generate uPNA bottom (**Product 10**).



**Figure A7. cRGD azide characterization a. ESI MS spectra b. HPLC trace**

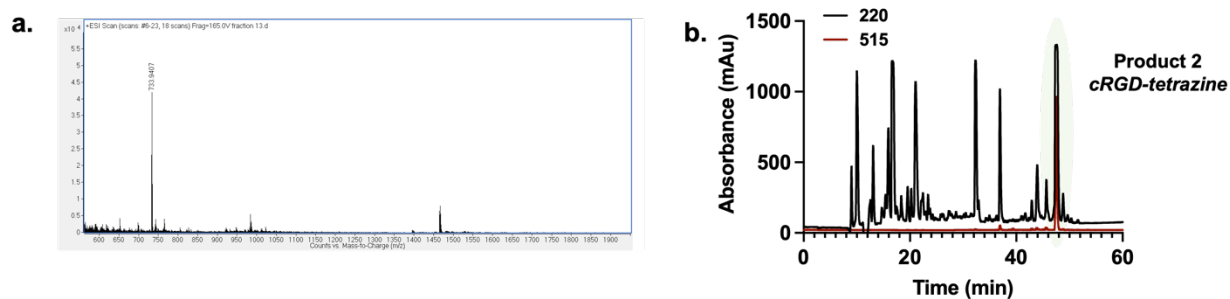


**Figure A8. Tetrazine cRGD azide characterization a. ESI MS spectra b. HPLC trace**

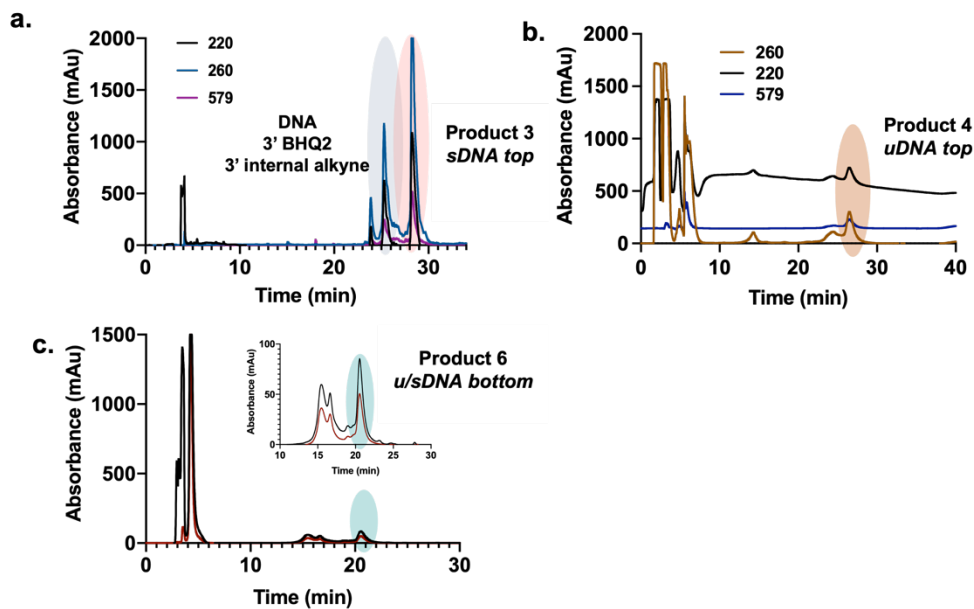


Figure A9. Chapter 3 DNA characterization a. HPLC trace of Product 3. b. HPLC trace of Product 4. c. HPLC trace of Product 6.

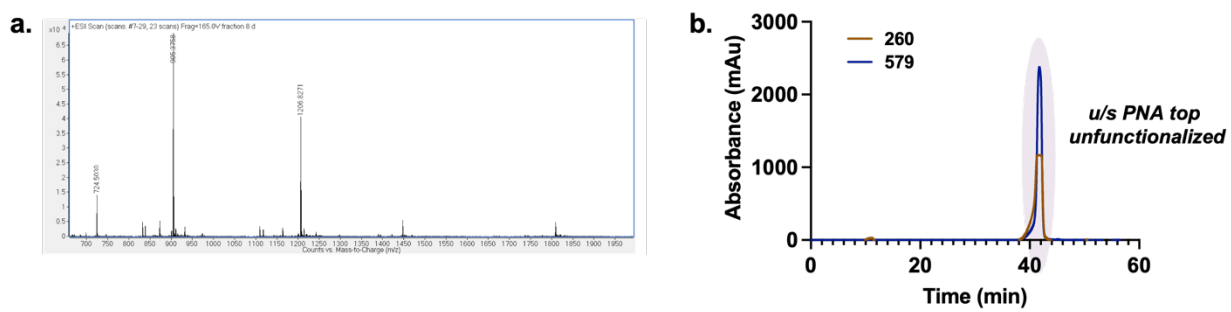


Figure A10. sPNA top characterization a. ESI MS spectra b. HPLC trace

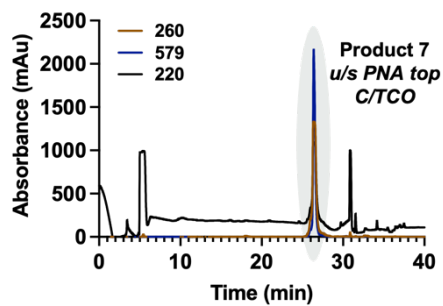


Figure A11. HPLC trace of sPNA top C terminal TCO

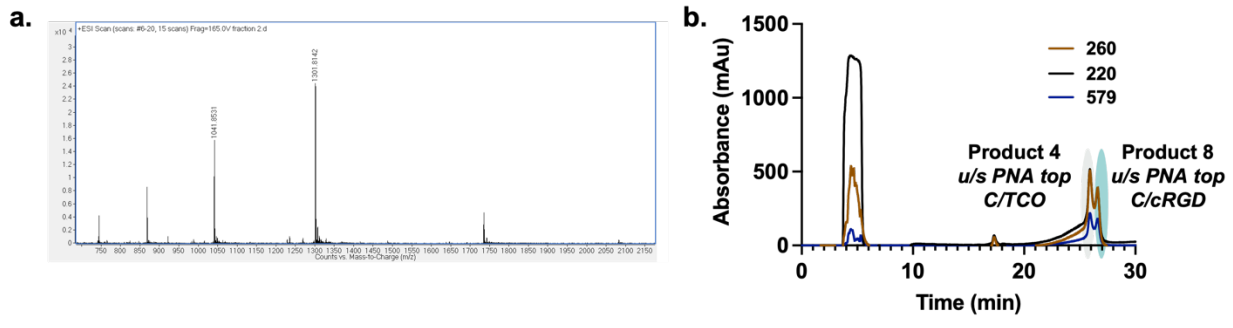


Figure A12. sPNA top C terminal cRGD characterization a. ESI MS spectra b. HPLC trace

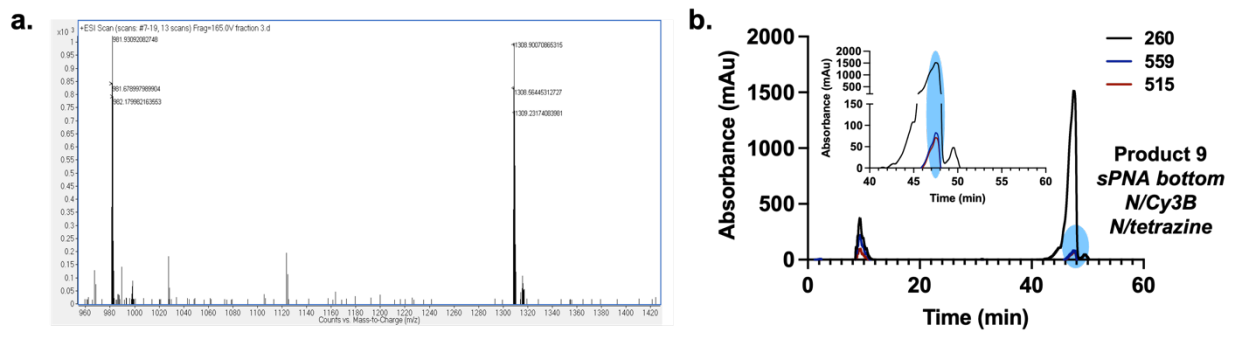


Figure A13. sPNA bottom N terminal Cy3B, N terminal methyltetrazine characterization a. ESI MS spectra b. HPLC trace

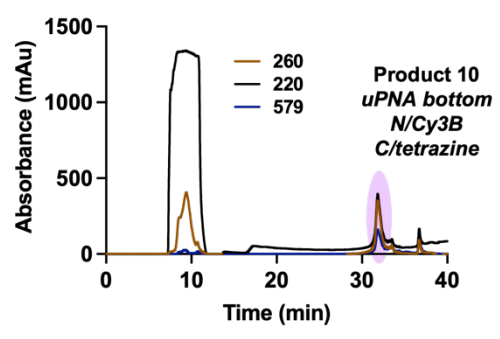


Figure A14. HPLC trace of uPNA bottom N terminal Cy3B, C terminal methyltetrazine characterization

### A.3 Cell adhesion receptors detect the force-extension curve of their ligands

#### A.3.1 Materials

##### Oligonucleotides

All custom synthesized oligonucleotides were purchased from Integrated DNA Technologies (Coralville, IA) and then transformed into tension probes. **Table A3** and **Figure A15** includes the sequences and information of chemical modifications for all purchased oligonucleotides used in this work.

##### Reagents

Cy3B-NHS ester (PA63101) was acquired from GE Healthcare Life Sciences. Cyclo[Arg-Gly-Asp-d-Phe-Lys(PEG-PEG)] (PCI-3696-PI), elsewhere abbreviated as cRGD, was acquired from Vivitide. (3-Aminopropyl)triethoxysilane (APTES, 440140, 99% purity), Latrunculin B (LatB, L5288-1MG,  $\geq 80\%$  purity), sulfuric acid (SX1244), *N,N*-diisopropylethylamine (*iPr*<sub>2</sub>EtN, 387649-100ML), sodium sulfate (238597-500G), sodium bicarbonate (S6014-500G), (+)-sodium L-ascorbate (A4034-100G), phosphate buffer saline tablet (P4417-50TAB), anhydrous methylsulfoxide (DMSO, MX1457-7) methanol (34860-4L-R), trifluoroacetic acid (TFA, TX1276-7), and TLC silica-gel 60 F<sub>254</sub> (1.05554.0001) were purchased from Millipore Sigma. 6-Azido-*N*-Boc-*L*-Norleucine (Boc-Lys(N<sub>3</sub>)-OH, A4543) was purchased from Acrotein. (S)-2-((tert-Butoxycarbonyl)amino)pent-4-ynoic acid (Boc-propargyl-Gly-OH, A201426, 97% purity) was purchased from Ambeed. *N,N,N',N'*-Tetramethyl-*O*-(*N*-succinimidyl)uronium tetrafluoroborate (TSTU,024891) was purchased from Oakwood Chemical. Methyltetrazine-PEG4-Amine (1012, >95% purity) and tris-hydroxypropyltriazolymethylamine (THPTA, 1010-

100) was purchased from Click Chemistry Tools. BHQ-2 succinimidyl ester (BHQ2-NHS BHQ-2000S-5) was purchased from Biosearch™ Technologies. Azido-NHS (BP-22467, 95% purity) and TCO-NHS (BP-22417, 95% purity) were purchased from BroadPharm. Dichloromethane (DCM, D143-4), hexanes (H292-4), and ethyl acetate (E195-4) were purchased from Fisher Chemicals. Cupric sulfate, 5-hydrate ( $\text{CuSO}_4 \cdot 5\text{H}_2\text{O}$ , 4844) was purchased from Mallinckrodt chemicals. Citric acid, monohydrate was purchased from Macron fine chemicals. Silica-gel (40930-25) was purchased from Sorbent Technologies. Triethylamine Acetate (TEAA, 2.0 M) solution was purchased from Glen Research. All other chemicals (unless otherwise stated) were purchased from Millipore Sigma and used without purification. All buffers were prepared with 18.2 M $\Omega$  MilliQ water.

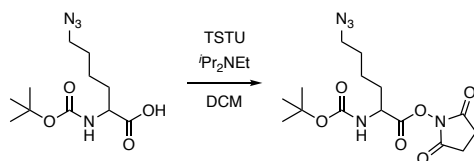
### **A.3.2 Equipment**

The major equipment that was used in this study includes Barnstead nanopure water purifying system (Thermo Fisher), high-performance liquid chromatography 1100 (Agilent) with AdvanceBio Oligonucleotide C18 column (653950-702, 4.6 x 150 mm, 2.7  $\mu\text{m}$ ) (Agilent), Electrospray ionization mass spectrometer (ESI-MS) (LTQ Orbitrap Velos, Thermo Fischer Scientific), LightCycler 96 qPCR instrument (Roche), and a Nikon Eclipse Ti microscope (Nikon), T100 thermocycler (Bio-Rad).

### A.3.3 Methods

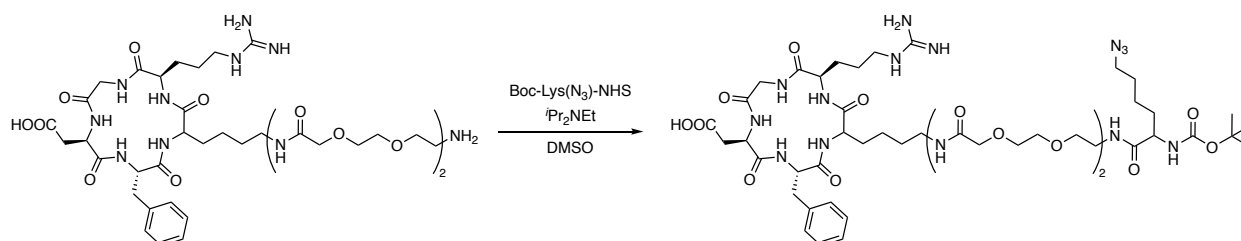
#### A.3.3.1 Synthesis of substructures for tension probes

##### Boc-Lys(N<sub>3</sub>)-NHS (**1**)



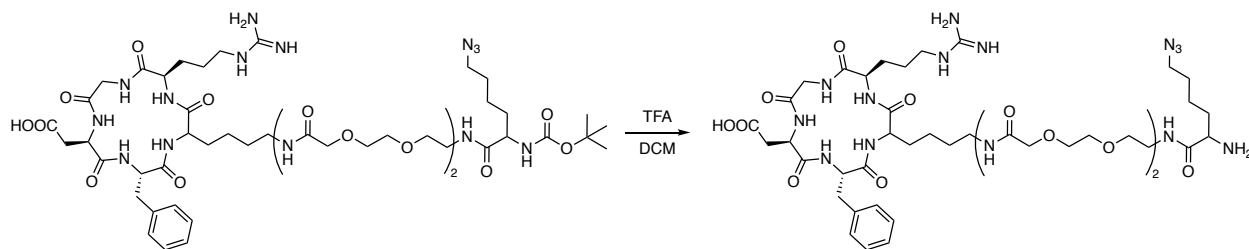
To a colorless solution of Boc-Lys(N<sub>3</sub>)-OH (107 mg, 0.392 mmol) and TSTU (287 mg, 0.953 mmol) in anhydrous dichloromethane (5 mL) was added *i*Pr<sub>2</sub>NEt (120 μL, 0.596 mmol) at room temperature under nitrogen atmosphere. The resulting dark-red solution was stirred for 20 hours at the same condition. Then, the solution was added 20 mL of dichloromethane, washed three times with an aqueous solution of 4%(w/v) citric acid and once with brine, dried over sodium sulfate, filtered, and concentrated under reduced pressure. The concentrated mixture was subjected to silica gel column ( $\varphi = 3$  cm, 20 mL of silica gel) eluted with a 1:1 mixture of hexanes and ethyl acetate ( $R_f = 0.54$ ) to obtain Boc-Lys(N<sub>3</sub>)-NHS (product **1**, 91.0 mg, 0.246 mmol, 63%) as a viscous yellow oil. <sup>1</sup>H NMR (CDCl<sub>3</sub>, 400 MHz)  $\delta$  5.03–5.00 (m, 1H), 4.71–4.68 (m, 1H), 3.31 (t,  $J = 6.8$  Hz, 2H), 2.85 (s, 4H), 2.04–1.95 (m, 1H), 1.90–1.78 (m, 1H), 1.71–1.60 (m, 4H), 1.46 (s, 9H). HRMS (ESI)  $m/z$  calcd. for C<sub>15</sub>H<sub>27</sub>N<sub>6</sub>O<sub>6</sub> [M+NH<sub>4</sub>]<sup>+</sup>: 387.1992; found: 387.1980 (**Fig. A31**).

##### cRGD-Lys(N<sub>3</sub>)-Boc (**2**)

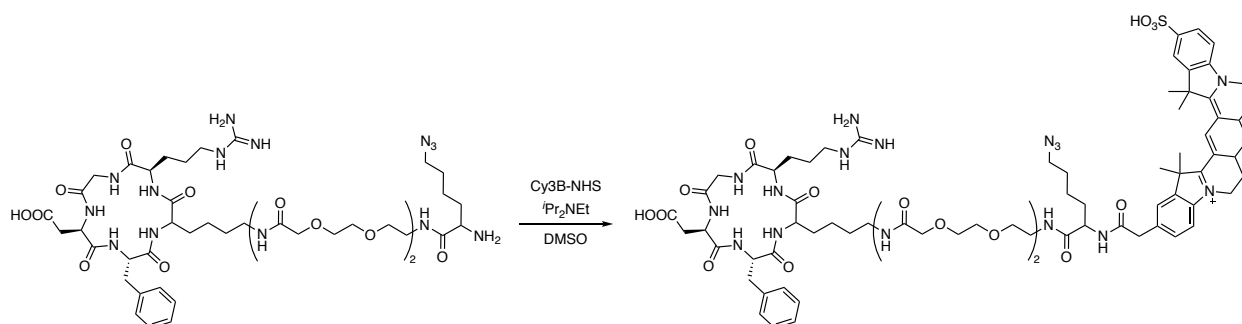


To a solution of cRGD-(PEG)<sub>2</sub>-NH<sub>2</sub> (5.0 mg, 5.6 μmol) and *i*Pr<sub>2</sub>NEt (5.0 μL, 29 μmol) in anhydrous DMSO (50 μL) was added Boc-Lys(N<sub>3</sub>)-NHS (12 mg, 34 μmol) in anhydrous DMSO (50 μL). After stirring for 30 min at room temperature, the reaction mixture was added to an 8:2 mixture of 18.2 MΩ MilliQ water and acetonitrile (400 μL) and filtered through a microcentrifuge filter (0.22 μm). The filtrate was subjected to reversed-phase HPLC (Alltima C18 5u, Alltech, 4.6 × 250 mm, 1.0 mL min<sup>-1</sup> flow rate; solvent A: 0.05% TFA in 18.2 MΩ MilliQ water, solvent B: 0.05% TFA in acetonitrile; starting condition: 80% A + 20% B, 2% per min gradient B for 14 min) to obtain 5.2 mg of cRGD-Lys(N<sub>3</sub>)-Boc (product **2**, 4.5 μmol, 81%) as a colorless solid. HRMS (ESI) *m/z* calcd. for C<sub>50</sub>H<sub>82</sub>N<sub>15</sub>O<sub>16</sub> [M+H]<sup>+</sup>: 1148.6058; found: 1148.6056 (**Fig. A32**).

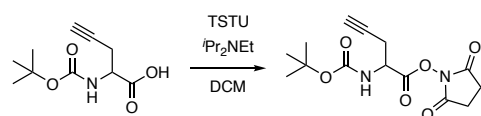
### cRGD-Lys(N<sub>3</sub>)-NH<sub>2</sub> (**3**)



cRGD-Lys(N<sub>3</sub>)-Boc (5.2 mg, 4.5 μmol) was dissolved in trifluoroacetic acid (TFA, 20 μL) and dichloromethane (80 μL) and stirred for 1 hour at room temperature. The resulting mixture was diluted with 900 μL of acetonitrile, and the solution was concentrated to 100 μL. The mixture was added to 18.2 MΩ MilliQ water (400 μL) and filtered through a microcentrifuge filter (0.22 μm). The filtrate was subjected to reversed-phase HPLC (Alltima C18 5u, Alltech, 4.6 × 250 mm, 1.0 mL min<sup>-1</sup> flow rate; solvent A: 0.05% TFA in 18.2 MΩ MilliQ water, solvent B: 0.05% TFA in acetonitrile; starting condition: 85% A + 15% B, 1% per min gradient B for 15 min) to obtain 3.8 mg of cRGD-Lys(N<sub>3</sub>)-NH<sub>2</sub> (product **3**, 3.6 μmol, 80%) as a colorless solid. HRMS (ESI) *m/z* calcd. for C<sub>45</sub>H<sub>74</sub>N<sub>15</sub>O<sub>14</sub> [M+2H]<sup>2+</sup>: 524.7804; found: 524.7784 (**Fig. A33**).

cRGD-Lys(N<sub>3</sub>)-Cy3B (**4**)

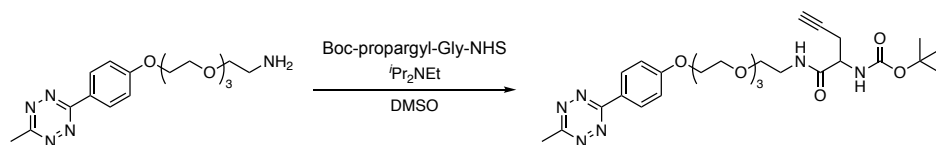
To a solution of cRGD-Lys(N<sub>3</sub>)-NH<sub>2</sub> (1.5 mg, 1.4 μmol) and *i*Pr<sub>2</sub>NEt (5.0 μL, 29 μmol) in anhydrous DMSO (40 μL) was added Cy3B-NHS (1.0 mg, 1.52 μmol) in anhydrous DMSO (20 μL). After stirring for 30 min at room temperature, the resulting mixture was diluted with 18.2 MΩ MilliQ water (440 μL) and filtered through a microcentrifuge filter (0.22 μm). The filtrate was subjected to reversed-phase HPLC (Alltima C18 5u, Alltech, 4.6 × 250 mm, 1.0 mL min<sup>-1</sup> flow rate; solvent A: 0.05% TFA in 18.2 MΩ MilliQ water, solvent B: 0.05% TFA in acetonitrile; starting condition: 77% A + 23% B, 1% per min gradient B for 20 min) to obtain 1.2 mg of cRGD-Lys(N<sub>3</sub>)-Cy3B (product **4**, 0.75 μmol, 54%) as a dark red solid. HRMS (ESI) *m/z* calcd. for C<sub>76</sub>H<sub>105</sub>N<sub>17</sub>O<sub>19</sub>S [M+H]<sup>2+</sup>: 795.8741; found: 795.8762 (**Fig. A34**).

Boc-propargyl-Gly-NHS (**5**)

To a colorless solution of Boc-propargyl-Gly-OH (213 mg, 1.00 mmol) and TSTU (602 mg, 2.00 mmol) in anhydrous dichloromethane (5 mL) was added *i*Pr<sub>2</sub>NEt (200 μL, 2.00 mmol) at room temperature under nitrogen atmosphere. The resulting pale-yellow solution was stirred for 20 hours

at the same condition. Then, the obtained dark-red solution was added 20 mL of dichloromethane, washed three times with an aqueous solution of 4%(w/v) citric acid and once with brine, dried over sodium sulfate, filtered, and concentrated under reduced pressure. The concentrated mixture was dissolved in 2 mL of dichloromethane and then slowly added 5 mL of hexanes. The supernatant was subjected to a silica gel column ( $\phi = 3$  cm, 20 mL of silica gel) eluted with a 10:7 mixture of hexanes and ethyl acetate ( $R_f = 0.27$ ) to obtain Boc-propargyl-Gly-NHS (product **5**, 262 mg, 0.844 mmol, 84%) as a colorless solid.  $^1\text{H NMR}$  ( $\text{CDCl}_3$ , 400 MHz)  $\delta$  5.36–5.28 (m, 1H), 4.89–4.85 (m, 1H), 2.90–2.78 (m, 6H), 2.04 (s, 1H), 1.46 (s, 9H). HRMS (ESI)  $m/z$  calcd. for  $\text{C}_{14}\text{H}_{19}\text{N}_2\text{O}_6\text{Na}$   $[\text{M}+\text{Na}]^+$ : 333.1063; found: 333.1048 (**Fig. A35**).

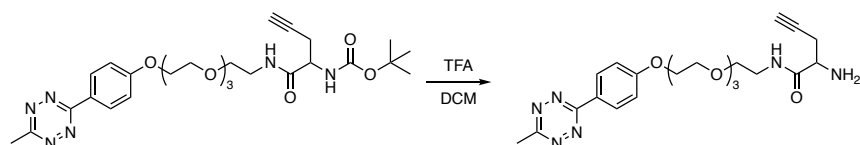
#### Boc-propargyl-Gly-PEG<sub>4</sub>-MeTz (**6**)



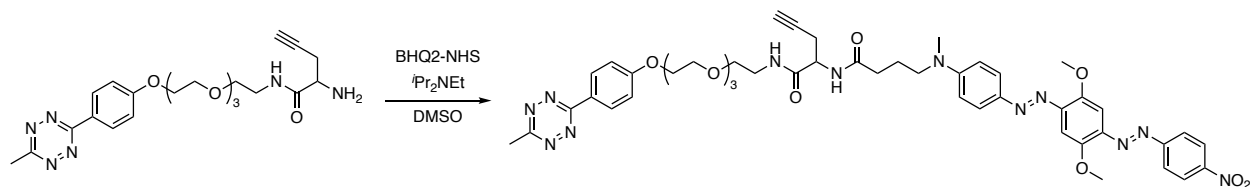
To a solution of Methyltetrazin-PEG<sub>4</sub>-NH<sub>2</sub> (200  $\mu\text{g}$ , 0.55  $\mu\text{mol}$ ) and *i*Pr<sub>2</sub>NEt (1  $\mu\text{L}$ , 6.8  $\mu\text{mol}$ ) in anhydrous DMSO (10  $\mu\text{L}$ ) was added Boc-propargyl-Gly-NHS (300  $\mu\text{g}$ , 0.97  $\mu\text{mol}$ ) in anhydrous DMSO (5  $\mu\text{L}$ ). After stirring for 2 hours at room temperature, the resulting mixture was diluted with a 1:1 solution of acetonitrile/18.2 M $\Omega$  MilliQ water (120  $\mu\text{L}$ ) and filtered through a microcentrifuge filter. The filtrate was subjected to reversed-phase HPLC (Alltima C18 5 $\mu$ , Alltech,  $4.6 \times 250$  mm, 1.2 mL  $\text{min}^{-1}$  flow rate; solvent A: 0.05% TFA in 18.2 M $\Omega$  MilliQ water, solvent B: 0.05% TFA in acetonitrile; starting condition: 70% A + 30% B, 2% per min gradient B for 14.5 min) to obtain 250  $\mu\text{g}$  of Boc-propargyl-Gly-PEG<sub>4</sub>-MeTz (product **6**, 0.45  $\mu\text{mol}$ , 46%) as

a red solid. HRMS (ESI)  $m/z$  calcd. for  $C_{27}H_{39}N_6O_7$   $[M+H]^+$ : 559.2875; found: 559.2872 (**Fig. A36**)

$NH_2$ -propargyl-Gly-PEG<sub>4</sub>-MeTz (**7**)



Boc-propargyl-Gly-PEG<sub>4</sub>-MeTz (250  $\mu$ g, 0.45  $\mu$ mol) was dissolved in trifluoroacetic acid (TFA, 20  $\mu$ L) and dichloromethane (80  $\mu$ L) and stirred for 1 hour at room temperature. The resulting mixture was diluted with 900  $\mu$ L of acetonitrile, and the solution was concentrated to 100  $\mu$ L. The mixture was added 1:4 mixture of acetonitrile/18.2 M $\Omega$  MilliQ water (400  $\mu$ L) and filtered through a microcentrifuge filter. The filtrate was subjected to reversed-phase HPLC (Alltima C18 5 $\mu$ , Alltech,  $4.6 \times 250$  mm, 1.2 mL  $min^{-1}$  flow rate; solvent A: 0.05% TFA in 18.2 M $\Omega$  MilliQ water, solvent B: 0.05% TFA in acetonitrile; starting condition: 90% A + 10% B, 2.3% per min gradient B for 16 min) to obtain 175  $\mu$ g of  $NH_2$ -propargyl-Gly-PEG<sub>4</sub>-MeTz (product **7**, 0.38  $\mu$ mol, 85%) as a red solid. HRMS (ESI)  $m/z$  calcd. For  $C_{22}H_{31}N_6O_5$   $[M+H]^+$ : 459.2350; found: 459.2347 (**Fig. A37**)

BHQ2-propargyl-Gly-PEG<sub>4</sub>-MeTz (**8**)

To a solution of NH<sub>2</sub>-propargyl-Gly-PEG<sub>4</sub>-MeTz (1.5 mg, 3.2 μmol) and *i*Pr<sub>2</sub>NEt (1 μL) in anhydrous DMSO (40 μL) was added BHQ2-NHS (1.0 mg, 1.6 μmol) in anhydrous DMSO (20 μL). After stirring for 30 min at room temperature, the resulting mixture was diluted with a 3:1 mixture of acetonitrile/18.2 MΩ MilliQ water (120 μL) and filtered through a microcentrifuge filter. The filtrate was subjected to reversed-phase HPLC (Alltima C18 5u, Alltech, 4.6 × 250 mm, 1.2 mL min<sup>-1</sup> flow rate; solvent A: 0.05% TFA in 18.2 MΩ MilliQ water, solvent B: 0.05% TFA in acetonitrile; starting condition: 40% A + 60% B, 1% per min gradient B for 10 min) to obtain 1.2 mg of BHQ2-propargyl-Gly-PEG<sub>4</sub>-MeTz (product **8**, 1.3 μmol, 79%) as a dark purple solid. HRMS (ESI) *m/z* calcd. For C<sub>47</sub>H<sub>55</sub>N<sub>12</sub>O<sub>10</sub> [M+H]<sup>+</sup>: 947.4159; found: 947.4155 (**Fig. A38**)

### A.3.3.2 Synthesis of DNA tension probes

Tension probes were synthesized by the sequential copper mediated azide-alkyne cyclization reaction (CuAAC), NHS-Amine coupling reaction, and strain promoted azide-alkyne cycloaddition reaction (SPAAC) or CuAAC. Synthetic scheme is described in the **Scheme S1**.

cRGD-Lys(N<sub>3</sub>)-Cy3B (cRGD/Cy3B-N<sub>3</sub>) or methyltetrazine-PEG<sub>4</sub>-N<sub>3</sub> was ligated to the corresponding alkyne modified strand (IDT) via 1,3-dipolar cycloaddition reaction. Briefly, a solution of 10 nmol of alkyne modified strand was reacted 1 hour at 50 °C with 40 nmol of azido reagents in the presence of sodium ascorbate (0.50 μmol), CuSO<sub>4</sub> (0.20 μmol), and THPTA (0.25

$\mu\text{mol}$ ) in 35  $\mu\text{L}$  (1: 2 = DMSO: 18.2 M $\Omega$  MilliQ water). The product was filtered through a microcentrifuge filter (0.22  $\mu\text{m}$ ). The filtrate was subjected to reverse-phase HPLC (AdvancedBio Oligonucleotides, Agilent, 4.6  $\times$  150 mm, 0.5 mL min<sup>-1</sup> flow rate; solvent A: 0.1 M triethylammonium acetate (TEAA), solvent B: acetonitrile) to desired products. Product **9**, shearing bottom (5'- methyltetrazine, internal- NH<sub>2</sub>, 3'- BHQ2): HPLC starting condition: 90% A + 10% B, 1% per min gradient B for 45 min, MS (ESI) calcd. For [M]<sup>+</sup>: 8663.9; found: 8662.7 (**Fig. A39**). Product **10**, shearing top (5'- cRGD/Cy3B, 3'- NH<sub>2</sub>): HPLC starting condition: 90% A + 10% B, 1% per min gradient B for 20 min and then 2% per min gradient B for 5 min, MS (ESI) calcd. for [M]<sup>+</sup>: 17508.2; found: 17507.5 (**Fig. A40**). Product **11**, unzipping (5'- cRGD/Cy3B, 3'- NH<sub>2</sub>): HPLC starting condition: 100% C (50 mM EDTA, 100 mM triethylamine, hydrochloric acid was used to adjust pH 7.2, 80% 18.2 M $\Omega$  MilliQ water/ 20% methanol) for 8 min to remove excess Cu ion, 90% A + 10% B for 3 min, and then 1% per min gradient B for 16 min, MS (ESI) calcd. For [M]<sup>+</sup>: 24006.3; found: 24004.3 (**Fig. A41**).

A solution of amine-modified oligonucleotide in 18.2 M $\Omega$  MilliQ water (6  $\mu\text{L}$ ) was added 2  $\mu\text{L}$  of 10X PBS and 2  $\mu\text{L}$  of an aqueous solution of 1 M NaHCO<sub>3</sub>. The solution was then added NHS-N<sub>3</sub> (300  $\mu\text{g}$ ) in DMSO (10  $\mu\text{L}$ ) and left for 1 hour. The product was filtered through a microcentrifuge filter (0.22  $\mu\text{m}$ ) with 30  $\mu\text{L}$  of an aqueous solution of 0.1 M TEAA. The filtrate was subjected to reverse-phase HPLC (AdvancedBio Oligonucleotides, Agilent, 4.6  $\times$  150 mm, 0.5 mL min<sup>-1</sup> flow rate; solvent A: 0.1 M triethylammonium acetate (TEAA), solvent B: acetonitrile; starting condition: 90% A + 10% B, 0.5% per min gradient B) to desired products. Product **12**, shearing bottom (5'- methyltetrazine, internal- N<sub>3</sub>, 3'- BHQ2): HPLC starting condition: 71% A + 29% B, 0.5% per min gradient B for 14 min, MS (ESI) calcd. For [M]<sup>+</sup>: 8746.0; found: 8745.7 (**Fig. A42**).

Product **13**, shearing top (5'- cRGD/Cy3B, 3'- N<sub>3</sub>): HPLC starting condition: 87% A + 13% B, 0.5% per min gradient B for 20 min, MS (ESI) calcd. for [M]<sup>+</sup>: 17591.3; found: 17590.5 (**Fig. A43**). Product **14**, unzipping (5'- cRGD/Cy3B, 3'- N<sub>3</sub>): HPLC starting condition: 90% A + 10% B, 1% per min gradient B for 20 min at 65 °C (**Fig. A444**). Because of the minimum change of HPLC retention time, unzipping (5'- cRGD/Cy3B, 3'- NH<sub>2</sub>) and unzipping (5'- cRGD/Cy3B, 3'- N<sub>3</sub>) strands were inseparable, and thus the obtained mixture was directly used for the following reaction.

To a solution of azide modified unzipping probe strand was reacted 1 hour at 50 °C with an excess amount of BHQ2-propargyl-Gly-PEG<sub>4</sub>-MeTz in the presence of sodium ascorbate (0.50 μmol), CuSO<sub>4</sub> (0.20 μmol), and THPTA (0.25 μmol) in 40 μL (1: 1 = DMSO: 18.2 MΩ MilliQ water). The product was filtered through a microcentrifuge filter (0.22 μm). The filtrate was subjected to reverse-phase HPLC (AdvancedBio Oligonucleotides, Agilent, 4.6 × 150 mm, 0.5 mL min<sup>-1</sup> flow rate; solvent A: 0.1 M triethylammonium acetate (TEAA), solvent B: acetonitrile; starting condition: 90% A + 10% B, 0.5% per min gradient B) to obtain the mixture of the desired product. Product **15**, reversible unzipping probe (5'- cRGD/Cy3B, 3'- BHQ2/MeTz): HPLC starting condition: 90% A + 10% B, 1% per min gradient B for 35 min at 65 °C, MS (ESI) calcd. for [M]<sup>+</sup>: 25036.4; found: 25035.8 (**Fig. A16**).

To a solution of azide modified reversible shearing top strand in 18.2 MΩ MilliQ water (10 μL) was added large excess amount of DBCO-PEG<sub>5</sub>-DBCO linker in DMSO (10 μL) and left for 1 hour. The resulting solution was filtered through a microcentrifuge filter (0.22 μm). The filtrate was subjected to reverse-phase HPLC (AdvancedBio Oligonucleotides, Agilent, 4.6 × 150 mm,

0.5 mL min<sup>-1</sup> flow rate; solvent A: 0.1 M triethylammonium acetate (TEAA), solvent B: acetonitrile; starting condition: 90% A + 10% B, 0.5% per min gradient B) to DBCO modified reversible shearing top strand. Product **16**, shearing top (5'- cRGD/Cy3B, 3'- DBCO): HPLC starting condition: 71% A + 29% B, 1% per min gradient B for 30 min, MS (ESI) calcd. for [M]<sup>+</sup>: 9600.9; found: 9601.0 (**Fig. A45**).

To a solution of DBCO modified reversible shearing top strand in 18.2 MΩ MilliQ water (10 μL) was added azide modified reversible shearing bottom strand and left for overnight at four °C. The resulting solution was filtered through a microcentrifuge filter (0.22 μm). The filtrate was subjected to reverse-phase HPLC (AdvancedBio Oligonucleotides, Agilent, 4.6 × 150 mm, 0.5 mL min<sup>-1</sup> flow rate; solvent A: 0.1 M triethylammonium acetate (TEAA), solvent B: acetonitrile; starting condition: 90% A + 10% B, 0.5% per min gradient B) to the reversible shearing probe. Product **17**, reversible shearing probe: HPLC starting condition: 90% A + 10% B, 1% per min gradient B for 40 min at 65 °C, MS (ESI) calcd. for [M]<sup>+</sup>: 27192.2; found: 27190.4 (**Fig. A17**).

Amine and alkyne modified TGT bottom strand (20 nmol) was mixed with excess Cy3B NHS ester (50 μg) in DMSO and allowed to react in an aqueous solution containing 10 % 10X PBS overnight at room temperature to generate **Product 18**. The mixture was purified using P2 gel filtration and reverse-phase HPLC (AdvancedBio Oligonucleotides, Agilent, 4.6 × 150 mm, solvent A: 0.1 M TEAA, solvent B: acetonitrile; starting condition: 90% A + 10% B, 1% per min gradient B, flow rate: 0.5 mL/min, **Fig. A46a**). Following concentration, the alkyne and Cy3B labeled DNA was reacted with methyltetrazine-PEG<sub>4</sub>-azide using CuAAC to generate **Product**

19. Briefly, 1 mg of methyltetrazine-PEG<sub>4</sub>-azide was dissolved in 20  $\mu$ l of 1:4 dimethylsulfoxide/H<sub>2</sub>O and warmed to 50 °C. The copper catalyst solution was prepared in a separate tube by combining, in the following order, 20 mM CuSO<sub>4</sub> (2  $\mu$ L), 50 mM THPTA (4  $\mu$ L), and 50 mM ascorbic acid (2  $\mu$ L). The reaction mixture was added to the Cy3B labeled DNA in 10  $\mu$ L 18.2 M $\Omega$  MilliQ water and warmed to 50 °C. Once warmed, the solution was added to the methyltetrazine-PEG<sub>4</sub>-azide with dropwise addition of dimethylsulfoxide to maintain solubility. The reaction proceeded at 50 °C for 1.5 h, and the resulting product was purified using P2 gel filtration and reverse-phase HPLC (AdvancedBio Oligonucleotides, Agilent, 4.6  $\times$  150 mm, solvent A: 0.1 M TEAA, solvent B: acetonitrile; starting condition: 90% A + 10% B, 1% per min gradient B, flow rate: 0.5 mL/min, **Fig. A46b**).

100 nmol of c(RGDfK)-PEG<sub>2</sub>-PEG<sub>2</sub>-NH<sub>2</sub> was reacted with an excess amount of NHS-azide in DMSO overnight to generate **Product 20**. cRGD-N<sub>3</sub> was purified via reverse-phase HPLC (Grace Alltech column, 4.6  $\times$  250 mm, solvent A: 0.05% TFA in 18.2 M $\Omega$  MilliQ water, solvent B: 0.05% TFA in acetonitrile; starting condition: 90% A + 10% B, 1% per min gradient B, flow rate 1 mL/min , **Fig. A46c**). Following concentration, the resulting azide functionalized cRGD was ligated to the alkyne and BHQ2 modified top strand using CuAAC to generate **Product 21**. Briefly, 10 nmol alkyne-labeled DNA in 18.2 M $\Omega$  MilliQ water was added to azide labelled c(RGDfK)-PEG<sub>2</sub>-PEG<sub>2</sub>-NH<sub>2</sub>). The copper catalyst solution was prepared in a separate tube by combining, in the following order, 20 mM CuSO<sub>4</sub> (2  $\mu$ L), 50 mM THPTA (4  $\mu$ L), and 50 mM ascorbic acid (2  $\mu$ L). The mixture was then added to the solution containing DNA and peptide and reacted at room temperature for 2 hours. The resulting product was purified using P2 gel filtration and reverse-phase HPLC (AdvancedBio Oligonucleotides, Agilent, 4.6  $\times$  150 mm, solvent A: 0.1 M TEAA,

solvent B: acetonitrile; starting condition: 90% A + 10% B, 1% per min gradient B, flow rate: 0.5 mL/min.

#### *A.3.3.3 Synthesis of fluorescently labeled human fibronectin*

To a solution of Human fibronectin (Corning #354008, 60  $\mu$ L, 1 mg/mL in 1X PBS), aqueous solution of 1M NaHCO<sub>3</sub> (10  $\mu$ L), and 10X PBS (10  $\mu$ L) was added a solution of Alexa Fluor 488 NHS ester (50  $\mu$ g) in DMSO (10  $\mu$ L) at 0 °C. The solution was kept at 0 °C for an hour, and then diluted with 450  $\mu$ L of 1X PBS. The unreacted Alexa Fluor 488 was removed by the centrifugal filtration through Amicon<sup>®</sup> ultra filter (3K). Briefly, the solution was transferred to the filter, and centrifuged at 13,000 rpm for 10 min. Then, the solution was diluted with 400  $\mu$ L of 1X PBS. After repeating the filtration procedure for five time, the supernatant was collected. Based on UV-vis measurement of Alexa-488 absorption, the Degree of Labeling (DOL) was determined as 5.2.

#### *A.3.3.4 Electron Spray Ionization (ESI) mass spectroscopy*

The molecular weight of the products was evaluated with an electron spray ionization (ESI) method using a Thermo Fisher Scientific Orbitrap. Small molecule samples were prepared in 18.2 M $\Omega$  MilliQ water and the spectra recorded in positive charge mode eluted with a mixture of 60% of 18.2 M $\Omega$  MilliQ water and 40% of acetonitrile containing 0.05% formic acid. For oligonucleotides, samples were prepared in the mixture of 70% 18.2 M $\Omega$  MilliQ water and 30% methanol containing 10  $\mu$ M ethylenediaminetetraacetic acid (EDTA), 0.0375% triethylamine, and 0.75% of 1,1,1,3,3,3-hexafluoro-2-propanol (HFIP) and recorded the spectra with negative charge mode eluted with same solution.(155) The obtained ESI-MS spectrum ( $m/z$ ) was then deconvoluted for the main peak to obtain average molecular weight for the oligonucleotides.

#### *A.3.3.5 Characterization of reversible probes*

Thermodynamic parameters ( $\Delta G$ ,  $\Delta H$ , and  $\Delta S$ ) of reversible shearing and unzipping probes were analyzed based on temperature-dependent fluorescence measurement (**Fig. A18, Table A4, A5, Note 2**). The unfolding behavior of the two constructs was modelled in oxDNA using previously published parameters and examples found at [dna.physics.ox.ac.uk](http://dna.physics.ox.ac.uk) website (**Note 3**).

#### *A.3.3.6 Surface preparation*

Surface preparation was modified from previously published protocols. Glass coverslips (#2 thickness, 25 mm diameter) were sequentially sonicated for 5 minutes in 18.2 M $\Omega$  MilliQ water and 200 proof ethanol. The coverslips were then dried in an oven (~110 °C) before immersing in freshly prepared piranha solution (3:1 H<sub>2</sub>SO<sub>4</sub> : H<sub>2</sub>O<sub>2</sub>) for 25 minutes. (**CAUTION: Piranha solution is highly reactive and explodes upon contact with organic solutions.**) Surfaces were then washed in 6 washes MilliQ water, followed by 3 washes ethanol. Surfaces were placed in a fourth wash of ethanol to which 3% of APTES was added for a 40-minute incubation. Following incubation, surfaces were washed in 3 washes ethanol and then baked in an oven (~ 110 °C) for 1 hour. A 4 mg/mL solution of trans-Cyclooctene NHS ester in DMSO was then added to each surface and incubated for  $\geq 12$  hours. Surfaces were stored at room temperature and used within 6 weeks of preparation.

#### *A.3.3.7 DNA Hybridization*

DNA oligonucleotides were hybridized at 200 nM in a 0.2 mL Thermowell tube. DNA was heated to 90 °C and then cooled at a rate of 1.3 °C min<sup>-1</sup> to 25 °C.

#### *A.3.3.8 Imaging chamber assembly*

*DNA Functionalization:* Before imaging, functionalized coverslips were placed into imaging chambers and washed with 5 mL 1X PBS. Surfaces were then incubated with 20 nM DNA probe solutions in 1X PBS (1 mL) for 1 hour and washed with 5 mL 1X PBS. Slides were then washed with cell imaging media (Tyrode's buffer for platelets, FluoroBrite DMEM Media, A1896701, Thermo-Fisher for fibroblast experiments) before plating cells.

*Fibronectin Functionalization:* Unfunctionalized coverslips were placed into imaging chambers and washed with 5 mL ethanol followed by 5 mL of MQ H<sub>2</sub>O. Surfaces were then incubated overnight at 4 °C with 0.1 µg/mL fibronectin. Slides were then washed with cell imaging media (Tyrode's buffer for platelets, FluoroBrite DMEM Media, A1896701, Thermo-Fisher for fibroblast experiments) before plating cells.

#### *A.3.3.9 Fibroblast staining*

*Actin:* Following trypsinization, cells in imaging media were incubated in a 1.5 mL Eppendorf tube with 0.5 µM SiR-actin + 5 µM verapamil on a rocker for 30 minutes. Cells were then added to surfaces for imaging.

*YAP/DAPI:* Cells were cultured on surfaces at 37 °C for either 1 or 3 hours. Surfaces were then washed with 1X PBS and the cells were fixed with 4% PFA in 1X PBS at room temperature for 10 min. Following 3 washes in 1X PBS, cells were permeabilized with 0.1% Triton X-100 in 1X PBS for 4 min. Surfaces were blocked in 2% BSA in 1X PBS overnight at 4 °C. After 1 wash with 1X PBS, surfaces were incubated with 300 µL 1:1000 dilution of YAP 1° antibody (Abcam, ab56701 Anti-YAP1 antibody [2F12] IgG2a) for 75 min. Surfaces were washed with 3 washes 1X PBS and placed in a fourth wash on a rocker for 15 min. Surfaces were then incubated in 300 µL

1:500 dilution YAP 2° antibody (Abcam, ab150115 Goat anti-Mouse IgG H&L, Alexa Fluor 647) + 2 drops/mL DAPI for 1 hour. Surfaces were washed 3 times with 1X PBS before imaging.

*Fibronectin<sub>cell</sub>*: Cells were cultured on surfaces at 37 °C for either 1 or 3 hours. Surfaces were then washed with 1X PBS and the cells were fixed with 4% PFA in 1X PBS at room temperature for 10 min. Surfaces were blocked in 2% BSA in 1X PBS overnight at 4 °C. After 1 wash with 1X PBS, surfaces were incubated with 300 µL 1:200 dilution of fibronectin 1° antibody (Abcam, ab2413, Anti-Fibronectin antibody) for 1 hour. Surfaces were washed with 3 washes 1X PBS and placed in a fourth wash on a rocker for 30 min. Surfaces were then incubated in 300 µL 1:500 dilution 2° antibody (Invitrogen, A21244 Goat anti-rabbit IgG 2°, Alexa Fluor 647) for 40 minutes. Surfaces were washed 3 times with 1X PBS before imaging.

*Fibronectin<sub>soln</sub>*: Cells were incubated on surfaces at 37 °C for 20 minutes before adding ~ 40 µg Alexa 488 labeled fibronectin (prepared by **SI 3.3**). Cells were then incubated for 1 hour at 37 °C prior to imaging.

*Integrins*: Cells for active and total integrin stain were acquired from the same passage of cells. For active integrins, cells were cultured on surfaces (density = 22,500 cells/surface) at 37 °C for 1 hour. Surfaces were then washed with 1X PBS and the cells were fixed with 4% PFA in 1X PBS at room temperature for 10 min. Surfaces were blocked in 2% BSA in 1X PBS overnight at 4 °C. After 1 wash with 1X PBS, surfaces were incubated with 300 µL 1:200 dilution of 1° antibody specific for the active conformation of integrins (Fisher Scientific, BD Biosciences 553715, CD29 Rat anti-Mouse unlabeled, clone: 9EG7) for 1 hour. Surfaces were washed with 3 washes 1X PBS and placed in a fourth wash on a rocker for 30 min. Surfaces were then incubated in 300 µL 1:500 dilution 2° antibody (Abcam, ab150167 Goat anti-Rat IgG 2°, Alexa Fluor 647) for 40 minutes. Surfaces were washed 3 times with 1X PBS before imaging. For total integrins, cells were cultured

on surfaces (density = 22,500 cells/surface) at 37 °C for 1 hour. Cells were scraped off of probe surfaces, fixed, and stained for total integrin number (1:30 BioLegend, APC anti-mouse/rat CD29 Antibody, Clone HM $\beta$ 1-1). Isotype controls were completed with 1:100 dilution of APC Armenian Hamster IgG Isotype Control, Clone HTK888.

#### *A.3.3.10 Platelet handling*

Non-activated platelets were incubated on probe surfaces for 1 hour at room temperature. Platelets were activated with 10  $\mu$ M ADP for 10 minutes at room temperature. The activated platelets were subjected to tension imaging without wash.

#### *A.3.3.11 Cell culture*

MEF-GFP-vin and MEF WT cells were cultured according to American Type Culture Collection (ATCC) guidelines. Briefly, cells were cultured in DMEM supplemented with penicillin/streptomycin and 10% fetal bovine serum (v/v). Cells were passaged every 2–3 days as required.

#### *A.3.3.12 Cell transfection*

MEF WT cells (passage 7) were seeded at a density of  $\sim$ 22,500 cells per well in a commercial 6-well cell culture plate and incubated at 37 °C, 5% CO<sub>2</sub> overnight. Cells were transfected with plasmids for either GFP Paxillin or GFP Integrin  $\beta$ 3 using standard transfection protocol. Briefly, 2  $\mu$ g of plasmid + 2  $\mu$ L jetOptimus reagent was diluted in 200  $\mu$ L jetOptimus buffer and allowed to incubate for 10 minutes at room temperature, forming the transfection mix. Following media replacement, the transfection mix was added to the well and cells were incubated at 37 °C, 5%

CO<sub>2</sub> for 4 hours. Following replacement with fresh media, cells were left overnight prior to imaging.

#### *A.3.2.13 Image Acquisition and Analysis*

Fluorescent images were acquired using TIRF with a 488 laser (focal adhesions, surface-deposited solution fibronectin), DAPI epifluorescence (nucleus), TRITC epifluorescence (tension), Cy5 epifluorescence (YAP, actin stain, fibronectin immunostain, and active integrin  $\beta$ 1). TIRF images were background subtracted by subtracting the fluorescence average of 3 areas of the surface that did not contain cells. Epifluorescence images were locally background subtracted and all analysis was completed in ImageJ.

*Tension image fluorescence:* Average fluorescence is measured by drawing a region of interest (ROI) around the fluorescent signal in the TRITC channel. Cell fluorescence is reported as % probes open which was determined by dividing the average fluorescence in an ROI by the fluorescence of an “open surface” (**Fig. A26**).

*Nuclear to cytoplasmic YAP localization:* DAPI and YAP fluorescent images are acquired at the same z-height. To determine the ratio of nuclear to cytoplasmic YAP, the DAPI fluorescent channel is used to generate a mask of the nucleus that is then applied to the YAP fluorescent channel to measure average fluorescence inside and outside of the nucleus. Total YAP was determined by measuring the YAP present within an ROI surrounding the entire cell, drawn in the RICM channel and then applied to the Cy5 channel.

*Focal Adhesion Analysis:* Focal adhesions were analyzed based on vinculin patterns according to previously published procedures (**Fig. A20**).

*Recovery of Fluorescent Tension Signal:* MEFs were cultured on RS and RU surfaces for 15

minutes prior to imaging at 37 °C. Observable tension signal was bleached for 7 seconds using a 561 laser at 100% power in TIRF excitation mode to reduce phototoxicity. Images were collected prior to bleaching, immediately after bleaching, and in 2 minute intervals up to 10 minutes. Signal recovery was determined by quantifying the fluorescent signal in a given ROI over time. Three ROIs per cell were plotted over time and the average percent recovery was determined for MEFs on RS and RU probes.

*Recovery of Paxillin and Integrin  $\beta$ 3*: MEFs were cultured on RS and RU surfaces for 30 minutes prior to imaging at 37 °C. Observable GFP paxillin or integrin  $\beta$ 3 signal was bleached for 10 seconds. Images were collected prior to bleaching, immediately after bleaching, and in 1 minute intervals up to 10 minutes. Signal recovery was determined by quantifying the fluorescent signal in a given focal adhesion ROI over time. Three ROIs per cell were plotted over time and the average percent recovery was determined for MEFs on RS and RU probes.

### A.3.4 Note 2 – van't Hoff Analysis of RS and RU probes

The simulated thermal melting curve (67 – 100 °C) of the probes was generated by using NUPACK “Compute melt” function. We used the 137 mM for Na<sup>+</sup> for the ionic strength, which is the sodium ion concentration of 1X PBS solution. For the experimental thermal melting curve, 100 μL solutions of RS and RU probes at 10 μM and 100 μM were prepared in 1X PBS in qPCR tubes. The probe solutions were heated to 95 °C for 3 minutes and then cooled at a rate of 1.3 °C min<sup>-1</sup> to 25 °C to hybridize. The solutions were then transferred to the 12 wells of a qPCR plate in 20 μL each for three individual measurements for a condition. Using the qPCR instrument (LightCycler 96), the plate was incubated at 37 °C for 5 min and then heated to 95 °C over 1900 seconds with Cy3B fluorescent measurements.

Because the thermodynamic equilibrium of DNA folded structure is an intramolecular transition, their thermodynamic parameters, including  $\Delta G$ ,  $\Delta H$ , and  $\Delta S$ , are concentration-independent.<sup>(125)</sup> Thus, the probe’s van’t Hoff equation for thermodynamic analysis can be adopted from the definition of Gibbs free energy equation.

$$\Delta G = \Delta H - T\Delta S = RT \ln K_a \quad (\text{eq1})$$

Where  $K_a$  is the equilibrium constant of probe transition, R is gas constant (1.9872 cal/K•mol), and T is the temperature in Kelvin (0 °C = 273.15 K).

As a result of the equation transformation,

$$\ln K_a = \frac{\Delta H}{R} \frac{1}{T} - \frac{\Delta S}{R} \quad (\text{eq 2})$$

The hairpin transition is between the fold and unfold states so that  $K_a$  could be expressed as follows.

$$K_a = \frac{[\text{unfold}]}{[\text{fold}]} \text{ (eq 3)}$$

Where [fold] and [unfold] is the concentration of each species.

Because the total concentration of both species is always same, the concentration of fold state can be expressed as follows.

$$c = [\text{unfold}] + [\text{fold}], \quad [\text{fold}] = c - [\text{unfold}] \text{ (eq 4)}$$

Where  $c$  is the total concentration of DNA probes.

Thus, the equation 3 can be transformed as:

$$K_a = \frac{[\text{unfold}]}{c - [\text{unfold}]} \text{ (eq 5)}$$

To estimate the concentration of unfold state, we used the fluorescence intensity at each temperature. Since the probe structures contain the Cy3B fluorophore and BHQ2 quencher, and fluorophore/quencher pairs locate close together when the DNA structures are folded. In contrast, fluorophore/quencher pairs are separated when they are unfolded. This structural change leads to the activation of fluorescence signal when they are in unfolded state. Thus, the concentration of unfolded species can be estimated by Cy3B fluorescence intensity and the total concentration of the DNA probe.

$$[\text{unfold}] = \frac{(F - F_{\min})}{(F_{\max} - F_{\min})} \times c \text{ (eq 6)}$$

Where the  $F$  is the Cy3B fluorescence intensity at each temperature,  $F_{\min}$  is the minimum Cy3B fluorescence intensity during the measurement, and  $F_{\max}$  is the maximum Cy3B fluorescence intensity during the measurement. Thus, the equilibrium constant ( $K_a$ ) can be expressed using Cy3B fluorescence intensity.

$$K_a = \frac{\frac{F - F_{\min}}{F_{\max} - F_{\min}} \times c}{c - \frac{F - F_{\min}}{F_{\max} - F_{\min}} \times c} = \frac{\frac{F - F_{\min}}{F_{\max} - F_{\min}}}{1 - \frac{F - F_{\min}}{F_{\max} - F_{\min}}} = \frac{F - F_{\min}}{F_{\max} - F} \quad (\text{eq7})$$

Based on the **EQ. 2** and **7**, we made the van't Hoff plot as the function of the  $\ln K_a$  and  $1/T$ , and determined the thermodynamic parameters of reversible probes. Note that we used  $15 < [\text{unfolded}] \% < 85$  to generate initial van't Hoff plot to reduce the contribution of experimental error.

As we mentioned above, the intramolecular interactions are theoretically concentration-independent; however, the thermal melting analysis of our RU and RS probes showed concentration-dependent behavior as indicated in the yellow circle (●, **Fig. A18**). We expected that those behaviors are the bi- or multi-molecular interaction of our reversible probes, most likely due to their long sequences (21 base pairing for the folded structure). Therefore, when we calculated the probes' thermodynamic parameters, including  $\Delta G$ ,  $\Delta H$ , and  $\Delta S$ , the parameters were concentration-dependent (**Table A4 and A5**). To exclude the bi- or multi-molecular contribution, we specifically used the  $50 < [\text{unfolded}] \% < 85$  to calculate thermodynamic parameters. This procedure provided the concentration-independent thermodynamic parameters. It should be noted that the difference between experimental values and NUPACK simulation is most likely due to the interaction between cRGD/Cy3B and BHQ2/tetrazine because it is known that introduction of fluorophore/quencher pair tends to result in the stabilization of the folded structure.(156)

### A.3.5 Note 3 - oxDNA simulation

RU and RS probes, polyT<sub>72</sub> chain, the DNA hairpin shearing probe,(37) irreversible unzipping of DNA duplex, and irreversible shearing of DNA duplex were modelled in oxDNA by adding harmonic traps to two terminal nucleotides of a DNA stand. The shearing of RS probe was modelled in oxDNA by adding harmonic traps to two terminal nucleotides of a DNA stand with the mutual trap at the 3'-3' linkage to mimic the covalent conjugation.

Harmonic traps were assigned a stiffness of 11.42 pN/nm each and one of the traps was moved at a given rate with respect to the other fixed trap. The effective stiffness constant of the two traps in series can be calculated using:

$$\frac{1}{k_{eff}} = \frac{1}{k_1} + \frac{1}{k_2} \quad (\text{eq 8})$$

where  $k_1$  and  $k_2$  are the stiffness constants of the two traps and  $k_{eff}$  is the effective stiffness constant. The  $k_{eff}$  of the system is calculated to be 5.71 pN/nm and the force is calculated by multiplying  $k_{eff}$  with the projected net displacement along the force axis. Net displacement is defined as the sum of displacements of the two terminal nucleotides from the respective trap centers. This force is plotted against the net displacement of the two nucleotides from their harmonic traps along with an exponential moving average (EMA) of the data points. The force tolerance  $F_{tol}$  is defined here as the force at which the total number of hydrogen bonds becomes zero and estimated using a peak finding SciPy algorithm on the force displacement curve.(157-160) This approach yields a force of 14 pN and 59 pN on the DNA unfolding for reversible unzipping and shearing probes, respectively, for a loading rate of  $5.62 \times 10^3$  nm. Also, for the DNA hairpin shearing probe, the quencher strand peeling and the hairpin shearing were happened at 50 pN and 55 pN, respectively, for a loading rate of  $5.62 \times 10^3$  nm.

Parameters were adopted from published literature and examples available at [dna.physics.ox.ac.uk](http://dna.physics.ox.ac.uk) website.(161)

oxDNA simulation parameters (comments are after #):

sim\_type = MD

T = 37C

steps = 5e9 #data extracted from simulation every 1e4 steps.

time\_scale = linear

interaction\_type = DNA2

use\_average\_seq = 1

verlet\_skin = 0.05

salt\_concentration = 0.156 # [Na+] in molar.

thermostat = john

newtonian\_steps = 103

diff\_coeff = 2.5

dt = 0.005

oxDNA trap forces were applied to two nucleotides 0 and 23 on the same DNA strand as described

for reversible unzipping probe,

particle = 0 (stiff = 0.2, rate = 0.2e-7, dir = 0, 0, -1) #rate is (length extension)/(simulation time step)

particle = 71 (stiff = 0.2, rate = 0.0, dir = 0, 0, 0)

for DNA hairpin shearing probe,

particle = 0 (stiff = 0.2, rate = 0.2e-7, dir = 0, 0, -1)

particle = 53 (stiff = 0.2, rate = 0.0, dir = 0, 0, 0)

for DNA pseudo-knot shearing probe,

particle = 20 (stiff = 0.2, rate = 0.2e-7, dir = 0, 0, -1)

particle = 71 (stiff = 0.2, rate = 0.0, dir = 0, 0, 0)

For DNA pseudo-knot shearing probe, we introduced the mutual trap to mimic the covalent bond as described

particle = 0, ref\_particle = 21 (stiff = 3., r0 = 1.2)

particle = 21, ref\_particle = 0 (stiff = 3., r0 = 1.2)

Directions are formatted as x, y, z. All values are in oxDNA units unless specified and the conversion factors for oxDNA units are:

1 unit of length = 0.8518 nm

1 unit of force = 48.63 pN

1 unit of time = 3.03 ps

1 unit of force constant = 57.09 pN/nm

## A.3.6 Figures, tables, and schemes

Name	Sequence (5' to 3')
Shearing Top	/5Hexynyl/ CAC AGC ACG GAG GCA CGA CAC TTT /3AmMO/
Shearing Bottom	/5Hexynyl/ TTT GTG TCG TGC CTC CGT GCT GTG /iUniAmM//3BHQ_2/
Shearing Complimentary	AAA GTG TCG TGC CTC CGT GCT GTG
Unzipping	/5Hexynyl/ <u>CAC AGC ACG GAG GCA CGA CAC</u> TTT <u>GTG TCG TGC CTC CGT GCT GTG</u> /3AmMO/
Unzipping Complimentary	<u>CAC AGC ACG GAG GCA CGA CAC</u> AAA <u>AAA AAA GTG TCG TGC CTC CGT GCT GTG</u>
56 pN TGT top	CAC AGC ACG GAG GCA CGA CAC /i5OctdU//3BHQ_2
56 pN TGT bottom	/5AmMC6/GTG TCG TGC CTC CGT GCT GTG /35OctdU/

iUniAmM = amine linked internally within DNA sequence. 5Hexynyl = 5' terminal alkyne. 3AmMO = 3' terminal amine. 3BHQ\_2 = BHQ2 ligated to 3' terminus. i5OctdU = alkyne linked internally within the DNA sequence. 5AmMC6 = 5' terminal amine. 35OctdU = 3' terminal alkyne

Table A3. Oligonucleotides used in Chapter 4.

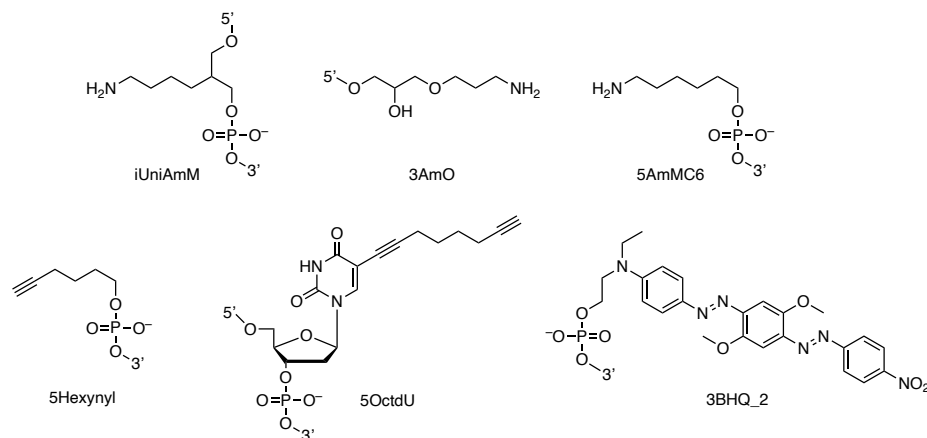
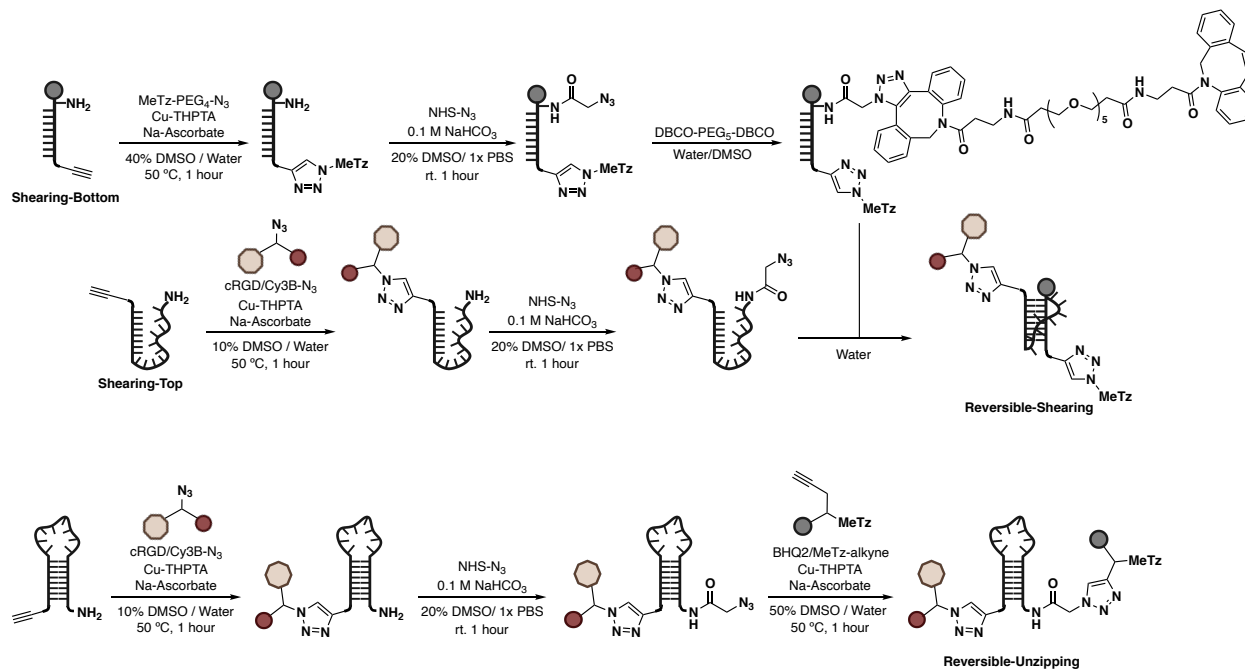
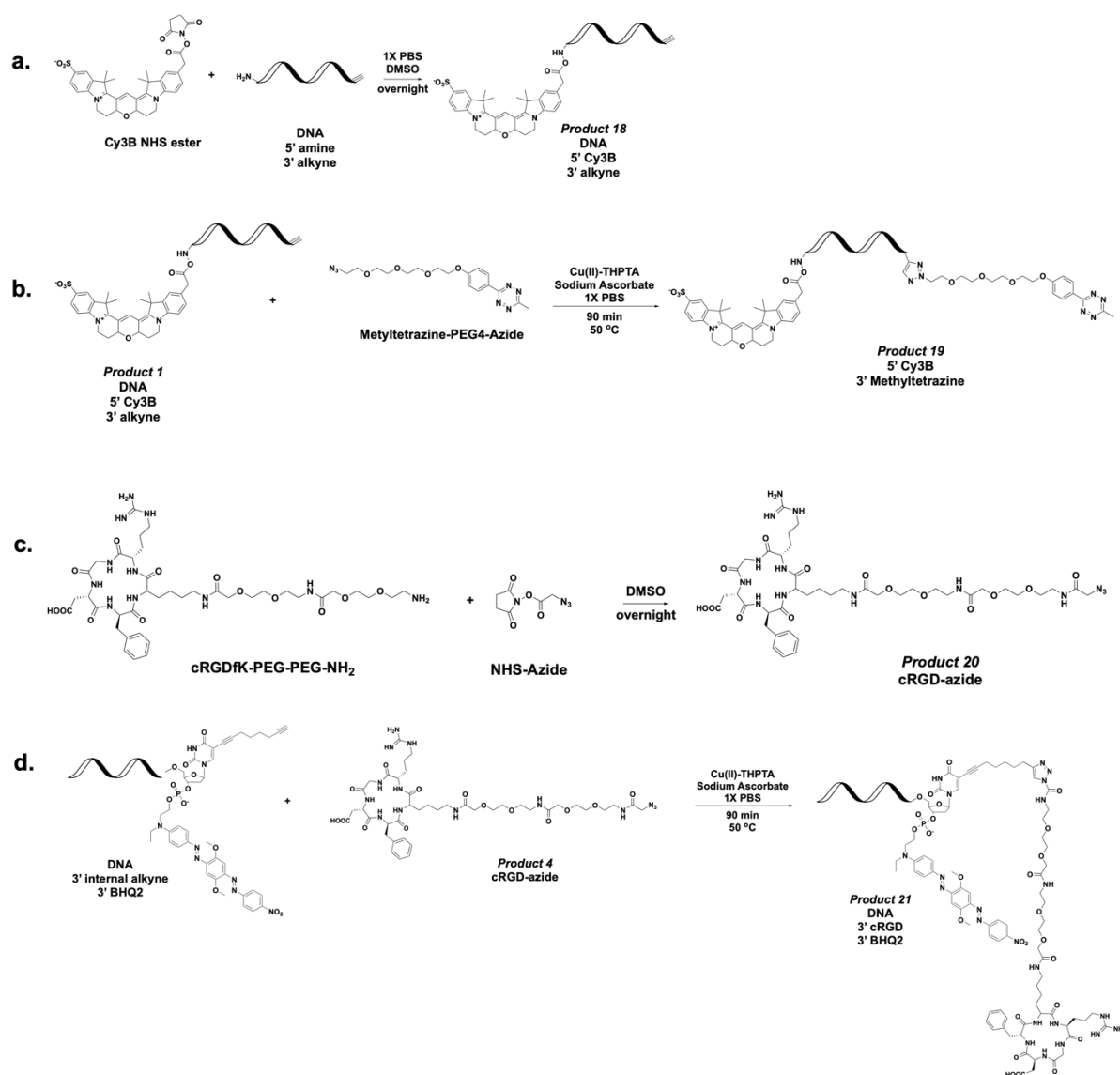


Figure A15. Chemical structures of oligo modifications used in Chapter 4.



**Scheme A1. Synthetic scheme to generate reversible shearing and unzipping probes.**



**Scheme A2. Synthesis of irreversible DNA probes.** **a.** Schematic showing coupling of Cy3B-NHS to DNA to generate **Product 18**. **b.** Schematic showing alkyne-azide cycloaddition reaction to conjugate tetrazine to Product 18, generating **Product 19**. **c.** Schematic showing the coupling between NHS-N<sub>3</sub> and cRGD-PEG-PEG-NH<sub>2</sub> to form cRGD-PEG-PEG-N<sub>3</sub> (**Product 20**). **d.** Schematic showing alkyne-azide cycloaddition to conjugate product 4 to BHQ2 labeled DNA, generating **Product 21**.

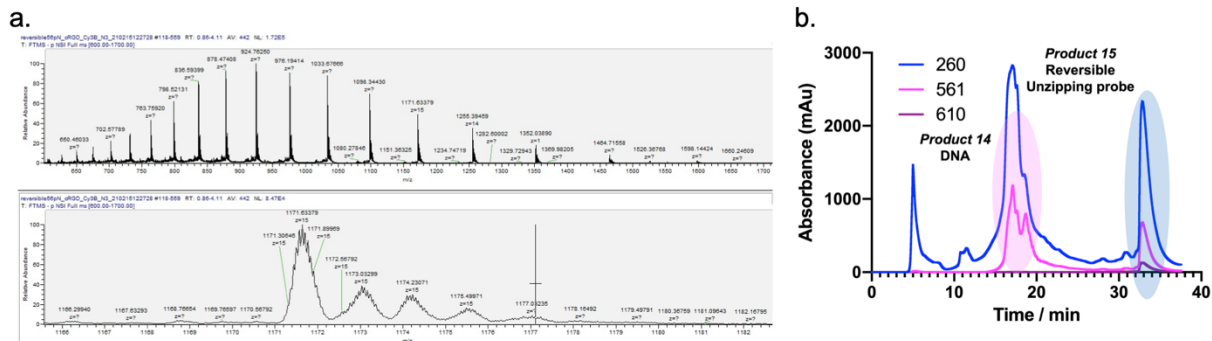


**Figure A16. Characterization of Chapter 4 product 15. a.** ESI MS spectra **b.** HPLC trace of product 15 (RU probe)

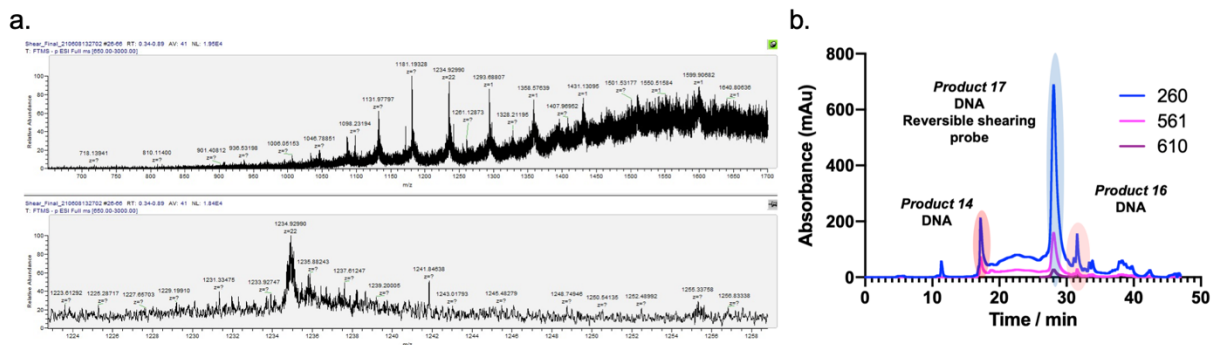


**Figure A17. Characterization of Chapter 4 product 17 a.** ESI MS spectra **b.** HPLC trace of product 17 (RS probe)

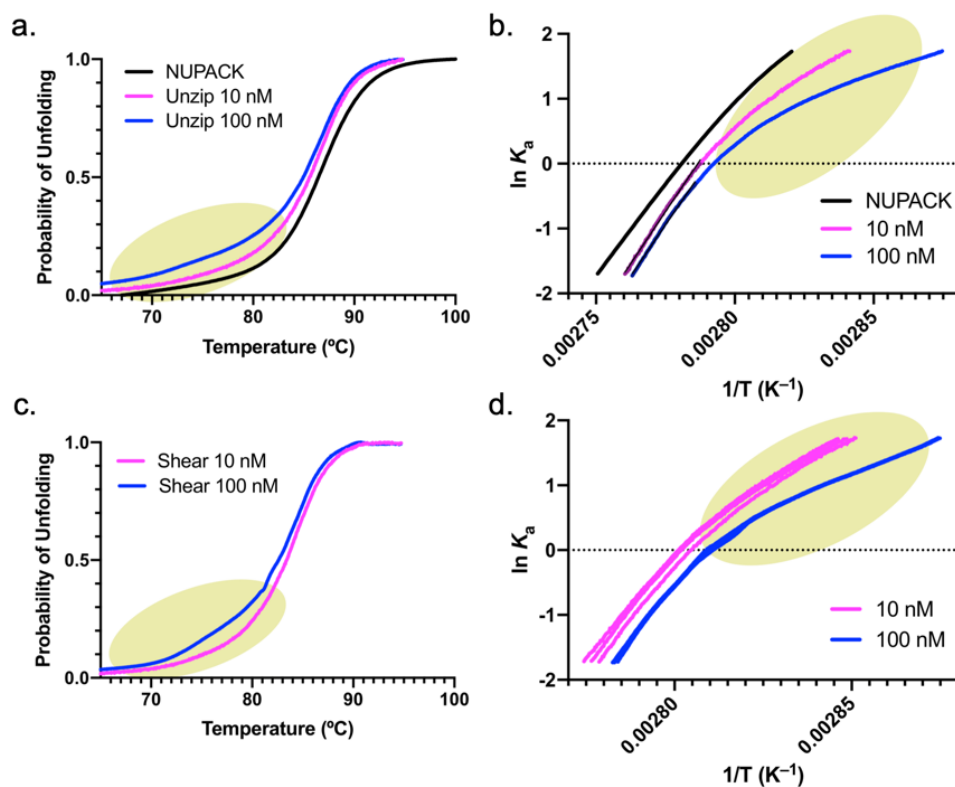


**Figure A18. DNA Thermal melting analysis reveals that RS and RU have identical  $\Delta G$  at 37 °C.** Temperature dependent DNA unfolding analysis adapted from fluorescent melting curve for RS probe (a) and RU probe (b) in 1X PBS solution. The van't Hoff plot of RS probe (c) and RU (d) probe generated from (a) and (b). Blue and magenta lines represent the probe concentration of 100 and 10 nM, respectively. The black lines were obtained by NUPACK simulation. Yellow circle (●) indicate the concentration dependent region.

	Simulated	RS probe			
	NUPACK	10 nM	10 nM limited	100 nM	100 nM limited
$T_m$ (°C)	86.3	$83.2 \pm 0.2$	$83.7 \pm 0.2$	$82.0 \pm 0.1$	$83.0 \pm 0.1$
$\Delta G_{37^\circ\text{C}}$ (kcal mol <sup>-1</sup> )	-13.6	$-12.1 \pm 0.2$	$-17.2 \pm 0.4$	$-8.66 \pm 0.32$	$-17.4 \pm 0.2$
$\Delta H$ (kcal mol <sup>-1</sup> )	-99.3	$-93.5 \pm 1.2$	$-132 \pm 3$	$-68.4 \pm 0.2$	$-134 \pm 2$
$\Delta S$ (cal K <sup>-1</sup> mol <sup>-1</sup> )	-276.2	$-262 \pm 3$	$-369 \pm 9$	$-193 \pm 1$	$-378 \pm 5$

**Table A4. Thermodynamic parameters of RS probes at indicated concentrations in 1X PBS.** The yellow highlights were calculated using concentration independent regions.

	Simulated	RU probe			
	NUPACK	10 nM	10 nM limited	100 nM	100 nM limited
$T_m$ (°C) <sup>a</sup>	86.3	85.3 ± 0.2	86.0 ± 0.2	84.1 ± 0.1	85.2 ± 0.1
$\Delta G_{37^\circ\text{C}}$ (kcal mol <sup>-1</sup> )	-13.6	-11.5 ± 0.3	-17.3 ± 0.6	-7.38 ± 0.1	-16.6 ± 0.3
$\Delta H$ (kcal mol <sup>-1</sup> )	-99.3	-85.1 ± 2.1	-126 ± 4	-56.0 ± 0.2	-123 ± 2
$\Delta S$ (cal K <sup>-1</sup> mol <sup>-1</sup> )	-276.2	-237 ± 6	-353 ± 12	-157 ± 1	-344 ± 6

**Table A5. Thermodynamic parameters of RU probes at indicated concentrations in 1X PBS.** The yellow highlights were calculated using concentration independent regions.

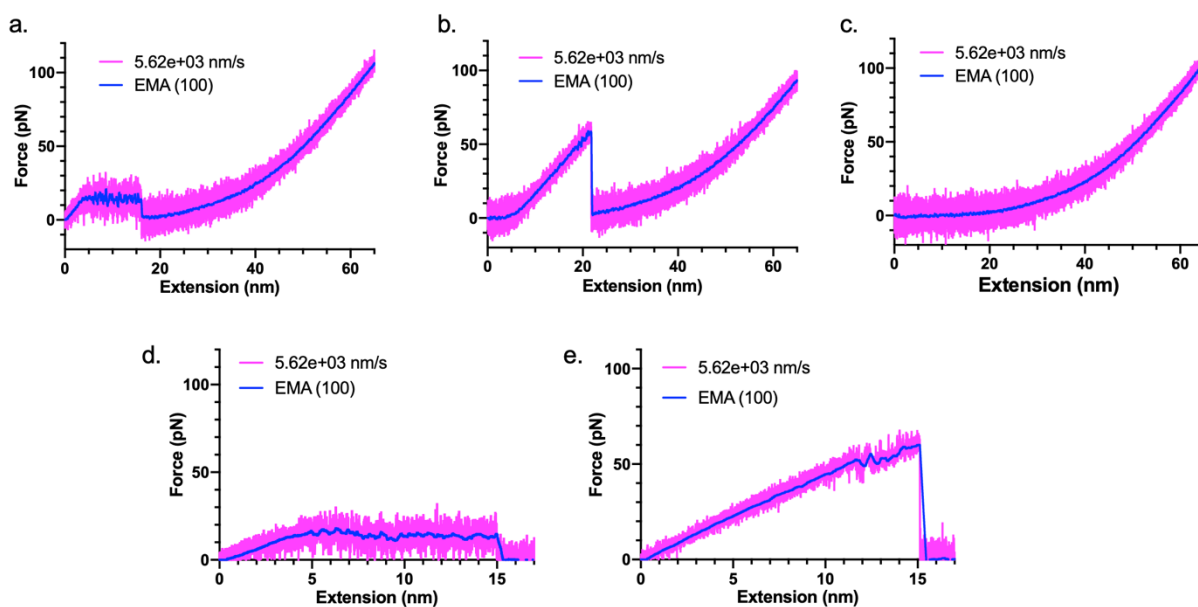


**Figure A19. Force extension curves simulated by oxDNA software. a. RU probe, b. RS probe, c. polyT<sub>72</sub> oligo nucleotides, d. irreversible unzipping of DNA duplex, e. irreversible shearing of DNA duplex using  $5.62 \times 10^3$  nm/s as a loading rate.**

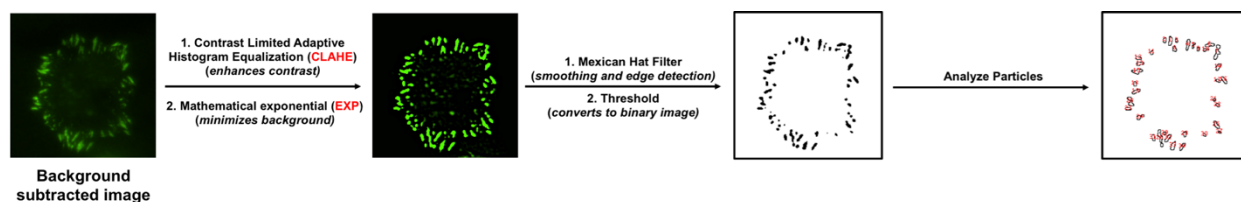


**Figure A20. Procedure for vinculin analysis using ImageJ.** Focal adhesions were analyzed based on vinculin patterns according to previously published procedures.(1) Briefly, vinculin images were acquired in TIRF with a 488 laser and background subtracted by subtracting the fluorescence average of 3 areas of the surface that did not contain cells. The local contrast of the image was increased by running CLAHE (Contrast Limited Adaptive Histogram Equalization) with the following values: block size = 19, histogram bins = 256 , maximum slope = 6, no mask and fast. Background was further minimized by applying the mathematical exponential (EXP). Smoothing and edge detection was done using the Mexican Hat filter with a radius of 5 before auto-thresholding the image with a dark background and converting to a mask. Vinculin was then quantified using the Analyze Particles command with the following values: size = 0.1 – infinity, circularity = 0.00 – 0.99, show = outlines, display “summarize”.

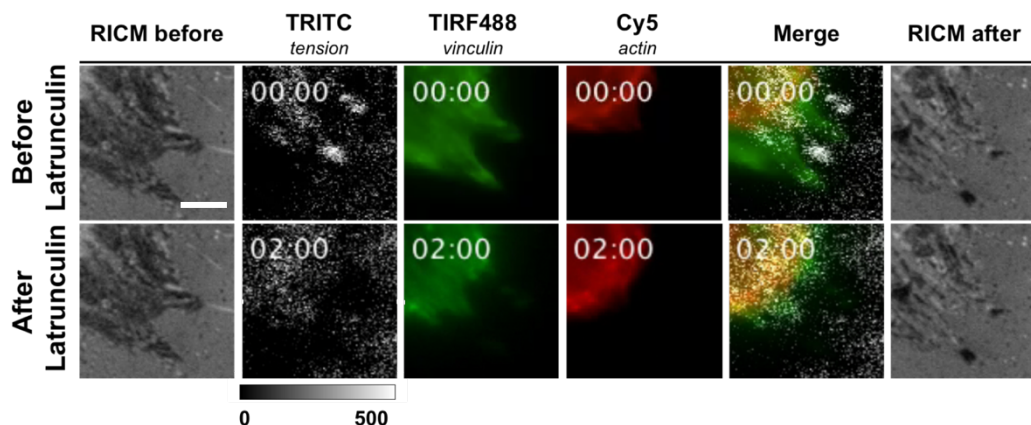


**Figure A21. Reversible probes report on real-time tension signal.** RICM, tension signal, vinculin-GFP, and F-actin images (SiR-actin) of MEF cells plated on IS probes before (top) and after (bottom) Latrunculin B (10  $\mu$ M) treatment. Treatment with Latrunculin B, a disruptor of actin polymerization, causes retraction of the cell cytoskeleton and a resulting loss of observable tension signal. Scale bar, 2  $\mu$ m.

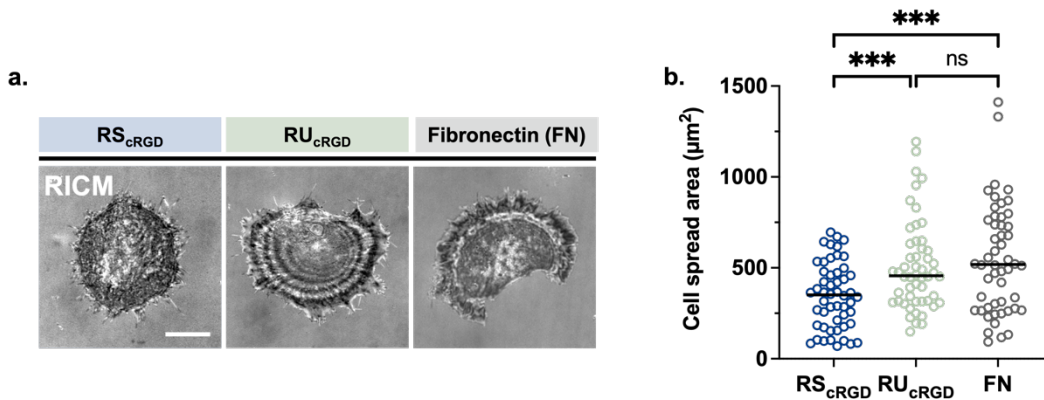


**Figure A22. Culturing cells on tension probes does not alter cell biology.** **a.** RICM of MEF cells plated on RS<sub>cRGD</sub>, RU<sub>cRGD</sub>, and fibronectin coated surfaces. **b.** Spread area of MEFs cultured on RS<sub>cRGD</sub>, RU<sub>cRGD</sub>, and FN coated surfaces. Spread area was measured by drawing a region of interest around MEFs in the RICM channel. Scale bar, 5 μm.

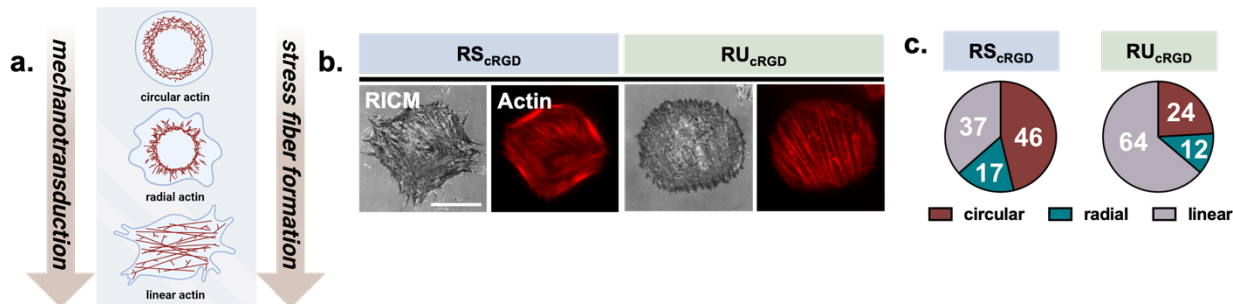


**Figure A23. Stress fiber formation is higher in MEFs plated on RU<sub>cRGD</sub> probes.** **a.** As cell mechanotransduction increases, stress fibers transition from circular to linear patterns. **b.** Stress fiber formation in MEFs. Cells were plated on RS<sub>cRGD</sub> and RU<sub>cRGD</sub> probes for one hour. Actin was stained using SiR-actin 647 and imaged using epifluorescence. **c.** Distribution of actin patterns in MEFs on RS<sub>cRGD</sub> and RU<sub>cRGD</sub> probes. Scale bar, 5 μm.

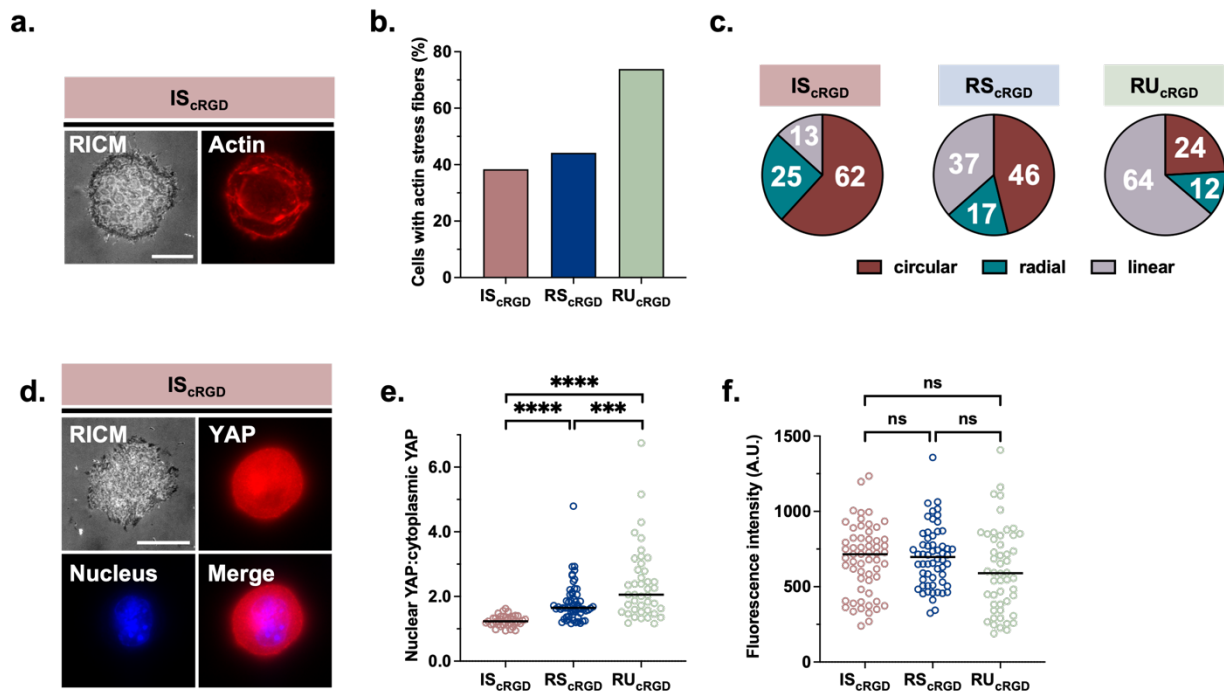


**Figure A24. MEFs plated on irreversible shearing cRGD (IS<sub>cRGD</sub>) probes have lower markers of mechanotransduction than MEFs plated on RS and RU probes.** **a.** RICM and F-actin images (SiR-actin) of MEF cells plated on IS<sub>cRGD</sub> probes for 1 hour. **b.** Plot of % cells displaying actin stress fibers on IS<sub>cRGD</sub>, RS<sub>cRGD</sub>, and RU<sub>cRGD</sub> probes. (n = 3 experiments, IS<sub>cRGD</sub> = 65 cells, RS<sub>cRGD</sub> = 53 cells, RU<sub>cRGD</sub> = 46 cells) **c.** Distribution of actin patterns in MEFs on IS<sub>cRGD</sub>, RS<sub>cRGD</sub>, and RU<sub>cRGD</sub> probes. (n = 3 experiments, IS<sub>cRGD</sub> = 76 cells, RS<sub>cRGD</sub> = 52 cells, RU = 58 cells) **d.** RICM, YAP, and nuclear staining (DAPI) images for MEFs cultured on IS<sub>cRGD</sub> probes for 1 hour. **e.** Plot of nuclear YAP:cytoplasmic YAP in MEFs plated on IS<sub>cRGD</sub>, RS<sub>cRGD</sub>, and RU<sub>cRGD</sub> probes at 1 hour. Cells cultured on IS<sub>cRGD</sub> probes had a significantly lower amount of YAP localized to their nucleus than cells plated on RS<sub>cRGD</sub> and RU<sub>cRGD</sub> probes. (n = 3 experiments, IS<sub>cRGD</sub> = 40 cells, RS<sub>cRGD</sub> = 59 cells, RU<sub>cRGD</sub> = 42 cells, IS<sub>cRGD</sub>: RS<sub>cRGD</sub> p = 0.0025, IS<sub>cRGD</sub>: RU<sub>cRGD</sub> p < 0.0001, RS<sub>cRGD</sub>: RU<sub>cRGD</sub> p = 0.0036) **f.** Plot of total YAP signal in MEF cells cultured on IS<sub>cRGD</sub>, RS<sub>cRGD</sub>, and RU<sub>cRGD</sub> probes for 1 hour. There was no significant difference in total YAP amount after 1 hour. (n = 3 experiments, IS<sub>cRGD</sub> = 40 cells, RS<sub>cRGD</sub> = 46 cells, RU<sub>cRGD</sub> = 25 cells, IS<sub>cRGD</sub>: RS<sub>cRGD</sub> p = 0.7222, IS<sub>cRGD</sub>: RU<sub>cRGD</sub>, p = 0.2063, RS<sub>cRGD</sub>: RU<sub>cRGD</sub>, p = 0.0551), Scale bars, 5  $\mu$ m.

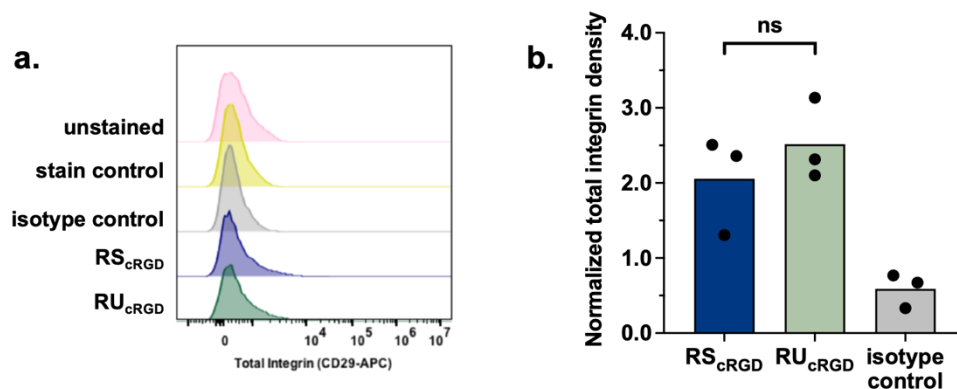


**Figure A25. Total integrin  $\beta 1$  levels are the same in cells plated on  $RS_{cRGD}$  and  $RU_{cRGD}$  probes.**

**a.** Representative flow plots of cells plated on  $RS_{cRGD}$  and  $RU_{cRGD}$  probes for 1 hour and immunostained for total integrin  $\beta 1$ . “Unstained” represents a control population of unstained cells, “stain control” represents a population of cells that were not plated on a surface but were stained with the CD29  $\beta 1$  antibody. **b.** Plot of normalized total integrin density in cells plated on  $RS_{cRGD}$  and  $RU_{cRGD}$   $RU$  probes and the isotype control (grey) from (a). There was not a significant difference in total integrin presentation in cells plated on  $RS_{cRGD}$  and  $RU_{cRGD}$  probes. Values were normalized to the stain control. ( $n = 3$  experiments, 10,000 cells,  $p = 0.4032$ )

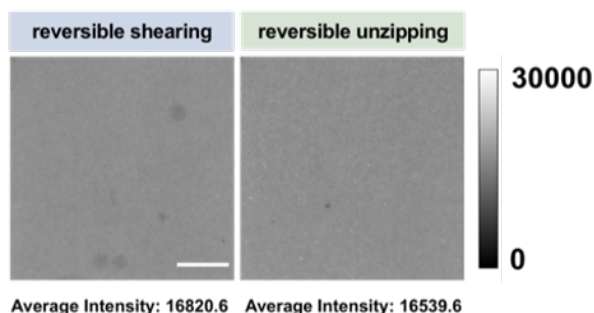


**Figure A26.  $RS_{cRGD}$  and  $RU_{cRGD}$  probe density on glass surface.** Surface density of probes was determined by measuring the value of an unquenched surface. Average intensity is the average of 10 regions of 3 surfaces for a total of 30 regions per probe type.

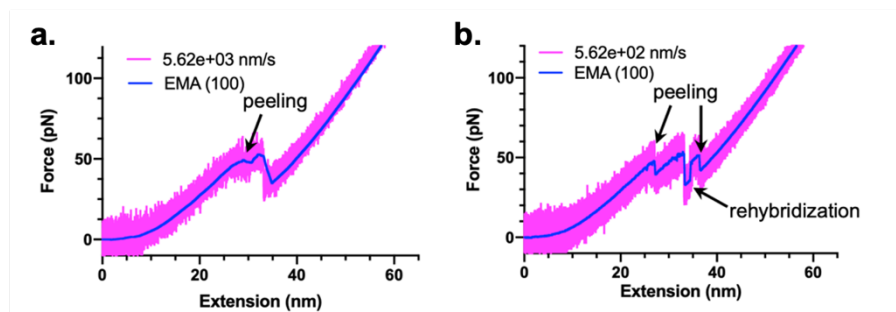


**Figure A27. Force extension curves of previously published work simulated by oxDNA software.** A reversible shearing probe reported by Zhang et al. using  $5.62 \times 10^3$  and  $5.62 \times 10^2$  nm/s as a loading, respectively. The magenta and blue lines represent the simulated spectra and exponential moving average (100) of simulated spectra, respectively.(37) The arrows shown in the (a) and (b) indicate the peeling of quencher strand, which undergo prior to the probe shearing events.

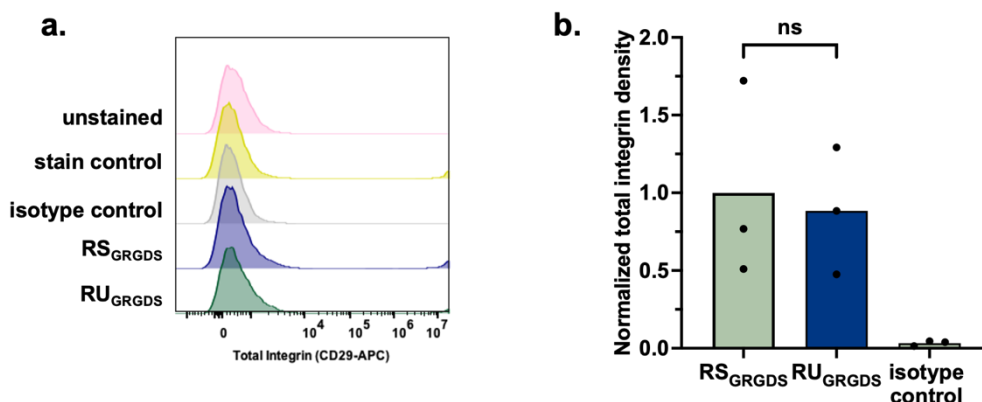


**Figure A28. Total integrin  $\beta 1$  levels are the same in cells plated on  $RS_{GRGDS}$  and  $RU_{GRGDS}$  probes.** **a.** Representative flow plots of cells plated on  $RS_{GRGDS}$  and  $RU_{GRGDS}$  probes for 1 hour and immunostained for total integrin  $\beta 1$ . “Unstained” represents a control population of unstained cells, “stain control” represents a population of cells that were not plated on a surface but were stained with the CD29  $\beta 1$  antibody. **b.** Plot of normalized total integrin density in cells plated on  $RS_{GRGDS}$  and  $RU_{GRGDS}$  probes and the isotype control (grey) from (a). There was not a significant difference in total integrin presentation in cells plated on  $RS_{GRGDS}$  and  $RU_{GRGDS}$  probes. Values were normalized to the stain control. ( $n = 3$  experiments, 10,000 cells,  $p = 0.8042$ )

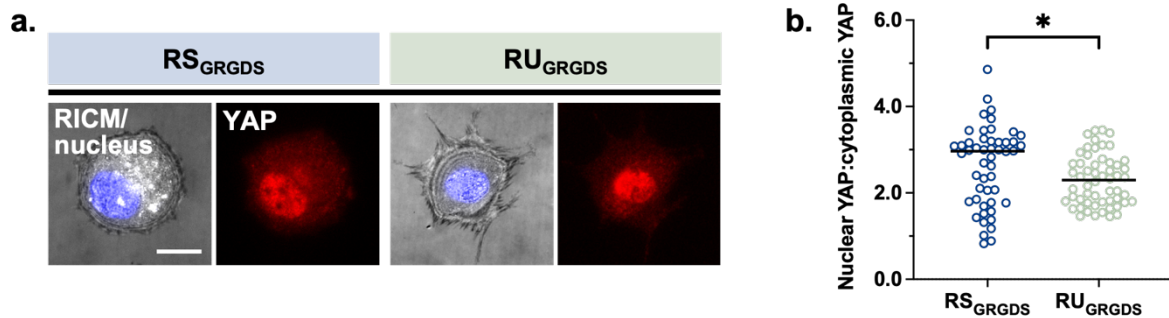


**Figure A29.** MEFs plated on  $RS_{GRGDS}$  probes have higher nuclear:cytoplasmic YAP translocation than MEFs plated on  $RU_{GRGDS}$  probes. **a.** RICM, YAP, and nuclear staining (DAPI) images for MEFs cultured on  $RS_{GRGDS}$  and  $RU_{GRGDS}$  probes for 1 hour. **b.** Plot of nuclear YAP:cytoplasmic YAP in MEFs plated on  $RS_{GRGDS}$  and  $RU_{GRGDS}$  probes for 1 hour. MEFs cultured on  $RS_{GRGDS}$  probes had slightly increased nuclear YAP localization than MEFs cultured on  $RU_{GRGDS}$  probes. ( $n = 3$  experiments,  $RS_{GRGDS} = 50$  cells  $RU_{GRGDS} = 56$  cells,  $p = 0.0302$ ,

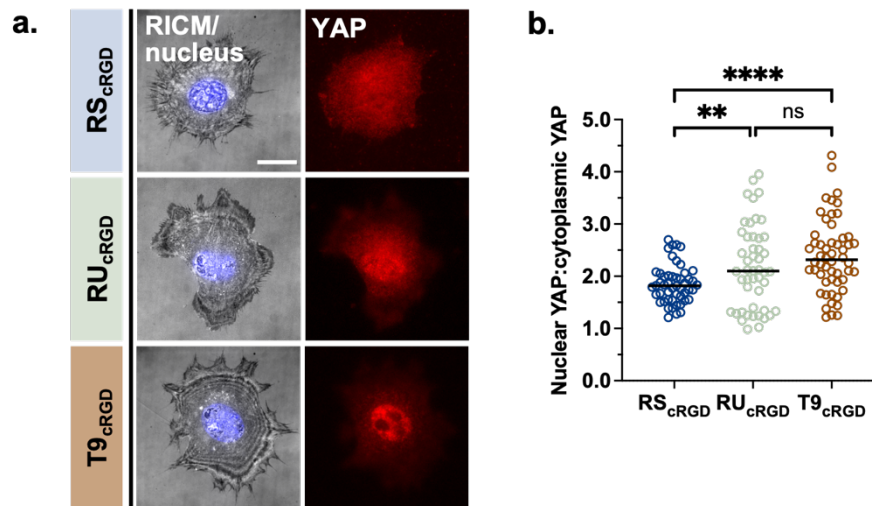


**Figure A30.** MEFs plated on  $T9_{cRGD}$  probes have higher nuclear:cytoplasmic YAP translocation than MEFs plated on  $RS_{cRGD}$  probes. **a.** RICM, YAP, and nuclear staining (DAPI) images for MEFs cultured on  $RS_{cRGD}$  and  $RU_{cRGD}$  and  $T9_{cRGD}$  probes for 1 hour. **b.** Plot of nuclear YAP:cytoplasmic YAP in MEFs plated on  $RS_{cRGD}$  and  $RU_{cRGD}$  and  $T9_{cRGD}$  probes for 1 hour. MEFs cultured on  $T9_{cRGD}$  probes had significantly higher nuclear YAP localization than MEFs cultured on  $RS_{cRGD}$  probes and similar levels of nuclear YAP localization to MEFs cultured on  $RU_{cRGD}$  probes. ( $n = 3$  experiments,  $RS_{cRGD} = 50$  cells  $RU_{cRGD} = 48$  cells,  $T9_{cRGD} = 54$  cells,  $RS_{cRGD}:RU_{cRGD}$   $p = 0.0060$ ,  $RS_{cRGD}:T9_{cRGD}$   $p < 0.0001$ ,  $RU_{cRGD}:T9_{cRGD}$   $p = 0.2294$ , scale bar, 5  $\mu$ m

A.3.19 ESI MS spectra, HPLC traces, and <sup>1</sup>H NMR spectra of the synthesized materials.

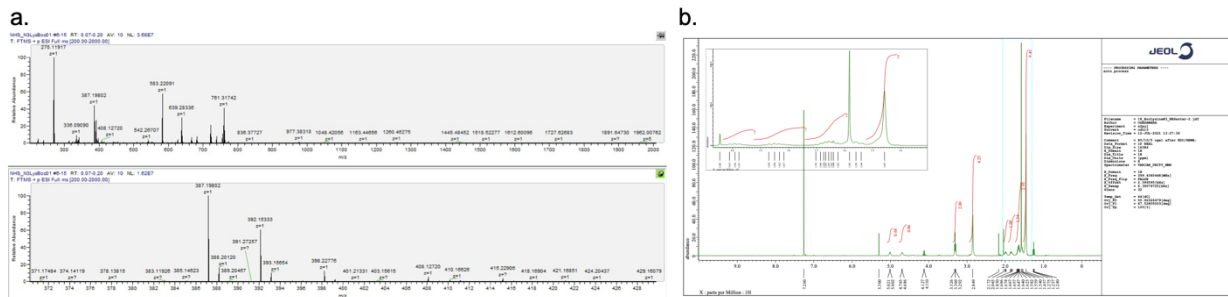


**Figure A31. Characterization of Chapter 4 product 1 a: ESI MS spectra b. <sup>1</sup>H NMR spectra of product 1. <sup>1</sup>H NMR spectra were acquired in CDCl<sub>3</sub> using NMR spectrometer (400 MHz, Varian).**

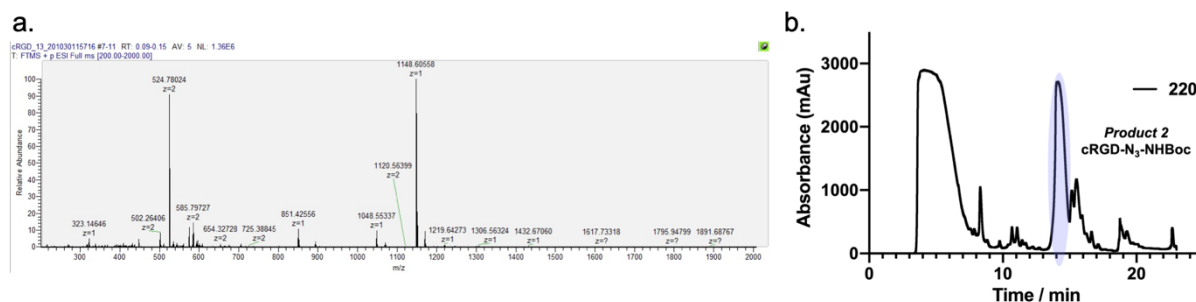


**Figure A32. Characterization of Chapter 4 product 2 a: ESI MS spectra b. HPLC trace of product 2**



**Figure A33. Characterization of Chapter 4 product 3 a. ESI MS spectra b. HPLC trace of product 3**



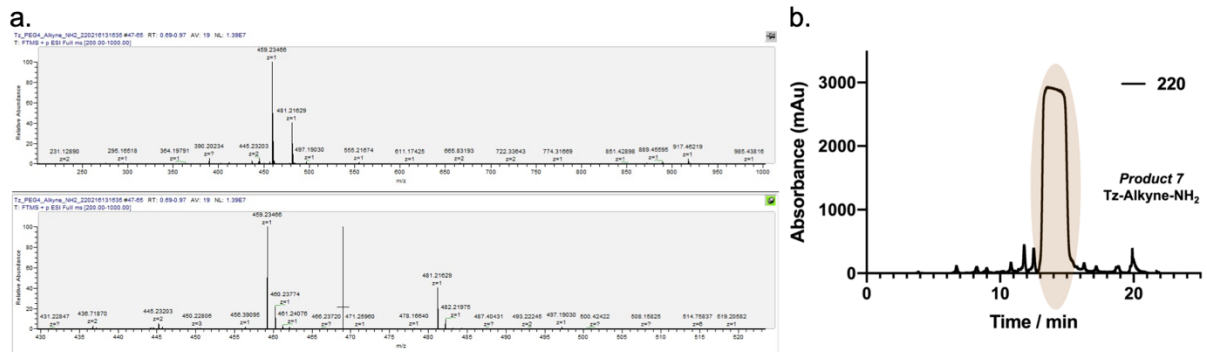


Figure A37. Characterization of Chapter 4 product 7 a. ESI MS spectra b. HPLC trace of product 7

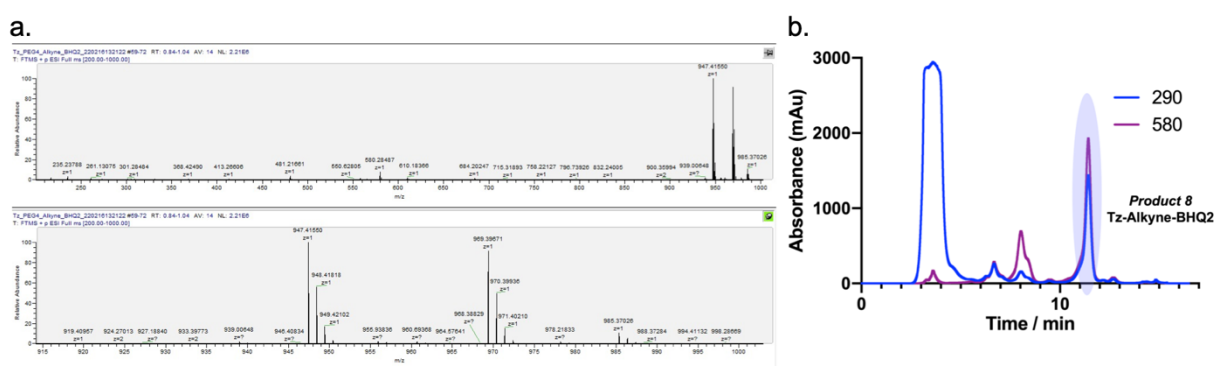


Figure A38. Characterization of Chapter 4 product 8. a. ESI MS spectra b. HPLC trace of product 8

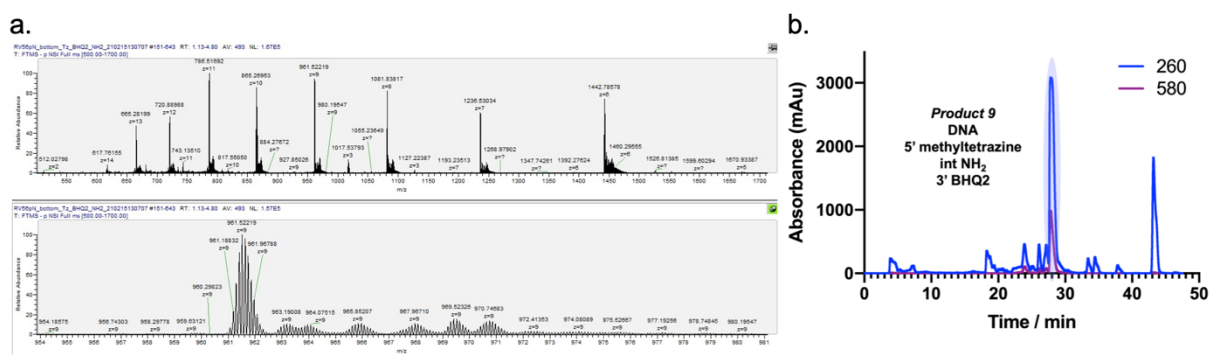


Figure A39. Characterization of Chapter 4 product 9. a. ESI MS spectra b. HPLC trace of product 9

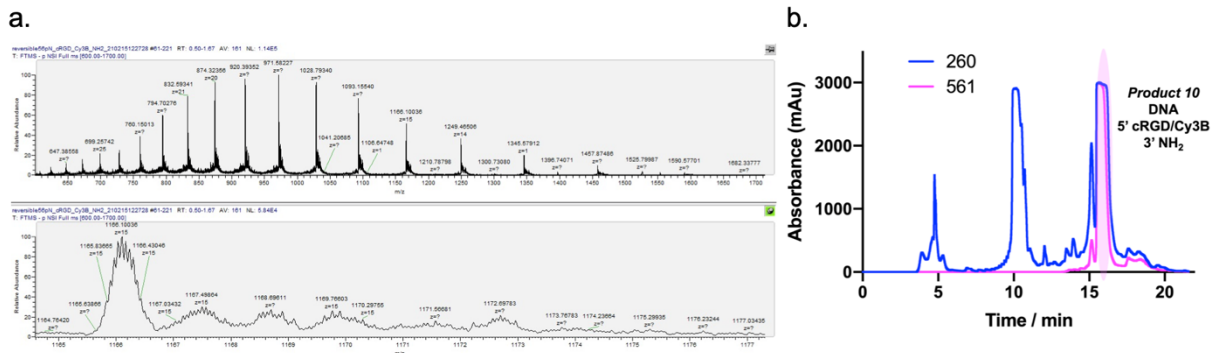


Figure A40. Characterization of Chapter 4 product 10. a. ESI MS spectra b. HPLC trace of product 10

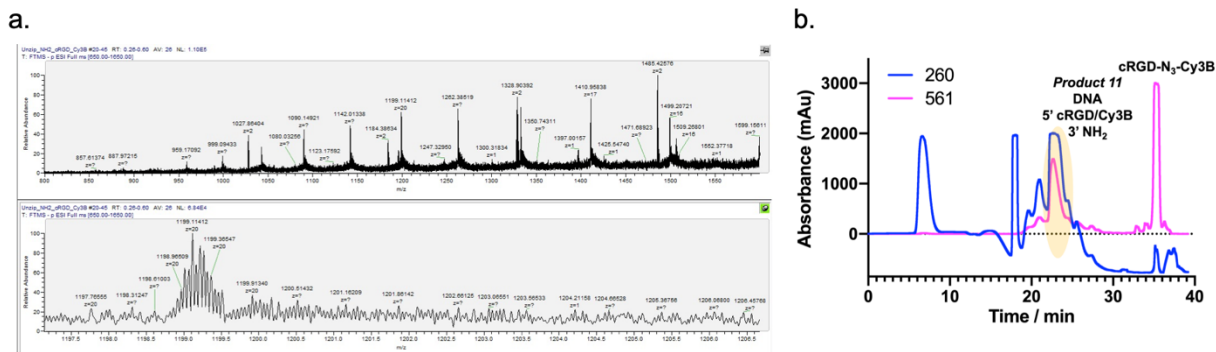


Figure A41. Characterization of Chapter 4 product 11. a. ESI MS spectra b. HPLC trace of product 11

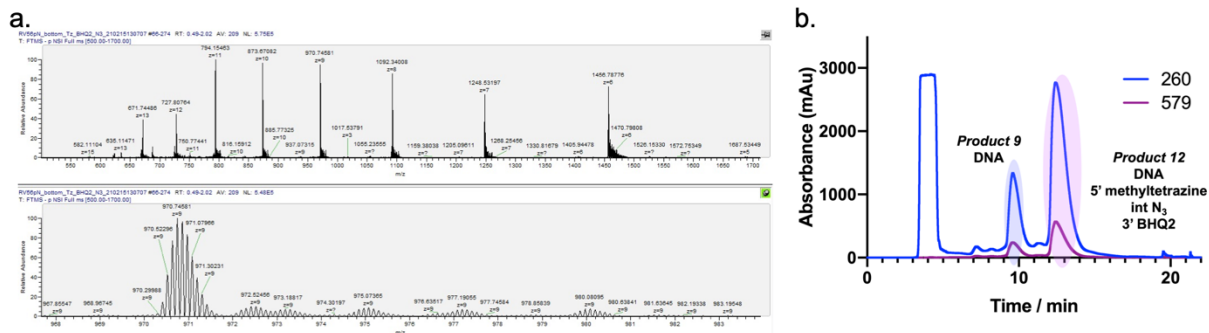


Figure A42. Characterization of Chapter 4 product 12. a. ESI MS spectra b. HPLC trace of product 12

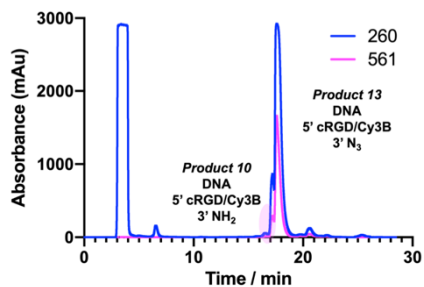


Figure A43. HPLC trace of product 13

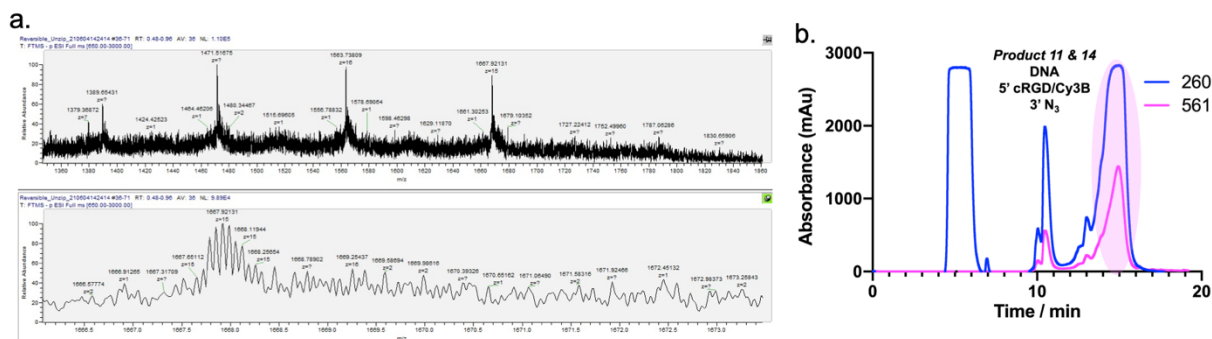


Figure A44. Characterization of Chapter 4 product 14. a. ESI MS spectra b. HPLC trace of product 14

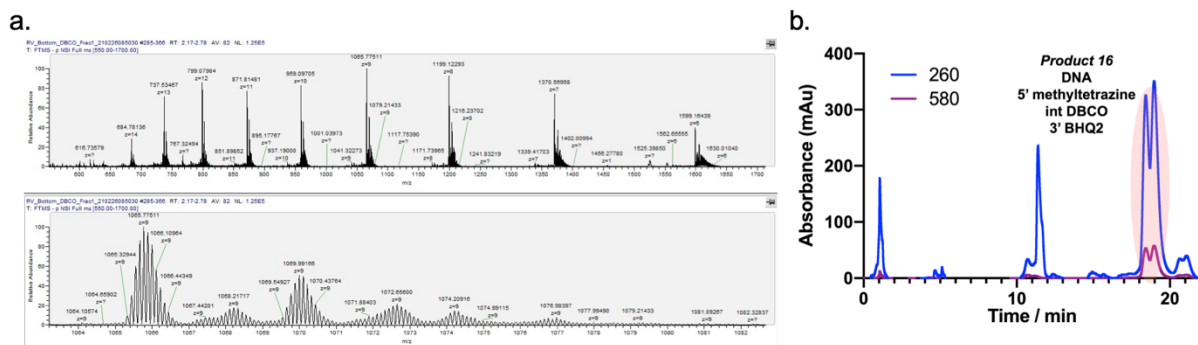


Figure A45. Characterization of Chapter 4 product 16. a. ESI MS spectra b. HPLC trace of product 16

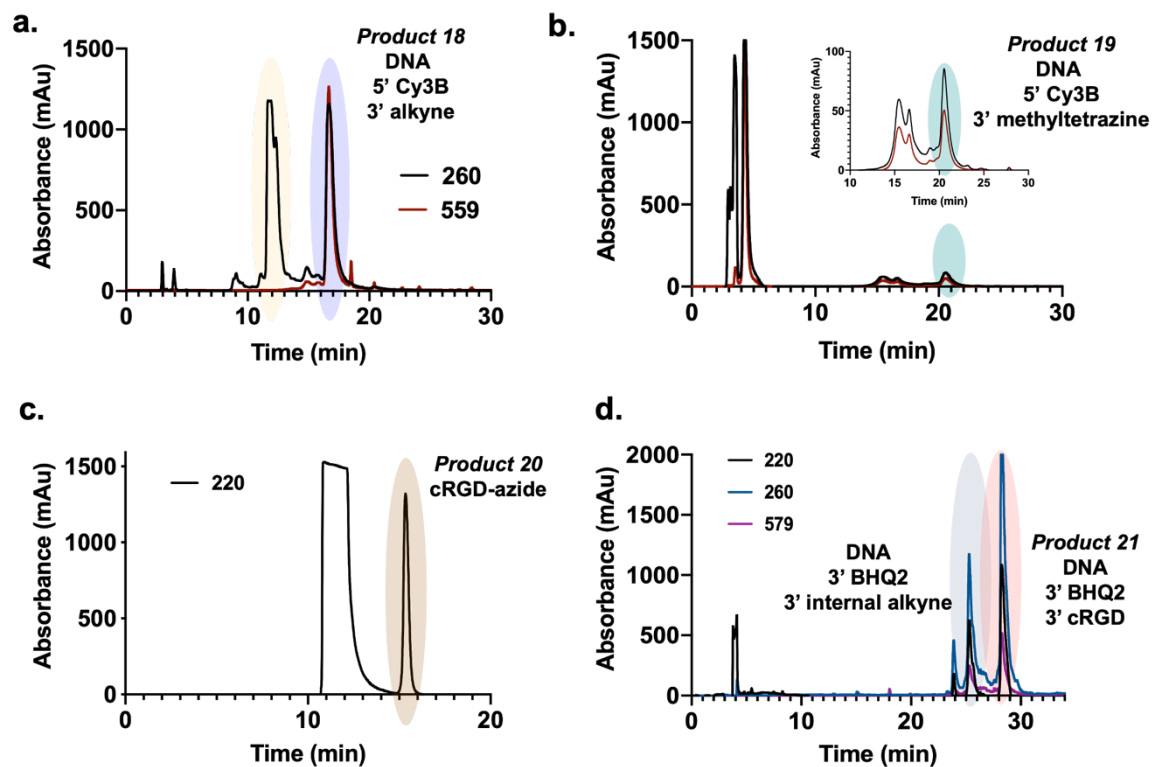


Figure A46. Characterization of irreversible shearing probes used in Chapter 4. a. HPLC trace of product 18, b. HPLC trace of product 19, c. HPLC trace of product 20, d. HPLC trace of product 21.

## APPENDIX B: GLOSSARY AND COMMON ABBREVIATIONS

**Actin** – A protein that works with myosin to form the contractile filaments of the cell that control cell adhesion and migration.

**Adenosine triphosphate (ATP)** – A molecule within the cell that, when hydrolyzed, provides the energy needed for cellular function.

**Aptamer** – Oligonucleotide or peptide molecules that are evolved to bind to a specific target molecule. **Autofluorescence** – Fluorescence emitted naturally by biological substances when they have absorbed light, regardless of the wavelength of the incoming light.

**Bleedthrough** – Similar to crosstalk. When the emission of the donor leaks into the emission channel of the acceptor.

**Bond vector** – The distance over which the direction of a particular vector exists within an ideal chain. **Cerulean** - Cerulean is a cyan fluorescent protein published in 2004, derived from *Aequorea victoria*. It has an excitation maximum of 433 and an emission maximum of 475.

**Chromophore** – The part of a fluorophore that absorbs light and is therefore responsible for its visible color.

**Contour length** – The length of a polymer at its maximum extension.

**Cortical tension** – Sustained contraction of the cell cytoskeleton that can pull cells into spherical shapes. **Crosstalk** – Crosstalk can occur between two dyes with similar absorbance and emission wavelengths, making it difficult to differentiate their signals in fluorescence imaging.

**Cytoplasm** – Gel-like liquid composed of water, salt, and proteins that fills the cell. The cell's organelles are located in the cytoplasm.

**Desmoplakin** – A protein component of desmosomes that maintains structural integrity of

cell-cell contacts. **Diffraction grating (DG)** – An optical component with periodic structure that splits and diffracts light into beams that travel in different directions.

**E-cadherin** – Proteins used in the formation of adheren junctions that enable cells to adhere to each other. **Epidermal growth factor receptor** – A protein in the cell membrane that acts as a receptor for epidermal growth factor.

**Excitation maximum** – The wavelength of light that a fluorophore absorbs most efficiently.

**Extracellular matrix (ECM)** – A collection of protein, collagen, glycoproteins, and enzymes that surrounds cells and provides structural and biochemical support.

**Fluorescence** – A form of luminescence in which light is emitted from a substance that has absorbed light from an excitation source.

**Fluorescence in situ hybridization (FISH)** – A method for visualizing nucleic acids in a cell. Fluorescent probes bind to a specific region of a nucleic acid sequence with high specificity, allowing researchers to study genes and chromosomes in the cell.

**Fluorescence lifetime imaging (FLIM)** – A method of imaging that measures the exponential decay of a fluorophore from an excited state.

**Fluorescence polarization (FP)** – Light emitted from a fluorophore has unequal intensities along the different axes of polarization. This phenomenon can be utilized molecular force sensors and fluorescence microscopy to determine the orientation of the force being generated by cell receptors.

**Fluorophore** – A molecule that can absorb photons from an excitation light and emit photons at a lower energy, resulting in measurable fluorescence.

**Focal adhesions** – Macromolecular assemblies of proteins in the cell that allow the cell to adhere to the surface and connect the cell cytoplasm to the extracellular matrix. Focal

adhesions are dynamic and grow and shrink in response to mechanical and biochemical cues.

**Förster resonance energy transfer (FRET)** – A non-radiative, distance-dependent physical process in which energy is transferred from an excited donor molecule to an acceptor molecule.

**Freely jointed chain model** – A subset of the ideal chain model that describes a polymer as a collection of rigid segments that are of equal length and connected by freely rotating joints.

**Freely rotating chain model** – A subset of the ideal chain model that describes a polymer as a collection of rigid segments that are of equal length. Within the chain of linear segments, the bond angle between adjacent monomers is fixed due to chemical bonding but the torsion angle of each segment can freely rotate

**Green Fluorescent Protein (GFP)** - GFP is a green fluorescent protein published in 2005, derived from

*Aequorea victoria*. It has an excitation maximum of 485 and an emission maximum of 510.

**Hooke's law** – The idea that the force needed to extend or compress a spring by some distance scales linearly with respect to the distance.

**Hybridization chain reaction (HCR)** – A method of enzyme free DNA amplification.

**Ideal chain model** – The simplest model to describe polymers. The ideal chain model assumes that like an ideal gas, there are no interactions between the individual monomers that make up the polymer.

**Ion channels** – Channels in the phospholipid membrane that allow for exchange of ions between the cell and the surrounding environment.

**Kuhn segments** – A theoretical way to describe the segments of a polymer. A polymer consists of  $n$  Kuhn segments that are freely jointed with each other.

**Linear unmixing** – A mathematical technique used for the decomposition of chemical

elements in an unknown by analyzing the spectral makeup relative to a library of standards.

**Mechanotransduction** – The ability of a cell to sense and convert external mechanical signals into biochemical signals that guide cell fate.

**Micropillar functionalized substrates** – A method for measuring the traction forces generated on the surface of the cell. Cells are plated on an elastic substrate functionalized with flexible micropillars. When a cell exerts tension, the micropillars are deflected and forces can be deduced from their displacement.

**Monte Carlo simulations** – A broad class of computational algorithms that rely on repeated random sampling to obtain numerical result.

**Myosin** – A motor protein that works with actin to form the contractile filaments of the cell that control cell adhesion and migration.

**Nucleic acids** – The “information carriers” of the cell. Nucleic acids are biopolymers composed of nucleotides, monomers consisting of a 5-carbon sugar, a phosphate group, and a nitrogenous base, that direct protein synthesis.

**Organelles** – The specialized structures inside of the cell. Each organelle (such as the mitochondria, Golgi body, or nucleus) has a specific function much like an organ has a specific function in the body.

**Osmotic stress** – Sudden changes in solute concentration around the cell that affects the transport of water through the cell membrane.

**Peptide nucleic acids (PNA)** – A synthetic nucleic acid analogue with an amide backbone. PNA retains the ability to Franklin-Watson-Crick base pair, but is resistant to degradation by all known enzymes and has increased binding affinity and thermal stability compared to natural nucleic acids.

**Persistence length** – The length over which a polymer stays straight when subject to fluctuations in temperature.

**Phospholipid membrane** – A membrane that forms a continuous barrier around the cell and consists of two layers of lipid molecules containing ion channels, proteins, cholesterol, and receptor molecules for cell adhesion.

**Photobleaching** – The photochemical destruction of a dye such that it is no longer able to fluoresce.

**Piconewton** – An SI unit of force equal to  $10^{-12}$  newtons.

**Podosomes** – Actin-rich structures on the outside of the cell membrane that serve as sites of attachment and degradation during cell migration.

**Polarization modulator (162)** – An optical component used to change the polarization of the light used to illuminate the sample.

**Polymers** – Natural and synthetic substances that are composed of similar subunits bound together.

**Protein secondary and tertiary structures** – The higher ordered structures that form as a sequence of amino acids fold. Secondary structures such as  $\alpha$ -helices and  $\beta$ -pleated sheets involve local interactions on the peptide. Tertiary structures are the 3-dimensional folded structures that result from interactions of the R groups on the peptide.

**Quencher** – A molecule that can absorb the energy emitted by a fluorophore, reducing the amount of observable fluorescent signal.

**Receptor molecules** – Molecules on the surface of the cell responsible for communicating extracellular cues into intercellular biochemical responses.

**Refractive index** – In optics, the refractive index of a material is a dimensionless value that

describes how well light travels through the material.

**Sliding filament theory** – The mechanism that allows cells to contract. Myosin binds to actin and then alters its configuration, causing the actin to slide across the myosin filament.

**Streptavidin** – A 66 kDa protein that binds to biotin with high affinity. The biotin-streptavidin interaction is one of the strongest non-covalent bonds known in nature.

**Super-resolution microscopy** – A class of imaging techniques with improved resolution compared to conventional fluorescence microscopy.

**Supported lipid bilayer (SLB)** – Lipid bilayers are immobilized to solid substrates and used as a platform to mimic the cell membrane.

**Traction force microscopy (TFM)** – A method for measuring the traction forces generated on the surface of a cell. Cells are plated on a gel containing fluorescent beads and traction forces are quantified by measuring displacement of the beads.

**Tetramethylrhodamine (TRITC)** – A fluorescent channel in epifluorescence imaging with a wavelength range of 532 – 613 nm.

**Venus** - Venus is a yellow fluorescent protein published in 2002, derived from *Aequorea victoria*. It has an excitation maximum of 515 and an emission maximum of 528.

**Vinculin** – A cytoplasmic, actin-binding protein involved in focal adhesion formation. Vinculin aids in transmitting and regulating mechanical force between the cytoskeleton and adhesion receptors.

**Worm-like chain (WLC) model** – A model used to describe a polymer as a flexible rod. Therefore, the WLC describes a polymer that is stiff over short distances and flexible over longer distances.

## APPENDIX C: PERMISSIONS



49 Spadina Ave. Suite 200  
Toronto ON M5V 2J1 Canada  
www.biorender.com

### Confirmation of Publication and Licensing Rights

March 1st, 2023  
Science Suite Inc.

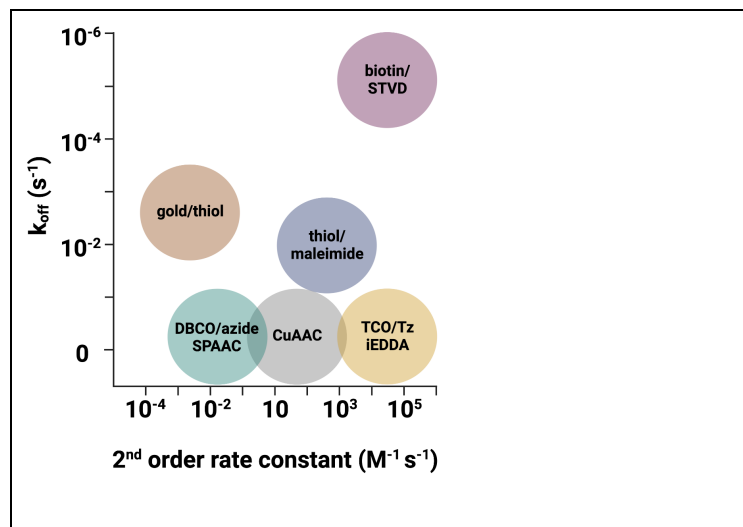
**Subscription:** Lab  
**Agreement number:** SP252N77SP  
**Journal name:** Bender, Rachel L\_Dissertation

To whom this may concern,

This document is to confirm that Rachel Bender has been granted a license to use the BioRender content, including icons, templates and other original artwork, appearing in the attached completed graphic pursuant to BioRender's [Academic License Terms](#). This license permits BioRender content to be sublicensed for use in journal publications.

All rights and ownership of BioRender content are reserved by BioRender. All completed graphics must be accompanied by the following citation: "Created with BioRender.com".

BioRender content included in the completed graphic is not licensed for any commercial uses beyond publication in a journal. For any commercial use of this figure, users may, if allowed, recreate it in BioRender under an Industry BioRender Plan.



For any questions regarding this document, or other questions about publishing with BioRender refer to our [BioRender Publication Guide](#), or contact BioRender Support at [support@biorender.com](mailto:support@biorender.com).



49 Spadina Ave. Suite 200  
Toronto ON M5V 2J1 Canada  
www.biorender.com

## Confirmation of Publication and Licensing Rights

March 1st, 2023  
Science Suite Inc.

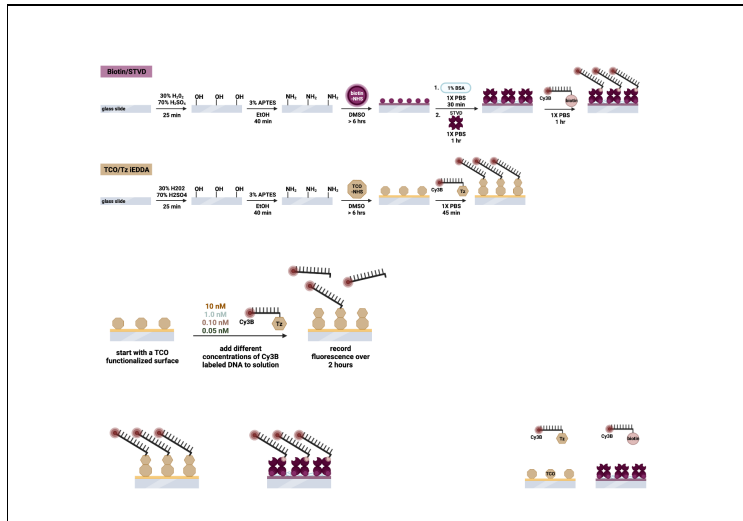
**Subscription:** Lab  
**Agreement number:** TL252N7BRC  
**Journal name:** Bender, Rachel L\_Dissertation

To whom this may concern,

This document is to confirm that Rachel Bender has been granted a license to use the BioRender content, including icons, templates and other original artwork, appearing in the attached completed graphic pursuant to BioRender's [Academic License Terms](#). This license permits BioRender content to be sublicensed for use in journal publications.

All rights and ownership of BioRender content are reserved by BioRender. All completed graphics must be accompanied by the following citation: "Created with BioRender.com".

BioRender content included in the completed graphic is not licensed for any commercial uses beyond publication in a journal. For any commercial use of this figure, users may, if allowed, recreate it in BioRender under an Industry BioRender Plan.



For any questions regarding this document, or other questions about publishing with BioRender refer to our [BioRender Publication Guide](#), or contact BioRender Support at [support@biorender.com](mailto:support@biorender.com).



49 Spadina Ave. Suite 200  
Toronto ON M5V 2J1 Canada  
www.biorender.com

## Confirmation of Publication and Licensing Rights

March 1st, 2023  
Science Suite Inc.

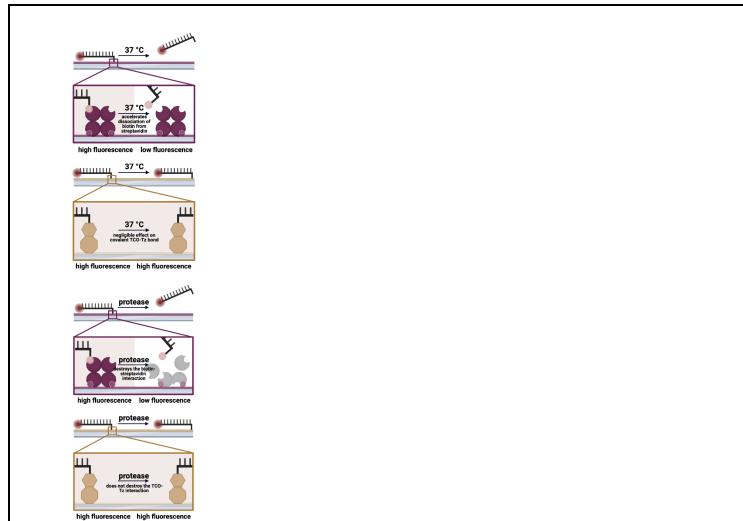
**Subscription:** Lab  
**Agreement number:** OC252N7SEG  
**Journal name:** Bender, Rachel L\_Dissertation

To whom this may concern,

This document is to confirm that Rachel Bender has been granted a license to use the BioRender content, including icons, templates and other original artwork, appearing in the attached completed graphic pursuant to BioRender's [Academic License Terms](#). This license permits BioRender content to be sublicensed for use in journal publications.

All rights and ownership of BioRender content are reserved by BioRender. All completed graphics must be accompanied by the following citation: "Created with BioRender.com".

BioRender content included in the completed graphic is not licensed for any commercial uses beyond publication in a journal. For any commercial use of this figure, users may, if allowed, recreate it in BioRender under an Industry BioRender Plan.



For any questions regarding this document, or other questions about publishing with BioRender refer to our [BioRender Publication Guide](#), or contact BioRender Support at [support@biorender.com](mailto:support@biorender.com).



49 Spadina Ave. Suite 200  
Toronto ON M5V 2J1 Canada  
www.biorender.com

## Confirmation of Publication and Licensing Rights

March 1st, 2023  
Science Suite Inc.

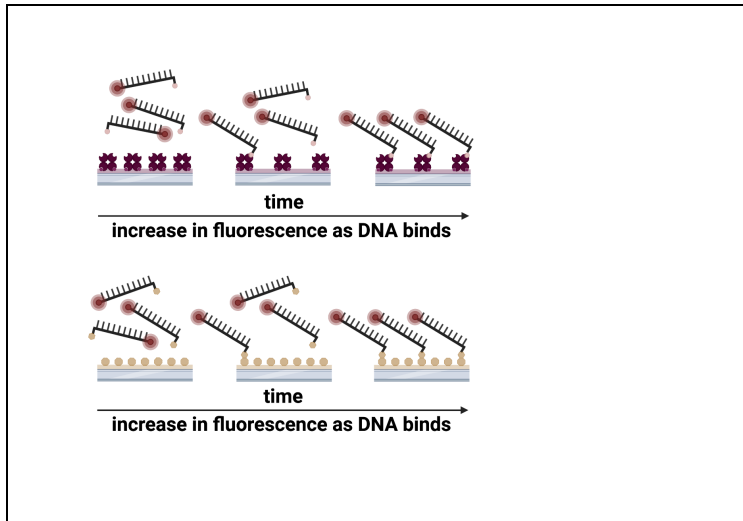
**Subscription:** Lab  
**Agreement number:** TD252N75IQ  
**Journal name:** Bender, Rachel L\_Dissertation

To whom this may concern,

This document is to confirm that Rachel Bender has been granted a license to use the BioRender content, including icons, templates and other original artwork, appearing in the attached completed graphic pursuant to BioRender's [Academic License Terms](#). This license permits BioRender content to be sublicensed for use in journal publications.

All rights and ownership of BioRender content are reserved by BioRender. All completed graphics must be accompanied by the following citation: "Created with BioRender.com".

BioRender content included in the completed graphic is not licensed for any commercial uses beyond publication in a journal. For any commercial use of this figure, users may, if allowed, recreate it in BioRender under an Industry BioRender Plan.



For any questions regarding this document, or other questions about publishing with BioRender refer to our [BioRender Publication Guide](#), or contact BioRender Support at [support@biorender.com](mailto:support@biorender.com).



49 Spadina Ave. Suite 200  
Toronto ON M5V 2J1 Canada  
www.biorender.com

## Confirmation of Publication and Licensing Rights

March 1st, 2023  
Science Suite Inc.

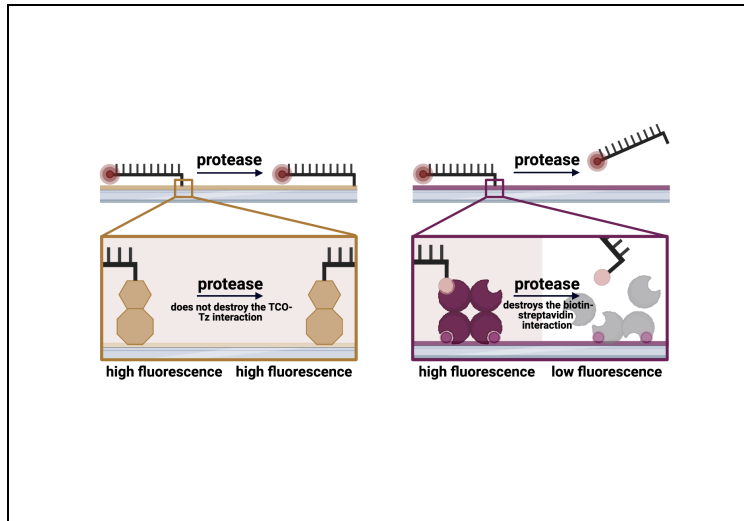
**Subscription:** Lab  
**Agreement number:** MF252N7R6M  
**Journal name:** Bender, Rachel L\_Dissertation

To whom this may concern,

This document is to confirm that Rachel Bender has been granted a license to use the BioRender content, including icons, templates and other original artwork, appearing in the attached completed graphic pursuant to BioRender's [Academic License Terms](#). This license permits BioRender content to be sublicensed for use in journal publications.

All rights and ownership of BioRender content are reserved by BioRender. All completed graphics must be accompanied by the following citation: "Created with BioRender.com".

BioRender content included in the completed graphic is not licensed for any commercial uses beyond publication in a journal. For any commercial use of this figure, users may, if allowed, recreate it in BioRender under an Industry BioRender Plan.



For any questions regarding this document, or other questions about publishing with BioRender refer to our [BioRender Publication Guide](#), or contact BioRender Support at [support@biorender.com](mailto:support@biorender.com).



49 Spadina Ave. Suite 200  
Toronto ON M5V 2J1 Canada  
www.biorender.com

## Confirmation of Publication and Licensing Rights

March 1st, 2023  
Science Suite Inc.

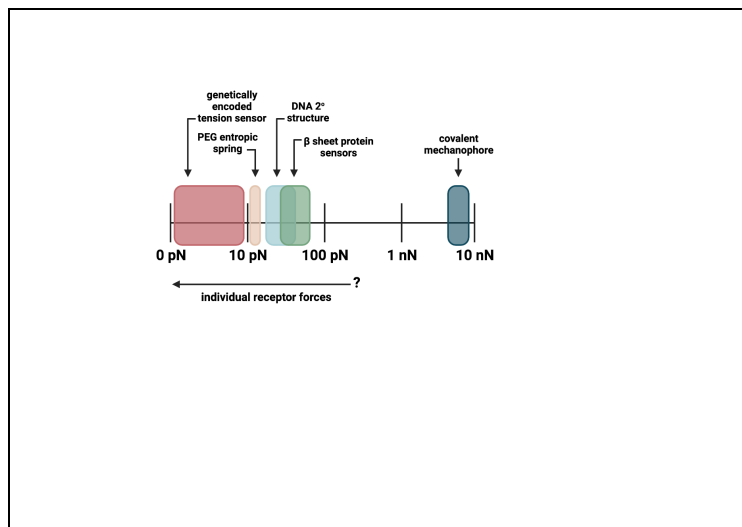
**Subscription:** Lab  
**Agreement number:** WW252N7U4J  
**Journal name:** Bender, Rachel L\_ Dissertation

To whom this may concern,

This document is to confirm that Rachel Bender has been granted a license to use the BioRender content, including icons, templates and other original artwork, appearing in the attached completed graphic pursuant to BioRender's [Academic License Terms](#). This license permits BioRender content to be sublicensed for use in journal publications.

All rights and ownership of BioRender content are reserved by BioRender. All completed graphics must be accompanied by the following citation: "Created with BioRender.com".

BioRender content included in the completed graphic is not licensed for any commercial uses beyond publication in a journal. For any commercial use of this figure, users may, if allowed, recreate it in BioRender under an Industry BioRender Plan.



For any questions regarding this document, or other questions about publishing with BioRender refer to our [BioRender Publication Guide](#), or contact BioRender Support at [support@biorender.com](mailto:support@biorender.com).



49 Spadina Ave. Suite 200  
 Toronto ON M5V 2J1 Canada  
 www.biorender.com

## Confirmation of Publication and Licensing Rights

March 1st, 2023  
 Science Suite Inc.

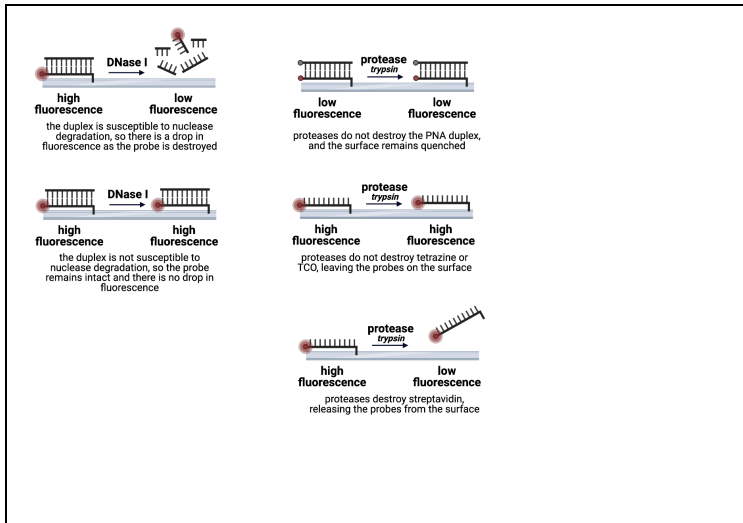
**Subscription:** Lab  
**Agreement number:** WQ252N7394  
**Journal name:** Bender, Rachel L\_Dissertation

To whom this may concern,

This document is to confirm that Rachel Bender has been granted a license to use the BioRender content, including icons, templates and other original artwork, appearing in the attached completed graphic pursuant to BioRender's Academic License Terms. This license permits BioRender content to be sublicensed for use in journal publications.

All rights and ownership of BioRender content are reserved by BioRender. All completed graphics must be accompanied by the following citation: "Created with BioRender.com".

BioRender content included in the completed graphic is not licensed for any commercial uses beyond publication in a journal. For any commercial use of this figure, users may, if allowed, recreate it in BioRender under an Industry BioRender Plan.



For any questions regarding this document, or other questions about publishing with BioRender refer to our BioRender Publication Guide, or contact BioRender Support at [support@biorender.com](mailto:support@biorender.com).



49 Spadina Ave. Suite 200  
Toronto ON M5V 2J1 Canada  
www.biorender.com

## Confirmation of Publication and Licensing Rights

March 1st, 2023  
Science Suite Inc.

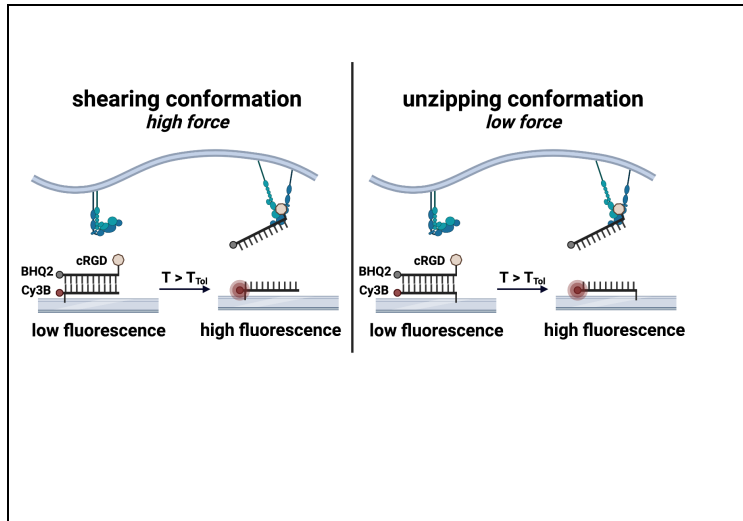
**Subscription:** Lab  
**Agreement number:** TB252N7PHN  
**Journal name:** Bender, Rachel L\_Dissertation

To whom this may concern,

This document is to confirm that Rachel Bender has been granted a license to use the BioRender content, including icons, templates and other original artwork, appearing in the attached completed graphic pursuant to BioRender's [Academic License Terms](#). This license permits BioRender content to be sublicensed for use in journal publications.

All rights and ownership of BioRender content are reserved by BioRender. All completed graphics must be accompanied by the following citation: "Created with BioRender.com".

BioRender content included in the completed graphic is not licensed for any commercial uses beyond publication in a journal. For any commercial use of this figure, users may, if allowed, recreate it in BioRender under an Industry BioRender Plan.



For any questions regarding this document, or other questions about publishing with BioRender refer to our [BioRender Publication Guide](#), or contact BioRender Support at [support@biorender.com](mailto:support@biorender.com).



49 Spadina Ave. Suite 200  
 Toronto ON M5V 2J1 Canada  
 www.biorender.com

## Confirmation of Publication and Licensing Rights

March 1st, 2023  
 Science Suite Inc.

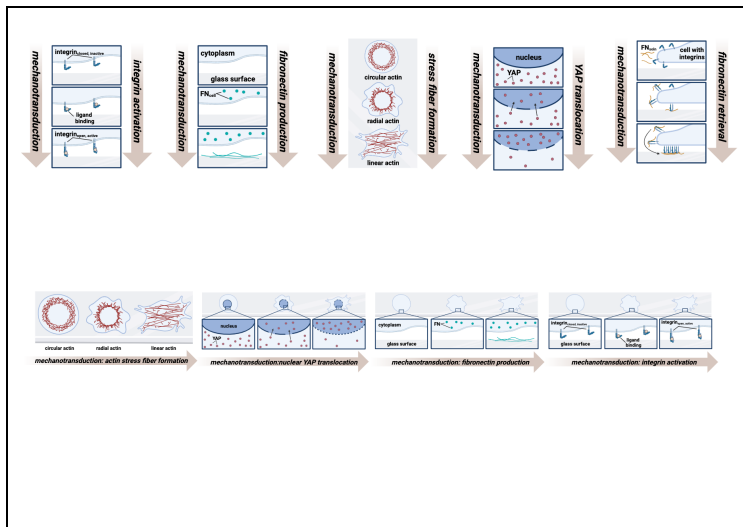
**Subscription:** Lab  
**Agreement number:** DX252N7KRF  
**Journal name:** Bender, Rachel L\_Dissertation

To whom this may concern,

This document is to confirm that Rachel Bender has been granted a license to use the BioRender content, including icons, templates and other original artwork, appearing in the attached completed graphic pursuant to BioRender's Academic License Terms. This license permits BioRender content to be sublicensed for use in journal publications.

All rights and ownership of BioRender content are reserved by BioRender. All completed graphics must be accompanied by the following citation: "Created with BioRender.com".

BioRender content included in the completed graphic is not licensed for any commercial uses beyond publication in a journal. For any commercial use of this figure, users may, if allowed, recreate it in BioRender under an Industry BioRender Plan.



For any questions regarding this document, or other questions about publishing with BioRender refer to our BioRender Publication Guide, or contact BioRender Support at [support@biorender.com](mailto:support@biorender.com).



49 Spadina Ave. Suite 200  
Toronto ON M5V 2J1 Canada  
www.biorender.com

## Confirmation of Publication and Licensing Rights

March 1st, 2023  
Science Suite Inc.

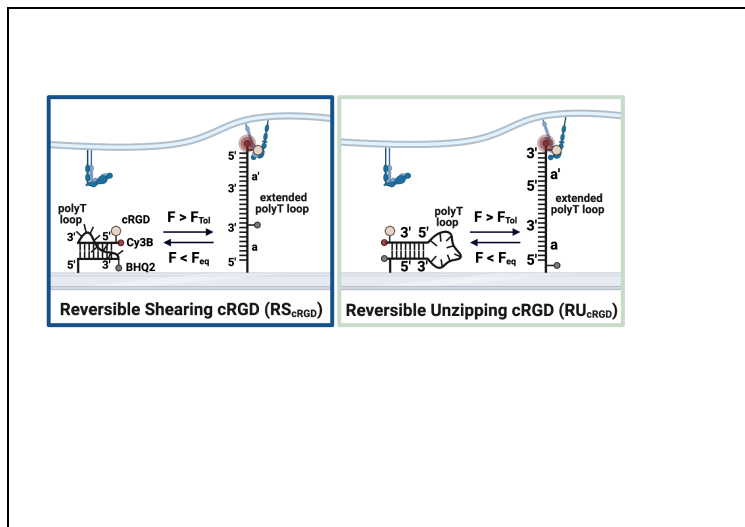
**Subscription:** Lab  
**Agreement number:** NR252N7N3B  
**Journal name:** Bender, Rachel L\_Dissertation

To whom this may concern,

This document is to confirm that Rachel Bender has been granted a license to use the BioRender content, including icons, templates and other original artwork, appearing in the attached completed graphic pursuant to BioRender's [Academic License Terms](#). This license permits BioRender content to be sublicensed for use in journal publications.

All rights and ownership of BioRender content are reserved by BioRender. All completed graphics must be accompanied by the following citation: "Created with BioRender.com".

BioRender content included in the completed graphic is not licensed for any commercial uses beyond publication in a journal. For any commercial use of this figure, users may, if allowed, recreate it in BioRender under an Industry BioRender Plan.



For any questions regarding this document, or other questions about publishing with BioRender refer to our [BioRender Publication Guide](#), or contact BioRender Support at [support@biorender.com](mailto:support@biorender.com).



49 Spadina Ave. Suite 200  
 Toronto ON M5V 2J1 Canada  
 www.biorender.com

## Confirmation of Publication and Licensing Rights

March 1st, 2023  
 Science Suite Inc.

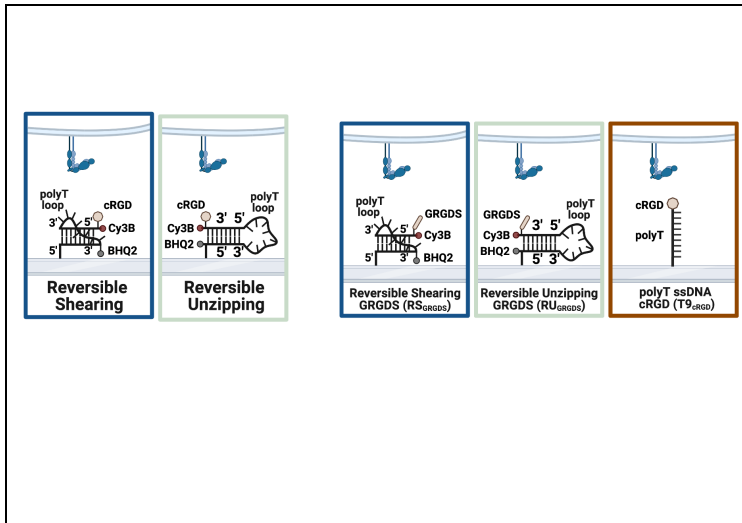
**Subscription:** Lab  
**Agreement number:** WY252N7DBA  
**Journal name:** Bender, Rachel L\_Dissertation

To whom this may concern,

This document is to confirm that Rachel Bender has been granted a license to use the BioRender content, including icons, templates and other original artwork, appearing in the attached completed graphic pursuant to BioRender's Academic License Terms. This license permits BioRender content to be sublicensed for use in journal publications.

All rights and ownership of BioRender content are reserved by BioRender. All completed graphics must be accompanied by the following citation: "Created with BioRender.com".

BioRender content included in the completed graphic is not licensed for any commercial uses beyond publication in a journal. For any commercial use of this figure, users may, if allowed, recreate it in BioRender under an Industry BioRender Plan.



For any questions regarding this document, or other questions about publishing with BioRender refer to our BioRender Publication Guide, or contact BioRender Support at [support@biorender.com](mailto:support@biorender.com).

MOLECULAR FORCE SENSORS

ACS IN FOCUS, 2022

C/O Eric Slater



Permission for this particular request is granted for print and electronic formats, and translations, at no charge. Figures and tables may be modified. Appropriate credit should be given. Please print this page for your records and provide a copy to your publisher. Requests for up to 4 figures require only this record. Five or more figures will generate a printout of additional terms and conditions. Appropriate credit should read: "Reprinted with permission from {COMPLETE REFERENCE CITATION}. Copyright {YEAR} American Chemical Society." Insert appropriate information in place of the capitalized words.

## REFERENCES

1. Horzum, U.; Ozdil, B.; Pesen-Okvur, D., Step-by-step quantitative analysis of focal adhesions. *MethodsX* **2014**, *1*, 56-59.
2. Wolff, J., Das Gesetz der Transformation der Knochen. *Deutsche Medizinische Wochenschrift* **1893**, *19*, 1222-1224.
3. Harris, A. K.; Wild, P.; Stopak, D., Silicone Rubber Substrata: A New Wrinkle in the Study of Cell Locomotion. *Science* **1980**, *208* (4440), 177-179.
4. Gupta, M.; Kocgozlu, L.; Sarangi, B. R.; Margadant, F.; Ashraf, M.; Ladoux, B., Micropillar substrates: a tool for studying cell mechanobiology. *Methods Cell Biol* **2015**, *125*, 289-308.
5. Hur, S. S.; Jeong, J. H.; Ban, M. J.; Park, J. H.; Yoon, J. K.; Hwang, Y., Traction force microscopy for understanding cellular mechanotransduction. *BMB Rep* **2020**, *53* (2), 74-81.
6. Style, R. W.; Boltanskiy, R.; German, G. K.; Hyland, C.; MacMinn, C. W.; Mertz, A. F.; Wilen, L. A.; Xu, Y.; Dufresne, E. R., Traction force microscopy in physics and biology. *Soft Matter* **2014**, *10* (23), 4047-4055.
7. Iskratsch, T.; Wolfenson, H.; Sheetz, M. P., Appreciating force and shape — the rise of mechanotransduction in cell biology. *Nature Reviews Molecular Cell Biology* **2014**, *15* (12), 825-833.
8. Sun, Z.; Guo, S. S.; Fässler, R., Integrin-mediated mechanotransduction. *Journal of Cell Biology* **2016**, *215* (4), 445-456.
9. Hynes, R. O., Integrins: Bidirectional, Allosteric Signaling Machines. *Cell* **2002**, *110* (6), 673-687.
10. Su, Y.; Xia, W.; Li, J.; Walz, T.; Humphries, M. J.; Vestweber, D.; Cabañas, C.; Lu, C.; Springer, T. A., Relating conformation to function in integrin  $\alpha 5\beta 1$ . *Proceedings of the National Academy of Sciences of the United States of America* **2016**, *113* (27), E3872-81.
11. Mould, A. P.; Barton, S. J.; Askari, J. A.; McEwan, P. A.; Buckley, P. A.; Craig, S. E.; Humphries, M. J., Conformational Changes in the Integrin  $\alpha 5\beta 1$  Domain Provide a

- Mechanism for Signal Transduction via Hybrid Domain Movement. *Journal of Biological Chemistry* **2003**, *278* (19), 17028-17035.
12. Lawson, C.; Schlaepfer, D. D., Integrin adhesions: who's on first? What's on second? Connections between FAK and talin. *Cell Adh Migr* **2012**, *6* (4), 302-6.
  13. Calderwood, D. A.; Campbell, I. D.; Critchley, D. R., Talins and kindlins: partners in integrin-mediated adhesion. *Nat Rev Mol Cell Biol* **2013**, *14* (8), 503-17.
  14. del Rio, A.; Perez-Jimenez, R.; Liu, R.; Roca-Cusachs, P.; Fernandez, J. M.; Sheetz, M. P., Stretching single talin rod molecules activates vinculin binding. *Science* **2009**, *323* (5914), 638-41.
  15. Mallik, R.; Rai, A. K.; Barak, P.; Rai, A.; Kunwar, A., Teamwork in microtubule motors. *Trends Cell Biol* **2013**, *23* (11), 575-82.
  16. Svoboda, K.; Block, S. M., Force and velocity measured for single kinesin molecules. *Cell* **1994**, *77* (5), 773-84.
  17. Wang, X.; Ha, T., Defining Single Molecular Forces Required to Activate Integrin and Notch Signaling. *Science (New York, N.Y.)* **2013**, *340* (6135), 991-994.
  18. Stabley, D. R.; Jurchenko, C.; Marshall, S. S.; Salaita, K. S., Visualizing mechanical tension across membrane receptors with a fluorescent sensor. *Nature Methods* **2012**, *9* (1), 64-67.
  19. Liu, Y.; Yehl, K.; Narui, Y.; Salaita, K., Tension Sensing Nanoparticles for Mechano-Imaging at the Living/Nonliving Interface. *Journal of the American Chemical Society* **2013**, *135* (14), 5320-5323.
  20. Ma, V. P.; Salaita, K., DNA Nanotechnology as an Emerging Tool to Study Mechanotransduction in Living Systems. *Small* **2019**, *15* (26), e1900961.
  21. Zhang, Y.; Ge, C.; Zhu, C.; Salaita, K., DNA-based digital tension probes reveal integrin forces during early cell adhesion. *Nature communications* **2014**, *5*, 5167.
  22. Glazier, R.; Brockman, J. M.; Bartle, E.; Mattheyses, A. L.; Destaing, O.; Salaita, K., DNA mechanotechnology reveals that integrin receptors apply pN forces in podosomes on

- fluid substrates. *Nature communications* **2019**, *10* (1), 4507.
23. Blakely, B. L.; Dumelin, C. E.; Trappmann, B.; McGregor, L. M.; Choi, C. K.; Anthony, P. C.; Duesterberg, V. K.; Baker, B. M.; Block, S. M.; Liu, D. R.; Chen, C. S., A DNA-based molecular probe for optically reporting cellular traction forces. *Nat Methods* **2014**, *11* (12), 1229-32.
  24. Strunz, T.; Oroszlan, K.; Schäfer, R.; Güntherodt, H.-J., Dynamic force spectroscopy of single DNA molecules. *Proceedings of the National Academy of Sciences* **1999**, *96* (20), 11277-11282.
  25. Mosayebi, M.; Louis, A. A.; Doye, J. P. K.; Ouldrige, T. E., Force-Induced Rupture of a DNA Duplex: From Fundamentals to Force Sensors. *ACS Nano* **2015**, *9* (12), 11993-12003.
  26. Chakrabarti, B.; Nelson, D. R., Shear unzipping of DNA. *J Phys Chem B* **2009**, *113* (12), 3831-6.
  27. de Gennes, P.-G., Maximum pull out force on DNA hybrids. *Comptes Rendus de l'Académie des Sciences - Series IV - Physics* **2001**, *2* (10), 1505-1508.
  28. Hatch, K.; Danilowicz, C.; Coljee, V.; Prentiss, M., Demonstration that the shear force required to separate short double-stranded DNA does not increase significantly with sequence length for sequences longer than 25 base pairs. *Phys Rev E Stat Nonlin Soft Matter Phys* **2008**, *78* (1 Pt 1), 011920.
  29. Yuan, X.; Wu, H.; Xu, H.; Xiong, H.; Chu, Q.; Yu, S.; Wu, G. S.; Wu, K., Notch signaling: an emerging therapeutic target for cancer treatment. *Cancer Lett* **2015**, *369* (1), 20-7.
  30. Chowdhury, F.; Li, I. T. S.; Ngo, T. T. M.; Leslie, B. J.; Kim, B. C.; Sokoloski, J. E.; Weiland, E.; Wang, X.; Chemla, Y. R.; Lohman, T. M.; Ha, T., Defining Single Molecular Forces Required for Notch Activation Using Nano Yoyo. *Nano Letters* **2016**, *16* (6), 3892-3897.
  31. Wang, Y.; LeVine, D. N.; Gannon, M.; Zhao, Y.; Sarkar, A.; Hoch, B.; Wang, X., Force-activatable biosensor enables single platelet force mapping directly by fluorescence imaging. *Biosens Bioelectron* **2018**, *100*, 192-200.

32. Hahn, J.; Wickham, S. F. J.; Shih, W. M.; Perrault, S. D., Addressing the instability of DNA nanostructures in tissue culture. *ACS nano* **2014**, *8* (9), 8765-8775.
33. Goel, A.; Chauhan, S. S., Role of proteases in tumor invasion and metastasis. *Indian journal of experimental biology* **1997**, *35* (6), 553-64.
34. Zhao, Y.; Sarkar, A.; Wang, X., Peptide nucleic acid based tension sensor for cellular force imaging with strong DNase resistance. *Biosensors and Bioelectronics* **2020**, *150*, 111959.
35. Nielsen, P. E.; Egholm, M.; Berg, R. H.; Buchardt, O., Sequence-selective recognition of DNA by strand displacement with a thymine-substituted polyamide. *Science* **1991**, *254* (5037), 1497-500.
36. Nielsen, P. E.; Haaima, G., Peptide nucleic acid (PNA). A DNA mimic with a pseudopeptide backbone. *Chemical Society Reviews* **1997**, *26* (2), 73-78.
37. Li, H.; Zhang, C.; Hu, Y.; Liu, P.; Sun, F.; Chen, W.; Zhang, X.; Ma, J.; Wang, W.; Wang, L.; Wu, P.; Liu, Z., A reversible shearing DNA probe for visualizing mechanically strong receptors in living cells. *Nat Cell Biol* **2021**, *23* (6), 642-651.
38. Sakamoto, S.; Putalun, W.; Vimolmangkang, S.; Phoolcharoen, W.; Shoyama, Y.; Tanaka, H.; Morimoto, S., Correction to: Enzyme-linked immunosorbent assay for the quantitative/qualitative analysis of plant secondary metabolites. *J Nat Med* **2018**, *72* (1), 43.
39. Sola, L.; Damin, F.; Gagni, P.; Consonni, R.; Chiari, M., Synthesis of clickable coating polymers by postpolymerization modification: applications in microarray technology. *Langmuir* **2016**, *32* (40), 10284-10295.
40. Zilio, C.; Bernardi, A.; Palmioli, A.; Salina, M.; Tagliabue, G.; Buscaglia, M.; Consonni, R.; Chiari, M., New “clickable” polymeric coating for glycan microarrays. *Sensors and Actuators B: Chemical* **2015**, *215*, 412-420.
41. Ross, T. D.; Coon, B. G.; Yun, S.; Baeyens, N.; Tanaka, K.; Ouyang, M.; Schwartz, M. A., Integrins in mechanotransduction. *Current Opinion in Cell Biology* **2013**, *25* (5), 613-618.
42. Martino, F.; Perestrelo, A. R.; Vinarský, V.; Pagliari, S.; Forte, G., Cellular Mechanotransduction: From Tension to Function. *Frontiers in Physiology* **2018**, *9*.

43. Göhring, J.; Kellner, F.; Schrangl, L.; Platzner, R.; Klotzsch, E.; Stockinger, H.; Huppa, J. B.; Schütz, G. J., Temporal analysis of T-cell receptor-imposed forces via quantitative single molecule FRET measurements. *Nature communications* **2021**, *12* (1), 2502.
44. Ma, R.; Kellner, A. V.; Ma, V. P.-Y.; Su, H.; Deal, B. R.; Brockman, J. M.; Salaita, K., DNA probes that store mechanical information reveal transient piconewton forces applied by T cells. *Proceedings of the National Academy of Sciences* **2019**, *116* (34), 16949.
45. Ma, V. P.-Y.; Liu, Y.; Blanchfield, L.; Su, H.; Evavold, B. D.; Salaita, K., Ratiometric Tension Probes for Mapping Receptor Forces and Clustering at Intermembrane Junctions. *Nano Letters* **2016**, *16* (7), 4552-4559.
46. Brockman, J. M.; Blanchard, A. T.; Pui-Yan, V.; Derricotte, W. D.; Zhang, Y.; Fay, M. E.; Lam, W. A.; Evangelista, F. A.; Mattheyses, A. L.; Salaita, K., Mapping the 3D orientation of piconewton integrin traction forces. *Nature Methods* **2018**, *15* (2), 115-118.
47. Kasputis, T.; Pannier, A. K., The role of surface chemistry-induced cell characteristics on nonviral gene delivery to mouse fibroblasts. *Journal of Biological Engineering* **2012**, *6* (1), 17.
48. Cai, S.; Wu, C.; Yang, W.; Liang, W.; Yu, H.; Liu, L., Recent advance in surface modification for regulating cell adhesion and behaviors. *Nanotechnology Reviews* **2020**, *9* (1), 971-989.
49. Zheng, N.; Fan, J.; Stucky, G. D., One-step one-phase synthesis of monodisperse noble-metallic nanoparticles and their colloidal crystals. *J Am Chem Soc* **2006**, *128* (20), 6550-1.
50. Xue, Y.; Li, X.; Li, H.; Zhang, W., Quantifying thiol-gold interactions towards the efficient strength control. *Nature communications* **2014**, *5* (1), 4348.
51. Osypova, A.; Thakar, D.; Dejeu, J.; Bonnet, H.; Van der Heyden, A.; Dubacheva, G. V.; Richter, R. P.; Defrancq, E.; Spinelli, N.; Coche-Guerente, L., Sensor based on aptamer folding to detect low-molecular weight analytes. *Analytical chemistry* **2015**, *87* (15), 7566-7574.
52. Spampinato, V.; Parracino, M. A.; La Spina, R.; Rossi, F.; Ceccone, G., Surface Analysis of Gold Nanoparticles Functionalized with Thiol-Modified Glucose SAMs for Biosensor Applications. *Frontiers in Chemistry* **2016**, *4*.

53. Yáñez-Sedeño, P.; González-Cortés, A.; Campuzano, S.; Pingarrón, J. M., Copper(I)-Catalyzed Click Chemistry as a Tool for the Functionalization of Nanomaterials and the Preparation of Electrochemical (Bio)Sensors. *Sensors (Basel)* **2019**, *19* (10).
54. Eeftens, J. M.; van der Torre, J.; Burnham, D. R.; Dekker, C., Copper-free click chemistry for attachment of biomolecules in magnetic tweezers. *BMC Biophys* **2015**, *8*, 9.
55. Ravasco, J. M. J. M.; Faustino, H.; Trindade, A.; Gois, P. M. P., Bioconjugation with Maleimides: A Useful Tool for Chemical Biology. *Chemistry – A European Journal* **2019**, *25* (1), 43-59.
56. González, M.; Bagatolli, L. A.; Echabe, I.; Arrondo, J. L. R.; Argaraña, C. E.; Cantor, C. R.; Fidelio, G. D., Interaction of Biotin with Streptavidin: THERMOSTABILITY AND CONFORMATIONAL CHANGES UPON BINDING \*. *Journal of Biological Chemistry* **1997**, *272* (17), 11288-11294.
57. Laitinen, O. H.; Hytönen, V. P.; Nordlund, H. R.; Kulomaa, M. S., Genetically engineered avidins and streptavidins. *Cellular and Molecular Life Sciences CMLS* **2006**, *63* (24), 2992-3017.
58. Chivers, C. E.; Crozat, E.; Chu, C.; Moy, V. T.; Sherratt, D. J.; Howarth, M., A streptavidin variant with slower biotin dissociation and increased mechanostability. *Nat Methods* **2010**, *7* (5), 391-3.
59. Kennedy, D. C.; McKay, C. S.; Legault, M. C. B.; Danielson, D. C.; Blake, J. A.; Pegoraro, A. F.; Stolorow, A.; Mester, Z.; Pezacki, J. P., Cellular Consequences of Copper Complexes Used To Catalyze Bioorthogonal Click Reactions. *Journal of the American Chemical Society* **2011**, *133* (44), 17993-18001.
60. Kim, E.; Koo, H., Biomedical applications of copper-free click chemistry: in vitro, in vivo, and ex vivo. *Chemical Science* **2019**, *10* (34), 7835-7851.
61. Sletten, E. M.; Bertozzi, C. R., From Mechanism to Mouse: A Tale of Two Bioorthogonal Reactions. *Accounts of Chemical Research* **2011**, *44* (9), 666-676.
62. Agard, N. J.; Prescher, J. A.; Bertozzi, C. R., A Strain-Promoted [3 + 2] Azide–Alkyne Cycloaddition for Covalent Modification of Biomolecules in Living Systems. *Journal of the American Chemical Society* **2004**, *126* (46), 15046-15047.

63. Presolski, S. I.; Hong, V.; Cho, S.-H.; Finn, M. G., Tailored Ligand Acceleration of the Cu-Catalyzed Azide–Alkyne Cycloaddition Reaction: Practical and Mechanistic Implications. *Journal of the American Chemical Society* **2010**, *132* (41), 14570-14576.
64. Chen, Y.; Tsao, K.; De Francesco, É.; Keillor, J. W., Ring Substituent Effects on the Thiol Addition and Hydrolysis Reactions of N-Arylmaleimides. *The Journal of Organic Chemistry* **2015**, *80* (24), 12182-12192.
65. Kang, K.; Park, J.; Kim, E., Tetrazine ligation for chemical proteomics. *Proteome Sci* **2016**, *15*, 15.
66. Srisa-Art, M.; Dyson, E. C.; deMello, A. J.; Edel, J. B., Monitoring of Real-Time Streptavidin–Biotin Binding Kinetics Using Droplet Microfluidics. *Analytical Chemistry* **2008**, *80* (18), 7063-7067.
67. Blackman, M. L.; Royzen, M.; Fox, J. M., Tetrazine Ligation: Fast Bioconjugation Based on Inverse-Electron-Demand Diels–Alder Reactivity. *Journal of the American Chemical Society* **2008**, *130* (41), 13518-13519.
68. Lang, K.; Chin, J. W., Bioorthogonal Reactions for Labeling Proteins. *ACS Chemical Biology* **2014**, *9* (1), 16-20.
69. Johann, K.; Svatunek, D.; Seidl, C.; Rizzelli, S.; Bauer, T. A.; Braun, L.; Koynov, K.; Mikula, H.; Barz, M., Tetrazine- and trans-cyclooctene-functionalised polypept(o)ides for fast bioorthogonal tetrazine ligation. *Polymer Chemistry* **2020**, *11* (27), 4396-4407.
70. García-Maceira, T.; García-Maceira, F. I.; González-Reyes, J. A.; Torres-Sánchez, L. A.; Aragón-Gómez, A. B.; García-Rubiño, M. E.; Paz-Rojas, E., Covalent Immobilization of Antibodies through Tetrazine-TCO Reaction to Improve Sensitivity of ELISA Technique. *Biosensors (Basel)* **2021**, *11* (12).
71. Wang, P.; Na, Z.; Fu, J.; Tan, C. Y. J.; Zhang, H.; Yao, S. Q.; Sun, H., Microarray immobilization of biomolecules using a fast trans-cyclooctene (TCO)–tetrazine reaction. *Chemical Communications* **2014**, *50* (80), 11818-11821.
72. Chivers, Claire E.; Koner, Apurba L.; Lowe, Edward D.; Howarth, M., How the biotin–streptavidin interaction was made even stronger: investigation via crystallography and a chimaeric tetramer. *Biochemical Journal* **2011**, *435* (1), 55-63.

73. Karawdeniya, B. I.; Damry, A. M.; Murugappan, K.; Manjunath, S.; Bandara, Y. M. N. D. Y.; Jackson, C. J.; Tricoli, A.; Neshev, D., Surface Functionalization and Texturing of Optical Metasurfaces for Sensing Applications. *Chemical Reviews* **2022**, *122* (19), 14990-15030.
74. Darko, A.; Wallace, S.; Dmitrenko, O.; Machovina, M. M.; Mehl, R. A.; Chin, J. W.; Fox, J. M., Conformationally strained trans-cyclooctene with improved stability and excellent reactivity in tetrazine ligation. *Chemical Science* **2014**, *5* (10), 3770-3776.
75. Clause, K. C.; Liu, L. J.; Tobita, K., Directed stem cell differentiation: the role of physical forces. *Cell communication & adhesion* **2010**, *17* (2), 48-54.
76. Galior, K.; Liu, Y.; Yehl, K.; Vivek, S.; Salaita, K., Titin-Based Nanoparticle Tension Sensors Map High-Magnitude Integrin Forces within Focal Adhesions. *Nano Letters* **2016**, *16* (1), 341-348.
77. Buchardt, O.; Egholm, M.; Berg, R. H.; Nielsen, P. E., Peptide nucleic acids and their potential applications in biotechnology. *Trends in Biotechnology* **1993**, *11* (9), 384-386.
78. Nielsen, P. E.; Egholm, M.; Berg, R. H.; Buchardt, O., Sequence-selective recognition of DNA by strand displacement with a thymine-substituted polyamide. *Science* **1991**, *254* (5037), 1497.
79. Nielsen, P. E.; Egholm, M., An introduction to peptide nucleic acid. *Current issues in molecular biology* **1999**, *1* (1-2), 89-104.
80. Quijano, E.; Bahal, R.; Ricciardi, A.; Saltzman, W. M.; Glazer, P. M., Therapeutic Peptide Nucleic Acids: Principles, Limitations, and Opportunities. *The Yale journal of biology and medicine* **2017**, *90* (4), 583-598.
81. Rasmussen, H.; Kastrup, J. S.; Nielsen, J. N.; Nielsen, J. M.; Nielsen, P. E., Crystal structure of a peptide nucleic acid (PNA) duplex at 1.7 Å resolution. *Nature Structural Biology* **1997**, *4*, 98.
82. Sinden, R. R., *DNA Structure and Function*. Elsevier Science: 1994.
83. De Costa, N. T. S.; Heemstra, J. M., Evaluating the effect of ionic strength on duplex stability for PNA having negatively or positively charged side chains. *PloS one* **2013**, *8* (3), e58670-e58670.

84. Hur, D.; Kim, M. S.; Song, M.; Jung, J.; Park, H., Detection of genetic variation using dual-labeled peptide nucleic acid (PNA) probe-based melting point analysis. *Biological procedures online* **2015**, *17*, 14-14.
85. Totsingan, F.; Marchelli, R.; Corradini, R., Molecular computing by PNA:PNA duplex formation. *Artificial DNA, PNA & XNA* **2011**, *2* (1), 16-22.
86. Wang, G.; Xu, X. S., Peptide nucleic acid (PNA) binding-mediated gene regulation. *Cell Research* **2004**, *14* (2), 111-116.
87. Schwarz, F. P.; Robinson, S.; Butler, J. M., Thermodynamic comparison of PNA/DNA and DNA/DNA hybridization reactions at ambient temperature. *Nucleic Acids Res* **1999**, *27* (24), 4792-800.
88. Cao, M.; Deng, L.; Xu, H., Study of PNA–DNA hybridization by AFM-based single-molecule force spectroscopy. *Colloids and Surfaces A: Physicochemical and Engineering Aspects* **2015**, *470*, 46-51.
89. Dutta, S.; Armitage, B. A.; Lyubchenko, Y. L., Probing of miniPEG $\gamma$ -PNA-DNA Hybrid Duplex Stability with AFM Force Spectroscopy. *Biochemistry* **2016**, *55* (10), 1523-1528.
90. Rogers, J. D.; Richardson, W. J., Fibroblast mechanotransduction network predicts targets for mechano-adaptive infarct therapies. *eLife* **2022**, *11*, e62856.
91. Chiquet, M.; Gelman, L.; Lutz, R.; Maier, S., From mechanotransduction to extracellular matrix gene expression in fibroblasts. *Biochimica et Biophysica Acta (BBA) - Molecular Cell Research* **2009**, *1793* (5), 911-920.
92. Schwartz, M. A., Integrins and extracellular matrix in mechanotransduction. *Cold Spring Harb Perspect Biol* **2010**, *2* (12), a005066-a005066.
93. Kechagia, J. Z.; Ivaska, J.; Roca-Cusachs, P., Integrins as biomechanical sensors of the microenvironment. *Nat. Rev. Mol. Cell Biol.* **2019**, *20* (8), 457-473.
94. Schürpf, T.; Springer, T. A., Regulation of integrin affinity on cell surfaces. *EMBO J.* **2011**, *30* (23), 4712-4727.
95. Wang, J.-h., Pull and push: Talin activation for integrin signaling. *Cell Res.* **2012**, *22* (11),

1512-1514.

96. Li, J.; Su, Y.; Xia, W.; Qin, Y.; Humphries, M. J.; Vestweber, D.; Cabañas, C.; Lu, C.; Springer, T. A., Conformational equilibria and intrinsic affinities define integrin activation. *EMBO J.* **2017**, *36* (5), 629-645.
97. Li, J.; Springer, T. A., Energy landscape differences among integrins establish the framework for understanding activation. *J. Cell. Biol.* **2017**, *217* (1), 397-412.
98. Welf, E. S.; Naik, U. P.; Ogunnaike, B. A., A spatial model for integrin clustering as a result of feedback between integrin activation and integrin binding. *Biophys J* **2012**, *103* (6), 1379-1389.
99. Case, L. B.; Waterman, C. M., Integration of actin dynamics and cell adhesion by a three-dimensional, mechanosensitive molecular clutch. *Nat. Cell Biol.* **2015**, *17* (8), 955-963.
100. Elosegui-Artola, A.; Oria, R.; Chen, Y.; Kosmalka, A.; Pérez-González, C.; Castro, N.; Zhu, C.; Trepap, X.; Roca-Cusachs, P., Mechanical regulation of a molecular clutch defines force transmission and transduction in response to matrix rigidity. *Nat. Cell Biol.* **2016**, *18* (5), 540-548.
101. Elosegui-Artola, A.; Trepap, X.; Roca-Cusachs, P., Control of Mechanotransduction by Molecular Clutch Dynamics. *Trends Cell Biol.* **2018**, *28* (5), 356-367.
102. Tan, S. J.; Chang, A. C.; Anderson, S. M.; Miller, C. M.; Prael, L. S.; Odde, D. J.; Dunn, A. R., Regulation and dynamics of force transmission at individual cell-matrix adhesion bonds. *Sci. Adv.* **2020**, *6* (20), eaax0317.
103. Lo, C.-M.; Wang, H.-B.; Dembo, M.; Wang, Y.-l., Cell movement is guided by the rigidity of the substrate. *Biophys J* **2000**, *79* (1), 144-152.
104. Califano, J. P.; Reinhart-King, C. A., Substrate Stiffness and Cell Area Predict Cellular Traction Stresses in Single Cells and Cells in Contact. *Cell Mol Bioeng* **2010**, *3* (1), 68-75.
105. Ghassemi, S.; Meacci, G.; Liu, S.; Gondarenko, A. A.; Mathur, A.; Roca-Cusachs, P.; Sheetz, M. P.; Hone, J., Cells test substrate rigidity by local contractions on submicrometer pillars. *Proc. Natl. Acad. Sci. U. S. A.* **2012**, *109* (14), 5328.

106. Wang, X.; Ha, T., Defining single molecular forces required to activate integrin and notch signaling. *Science* **2013**, *340* (6135), 991-994.
107. Liu, Y.; Blanchfield, L.; Ma, V. P.-Y.; Andargachew, R.; Galior, K.; Liu, Z.; Evavold, B.; Salaita, K., DNA-based nanoparticle tension sensors reveal that T-cell receptors transmit defined pN forces to their antigens for enhanced fidelity. *Proc. Natl. Acad. Sci. U. S. A.* **2016**, *113* (20), 5610.
108. Sarkar, A.; LeVine, D. N.; Kuzmina, N.; Zhao, Y.; Wang, X., Cell Migration Driven by Self-Generated Integrin Ligand Gradient on Ligand-Labile Surfaces. *Curr. Biol.* **2020**, *30* (20), 4022-4032.e5.
109. Glazier, R.; Brockman, J. M.; Bartle, E.; Mattheyses, A. L.; Destaing, O.; Salaita, K., DNA mechanotechnology reveals that integrin receptors apply pN forces in podosomes on fluid substrates. *Nat. Commun.* **2019**, *10* (1), 4507.
110. Ma, V. P.-Y.; Hu, Y.; Kellner, A. V.; Brockman, J. M.; Velusamy, A.; Blanchard, A. T.; Evavold, B. D.; Alon, R.; Salaita, K., The magnitude of LFA-1/ICAM-1 forces fine-tune TCR-triggered T cell activation. *Sci. Adv.* **2022**, *8* (8), eabg4485.
111. Rashid, S. A.; Blanchard, A. T.; Combs, J. D.; Fernandez, N.; Dong, Y.; Cho, H. C.; Salaita, K., DNA Tension Probes Show that Cardiomyocyte Maturation Is Sensitive to the Piconewton Traction Forces Transmitted by Integrins. *ACS Nano* **2022**, 10.1021/acsnano.1c04303.
112. Wang, X.; Sun, J.; Xu, Q.; Chowdhury, F.; Roein-Peikar, M.; Wang, Y.; Ha, T., Integrin Molecular Tension within Motile Focal Adhesions. *Biophys J* **2015**, *109* (11), 2259-2267.
113. Li, H.; Zhang, C.; Hu, Y.; Liu, P.; Sun, F.; Chen, W.; Zhang, X.; Ma, J.; Wang, W.; Wang, L.; Wu, P.; Liu, Z., A reversible shearing DNA probe for visualizing mechanically strong receptors in living cells. *Nat. Cell Biol.* **2021**, *23* (6), 642-651.
114. Galior, K.; Liu, Y.; Yehl, K.; Vivek, S.; Salaita, K., Titin-Based Nanoparticle Tension Sensors Map High-Magnitude Integrin Forces within Focal Adhesions. *Nano Lett.* **2016**, *16* (1), 341-348.
115. Blakely, B. L.; Dumelin, C. E.; Trappmann, B.; McGregor, L. M.; Choi, C. K.; Anthony, P. C.; Duesterberg, V. K.; Baker, B. M.; Block, S. M.; Liu, D. R.; Chen, C. S., A DNA-based molecular probe for optically reporting cellular traction forces. *Nat. Methods* **2014**, *11* (12), 1229-1232.

116. Chowdhury, F.; Li, I. T. S.; Leslie, B. J.; Doğanay, S.; Singh, R.; Wang, X.; Seong, J.; Lee, S.-H.; Park, S.; Wang, N.; Ha, T., Single molecular force across single integrins dictates cell spreading. *Integr. Biol.* **2015**, *7* (10), 1265-1271.
117. LaCroix, A. S.; Lynch, A. D.; Berginski, M. E.; Hoffman, B. D., Tunable molecular tension sensors reveal extension-based control of vinculin loading. *eLife* **2018**, *7*, e33927.
118. Fisher, T. E.; Marszalek, P. E.; Oberhauser, A. F.; Carrion-Vazquez, M.; Fernandez, J. M., The micro-mechanics of single molecules studied with atomic force microscopy. *J. Physiol.* **1999**, *520* (1), 5-14.
119. Kong, F.; Garcia, A. J.; Mould, A. P.; Humphries, M. J.; Zhu, C., Demonstration of catch bonds between an integrin and its ligand. *J. Cell. Biol.* **2009**, *185* (7), 1275-1284.
120. Strohmeyer, N.; Bharadwaj, M.; Costell, M.; Fassler, R.; Muller, D. J., Fibronectin-bound alpha5beta1 integrins sense load and signal to reinforce adhesion in less than a second. *Nat. Mater.* **2017**, *16* (12), 1262-1270.
121. Chen, Y.; Lee, H.; Tong, H.; Schwartz, M.; Zhu, C., Force regulated conformational change of integrin  $\alpha V\beta 3$ . *Matrix Biol.* **2017**, *60*, 70-85.
122. Kong, F.; Li, Z.; Parks, W. M.; Dumbauld, D. W.; García, A. J.; Mould, A. P.; Humphries, M. J.; Zhu, C., Cyclic mechanical reinforcement of integrin-ligand interactions. *Mol. Cell* **2013**, *49* (6), 1060-1068.
123. Zhang, Y.; Ge, C.; Zhu, C.; Salaita, K., DNA-based digital tension probes reveal integrin forces during early cell adhesion. *Nat. Commun.* **2014**, *5*, 5167.
124. Bender, R. L.; Salaita, K., Molecular Force Sensors. In *ACS In Focus* [Online] American Chemical Society: 2021; pp. -1. <https://doi.org/10.1021/acsinfocus.7e4008>.
125. Mergny, J. L.; Lacroix, L., Analysis of thermal melting curves. *Oligonucleotides* **2003**, *13* (6), 515-537.
126. Brockman, J. M.; Su, H.; Blanchard, A. T.; Duan, Y.; Meyer, T.; Quach, M. E.; Glazier, R.; Bazrafshan, A.; Bender, R. L.; Kellner, A. V.; Ogasawara, H.; Ma, R.; Schueder, F.; Petrich, B. G.; Jungmann, R.; Li, R.; Mattheyses, A. L.; Ke, Y.; Salaita, K., Live-cell super-resolved PAINT imaging of piconewton cellular traction forces. *Nat. Methods* **2020**, *17* (10), 1018-1024.

127. Woodside, M. T.; Behnke-Parks, W. M.; Larizadeh, K.; Travers, K.; Herschlag, D.; Block, S. M., Nanomechanical measurements of the sequence-dependent folding landscapes of single nucleic acid hairpins. *Proc. Natl. Acad. Sci. U. S. A.* **2006**, *103* (16), 6190.
128. Zhang, Y.; Qiu, Y.; Blanchard, A. T.; Chang, Y.; Brockman, J. M.; Ma, V. P.; Lam, W. A.; Salaita, K., Platelet integrins exhibit anisotropic mechanosensing and harness piconewton forces to mediate platelet aggregation. *Proc. Natl. Acad. Sci. U. S. A.* **2018**, *115* (2), 325-330.
129. Brockman, J. M.; Blanchard, A. T.; Pui-Yan, V.; Derricotte, W. D.; Zhang, Y.; Fay, M. E.; Lam, W. A.; Evangelista, F. A.; Mattheyses, A. L.; Salaita, K., Mapping the 3D orientation of piconewton integrin traction forces. *Nat. Methods* **2018**, *15* (2), 115-118.
130. Duan, Y.; Glazier, R.; Bazrafshan, A.; Hu, Y.; Rashid, S. A.; Petrich, B. G.; Ke, Y.; Salaita, K., Mechanically Triggered Hybridization Chain Reaction. *Angew. Chem. Int. Ed.* **2021**, *60* (36), 19974-19981.
131. Hu, Y.; Ma, V. P.-Y.; Ma, R.; Chen, W.; Duan, Y.; Glazier, R.; Petrich, B.; Li, R.; Salaita, K., DNA-based microparticle tension sensors ( $\mu$ TS) for measuring cell mechanics in non-planar geometries and for high-throughput quantification. *Angew. Chem. Int. Ed.* **2021**, *n/a* (n/a).
132. Blanchard, A.; Combs, J. D.; Brockman, J. M.; Kellner, A. V.; Glazier, R.; Su, H.; Bender, R. L.; Bazrafshan, A. S.; Chen, W.; Quach, M. E.; Li, R.; Mattheyses, A. L.; Salaita, K., Turn-key mapping of cell receptor force orientation and magnitude using a commercial structured illumination microscope. *Nat. Commun.* **2021**, *12* (1), 4693.
133. Roy, B.; Yuan, L.; Lee, Y.; Bharti, A.; Mitra, A.; Shivashankar, G. V., Fibroblast rejuvenation by mechanical reprogramming and redifferentiation. *Proc. Natl. Acad. Sci. U. S. A.* **2020**, *117* (19), 10131.
134. Peng, G. E.; Wilson, S. R.; Weiner, O. D., A pharmacological cocktail for arresting actin dynamics in living cells. *Mol. Biol. Cell* **2011**, *22* (21), 3986-3994.
135. Panciera, T.; Azzolin, L.; Cordenonsi, M.; Piccolo, S., Mechanobiology of YAP and TAZ in physiology and disease. *Nat. Rev. Mol. Cell Biol.* **2017**, *18* (12), 758-770.
136. Jalal, S.; Shi, S.; Acharya, V.; Huang, R. Y.-J.; Viasnoff, V.; Bershadsky, A. D.; Tee, Y. H., Actin cytoskeleton self-organization in single epithelial cells and fibroblasts under

- isotropic confinement. *J Cell Sci* **2019**, *132* (5), jcs220780.
137. To, W. S.; Midwood, K. S., Plasma and cellular fibronectin: distinct and independent functions during tissue repair. *Fibrogenesis & Tissue Repair* **2011**, *4* (1), 21.
138. Su, Y.; Xia, W.; Li, J.; Walz, T.; Humphries, M. J.; Vestweber, D.; Cabañas, C.; Lu, C.; Springer, T. A., Relating conformation to function in integrin  $\alpha 5\beta 1$ . *Proc. Natl. Acad. Sci. U. S. A.* **2016**, *113* (27), E3872-81.
139. López-Ceballos, P.; Herrera-Reyes, A. D.; Coombs, D.; Tanentzapf, G., In vivo regulation of integrin turnover by outside-in activation. *J Cell Sci* **2016**, *129* (15), 2912-24.
140. Hostetler, M. J.; Templeton, A. C.; Murray, R. W., Dynamics of Place-Exchange Reactions on Monolayer-Protected Gold Cluster Molecules. *Langmuir* **1999**, *15* (11), 3782-3789.
141. Shen, B. Q.; Xu, K.; Liu, L.; Raab, H.; Bhakta, S.; Kenrick, M.; Parsons-Reponte, K. L.; Tien, J.; Yu, S. F.; Mai, E.; Li, D.; Tibbitts, J.; Baudys, J.; Saad, O. M.; Scales, S. J.; McDonald, P. J.; Hass, P. E.; Eigenbrot, C.; Nguyen, T.; Solis, W. A.; Fuji, R. N.; Flagella, K. M.; Patel, D.; Spencer, S. D.; Khawli, L. A.; Ebens, A.; Wong, W. L.; Vandlen, R.; Kaur, S.; Sliwkowski, M. X.; Scheller, R. H.; Polakis, P.; Junutula, J. R., Conjugation site modulates the in vivo stability and therapeutic activity of antibody-drug conjugates. *Nat. Biotechnol.* **2012**, *30* (2), 184-9.
142. Bosaeus, N.; El-Sagheer, A. H.; Brown, T.; Åkerman, B.; Nordén, B., Force-induced melting of DNA--evidence for peeling and internal melting from force spectra on short synthetic duplex sequences. *Nucleic Acids Res.* **2014**, *42* (12), 8083-91.
143. Romano, F.; Chakraborty, D.; Doye, J. P.; Ouldrige, T. E.; Louis, A. A., Coarse-grained simulations of DNA overstretching. *J. Chem. Phys.* **2013**, *138* (8), 085101.
144. Ham, T. R.; Collins, K. L.; Hoffman, B. D., Molecular tension sensors: moving beyond force. *Curr. Opin. Biomed. Eng.* **2019**, *12*, 83-94.
145. Li, J.; Springer Timothy, A., Integrin extension enables ultrasensitive regulation by cytoskeletal force. *Proc. Natl. Acad. Sci. U. S. A.* **2017**, *114* (18), 4685-4690.
146. Nordenfelt, P.; Elliott, H. L.; Springer, T. A., Coordinated integrin activation by actin-dependent force during T-cell migration. *Nat. Commun.* **2016**, *7* (1), 1-15.

147. Parsons, J. T.; Horwitz, A. R.; Schwartz, M. A., Cell adhesion: integrating cytoskeletal dynamics and cellular tension. *Nat. Rev. Mol. Cell Biol.* **2010**, *11* (9), 633-643.
148. Swaminathan, V.; Kalappurakkal, J. M.; Mehta, S. B.; Nordenfelt, P.; Moore, T. I.; Koga, N.; Baker, D. A.; Oldenbourg, R.; Tani, T.; Mayor, S., Actin retrograde flow actively aligns and orients ligand-engaged integrins in focal adhesions. *Proc. Natl. Acad. Sci. U. S. A.* **2017**, *114* (40), 10648-10653.
149. Mitchison, T.; Kirschner, M., Cytoskeletal dynamics and nerve growth. *Neuron* **1988**, *1* (9), 761-772.
150. Elosegui-Artola, A.; Trepap, X.; Roca-Cusachs, P., Control of Mechanotransduction by Molecular Clutch Dynamics. *Trends in Cell Biology* **2018**, *28* (5), 356-367.
151. Kubow, K. E.; Vukmirovic, R.; Zhe, L.; Klotzsch, E.; Smith, M. L.; Gourdon, D.; Luna, S.; Vogel, V., Mechanical forces regulate the interactions of fibronectin and collagen I in extracellular matrix. *Nature communications* **2015**, *6* (1), 8026.
152. Singh, P.; Carraher, C.; Schwarzbauer, J. E., Assembly of fibronectin extracellular matrix. *Annu Rev Cell Dev Biol* **2010**, *26*, 397-419.
153. Baneyx, G.; Baugh, L.; Vogel, V., Fibronectin extension and unfolding within cell matrix fibrils controlled by cytoskeletal tension. *Proceedings of the National Academy of Sciences* **2002**, *99* (8), 5139-5143.
154. Lin, G. L.; Cohen, D. M.; Desai, R. A.; Breckenridge, M. T.; Gao, L.; Humphries, M. J.; Chen, C. S., Activation of beta 1 but not beta 3 integrin increases cell traction forces. *FEBS Lett* **2013**, *587* (6), 763-9.
155. Hail, M. E.; Elliott, B.; Anderson, K., High-Throughput Analysis of Oligonucleotides Using Automated Electrospray Ionization Mass Spectrometry. *Am. Biotechnol. Lab.* **2004**, *12* (12), 12-14.
156. Zimmers, Z. A.; Adams, N. M.; Gabella, W. E.; Haselton, F. R., Fluorophore-Quencher Interactions Effect on Hybridization Characteristics of Complementary Oligonucleotides. *Anal Methods* **2019**, *11* (22), 2862-2867.
157. Harris, C. R.; Millman, K. J.; van der Walt, S. J.; Gommers, R.; Virtanen, P.; Cournapeau, D.; Wieser, E.; Taylor, J.; Berg, S.; Smith, N. J.; Kern, R.; Picus, M.;

- Hoyer, S.; van Kerkwijk, M. H.; Brett, M.; Haldane, A.; del Río, J. F.; Wiebe, M.; Peterson, P.; Gérard-Marchant, P.; Sheppard, K.; Reddy, T.; Weckesser, W.; Abbasi, H.; Gohlke, C.; Oliphant, T. E., Array programming with NumPy. *Nature* **2020**, *585* (7825), 357-362.
158. Virtanen, P.; Gommers, R.; Oliphant, T. E.; Haberland, M.; Reddy, T.; Cournapeau, D.; Burovski, E.; Peterson, P.; Weckesser, W.; Bright, J.; van der Walt, S. J.; Brett, M.; Wilson, J.; Millman, K. J.; Mayorov, N.; Nelson, A. R. J.; Jones, E.; Kern, R.; Larson, E.; Carey, C. J.; Polat, İ.; Feng, Y.; Moore, E. W.; VanderPlas, J.; Laxalde, D.; Perktold, J.; Cimrman, R.; Henriksen, I.; Quintero, E. A.; Harris, C. R.; Archibald, A. M.; Ribeiro, A. H.; Pedregosa, F.; van Mulbregt, P.; Vijaykumar, A.; Bardelli, A. P.; Rothberg, A.; Hilboll, A.; Kloeckner, A.; Scopatz, A.; Lee, A.; Rokem, A.; Woods, C. N.; Fulton, C.; Masson, C.; Häggström, C.; Fitzgerald, C.; Nicholson, D. A.; Hagen, D. R.; Pasechnik, D. V.; Olivetti, E.; Martin, E.; Wieser, E.; Silva, F.; Lenders, F.; Wilhelm, F.; Young, G.; Price, G. A.; Ingold, G.-L.; Allen, G. E.; Lee, G. R.; Audren, H.; Probst, I.; Dietrich, J. P.; Silterra, J.; Webber, J. T.; Slavič, J.; Nothman, J.; Buchner, J.; Kulick, J.; Schönberger, J. L.; de Miranda Cardoso, J. V.; Reimer, J.; Harrington, J.; Rodríguez, J. L. C.; Nunez-Iglesias, J.; Kuczynski, J.; Tritz, K.; Thoma, M.; Newville, M.; Kümmerer, M.; Bolingbroke, M.; Tartre, M.; Pak, M.; Smith, N. J.; Nowaczyk, N.; Shebanov, N.; Pavlyk, O.; Brodtkorb, P. A.; Lee, P.; McGibbon, R. T.; Feldbauer, R.; Lewis, S.; Tygier, S.; Sievert, S.; Vigna, S.; Peterson, S.; More, S.; Pudlik, T.; Oshima, T.; Pingel, T. J.; Robitaille, T. P.; Spura, T.; Jones, T. R.; Cera, T.; Leslie, T.; Zito, T.; Krauss, T.; Upadhyay, U.; Halchenko, Y. O.; Vázquez-Baeza, Y.; SciPy, C., SciPy 1.0: fundamental algorithms for scientific computing in Python. *Nat. Methods* **2020**, *17* (3), 261-272.
159. Reback, J., pandas-dev/pandas: Pandas 1.4.2. **2022**, doi:10.5281/zenodo.6408044.
160. Hunter, J. D., Matplotlib: A 2D Graphics Environment. *Compt. Sci. Eng.* **2007**, *9* (3), 90-95.
161. Engel, M. C.; Smith, D. M.; Jobst, M. A.; Sajfutdinow, M.; Liedl, T.; Romano, F.; Rovigatti, L.; Louis, A. A.; Doye, J. P. K., Force-Induced Unravelling of DNA Origami. *ACS Nano* **2018**, *12* (7), 6734-6747.
162. DeClerck, Y. A.; Mercurio, A. M.; Stack, M. S.; Chapman, H. A.; Zutter, M. M.; Muschel, R. J.; Raz, A.; Matrisian, L. M.; Sloane, B. F.; Noel, A.; Hendrix, M. J.; Coussens, L.; Padarathsingh, M., Proteases, extracellular matrix, and cancer: a workshop of the path B study section. *Am J Pathol* **2004**, *164* (4), 1131-1139.































